ABSTRACT

Title of dissertation: BROADBAND PERMITTIVITY CHARACTERIZATION OF TUNABLE DIELECTRIC THIN FILMS FOR MILLIMETER-WAVE DEVICES

Eric J. Marksz
Doctor of Philosophy, 2020

Dissertation directed by: Professor Ichiro Takeuchi
Department of Materials Science and Engineering
Dr. Nathan Orloff
National Institute of Standards and Technology

The use of millimeter-wave carrier frequencies has the potential to revolutionize wireless telecommunications by providing a massive increase in available bandwidth. However, millimeter-wave communications are hindered by poor atmospheric and building penetration, and require complicated RF front-end architectures. Tunable dielectric thin films offer a fast, compact, and cost-effective way to overcome many of the challenges facing the use of millimeter-wave spectrum. Few materials have been characterized in the millimeter-wave regime where measurements become increasingly challenging as test signal wavelengths approach the physical size of devices. The few tunable dielectric materials that have been studied at these frequencies suffered from high dielectric loss or other limitations. In this dissertation, we address both the measurement and materials challenges that have limited the commercial implementation of tunable millimeter-wave devices.

In this work, we describe our implementation of a unified on-wafer approach to measure the relative permittivity of thin films and substrates across a continuous frequency band from 100 Hz to 110 GHz. We achieve this ultra-wide bandwidth by combining electrical measurements of on-wafer planar capacitors and transmission lines, and use finite-element simulations to connect our electrical measurements to material properties.

Motivated by the need for better tunable dielectrics, we also developed a high-throughput technique to accelerate the discovery of tunable dielectric thin films. We discuss this technique, which is inspired by the principles of combinatorial materials science and the "Materials Genome Initiative". Our technique enables the characterization of many unique material compositions using a single 10 mm composition-spread thin film chip. In addition to speeding up the synthesis, fabrication, and measurement steps, the single-sample nature of this approach provides extreme consistency in the processing variables that impact dielectric properties.

Finally, we present another approach to tunable dielectric materials discovery with our development of $(SrTiO_3)_{n-1}(BaTiO_3)_1SrO$ thin films incorporating "targeted chemical pressure". These atomically-precise, strain-engineered superlattices achieve unparalleled performance, with measured relative tunability of almost 50 % and low dielectric loss even beyond 100 GHz. We discuss our use of the materials-by-design approach, which incorporates collaboration between theory, synthesis, and characterization, to overcome barriers to commercial integration without sacrificing advantageous material properties.

Broadband Permittivity Characterization of Tunable Dielectric Thin Films for Millimeter-wave Devices

by

Eric J. Marksz

Dissertation submitted to the Faculty of the Graduate School of the
University of Maryland, College Park in partial fulfillment
of the requirements for the degree of
Doctor of Philosophy
2020

Advisory Committee:
Professor Ichiro Takeuchi, Chair and Advisor
Professor Steven M. Anlage, Dean's Representative
Professor John P. Cumings
Dr. Nathan D. Orloff, Co-Advisor
Professor Lourdes G. Salamanca-Riba

© Copyright by
Eric J. Marksz
2020

Acknowledgements

I certainly couldn't have made it to where I am today without the help of so many mentors and friends, and my family.

Firstly, I thank my advisors Dr. Nathan Orloff and Prof. Ichiro Takeuchi. When I first encountered Nate during my Summer fellowship at NIST in 2014, I could tell I had found someone with infectious enthusiasm for research, and he has been both a mentor and friend since then. I've learned from Nate that the simple question "Why not?" can be a seed for profound ideas. Likewise, Ichiro empowered me to play a major role in setting the direction of my research. Regardless of my geographic location, Ichiro provided consistent guidance, feedback, and especially encouragement. I can't express how lucky I feel for the mentorship I've had during my graduate studies. I'd also like to thank the members of my committee, Prof. Steven Anlage, Prof. John Cumings, and Prof. Lourdes Salamanca-Riba for their insightful comments and questions on this work. Additionally, this work wouldn't have been possible without my key collaborators at Cornell, Natalie Dawley and Darrell Schlom, and our group leader at NIST, Jim Booth.

Along the way, there have been a few folks who have had greater influence than they probably realize on the path I've taken, particularly Mary Ellen Scott, Paul Bosley, Stergios Lazos, Bill Layton, and Helen Wetzler. I also appreciate all I learned from my undergraduate research advisor at Pitt, Prof. Jung-Kun Lee, my NIST SURF mentor Dr. Jabez McClelland, and my labmates in both groups.

Thank you to the friends I've made in Maryland (Yangang, Xiaohang, Seunghun, Naila, Gilad, John, and many more) and Colorado (Aaron, Angela, Nina,

Chris, Jasper, and many more) - for teaching me new experimental techniques, helping me out when I need a second opinion on something, and especially for making sure I don't forget how fun our work can be.

I owe a great deal to my family. Thank you to my brother, Michael, for sharing your hobbies with me, new and old, and always showing genuine interest in my research. Thank you to my sister, Amelia, for enjoying the great outdoors with me and dropping off excellent snacks to cheer me up when my projects seemed insurmountable. Most of all, thank you to my Mom, and my Dad. You've supported me, advocated for me, and challenged me to be my best since Day 1. The opportunities, friendship, and inspiration you've given me are immeasurable, and this wouldn't have been possible without you. Nothing would have been possible without you.

And finally, to my darling Youngsoo. Over the last seven years, we have forged a bond that has quite literally transcended space and time. Thank you for cheering me on when I faced challenges, and for celebrating the triumphs large and small. I can't wait for us to write the next chapter, together. 널 정말 사랑해.

Table of Contents

List of Tables viii

List of Figures ix

List of Abbreviations xvi

1 Overview and Introduction 1
- 1.1 Overview of dissertation 1
- 1.2 Tunable dielectric materials and tunable devices 3
  - 1.2.1 Historical perspective 3
  - 1.2.2 Tunable dielectric materials 5
    - 1.2.2.1 What makes a dielectric material "tunable"? 6
    - 1.2.2.2 Fundamental concepts of ferroelectricity 7
    - 1.2.2.3 Loss mechanisms in tunable dielectric materials . . . 14
    - 1.2.2.4 Why are permittivity measurements so important? . 18
  - 1.2.3 Tunable microwave and millimeter-wave devices 21
    - 1.2.3.1 The role of tunable devices in telecommunications . . 22
    - 1.2.3.2 Design and use of ferroelectric tunable devices 25

2 Relative permittivity characterization techniques for tunable thin films from 100 Hz to 110 GHz 29
- 2.1 Overview 29
  - 2.1.1 Comparison of permittivity characterization techniques 30
- 2.2 On-wafer thin film permittivity characterization with planar capacitors and transmission lines 34
  - 2.2.1 Measurement technique overview 35
  - 2.2.2 Measurement instrumentation 36
  - 2.2.3 On-wafer devices for permittivity characterization 39
    - 2.2.3.1 Co-planar Waveguides (CPWs) 39
    - 2.2.3.2 Planar Interdigital Capacitors (IDCs) 48
    - 2.2.3.3 Calibration-specific devices 51
  - 2.2.4 On-wafer device layouts and patterns 52
    - 2.2.4.1 Calibration chips 53
    - 2.2.4.2 Test samples 55
  - 2.2.5 Calibration procedures 57
    - 2.2.5.1 Calibration from 100 MHz to 110 GHz 59
    - 2.2.5.2 Calibration from 1 MHz to 100 MHz 62
    - 2.2.5.3 Calibration from 100 Hz to 1 MHz 63
  - 2.2.6 Test sample measurement and analysis 63
    - 2.2.6.1 Measurement and analysis of CPWs 64
    - 2.2.6.2 Measurement and analysis of IDCs 66
  - 2.2.7 Finite-element modeling (FEM) 70
    - 2.2.7.1 Resistance (R') and inductance (L') simulations . . . 72

2.2.7.2 Capacitance (C') and conductance (G') simulations . 73
2.2.8 Electric-field tunability measurements 76
2.3 Outlook 78

3 Broadband permittivity characterization of a homogeneous dielectric thin film 79
3.1 Overview 79
3.1.1 Material under test: $Ba_{0.5}Sr_{0.5}TiO_3$ 79
3.1.2 Growth and basic characterization of the $Ba_{0.5}Sr_{0.5}TiO_3$ film . 80
3.1.3 On-wafer devices and fabrication 82
3.2 Broadband permittivity measurements of the LSAT substrate and $Ba_{0.5}Sr_{0.5}TiO_3$ thin film 84
3.2.1 Measurements and analysis of CPWs 84
3.2.2 Measurements and analysis of IDCs 87
3.2.3 Extracting relative permittivity from the measured capacitance and conductance 90
3.3 Outlook 96

4 Broadband characterization of composition-spread tunable dielectric films 97
4.1 Overview: A need for faster materials discovery and development . . . 97
4.1.1 Accelerating materials discovery with combinatorial synthesis 98
4.1.2 Prior studies of composition-spread dielectric thin films 100
4.1.3 Measuring the millimeter-wave dielectric properties of composition-spread dielectric thin films 102
4.2 Synthesis of composition-spread thin films 103
4.2.1 Selection of materials system 103
4.2.2 Combinatorial pulsed laser deposition 103
4.3 Structural and compositional characterization 106
4.3.1 X-ray diffraction 106
4.3.2 Wavelength-dispersive x-ray spectroscopy 109
4.3.3 Atomic force microscopy 111
4.3.4 Scanning electron microscopy 111
4.4 Transmission line permittivity measurement technique for composition-spread thin films 112
4.4.1 Device selection, design, and fabrication 113
4.4.2 Complex permittivity and electric-field tunability measurement conditions 115
4.5 Broadband permittivity measurement of the $Ba_{1-x}Sr_xTiO_3$ composition-spread thin films 116
4.5.1 Composition-dependent permittivity of $Ba_{1-x}Sr_xTiO_3$ 116
4.5.2 Composition-dependent loss tangent of $Ba_{1-x}Sr_xTiO_3$ 119
4.5.3 Electric-field dependence of the permittivity 120
4.6 Modeling the composition-dependent permittivity behavior of $Ba_{1-x}Sr_xTiO_3$ 122
4.7 Outlook 125

5 Development and characterization of $(SrTiO_3)_{n-1}(BaTiO_3)_1SrO$ Ruddlesden-Popper superlattices 127
5.1 Overview: Ruddlesden-Popper phases, strain engineering, and targeted chemical pressure . . . 127
5.1.1 Ruddlesden-Popper tunable dielectric thin films . . . 127
5.1.2 Strain engineering to induce ferroelectricity . . . 130
5.1.3 The inherent limitations on strain-engineered materials . . . 132
5.1.4 Enabling thicker tunable films with targeted chemical pressure 134
5.2 Growth and structural analysis of $(SrTiO_3)_{n-1}(BaTiO_3)_1SrO$ thin films 138
5.2.1 Film synthesis . . . 138
5.2.2 Structural characterization . . . 140
5.2.2.1 X-ray diffraction measurements . . . 140
5.2.2.2 Transmission electron microscopy measurements . . . 141
5.3 Dielectric property measurements of the $(SrTiO_3)_{n-1}(BaTiO_3)_1SrO$ films . . . 144
5.3.1 Ferroelectric transition temperature measurements . . . 144
5.3.2 Complex permittivity of 100 nm thick $n = 6$ $(SrTiO_3)_{n-1}(BaTiO_3)_1SrO$ films . . . 145
5.3.3 Electric field dependence of the dielectric properties . . . 148
5.3.4 $(SrTiO_3)_{n-1}(BaTiO_3)_1SrO$ as a high-performance millimeter-wave tunable dielectric . . . 152
5.4 Discussion and outlook . . . 154

6 Conclusions and future directions 156
6.1 Summary of results . . . 156
6.2 Future Directions . . . 160
6.2.1 Metrology development . . . 160
6.2.2 Exploration of new materials . . . 163

A Additional relevant information 166
A.1 Publications related to this work . . . 166
A.2 Wafer-probing station configuration . . . 168
A.3 Electric-field dependent permittivity measurement configuration . . . 169
A.4 Bi-directional test patterns for measurements of anisotropic materials 170
A.5 Additional experimental data . . . 171

B Notable concepts and additional descriptive information pertaining to our permittivity measurements and analysis 174
B.1 Definition of S-parameters and conversion from a and b waves . . . 174
B.2 Conversion between S-parameters and T-parameters . . . 176
B.3 Conversion between S-parameters and Y-parameters . . . 176
B.4 Impedance transformers . . . 177
B.5 Calculating R', L', C' and G' from γ and Z_c . . . 178
B.6 Analysis and Error Propagation for CPW and IDC measurements . . . 179

C Detailed description of device fabrication techniques 187
C.1 Cleaning 188
C.2 Resist coating 189
C.3 Exposure 191
C.4 Developing 191
C.5 Deposition 192
C.6 Lift-off 193
C.7 Inspection and measurement 194

List of Tables

I A comparison of notable tunable RF technologies. Inspired by [32, 30]. 25

II Cole-Cole Model parameters and relative tunability of $Ba_{1-x}Sr_xTiO_3$ 124

List of Figures

1.1 (top) The "pseudo-cubic" tetragonal $BaTiO_3$ unit cell ($T < T_C$). (bottom left) In the absence of an applied field, the Ti^{4+} cation resides in the center of the unit cell if it has not been previously poled. (bottom middle) When an external electric field is applied (yellow arrow), the Ti^{4+} cation displaces along the axis of polarization (orange arrow), creating a net polarization. (bottom right) Even after the electric field is removed, it is energetically favorable for the ferroelectric $BaTiO_3$ to retain a spontaneous polarization. 8

1.2 The free energy vs. polarization landscape in the (left) ferroelectric and (right) paraelectric states of a second-order ferroelectric material. 10

1.3 The relative permittivity vs. electric field tuning curves in the (left) ferroelectric and (right) paraelectric states. 12

1.4 In the literature, there are large discrepancies in the measured loss tangents of ostensibly similar materials. Here we compare the measurements of $Ba_{1-x}Sr_xTiO_3$ films from Vorobiev *et al.* ($x = 0.75$) [59], Booth *et al.* ($x = 0.70$) [68], Zhang *et al.* ($x = 0.75$) [69], and Meyers *et al.* ($x = 0.71$) [46]. 19

1.5 (left) Global data traffic is predicted to continue growing exponentially, putting more strain on networks. (right) In addition to an increase in the amount of data consumed per device, the overall number of devices is increasing too. Internet-of-things (IoT) devices will make up about half of all connected devices by 2022, according to the Cisco VNI [71]. 22

1.6 (left) Atmospheric attenuation is a significant challenge facing millimeter-wave telecommunications [73, 77]. (right) Phased-array antennas can help mitigate atmospheric effects by creating powerful and agile directed beams. 24

1.7 The performance of an RF varactor depends heavily on the materials from which the device is made, and how the device is designed. Inspired by [85]. 26

2.1 There are many factors to consider when choosing the best dielectric property characterization technique for an experiment. Highlighted in bold are factors that are relevant to our work. 30

2.2 Permittivity characterization techniques use a variety of test fixtures for measurement. (left) The split-cylinder resonator technique. (center) A near-field scanning probe system. (right) On-wafer permittivity characterization devices. Images in the left and center panels have been reproduced from Ref. [42]. 32

2.3 We use on-wafer interdigital capacitors (IDCs) and co-planar waveguides (CPWs) to measure the relative permittivity of thin films from 100 Hz to 110 GHz. 33

2.4 Our typical measurement configuration includes two Source-Measure Units (SMUs) for DC resistance measurements, an LCR meter for measurements below 1 MHz, and one or two Vector Network Analyzers (VNAs) for measurements up to 110 GHz. The SMU and LCR meter test signals are routed through the VNA that is connected to the probes via phase-stable coaxial cables. 38
2.5 (top left) A plan-view image of a CPW with labels for several key parts of the device. (top right) A diagram of a CPW with the distributed circuit model used to describe transmission lines. (bottom) A cross-section diagram of the CPW which highlights how the electric fields in the CPW interact with the adjacent dielectric layers. 41
2.6 (left) α describes how the incident wave is attenuated as it travels along a transmission line of length, l. (right) β describes the phase shift of the propagating wave (dashed line) relative to the incident wave (*i.e.,* if $\beta = 0$, solid line) as it travels along a transmission line of length, l. 45
2.7 (left) A picture of a typical on-wafer IDC. (right) A diagram of the interdigitated portion of the IDC, highlighting the active length region and the π-network circuit model used to describe the IDCs. 49
2.8 Notable calibration-specific devices, including the short-circuit reflect (S1), series resistor (Rs), series capacitor (Cs), and series open (Os). The red dashed lines indicate the default reference planes. 51
2.9 A typical calibration chip with highlighted regions showing the different calibrations that can be performed. Non-highlighted regions hold duplicate devices for redundancy. 54
2.10 A test sample with the IDCs and CPWs highlighted. Additional devices are for redundancy or other experiments. 56
2.11 Calibrations allow us to "de-embed" the S-parameters of our on-wafer device (here, a 620 µm-long CPW transmission line) by correcting for the unwanted effects of cables, connectors, and probes that are included in the raw measurement data. 57
2.12 We measure multiple IDCs with different active lengths, and use the relationship between the admittance, $Y_{S,IDC}$, and the active length to determine the admittance per unit length of the active length region, Y_l'. We do this at every frequency point, f_n. 69
2.13 (left) We create finite element models of the on-wafer devices for our analysis. (center) The solver refines the mesh until the solution converges. (right) The electric fields are strongest in and around the gaps between the center conductor and ground planes of the CPWs. . 70
2.14 The simulated R' agrees quite well with the value estimated from measurement, indicating the validity of our 2D finite element model of the CPW transmission lines. 73
2.15 We use finite element modeling to obtain a mapping function relating the measured C' and G' to the real and imaginary parts of the relative permittivity, respectively. 75

2.16 A measurement of the permittivity of a tunable dielectric thin film from 1 GHz to 40 GHz, spanning applied fields from $-75\,\mathrm{kV\,cm^{-1}}$ to $75\,\mathrm{kV\,cm^{-1}}$ 77

3.1 (left) The $BaTiO_3$ unit cell. (right) The $Ba_{0.5}Sr_{0.5}TiO_3$ unit cell, showing the random substitution of some Ba^{2+} ions with Sr^{2+} ions. 80
3.2 A diagram illustrating the PLD growth process. 81
3.3 The $\Theta-2\Theta$ XRD scan of the 500 nm thick $Ba_{0.5}Sr_{0.5}TiO_3$ film, taken at room temperature, suggests a preferential orientation of the film matching that of the LSAT substrate. 82
3.4 A microscope image of the patterned companion substrate. 83
3.5 The components of the propagation constant for the substrate and film from 100 MHz to 110 GHz. 85
3.6 The resistance and inductance per unit length of the CPWs on the LSAT substrate. 86
3.7 The capacitance and conductance per unit length for the LSAT substrate and $Ba_{0.5}Sr_{0.5}TiO_3$ thin film sample. 87
3.8 The total measured capacitance of the four IDCs on the LSAT substrate (*i.e.,* I1 to I4). The *active length* of each IDC is noted in the legend. 88
3.9 (left) The total measured capacitance, C_{IDC}, vs. active length for the IDCs on the LSAT substrate. (right) The total measured conductance, G_{IDC}, vs. active length. Both panels include several lines - each line corresponds to a specific measured frequency point between 1 kHz and 1 MHz. 89
3.10 The broadband capacitance per unit length of the IDCs (C'_{IDC}) and of the CPWs (C') for the LSAT substrate and the $Ba_{0.5}Sr_{0.5}TiO_3$ film. The shaded regions denote the 95 % CIs 90
3.11 The mapping functions obtained from finite element simulations, which relate the measured capacitance per unit length to the relative permittivity of the thin film for the IDCs and CPWs. 91
3.12 The real part of the relative permittivity of the LSAT substrate and $Ba_{0.5}Sr_{0.5}TiO_3$ film, measured from 100 Hz to 110 GHz. Shaded regions indicate the 95 % CIs. 92
3.13 The measured loss tangent of the LSAT substrate and $Ba_{0.5}Sr_{0.5}TiO_3$ film, measured from 100 Hz to 110 GHz. Shaded regions indicate 95 % CIs. 93
3.14 The relative uncertainty in the measured dielectric constant of the $Ba_{0.5}Sr_{0.5}TiO_3$ film from 100 Hz to 110 GHz. 94

4.1 The Materials Genome Initiative seeks to leverage computational and experimental tools, as well as digital data, to discover and rapidly develop advanced materials to meet challenges in a variety of disciplines. From [116]. 98

4.2 The PLD chamber configured for combinatorial synthesis. The target carousel enables selection of the desired precursor target, and the shadow mask controls the spatial distribution of deposited material from the selected target. 104
4.3 The growth process of a composition spread thin film. Thickness wedges of the constituent materials are stacked in an alternating sequence to create the film. 105
4.4 $\Theta - 2\Theta$ XRD scan of the composition-spread film from $2\Theta = 10°$ to $2\Theta = 90°$ for a composition of approximately $x \approx 0.5$. 107
4.5 (top left) A short range $\Theta - 2\Theta$ scan confirmed that the $(202)_{subs}$ and $(202)_{film}$ peaks are adjacent. (top right) A schematic illustrating the relation between the film and substrate diffraction peaks. (bottom) Full-circle Φ scan of a single composition in the middle of the composition-spread film. 108
4.6 The diffraction pattern near the $(002)_{film}$ and $(002)_{subs}$ peaks illustrates the shift in the film lattice parameter across the composition gradient. 109
4.7 XRD and WDS scans were consistent with each other, and showed a linear gradient in the Ba/Sr ratio, as well as the BTO and STO regions on either side of the gradient region. 110
4.8 AFM scans at different points along the composition gradient. 111
4.9 Cross-sectional SEM image of a $Ba_{1-x}Sr_xTiO_3$ composition-spread film. Courtesy of Justin Pearson, UMD. 112
4.10 Optical microscope image of the patterned composition-spread $Ba_{1-x}Sr_xTiO_3$ chip. Each vertical column of devices corresponds to a complete multiline TRL measurement set which can be used to measure a unique point along the composition gradient. 114
4.11 (top) The composition-dependent dielectric constant curves at 1 GHz, 10 GHz and 110 GHz. (bottom) The frequency-dependent dielectric constant for all fourteen measured compositions x in $Ba_{1-x}Sr_xTiO_3$ from 100 MHz to 110 GHz. 118
4.12 The frequency-dependent loss tangent for all fourteen measured compositions x in $Ba_{1-x}Sr_xTiO_3$ from 100 MHz to 110 GHz. 119
4.13 The dielectric constant tuning curves for $Ba_{0.68}Sr_{0.32}TiO_3$ at 5 GHz, 20 GHz, and 40 GHz 120
4.14 The composition-dependent relative tunability, n_r, at measurement frequencies of 5 GHz, 20 GHz, and 40 GHz 121
4.15 The 40 GHz room temperature dielectric constant tuning curves for five notable compositions x in $Ba_{1-x}Sr_xTiO_3$ illustrating the shift in tuning behavior across the ferroelectric-paraelectric transition. 121
4.16 The Cole-Cole model parameters for all measured compositions x in $Ba_{1-x}Sr_xTiO_3$ 123

5.1 The unit cells of the $n = 2$ to 6 $(SrTiO_3)_{n-1}(BaTiO_3)_1SrO$ Ruddlesden-Popper superlattices. These are identical to the $(SrTiO_3)_nSrO$ Ruddlesden-Popper superlattices, with the exception of a BaO layer (red) substituted for a SrO layer. 128
5.2 Stoichiometric $n = 6$ $(SrTiO_3)_nSrO$ films incorporate horizontal $(SrO)_2$ planes every n layers in the growth direction (top left). These layers may also naturally form in the vertical direction (top right). The density of these vertical $(SrO)_2$ planes fluctuates in response to local non-stoichiometry (bottom left and right). From Ref. [64] 129
5.3 The device tunability of a planar microwave device increases with the thickness of the tunable thin film. Shown here are the results for simulated devices incorporating both $n = 6$ $(SrTiO_3)_nSrO$ films and more tunable $n = 6$ $(SrTiO_3)_{n-1}(BaTiO_3)_1SrO$ films. 133
5.4 First-principles calculations enabled us to determine the polar ground states of the Ruddlesden-Popper superlattices in a variety of strain conditions and atomic configurations. The most relevant calculations, shown here, guided our study to obtain thicker tunable, low-loss dielectric films. Theorist: Gerhard Olsen, Cornell 135
5.5 The low-strain case (0.8 % mismatch) (left) supports a small ferroelectric instability which allows for only a low degree of polarization. Randomly doping the perovskite layers with a larger A-site cation, can introduce an isotropic strain to the film which increases the in-plane polarization a small amount. However, if the larger cations are targeted into a single layer to create targeted chemical pressure, the increase can be significant. 136
5.6 A schematic of the molecular beam epitaxy chamber. 139
5.7 (left) The $\Theta - 2\Theta$ diffraction pattern for the 100 nm thick $n = 6$ $(SrTiO_3)_{n-1}(BaTiO_3)_1SrO$ film on $DyScO_3$. Substrate peaks are indicated by a $\star$. (right) Rocking curve comparing the width of the $(00\underline{28})_{film}$ and $(220)_{subs}$ peaks. Courtesy of Natalie Dawley, Cornell. . 141
5.8 HAADF-STEM (left) and bright field STEM (right) images of the $n = 6$ $(SrTiO_3)_{n-1}(BaTiO_3)_1SrO$ thin film on (110) $DyScO_3$. Note: each panel depicts a distinct region of the film. Microscopist: Megan Holtz, Cornell. 142
5.9 (top) Annular dark field (ADF) STEM images and EELS signals of the $n = 6$ $(SrTiO_3)_{n-1}(BaTiO_3)_1SrO$ film that illustrate the formation of the Ruddlesden-Popper structure and inclusion of the targeted BaO layer. (bottom) Larger-area STEM images that depict the horizontal and vertical $(SrO)_2$ planes that are present in the film. Microscopist: Megan Holtz, Cornell. 143

5.10 (left) The T_C as a function of n, obtained from the peak dielectric constant value (@ 10 kHz) observed during temperature sweeps. (right) The free energy landscape of the in-plane polar distortion for $n = 2, 4, 6$ compounds of the $(SrTiO_3)_{n-1}(BaTiO_3)_1SrO$ and $(SrTiO_3)_nSrO$ strained commensurately to (110) $DyScO_3$ substrates obtained from first-principles calculations. 145
5.11 The dielectric property measurement test devices patterned on the surface of the 100 nm $n = 6$ $(SrTiO_3)_{n-1}(BaTiO_3)_1SrO$ film. 146
5.12 The real and imaginary parts of the complex permittivity from 600 Hz to 110 GHz, including 95 % confidence intervals (shaded regions). 147
5.13 The dielectric constant and loss tangent of the 100 nm $n = 6$ $(SrTiO_3)_{n-1}(BaTiO_3)_1SrO$ film in the millimeter-wave telecommunications-relevant frequency bandwidth spanning from 10 GHz to 110 GHz. 148
5.14 The dielectric constant tuning curves for the $n = 6$ $(SrTiO_3)_{n-1}(BaTiO_3)_1SrO$ film at 5 GHz, 20 GHz, and 40 GHz. Also shown is the 40 GHz tuning curve for the $n = 6$ $(SrTiO_3)_nSrO$ film described in Ref. [64] and the 40 GHz tuning curve for the $Ba_{0.2}Sr_{0.8}TiO_3$ film described in Chapter 4. 149
5.15 The frequency-dependent dielectric constant of the 100 nm $n = 6$ $(SrTiO_3)_{n-1}(BaTiO_3)_1SrO$ film from 100 MHz to 40 GHz under a range of applied electric fields ranging from $0\,\mathrm{kV\,cm^{-1}}$ to $400\,\mathrm{kV\,cm^{-1}}$. 151
5.16 The frequency-dependent loss tangent of the 100 nm $n = 6$ $(SrTiO_3)_{n-1}(BaTiO_3)_1SrO$ film from 500 MHz to 40 GHz under a range of applied electric fields ranging from $0\,\mathrm{kV\,cm^{-1}}$ to $400\,\mathrm{kV\,cm^{-1}}$. 152
5.17 The figure of merit (FOM, eqn. 5.1 LaTeX Error: Can be used only in preambleSee the LaTeX manual or LaTeX Companion for explanation.Your command was ignored.Type I ¡command¿ ¡return¿ to replace it with another command,or ¡return¿ to continue without it.5.1) for the 100 nm $n = 6$ $(SrTiO_3)_{n-1}(BaTiO_3)_1SrO$ film, along with curves for other notable reports of high-performance tunable dielectric thin films for comparison. 153

A.1 One of the wafer-probing station configurations we use for the dielectric property measurements. 168
A.2 A diagram of the measurement instrumentation as configured for the electric-field dependent permittivity measurements. 169
A.3 An image showing how the bias tees are connected to the VNA. . . . 170
A.4 An image showing a bidirectional test pattern used to measure anisotropic materials. 171
A.5 The $\Theta - 2\Theta$ XRD patterns for the 50 nm thick $(SrTiO_3)_{n-1}(BaTiO_3)_1SrO$ films from $n = 2$ to $n = 6$. Courtesy of Natalie Dawley. 172

A.6 HAADF-STEM images of the the 50 nm thick $(SrTiO_3)_{n-1}(BaTiO_3)_1SrO$ films from $n = 2$ to $n = 6$. Microscopist: Megan Holtz. 173

B.1 A graphic illustrating the S-parameters for a two-port network. 175
B.2 Compared with a simulated value for the distributed resistance, R', the value extracted from γ and Z_c displays significant variation at high frequencies. 179

C.1 The general process flow sequence for lift-off fabrication of devices on chips and wafers. 187
C.2 An illustration of the key steps in our device fabrication process. . . . 188
C.3 Spin curves for the LOR 5A and LOR 10A resists. 190

List of Abbreviations

AC	Alternating Current
AFM	Atomic Force Microscopy
CI	Confidence Interval
CAD	Computer-Aided Design
CPW	Co-Planar Waveguide
DC	Direct Current
DFT	Density Functional Theory
DPT	Diffuse Phase Transition
DUT	Device Under Test
EELS	Electron Energy-Loss Spectroscopy
EPMA	Electron-Probe Micro-Analyzer
FEM	Finite-Element Method
FOM	Figure-Of-Merit
FDTD	Finite-Difference Time Domain
GSG	Ground-Signal-Ground
HAADF	High-Angle Annular Dark Field
HF	High Frequency
IDC	Inter-Digital Capacitor
LF	Low Frequency
LOR	Lift-Off Resist
MBE	Molecular Beam Epitaxy
MEMS	Micro-Electro-Mechanical System
MGI	Materials Genome Initiative
MMIC	Monolithic Microwave Integrated Circuit
NIST	U.S. National Institute of Standards and Technology
OSLT	Open-Short-Load-Thru
PCB	Printed Circuit Board
PLD	Pulsed Laser Deposition
PVD	Physical Vapor Deposition
RF	Radio-Frequency
RHEED	Reflection High-Energy Electron Diffraction
SMU	Source-Measure Unit
STEM	Scanning Transmission Electron Microscopy
T_C	Curie Temperature
TEM	Transmission Electron Microscopy
TEM	Transverse Electro-Magnetic
TRL	Thru-Reflect-Line
VNA	Vector Network Analyzer
WDS	Wavelength Dispersive X-Ray Spectroscopy
XRD	X-Ray Diffraction
Z_{REF}	Reference Impedance
Z_C	Characteristic Impedance

Chapter 1

Overview and Introduction

1.1 Overview of dissertation

This dissertation describes ideal techniques to measure the dielectric properties of thin films from 100 Hz to 110 GHz, and demonstrates these techniques by using them to measure a variety of tunable dielectric thin films that are relevant to adaptive electronics for next-generation telecommunications.

We begin by discussing the "Why?" and "How?" of this work. Chapter 1 provides fundamental background on tunable dielectric materials, explores some key challenges facing the commercial application of tunable dielectrics, and details how tunable devices can improve next-generation telecommunications. This chapter also introduces why accurate broadband measurements of the dielectric properties are crucial in facilitating the search for better materials. Chapter 2 continues that discussion and provides a detailed description of our measurement techniques. We demonstrate the practical application of these techniques in Chapter 3 by characterizing the dielectric properties of a homogeneous barium strontium titanate thin film.

The two subsequent chapters illustrate the value of combining our measurement techniques with novel concepts in materials science to rapidly explore and

develop new tunable dielectrics with enhanced properties. Chapter 4 details our design and optimization of a metrology scheme that leverages combinatorial synthesis to rapidly characterize the dielectric properties of composition-spread thin films. Chapter 5 discusses our use of the “materials by design” approach to develop and implement tunable dielectric superlattice films incorporating “targeted chemical pressure”, which have exceptional performance at millimeter-wave frequencies. This work enabled the growth of thicker strain-engineered tunable dielectric films - an important step toward production-scale integration.

1.2 Tunable dielectric materials and tunable devices

1.2.1 Historical perspective

The establishment of ferroelectricity in Rochelle Salt by Valasek a century ago revealed a class of materials with incredible technological potential [1]. Twenty years later, in the midst of the second World War, a desire for high-κ capacitors fueled research on the ferroelectric ABO_3-perovskite $BaTiO_3$ [2, 3, 4, 5, 6]. During that time, scientists developed a deeper understanding of the physics of ferroelectric ceramics, and began to theorize new devices based on these materials [7, 8, 9].

Ferroelectric ceramics, which also posses strong pyro- and piezo-electric properties quickly found their way into high-κ capacitors, thermistors, and acoustic transducers [10, 11, 12, 13, 14]. It took some time, however, for ferroelectric materials to be integrated into proper microwave-frequency electronics, with the first notable example appearing in 1962 and highlighting the interesting nonlinear electrical behavior of ferroelectrics for harmonic generation [15]. Although scientists continued to discover new ferroelectric compounds and develop the theory of ferroelectricity, there were few significant reports of ferroelectrics in microwave-frequency electronics for a number of years. Ferroelectric microwave devices returned to the spotlight in the 1990s when personal mobile communications began to flourish [16]. Up to that point, the largest application of ferroelectrics was in non-volatile memory [17, 18, 19]. Increased demand for miniaturized microwave devices and advances in materials and electronics technology precipitated an explosion in research on *tunable microwave devices*. In these devices, some aspect of the device performance, such as

operating frequency, can be modified on the fly. One of the most effective ways to create a tunable device is to incorporate ferroelectric materials.

During that boom in ferroelectrics research for high-frequency devices, there were significant advances in thin film synthesis, property enhancement through chemical doping or processing, and device integration [20, 21, 22, 23, 24]. While ferroelectrics for non-volatile memory devices were relatively well-developed, memory devices have different property requirements (large coercivity, long fatigue life, low current leakage) than tunable microwave devices (low dielectric loss, high relative tunability). Despite extensive research, tunable dielectric materials and devices remained more lossy and less tunable than was originally hoped [25]. Although some of the initial excitement tapered off, research on ferroelectrics for tunable microwave electronics remained a popular topic well in to the mid-2000s. A number of informative reviews and books on ferroelectric materials for microwave devices were written during and since that time [26, 27, 28, 29, 30, 31, 32, 33].

The emerging next generation of telecommunications yet again beckons the development of efficient tunable devices, not only in the microwave regime, but also in the millimeter-wave regime ($>$ 30 GHz) [34, 35, 36]. The wide available bandwidth at millimeter-wave frequencies supports high data-rate, low-latency communications, but operating in the millimeter-wave regime comes with additional complexity. Atmospheric attenuation and poor signal penetration through building materials necessitates the use of beam-forming electronics, and frequency-agile filters are needed to simplify the architecture of devices communicating across many frequency bands. Tunable dielectric materials offer an opportunity to realize these technologies in a

cost- and energy-efficient way.

Continued improvements to thin film processing, the application of computational modeling and informatics, and a few entirely new approaches to the design of ferroelectric materials have made commercially-viable tunable microwave and millimeter-wave devices seem more realistic [37, 38]. However, before designing a device, the constituent materials must be characterized extensively. While there are a number of techniques for measuring the electronic properties of tunable dielectric thin films at low microwave frequencies [39, 40, 41, 42, 43], reliable materials measurements at high microwave and millimeter-wave frequencies have lagged behind and only emerged within the last decade or so. During the previous rush of research on tunable dielectrics, the wide variety of characterization techniques may have even hindered the development of better tunable dielectrics by making it difficult to compare results across different reports in the literature. In many ways, the establishment of more standard and reliable characterization techniques is needed to facilitate the discovery of better tunable dielectrics for next-generation telecommunications devices.

1.2.2 Tunable dielectric materials

To fully appreciate the value of tunable devices and the remaining challenges facing their implementation, we must first have at least a cursory understanding of the principles of tunable dielectric materials. In the coming sections, we provide a brief - but by no means all-encompassing - primer on some of the aspects most

relevant to our work.

1.2.2.1 What makes a dielectric material "tunable"?

Dielectric materials are considered "tunable" when their relative permittivity changes *appreciably* in the presence of an external electric field. The relative permittivity, ε_r, is a complex-valued proportionality constant that describes the degree to which electric charge is displaced in the presence of some electric field, E. When studying tunable dielectric materials, we are concerned with the relative displacement of bound charge within dielectric media, expressed as the polarization of the charged species, P. With this in mind, the relative permittivity, ε_r, is:

$$\varepsilon_r \approx \frac{1}{\varepsilon_0}\frac{\partial P}{\partial E}, \tag{1.1}$$

where ε_0 is the permittivity of free space ($\varepsilon_0 = 8.854 \times 10^{-12}$ m^{-3} kg^{-1} s^4 A^2). The permittivity of a material is tunable when the quantity $\partial P/\partial E$ is itself dependent on the polarization, P. This dependence is strong in a class of technologically-relevant tunable dielectric materials known as ferroelectrics - even when these materials are not operating in the "ferroelectric state". In fact, most ferroelectric-based microwave devices operate in the "paraelectric state" [44]. The implications of this statement will be made more clear in the next section, in which we discuss some general principles of ferroelectricity.

1.2.2.2 Fundamental concepts of ferroelectricity

Ferroelectric materials can maintain a reversible spontaneous electrical polarization, even in the absence of an external electric field. In this way, ferroelectrics are the electrical analogue of ferromagnets and have some similar applications - such as non-volatile memory devices. In the same way that ferromagnetic materials become paramagnetic and lose their spontaneous magnetization above a certain temperature, ferroelectric materials become paraelectric above some temperature, T_C, called the ferroelectric Curie temperature. This ferroelectric-to-paraelectric transition often coincides with a structural phase transition in the material, for example, the tetragonal-to-cubic transition that occurs in $BaTiO_3$ on heating past 403 K [45].

$BaTiO_3$ is an approachable example of a ferroelectric crystal, due its simple ABO_3 perovskite-type structure. Figure 1.1 depicts the $BaTiO_3$ unit cell, with Ba^{2+} cations placed on corner "A" sites, the Ti^{4+} cation at the body-center "B" site, and O^{2-} anions located on the face centers. The O^{2-} anions form an octahedron surrounding the Ti^{4+} cation. Ferroelectric crystals belong exclusively to polar, non-centrosymmetric point groups [9]. For example, our ferroelectric $BaTiO_3$ has a "pseudo-cubic" tetragonal structure with non-centrosymmetric point group $4mm$, but becomes paraelectric and loses its spontaneous polarization when it transforms to the centrosymmetric cubic phase with point group $m\bar{3}m$ upon heating past T_C.

Figure 1.1 also illustrates the mechanics of the polarization process in $BaTiO_3$. Before the crystal is poled (i.e. before an external electric field is applied) the Ti^{4+} cation is centered in the oxygen octahedron. The Ti^{4+} cation shifts along the polar

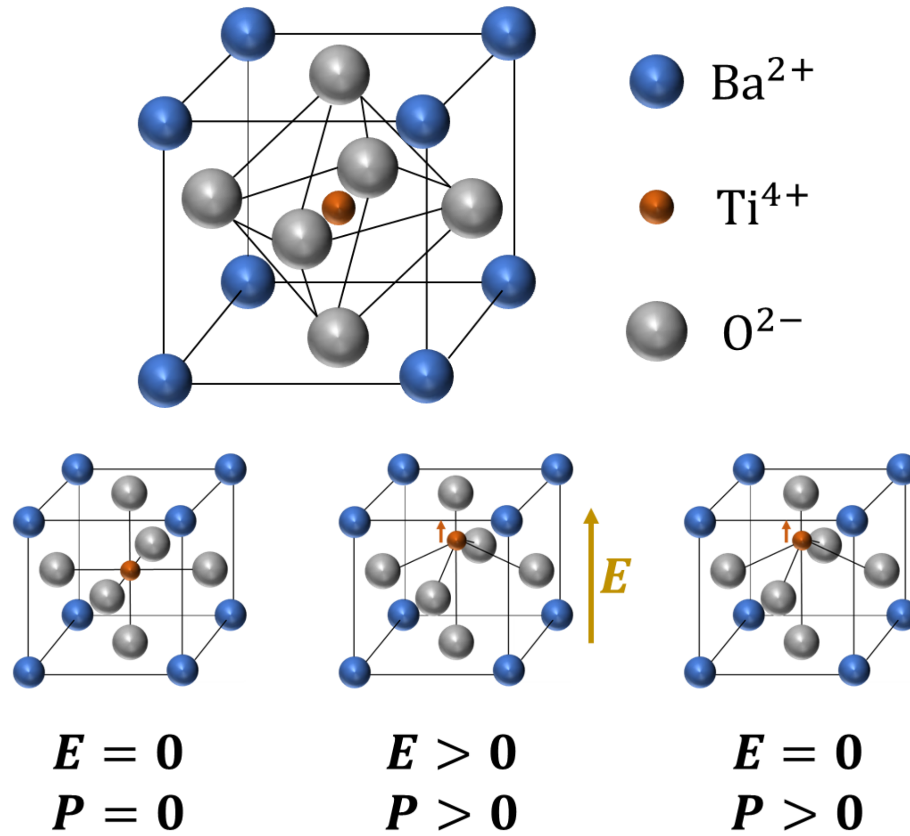

Figure 1.1. (top) The "pseudo-cubic" tetragonal $BaTiO_3$ unit cell ($T < T_C$). (bottom left) In the absence of an applied field, the Ti^{4+} cation resides in the center of the unit cell if it has not been previously poled. (bottom middle) When an external electric field is applied (yellow arrow), the Ti^{4+} cation displaces along the axis of polarization (orange arrow), creating a net polarization. (bottom right) Even after the electric field is removed, it is energetically favorable for the ferroelectric $BaTiO_3$ to retain a spontaneous polarization.

axis of the crystal (the “long” c-axis, parallel to the electric field vector in this example) in response to the external electric field. The relative displacement of the Ti^{4+} cation and the O^{2-} anions provides the net electrical polarization. Since the polarization arises from this sudden displacement in the material, $BaTiO_3$ is considered a “displacive-type” ferroelectric. The other type, “order-disorder” ferroelectrics, generally have low relative permittivity values and are not viable for tunable dielectric devices at microwave frequencies.

Ferroelectrics retain a spontaneous polarization because is energetically unfavorable for the Ti^{4+} cation to return to the center of the oxygen octahedron. This process is described by the Landau-Devonshire phenomenalogical theory [7]. Considering a simple one-dimensional crystal, the three-term expansion of the Helmholtz free energy, F, is:

$$F = \frac{\alpha}{2}P^2 + \frac{\beta}{4}P^4 + \frac{\gamma}{6}P^6 - EP, \tag{1.2}$$

where α, β, and γ are empirically determined coefficients and EP describes the electrostatic energy. The signs and magnitudes of α, β, and γ ultimately provide the free-energy underpinning of ferroelectric behavior. To begin, α is defined as:

$$\alpha = \frac{T - T_C}{C}, \tag{1.3}$$

where C is the Curie-Weiss constant with units of temperature and T_C is the Curie temperature. In all known ferroelectrics, C and the coefficient γ have positive values. Since C is positive, when $T < T_C$, α is negative. When α is negative, the free energy

is *lower* for non-zero polarizations within some small range before the higher-order terms in Equation 1.2 become dominant. We illustrate this concept in the left panel of Figure 1.2, which depicts the free-energy landscape for a second-order (*i.e.*, $\beta > 0$) ferroelectric material. This "double-well" potential disappears when T exceeds T_C and the material enters the paraelectric state where $\alpha > 0$. The free-energy landscape in the paraelectric state is shown in the right panel of Figure 1.2.

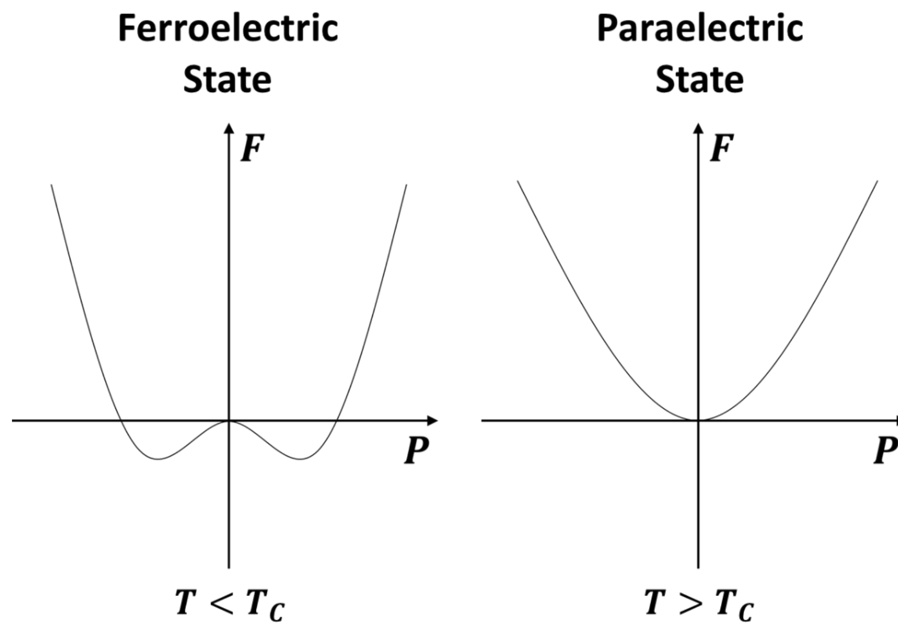

Figure 1.2. The free energy vs. polarization landscape in the (left) ferroelectric and (right) paraelectric states of a second-order ferroelectric material.

The interplay of the coefficients α, β, and γ dictates the observable dielectric behavior of a material, too. For example, the relative permittivity is linked to the curvature of the free-energy landscape and the magnitude of the spontaneous polarization corresponds to the location of the potential-well minima along the polarization axis. The locations of these potential-well minima occur where $\delta F/\delta P = 0$. When we consider that condition alongside Equation 1.3, we can obtain the equi-

librium relationship between the applied electric field and the polarization in our ferroelectric crystal:

$$E = \alpha P + \beta P^3 + \gamma P^5. \tag{1.4}$$

Finally, combining Equation 1.4 with Equation 1.1 yields an expression describing the relative permittivity of a material, which exhibits a non-linear dependence on the polarization:

$$\varepsilon_r = \frac{1}{\varepsilon_0}\frac{\partial P}{\partial E} = \frac{1}{\varepsilon_0}\frac{1}{\alpha + 3\beta P^2 + 5\gamma P^4}. \tag{1.5}$$

The origin of tunable relative permittivity in materials becomes clear when we consider Equation 1.5. As we manipulate the polarization with an electric field, the relative permittivity changes. In general, the application of such an external electric field "tunes" the relative permittivity of a ferroelectric material in the manner seen in Figure 1.3.

As the electric field is applied and the material is polarized, the relative permittivity decreases. Eventually, the rate of decrease slows and saturation occurs. This happens when the charged species in the material have displaced nearly as far as they can in the crystal lattice, so increasing the electric field strength leads to little additional polarization (see Eqn. 1.4). The dielectric breakdown strength of the material places a practical limit on the maximum applied field strength. If the applied electric field exceeds the breakdown strength, then a short-circuit failure can occur and permanently damage the material. Defects can reduce the breakdown strength;

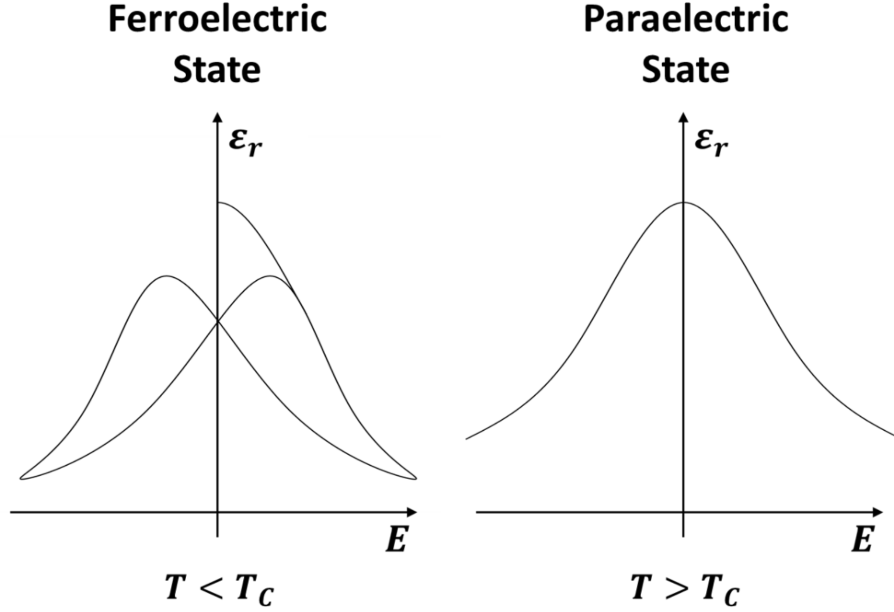

Figure 1.3. The relative permittivity vs. electric field tuning curves in the (left) ferroelectric and (right) paraelectric states.

sometimes breakdown will occur long before the tunability curve has saturated.

The hysteresis we observe in Figure 1.3 comes from the potential barrier between the two minima in the free-energy landscape of the ferroelectric state (Figure 1.2). As we discussed, the defining characteristic of ferroelectric materials is their ability to maintain a non-zero polarization after the external electric field has been removed. When the polarity of the applied electric field is reversed, there is some coercive electric field strength which much be applied in order overcome the energetic barrier and reverse the polarization of the material.

Equation 1.5 also hints at why the permittivity is greatest when T is near T_C. In we consider the un-polarized state ($P = 0$), Equation 1.5 can be rearranged to express the relative permittivity as:

$$\varepsilon_r = \frac{1}{\varepsilon_0} \frac{C}{T - T_C}. \tag{1.6}$$

As such, when T approaches T_C, the permittivity theoretically diverges. In most displacive-type ferroelectrics, the Curie-Weiss constant, C, is rather large - on the order of $\sim 10^5$ K. With such large values for C, these materials tend to have high relative permittivity ($\varepsilon_r > 300$) even several hundred degrees above T_C in the paraelectric state where losses are lower. High relative permittivity in the paraelectric state facilitates the use of these materials in miniaturized tunable devices.

The typical tuning behavior of a material in the paraelectric state is depicted in the right panel of Figure 1.3. Tunability persists in the paraelectric state near T_C for a similar reason that the relative permittivity is high, even far above T_C. When α is small, the bottom of the free-energy landscape is still relatively "flat", *i.e.,* $\partial F/\partial P$ is small. In this case, the energy cost to polarize the material is minimal, so the permittivity can still be tuned with an electric field. However, once T increases too far above T_C, α becomes large, and the walls of the potential well become so "steep" that no appreciable tuning can be observed.

Regardless if the material is in the paraelectric state or ferroelectric state, we use the relative tunability, n_r, to quantify how much the permittivity changes relative to the base, un-tuned value. This quantity is defined as:

$$n_r = \frac{\varepsilon_r(0) - \varepsilon_r(P_{DC})}{\varepsilon_r(0)}, \tag{1.7}$$

where $\varepsilon_r(0)$ is the relative permittivty in the absence of an external electric field (*i.e.,*

$E_{DC} = 0$) and $\varepsilon_r(P_{DC})$ is the permittivity of the material polarized by the external electric field E_{DC}. Under typical fields in the hundreds of kV/cm, a tunable dielectric thin film of $Ba_{0.25}Sr_{0.75}TiO_3$ which is paraelectric at room temperature can have a relative tunability of $n_r \approx 20\%$ to 40% [46]. On the other hand, a material like $Ba_{0.8}Sr_{0.2}TiO_3$ which is ferroelectric at room temperature can exhibit $n_r > 95\%$ [47]. Although the tunability is less, operation in the paraelectric state is generally preferable for device applications, since the dielectric losses are smaller. We explain why in the next section.

1.2.2.3 Loss mechanisms in tunable dielectric materials

Dielectric loss is the most significant obstacle to the implementation of tunable dielectric materials at millimeter-wave frequencies. This is because dielectric loss represents the conversion of some of the electromagnetic energy to thermal energy (*i.e.,* phonons). In addition to reducing the energy efficiency of devices, this leads to heating which can affect device operation. As we mentioned previously, the relative permittivity of a material is a *complex* quantity:

$$\varepsilon_r = \varepsilon' - i\varepsilon'' \tag{1.8}$$

where the real part, ε', is sometimes referred to as the dielectric constant of the material, especially at low frequencies, and the imaginary part, ε'', is the dielectric loss of the material. These two terms can be thought of as the components of the polarization response that are in-phase and out-of-phase with an applied AC field,

respectively. In one example, dielectric loss can occur when a particular polarization mechanism may be too “slow” to follow the rapidly oscillating electric field. When this happens, the oscillation of the polarization lags slightly behind the oscillation of the electric field, dissipating, rather than storing, some of the energy. This phenomenon is often referred to as “relaxation”.

When discussing dielectric materials for AC devices, losses are typically quantified using the loss tangent, $\tan\delta$. The loss tangent is the ratio of dielectric loss to the dielectric constant:

$$\tan\delta = \frac{\varepsilon''}{\varepsilon'} \tag{1.9}$$

High-loss materials ($\tan\delta > 0.2$) are not ideal for most device applications because the significant dissipation reduces power efficiency and complicates thermal management. There are several low-loss crystalline substrates for high-frequency integrated circuits, but tunable and high-dielectric constant films tend to be much lossier [33]. In tunable dielectric films at millimeter-wave frequencies, both *intrinsic* and *extrinsic* losses can be severe.

There are two categories of dielectric loss: *intrinsic* loss and *extrinsic* loss. Intrinsic losses are phonon-mediated losses that are present even in perfect single crystals [48]. The three- and four-quantum loss mechanisms are sources of intrinsic dielectric loss. In these mechanisms, one or two phonons, respectively, interact with a quantum of electromagnetic energy $\hbar\omega$ from the AC signal which is absorbed to produce a phonon with a slightly higher energy [49, 50]. In the three-quantum

mechanism, the extinguished and created phonons must be close in energy, since the quantum of microwave energy is typically several orders of magnitude smaller than the energy of the phonons. The addition of a second incident phonon in the four-quantum mechanism provides an extra degree of freedom regarding the extinguished and created phonon energies, but the probability of occurrence is reduced. Generally, three-quantum losses play a larger role in the overall dielectric loss at microwave and millimeter-wave frequencies [51].

Another notable intrinsic loss mechanism is quasi-Debye loss, which is similar to the three-quantum mechanism but describes transitions between the same phonon branch. These losses stem from the AC field-induced modulation of the phonon distribution function in non-centrosymmetric crystals [52]. In non-centrosymmetric materials, the phonon frequencies are linear functions of a small applied electric field. As a result an AC test signal can lead to time modulation of the distribution of phonon frequencies. The relaxation of the phonon distribution function leads to dielectric loss in a similar manner that the relaxation of gas dipoles leads to loss in the Debye theory, hence the quasi-Debye moniker [53]. This mechanism can be prominent in tunable dielectrics. Even when a tunable dielectric is used in the centrosymmetric, paraelectric state, the DC electric field used to induce tuning will drive the material to be non-centrosymmetric, opening the door for quasi-Debye losses. Quasi-Debye losses can exceed the three- and four-quantum losses in the microwave and millimeter-wave regime [54]. We refer the reader to Refs. [55, 56, 48, 25] for more in-depth discussion of quasi-Debye and other intrinsic loss mechanisms. In our work, we primarily focus on extrinsic losses, since they can be severe in tunable

dielectric films and in many ways provide more opportunities for improvement.

Extrinsic losses arise from defects in the material, such as point defects, dislocations, or grain boundaries [57, 58, 59, 60]. While grain boundaries can develop space charge that may negatively effect properties [61], point defects like oxygen vacancies are perhaps the most pernicious defect when it comes to tunable dielectric thin films [62]. These charged point defects move in response to the the AC field, transducing electromagnetic energy into acoustic waves that scatter and eventually decay. Extrinsic losses can dominate the overall loss in thin films because films often have large defect concentrations relative to bulk crystals [63]. Careful growth and processing techniques can reduce the extrinsic losses in tunable thin films in the microwave and millimeter-wave regimes [46]. Indeed, minimizing the number of point defects and mitigating their harmful effects has led to some of the best tunable dielectric films to date [64].

There are a couple additional sources of loss that only affect materials in the ferroelectric state. All ferroelectric materials are piezoelectric and naturally transduce some of the AC electromagnetic signal to acoustic waves. Additionally, the frictional motion of ferroelectric domain walls increases loss [65], though one interesting study took advantage of resonant domain wall motion to enhance properties in a narrow band [47].

Tunable dielectric devices can avoid piezoelectric and domain wall losses by operating the paraelectric state. However, in some circumstances, these losses can be present in the paraelectric state, albeit to a much smaller degree. Local strain fields or charge near defects can stabilize "nano-polar regions" (NPRs) [66, 67].

Though the theoretical understanding of NPRs is limited, these regions appear to act as small, polar ferroelectric volumes in the material even above T_C, increasing the overall loss tangent.

Much of the burst of research on tunable dielectric films in the early 2000s attempted to reduce losses to low levels ($\tan\delta < 0.02$) without decreasing relative tunability ($n_r > 50\%$) by optimizing processing conditions to improve crystallinity and reduce defect concentrations. However, truly ideal properties for tunable devices remain elusive in the millimeter-wave regime without complicated synthesis or other constraints that inhibit commercial application.

1.2.2.4 Why are permittivity measurements so important?

Inadequate materials characterization has been one of the biggest impediments to the development of better tunable dielectrics, and to the implementation of millimeter-wave telecommunications as a whole. Naturally, if one wishes to design any electronic device operating at millimeter-wave frequencies, it is imperative to have a confident understanding of the millimeter-wave dielectric properties of the constituent materials. Unfortunately, reports of these properties are not common in the literature (especially for thin films above 40 GHz), and there is often surprisingly large discrepancy between the few reports that do exist. This critical point is made abundantly clear in Figure 1.4, which illustrates vast discrepancies between measurements of the microwave-frequency loss tangent of similar $Ba_{1-x}Sr_xTiO_3$ thin films with $x \approx 0.75$.

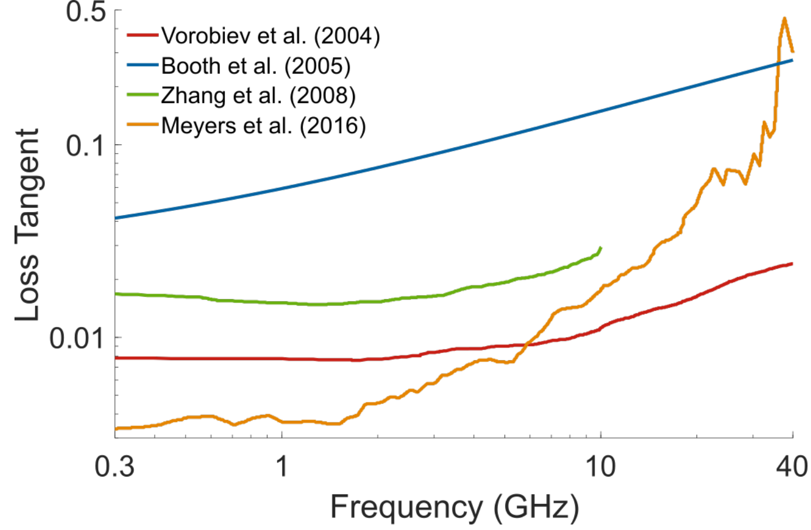

Figure 1.4. In the literature, there are large discrepancies in the measured loss tangents of ostensibly similar materials. Here we compare the measurements of $Ba_{1-x}Sr_xTiO_3$ films from Vorobiev *et al.* ($x = 0.75$) [59], Booth *et al.* ($x = 0.70$) [68], Zhang *et al.* ($x = 0.75$) [69], and Meyers *et al.* ($x = 0.71$) [46].

The difference in the loss tangents of the materials shown in Figure 1.4 is more than an order of magnitude at certain frequencies - which would have an extreme impact on device performance. Defect concentrations, and by extension extrinsic losses, can be extremely sensitive to processing conditions in tunable dielectric thin films. Given that the films in each study were grown in different labs using different processes, it is entirely possible that the results are as different as they appear. However, we also note that these studies used a variety of characterization techniques, with each presumably offering a different level of accuracy. The mixing of techniques complicates attempts to compare results between studies, something which is already difficult in the world of tunable dielectrics. The potential for ambiguous measurement results is amplified at microwave and millimeter-wave frequencies, where thin film permittivity measurements require careful calibrations, precise microfabrication, expensive instrumentation, and a well-thought-out approach to modeling test

devices to achieve a reliable result. Even when claiming exceptional results, very few studies provide sufficient detail on their high-frequency measurements, and almost none report uncertainties.

Returning to Figure 1.4, we note that the 2004 study (Ref. [59]) appeared to obtain a loss tangent below approximately 0.02 up to 40 GHz, and reported relative tunability in excess of 40 %. These properties would be advantageous for a tunable dielectric device, and such high performance appeared to spur a number of subsequent studies over the next decade or so by other groups seeking to attain the same or better properties. However, until the 2016 study (Ref. [46]), comparable properties had not really been demonstrated. Even in that study - which used significantly more advanced growth and fabrication techniques as well as characterization techniques offering a clear path to calibration and correction for parasitics - the exceptionally low loss gave way above approximately 10 GHz. The 2008 study (Ref. [69]) appeared to be a fairly faithful reproduction of the 2004 study, even using the same concentric parallel-plate technique to measure the dielectric properties, but still reported losses more than twice as high. The developers of the characterization technique used in Refs. [59] and [69] encountered difficulty when measuring above a few GHz [39]. More importantly, they noted the potential to skew the loss tangent by over-correcting for parasitic effects - which can be particularly challenging at high frequencies when devices begin to behave as distributed circuits. While the authors of Ref. [59] addressed many of the concerns and made significant positive advances to this measurement technique, some of their following work indicated uncertainties exceeding 50 % at millimeter-wave frequencies even when considering only a couple

error mechanisms [40]. Our own analysis of additional error mechanisms in these techniques supports the notion that the uncertainties could be even greater.

Examples like we just described - exciting results in the literature shrouded by *possible* measurement questions - are not rare [70]. The establishment of more standard high-frequency measurement techniques and reporting of uncertainties in measurement has the potential to accelerate progress in tunable materials development. In the best case, we determine that uncertainties across measurement techniques are small, and we know to focus our efforts on improving reproducability in materials synthesis. We provide some additional discussion of a few different approaches to measure relative permittivity in Chapter 2, before describing the techniques we use in detail, and we even address some opportunities to improve sample-to-sample processing consistency in Chapter 4.

1.2.3 Tunable microwave and millimeter-wave devices

Now that we have at least a basic familiarity with some of the basic characteristics of tunable dielectrics, we can explore why tunable devices are useful for next-generation telecommunications, and how tunable dielectric films are used to create these devices. After all, tunable dielectrics are just one piece of the puzzle - and the exciting device applications provide the incentive to research these materials.

1.2.3.1 The role of tunable devices in telecommunications

Mobile network traffic has grown exponentially in recent years and this trend shows no sign of slowing (Figure 1.5) [71]. Users are not only consuming more data per device, but the number of devices is also steadily increasing. For example, the advent of internet-of-things (IoT) technology has created new opportunities for connected devices in both industrial and consumer settings [72]. To alleviate network crowding and mitigate conflict with other devices, next-generation networks will span from the frequencies we use today in the hundreds of MHz all the way to the wide-open, largely unlicensed, millimeter-wave regime [73]. The vast bandwidth available at millimeter-wave frequencies is exciting, because it can enable new high-capacity technologies in remote medicine, automation, and even home entertainment.

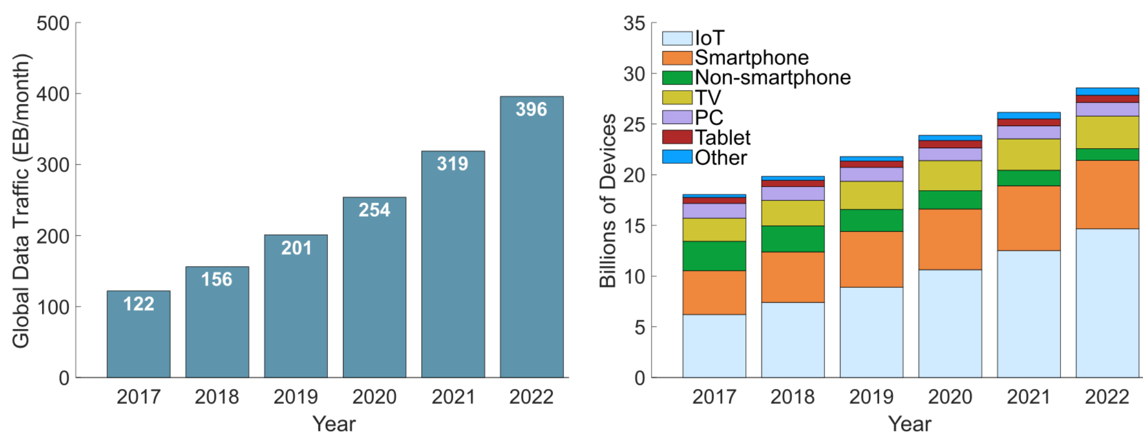

Figure 1.5. (left) Global data traffic is predicted to continue growing exponentially, putting more strain on networks. (right) In addition to an increase in the amount of data consumed per device, the overall number of devices is increasing too. Internet-of-things (IoT) devices will make up about half of all connected devices by 2022, according to the Cisco VNI [71].

Many electronic components must work in harmony to communicate across

such a broad frequency range. For example, RF filters are used to reject interference from nearby devices. In the early 2000s, handsets only needed three to seven filters [74]. Modern handsets that operate with 2G/3G/4G/WiFi/Bluetooth/GPS functionalities often need as many as 40 discrete filters [75]. Next-generation devices may need to cram more than 100 filters into a 5G-capable handset, consuming valuable space and increasing cost. “Frequency-agile filters”, can be tuned to different frequency bands with a DC voltage [76]. Since a single frequency-agile filter covers two or more frequency bands, fewer physical filters are needed, reducing the size and complexity of the RF front-end. Ferroelectric tunable varactors (variable capacitors) are one foundational component of frequency-agile filters.

Frequency-agile filters are not the only tunable device for next-generation telecommunications. Millimeter-wave bands suffer from severe atmospheric attenuation (Figure 1.6). Absorption peaks for O_2 and H_2O at millimeter-wave frequencies can attenuate signals by more than 20 dB/km [77, 73]. Therefore, devices must transmit high-power signals, quickly draining batteries and potentially worsening intermodulation distortion. Phased-array antennas produce a powerful directed-beam from the constructive interference of multiple weaker isotropic transmissions [78]. In a phased-array antenna (Figure 1.6), an identical signal is transmitted from each antenna in an array of spatially-distinct antennas. Tunable phase shifters modulate the phase of each signal to steer the directed beam. Tunable dielectric phase shifters are ideal for this purpose due to their fast tuning speed (< 10 ns) and small size [32]. Tunable matching networks, baluns, and reconfigurable antennas are other examples of tunable RF devices which can be based on tunable dielec-

tric films [79, 80]. Thin-film-based ferroelectric frequency-agile filters and oscillators [81], reconfigurable antennas [82], and tunable phase-shifters [83] have already been demonstrated.

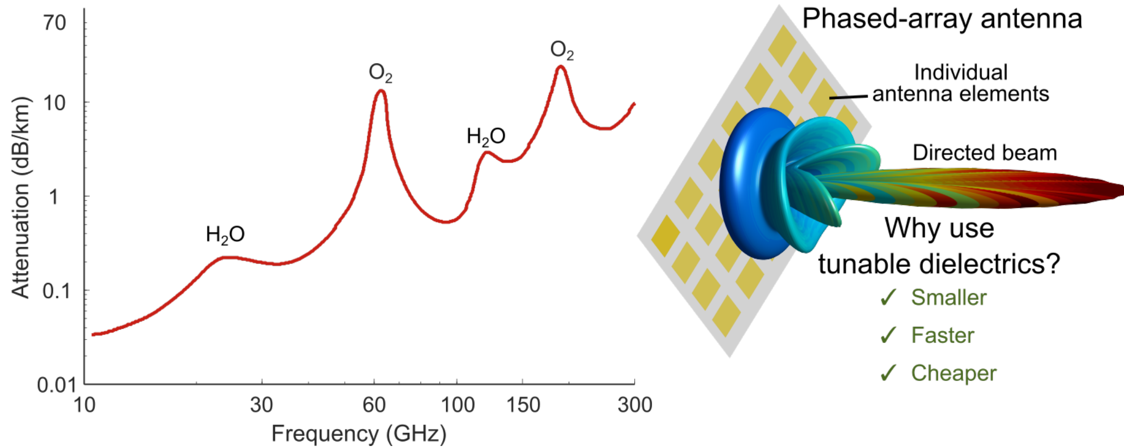

Figure 1.6. (left) Atmospheric attenuation is a significant challenge facing millimeter-wave telecommunications [73, 77]. (right) Phased-array antennas can help mitigate atmospheric effects by creating powerful and agile directed beams.

There are other ways to make tunable devices without using ferroelectric films. These technologies, such as semiconductor varactor diodes, magnetic ferrite-based devices, and RF MEMS/NEMS varactors each come with their own merits and drawbacks [27, 30, 32]. Ferroelectric devices are compelling since they can be cheaper and faster than RF MEMS and achieve higher Q-factors ($Q = [\tan\delta]^{-1}$) than semiconductor varactor diodes. While ferrite-based devices have a rich history in microwave electronics [84], they generally switch more slowly and require an external variable magnetic field source. Table I provides a comparison of some key properties across these different technologies.

Device type	Tuning Speed	Q-factor (1 GHz)	Cost	Power Handling	Linearity	Lifetime
Semiconductor	< 1 ns	~ 200	low	~ 1 W	low	high
RF MEMS	> 1 ms	~ 500	high	< 5 W	high	low
Ferrite	< 5 ms	> 3000	moderate	$\gg 5$ W	high	high
Ferroelectric	< 1 ns	> 200	low	~ 5 W	high	high

TABLE I. A comparison of notable tunable RF technologies. Inspired by [32, 30].

1.2.3.2 Design and use of ferroelectric tunable devices

The performance of tunable communications devices is intimately connected to both the properties of the constituent materials (dielectrics and conductors) and the device design. For example, a varactor with a highly tunable dielectric may offer minimal overall device tunability if the tunable dielectric layer is too thin, or if the device is not adequately designed to concentrate the electric fields in the tunable material. Although the relationships between properties and design are rarely straightforward, Figure 1.7 relates some critical points of consideration in the development of RF varactors.

Ferroelectric tunable devices are typically constructed on low-loss substrates like $LaAlO_3$, MgO, SiO_2, or Al_2O_3 [33]. Silicon is ideal for large-scale commercial integration, but is poorly lattice matched with many ferroelectric materials and typically quite lossy at millimeter-wave frequencies [32]. As we mentioned, ferroelectric varactors are the basic building block of most ferroelectric-based tunable devices. Parallel-plate varactors are a simple example. In these varactors, an electrode layer (*e.g.,* Au, Al, $SrRuO_3$) is first deposited on the substrate, and then the ferroelectric thin film is grown on the electrode via physical vapor (PVD), chemical vapor (CVD), or chemical solution (CSD) deposition techniques. Finally, a top electrode layer is patterned on top of the thin film to complete a parallel-plate structure. The

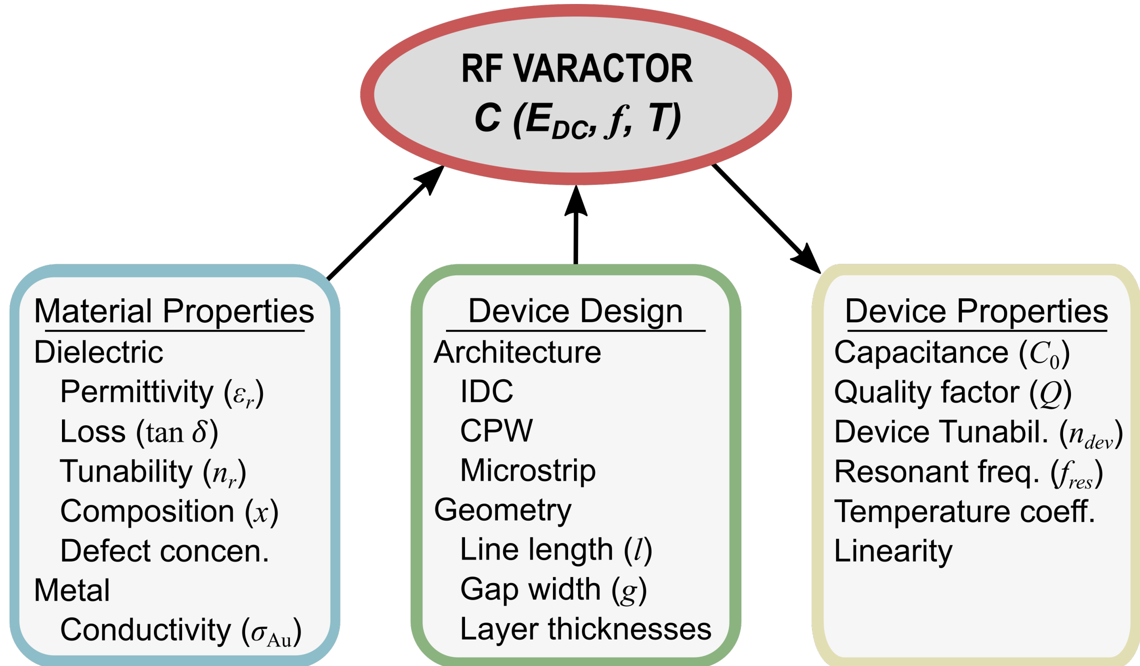

Figure 1.7. The performance of an RF varactor depends heavily on the materials from which the device is made, and how the device is designed. Inspired by [85].

capacitance of such a varactor follows the basic relationship: $C = (\varepsilon_0 \varepsilon_r A)/d$ where A is the area of the electrodes and d is the distance between the electrodes (*i.e.*, the thickness of the ferroelectric film). Therefore, when we tune the relative permittivity, ε_r, as described in Section 1.2.2.2, the capacitance of the varactor tunes by a proportional amount.

We note that the parallel-plate varactor provides a simple example, but at microwave and millimeter-wave frequencies, planar capacitors and waveguides are commonly used. These devices require only a top electrode layer which simplifies fabrication, negates the need to contact the back electrode, and does not interfere with lattice-matching between the film and substrate for epitaxial growth.

We can obtain tunable functionality in a device by incorporating these varactors. For example, a tunable delay line (comparable function to a tunable phase

shifter) can be designed so that the delay time depends on the capacitance of a varactor. As we tune the capacitance of the varactor with a DC voltage, the delay time changes. This inter-dependence of device function and varactor capacitance is the core operating principle of all ferroelectric-based tunable devices. Co-planar waveguides, which we discuss in great detail in Chapter 2, can actually function as tunable delay lines when patterned on a tunable thin film. For simplicity, we consider a lossless section of waveguide (*i.e.,* perfect conductors and lossless dielectric) which we represent with the following circuit model:

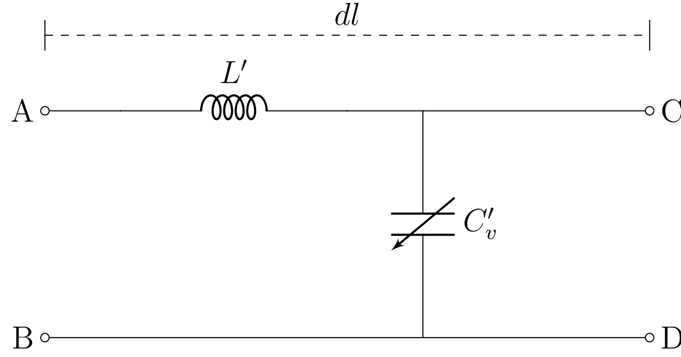

Here, dl represents some length of waveguide with an inductance L' and tunable capacitance C'_v. The DC field-dependent delay time of this configuration, $\tau(E_{DC})$ is approximated by [30]:

$$\tau(E_{DC}) = \sqrt{L' \cdot C'_v(E_{DC})} = \frac{l}{c_0} \cdot \sqrt{\varepsilon_{eff}(E_{DC})} \qquad (1.10)$$

where E_{DC} is the DC field applied to induce tuning, l is the length of the delay line, c_0 is the speed of light in free space and ε_{eff} is the *effective* permittivity of the line. As the relative permittivity of the tunable dielectric film is modified by an applied DC electric field, the effective permittivity also changes by some proportional, but

smaller amount. The change in effective permittivity in turn modifies the delay time by $\Delta\tau(E_{DC})$, taken relative to the delay time in the absence of the applied DC field. The effective permittivity is a convolution of the permittivities of all the media that comprise the waveguide (*e.g.,* the tunable film, substrate, and air), and can be approximated by simulation or conformal mapping.

Our example of a lossless delay line is simple, but illustrates some of the most fundamental concepts of tunable RF devices. In reality, devices made of real conductors and dielectrics are lossy. The figure of merit used to compare delay lines:

$$FOM \approx \frac{\tan\delta}{\Delta\tau(E_{DC})}, \tag{1.11}$$

drives home the importance of maximizing tunability and minimizing loss. As we have mentioned throughout this chapter, reliable characterization of these quantities is a requisite step to develop better tunable dielectric materials and devices. The next chapter presents the characterization techniques we use to measure the broadband dielectric properties of tunable thin films up to 110 GHz.

Chapter 2

Relative permittivity characterization techniques for tunable thin films from 100 Hz to 110 GHz

2.1 Overview

In Chapter 1, we discussed some fundamental aspects of tunable dielectric materials and devices. We noted that accurate measurements of the relative permittivity of thin films are crucial to design new microelectronics and efficiently search for better materials. Especially at millimeter-wave frequencies, even simple measurements can require expensive instrumentation, careful calibrations, and detailed sample preparation to produce consistent results. Isolating the relative permittivity of very thin films can prove particularly challenging, and characterization across a broad range of frequencies and applied voltages is often needed to understand how a material will perform in a real device.

In this chapter, we describe how we overcome many of these measurement challenges and characterize the relative permittivity of thin films from 100 Hz to 110 GHz under a variety of operating conditions. We do this using on-wafer (*i.e.,* microfabricated) capacitors and transmission lines, which enable consistent fabrication, robust calibration, and relatively simple analysis. In the next section, we will compare on-wafer transmission line and capacitor measurements with some other

popular characterization techniques, before moving on to describe our complete measurement methodology.

2.1.1 Comparison of permittivity characterization techniques

The many forms, types, and applications of dielectric materials - from industrial protective coatings and mineral oil-filled transformers to the tiniest transistors - have led to an abundance of methods to characterize relative permittivity. Most of these techniques involve using fixtures like resonant cavities [86], scanning probes [87], lumped-element capacitors [88] or transmission lines [89] to determine how a material-under-test interacts with electromagnetic fields. Ref. [42] provides an excellent introduction to many techniques and offers some guidance regarding their benefits and drawbacks - with a particular focus on high-frequency measurements. Here, we discuss a couple of the more common techniques.

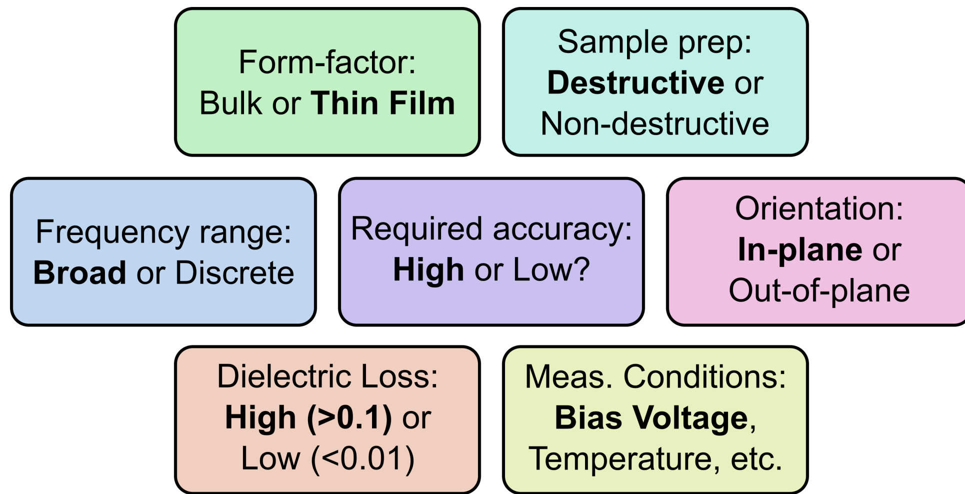

Figure 2.1. There are many factors to consider when choosing the best dielectric property characterization technique for an experiment. Highlighted in bold are factors that are relevant to our work.

The best characterization technique for a given experiment depends on a num-

ber of aspects, like sample form factor, desired frequency and bandwidth, and dielectric loss (Figure 2.1).

In our experiments, we are most concerned with measuring the broadband relative permittivity of tunable dielectric thin films up to millimeter-wave frequencies. Thin films are special for two reasons. First, thin film synthesis techniques offer a way to create novel materials that don't form naturally. Second, modern microelectronics - the main application of tunable dielectrics - are constructed of thin films. With telecommunications spanning frequencies from the hundreds of MHz to the tens of GHz, *broadband* permittivity measurements have become especially important. Furthermore, observing how the permittivity changes with frequency can reveal interesting materials behavior - like the timescales and mechanisms underlying polarization [90].

Some measurement techniques meet our needs, others do not. Split-cylinder (Figure 2.2) or other resonator techniques provide extremely accurate measurements (within 1%) at GHz frequencies with minimal sample preparation. However, this technique loses sensitivity when measuring lossy materials (e.g., $\tan\delta > 0.02$), and the difficulty in quantifying the fractional volume of the thin film relative to a large substrate can increase uncertainty. Perhaps most importantly, measurements are restricted to discrete resonant frequencies dictated by the geometric dimensions of the machined test fixtures.

Scanning-probe techniques (Figure 2.2) can also be used to measure relative permittivity - and many other properties of materials [91, 92, 93, 94]. These measurements are unique in that they can explore dielectric properties at the sub-micron

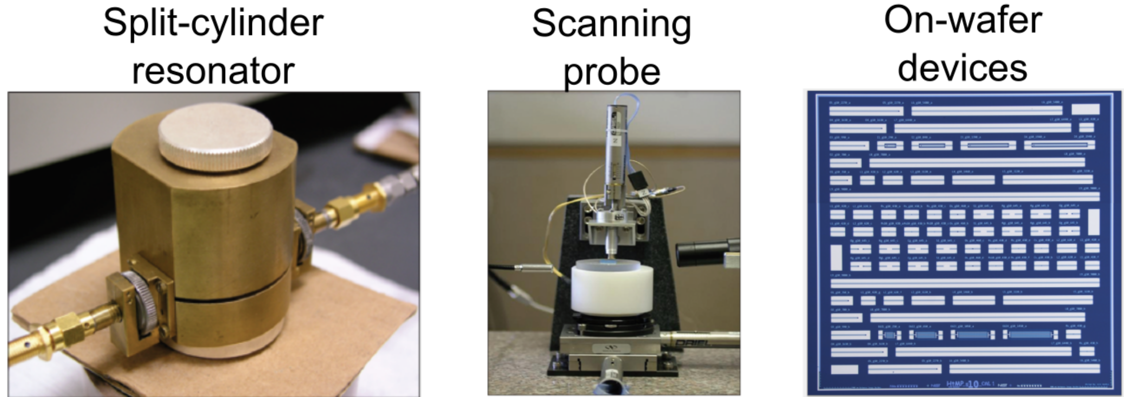

Figure 2.2. Permittivity characterization techniques use a variety of test fixtures for measurement. (left) The split-cylinder resonator technique. (center) A near-field scanning probe system. (right) On-wafer permittivity characterization devices. Images in the left and center panels have been reproduced from Ref. [42].

scale. Generally, the primary test fixture consists of some type of resonator terminated by a probe (*e.g.,* AFM-style tip) [95]. When the probe tip is brought near a dielectric material, coupling between the tip and sample modifies the effective impedance of the probe tip, in turn perturbing the behavior of the resonator. The complex permittivity of the material can be extracted by analyzing the shifts in resonant frequency and quality factor. These measurements are fast and achieve unparalleled spatial resolution, but they are more limited in their ability to provide quantitative measurements at millimeter-wave frequencies [96]. Beyond approximately 10 GHz, the electrostatic approximation and lumped-element models used in the measurement analysis can begin to break down. We discuss scanning probe measurements further in Chapter 4, as these measurements were common in previous studies of combinatorial tunable dielectric films.

On-wafer lumped-element capacitors are commonly used to measure the broadband permittivity of thin films up to a few GHz. Co-planar interdigital capacitors

(IDCs, Figure 2.3) are patterned on the surface of a test sample and used to measure the in-plane components of the permittivity tensor. Thin film parallel-plate capacitors like the one we described in Section 1.2.3.2 can be used to measure the out-of-plane components. Capacitor measurements are relatively simple, but can only be used up to at most a few GHz, at which point the test signal wavelengths begin to approach the physical size of the IDCs. As a result, the device beings to show distributed effects and the lumped-element approximation made in the analysis becomes tenuous.

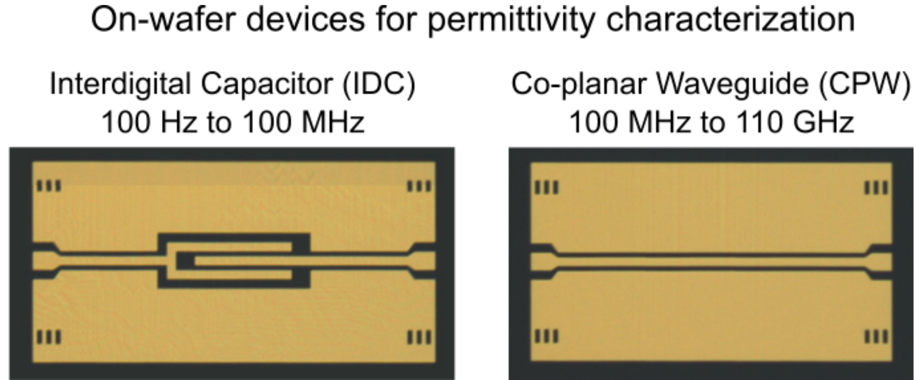

Figure 2.3. We use on-wafer interdigital capacitors (IDCs) and co-planar waveguides (CPWs) to measure the relative permittivity of thin films from 100 Hz to 110 GHz.

Fortunately, on-wafer transmission line measurements begin to thrive in the tens of MHz and can provide accurate results beyond 100 GHz. Co-planar waveguides (CPWs, Figure 2.3) are a simple type of transmission line to fabricate and measure [97]. We pattern CPWs directly on the thin film so that the permittivity of the film will affect the propagation of an electromagnetic wave along the CPW. CPW measurements are less sensitive than resonator measurements, since the propagating wave typically transits the CPW once with minimal reflection, as opposed to repeatedly passing through the material in a resonant cavity. As a result, mea-

surements of materials with a loss tangent below approximately 0.005 are difficult and can have large uncertainties. Since losses in tunable dielectrics tend to be quite large, this is generally not an issue in our experiments.

While each technique has benefits, on-wafer IDC and CPW measurements are an ideal way to characterize the broadband relative permittivity of thin films. It is true that these devices lack the pinpoint accuracy of cavity resonators, the high resolution of scanning probe techniques, and require significant sample preparation. However, they enable simple, broadband, quantitative characterization of thin film permittivity up to millimeter-wave frequencies under a range of operating conditions (voltage, temperature, etc.). In the next section, we detail how we use IDCs and CPWs to measure the permittivity of tunable dielectric thin films.

2.2 On-wafer thin film permittivity characterization with planar capacitors and transmission lines

Measuring the relative permittivity of a film from 100 Hz to 110 GHz requires stitching together measurement data from multiple instruments and on-wafer devices. It can be cumbersome to keep track of the many parts of this technique, so we first provide an overview of our measurement procedure to illustrate how everything fits together.

2.2.1 Measurement technique overview

Assuming the measurement instrumentation (Section 2.2.2) is configured and operating in a steady state, we first obtain the test samples and prepare them for fabrication. We either grow our own thin films via pulsed laser deposition (PLD) or receive films from collaborators that may be grown via other techniques. We then fabricate the on-wafer test devices (Section 2.2.3) using the techniques described in Appendix C. In addition to the thin film test samples, we also fabricate devices on a "companion substrate" and if necessary, fabricate on-wafer calibration chips (Section 2.2.4.1). The companion substrate is simply a bare substrate of the same type that the thin films are grown on. We use this additional test sample to characterize the permittivity of the substrate material, characterize the conductor properties of the test devices, and validate our finite element simulations.

Once the samples are prepared, we begin our measurements with calibrations (Section 2.2.5). Calibrations are required because raw measurements include the effects of all components in the measurement system like cables, connectors, and probes, in addition to the test device. Calibrations allow us to account for the unwanted effects and isolate the electrical behavior of our tiny on-wafer test device. For these procedures, we use custom-fabricated on-wafer calibration chips like the one shown in the right panel of Figure 2.2.

After calibration we measure the test samples, including the companion substrate (Section 2.2.6). Briefly, we measure multiple IDCs with different lengths at frequencies below approximately 100 MHz using the combination of an LCR meter

and a vector network analyzer (VNA). Above 100 MHz, we use a VNA to measure multiple CPWs with different lengths, and a “reflect” device, which we describe later.

In the final stage, we analyze the calibrated test sample measurements to extract the relative permittivity of the materials under test. The analysis for both the CPW and IDC devices can be broken into two key steps. First, we calculate the fundamental circuit parameters of the test devices from our measurements (Sections 2.2.6.1 and 2.2.6.2). Finally, we use finite element simulations (Section 2.2.7) of the test devices to map those circuit parameters to the relative permittivity of the constituent materials.

2.2.2 Measurement instrumentation

We perform all of our measurements on a probe station (example in Appendix A). Samples are affixed to a temperature-controlled stage by vacuum to prevent motion. We contact the on-wafer devices with ground-signal-ground (GSG) probes. These probes act as a transition from coaxial cable to a planar three-pronged tip that can connect directly to the on-wafer devices.

The probes are mounted on three-axis manipulators that enable precise alignment with the on-wafer devices. After making initial contact, we lower the probes some additional amount to make the probe tips “skate” approximately 10 µm across the device, which ensures consistent electrical contact. We use a video-enabled microscope to aid in probe alignment. Our IDCs and CPWs are all “two-port” devices

and require two probes - one in contact with each side of the device. Two-port devices enable measurement of both reflection and transmission of a test signal in the forward (sourced from port 1) and reverse (sourced from port 2) directions.

There is no single test instrument that adequately covers our entire nine decade measurable frequency bandwidth, so we combine several individual pieces of equipment (Figure 2.4). We use two source-measure units (SMUs) to measure the DC resistance of the test devices. DC resistance measurements are required for some calibrations, enable us to determine the conductivity values of the gold layers to use in our finite element models, and provide an early warning of bad measurements. For example, an outlying DC resistance measurement typically indicates bad probe contact or a defective device.

In the low-frequency (LF) regime from 100 Hz to 1 MHz we use an LCR meter, which sources an AC voltage and measures the phase-sensitive voltage-to-current ratio (the complex impedance) of the device under test (DUT). In our configuration, the LCR meter calculates and records an equivalent capacitance and dissipation factor of the device under test [98]. We use these quantities to obtain the complex relative permittivity with minimal analysis.

In the radio-frequency (RF) regime from 1 MHz to approximately 100 MHz, we use a four-sampler VNA which sources an AC signal and measures the Scattering (S-) parameters. S-parameters are ratios of the quantities a_i and b_i, which represent the incident and reflected/transmitted waves at port i, respectively. A full description of how S-parameters are defined is included in Appendix B.

In the high-frequency (HF) regime from 100 MHz to 110 GHz, we again use

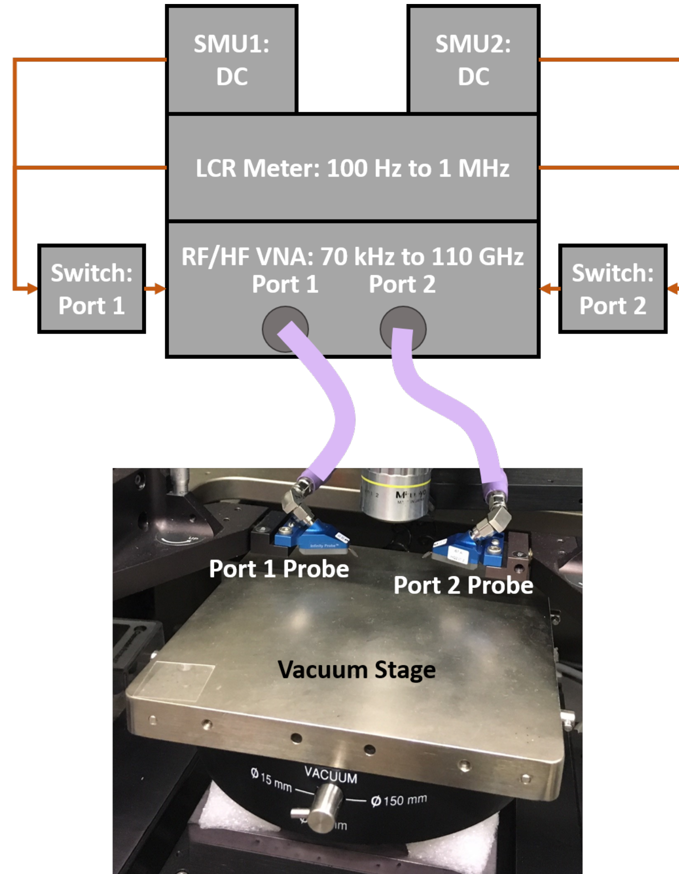

Figure 2.4. Our typical measurement configuration includes two Source-Measure Units (SMUs) for DC resistance measurements, an LCR meter for measurements below 1 MHz, and one or two Vector Network Analyzers (VNAs) for measurements up to 110 GHz. The SMU and LCR meter test signals are routed through the VNA that is connected to the probes via phase-stable coaxial cables.

a VNA to measure S-parameters. We often perform the RF and HF measurements with a single "broadband" VNA. This is a unified instrument which includes multiple sources and receivers for the different frequency regimes, as well as frequency-doubling millimeter-wave extender heads that enable measurements up to 110 GHz. In this work, the abbreviations LF, RF, and HF are simply used for clarity when describing our different measurement frequency regimes, and are not related to International Telecommunications Union (ITU) band designations.

Only one instrument can be connected directly to the probes. Typically, this

will be the VNA that measures at the highest frequency. To minimize the number of probe landings and tedium of performing our measurements, we connect the other instruments to programmable switches. These switches route the test signals from the SMUs, LCR meter, and any other instrument through the HF VNA which is connected to the probes. Therefore, we only need one probe landing to measure a DUT across the entire frequency range. The measurements are controlled with data acquisition software written in LabView and Python. This software feeds measurement settings to the instruments via a GPIB interface, starts the measurements, and records the data.

2.2.3 On-wafer devices for permittivity characterization

Each calibration chip and test sample includes sets of CPWs and IDCs with varying lengths. In this section we describe the structure of these devices and provide some fundamental details related to their use.

2.2.3.1 Co-planar Waveguides (CPWs)

In this section, we describe four key topics related to our use of CPWs for permittivity measurements. First, we describe the physical structure of the CPW. Second, we present a circuit model which describes the behavior of the CPW. Third, we detail how the circuit parameters in that model are linked to the properties of the materials under test. Finally, we discuss a key quantity called the propagation constant, γ, which describes how electromagnetic waves propagate in the CPW. Our

technique involves extracting the material properties from measurements of γ, but this is not discussed in detail until Section 2.2.6.1.

Figure 2.5 shows a picture and diagram of a typical on-wafer CPW. A CPW is comprised of three conductors: a signal line (the "center conductor"), and two ground planes separated from the center conductor by a gap. In all of our CPWs, the center conductors are 20 µm wide. On the left and right sides of each CPW are "landing pads", which are the designated region where we connect the probes and are highlighted in green in Figure 2.5. Each landing pad is 60 µm long and has alignment marks in the ground planes to facilitate consistent probe placement. For the CPWs, our calibrations set the measurement reference planes at the end of the landing pads. We describe reference planes further in Section 2.2.5, but fundamentally, this means that the electrical behavior of the landing pads, probes, etc. are accounted for and removed by our calibrations. Between the reference planes, the CPW has an invariant cross-section.

At low frequencies, lumped-element circuit models are often used to describe electrical devices. A lumped-element model represents a device as a network of discrete circuit elements (*e.g.,* resistors, capacitors) connected by perfectly conducting wires. Lumped-element approximations break down at high frequencies where short signal wavelengths mean that voltages and currents vary spatially within a device. In this case, we must use a distributed circuit model, which breaks the device into a network of circuit elements representative of some infinitesimal section of the device. One of the benefits of using CPWs is their well-established distributed circuit model.

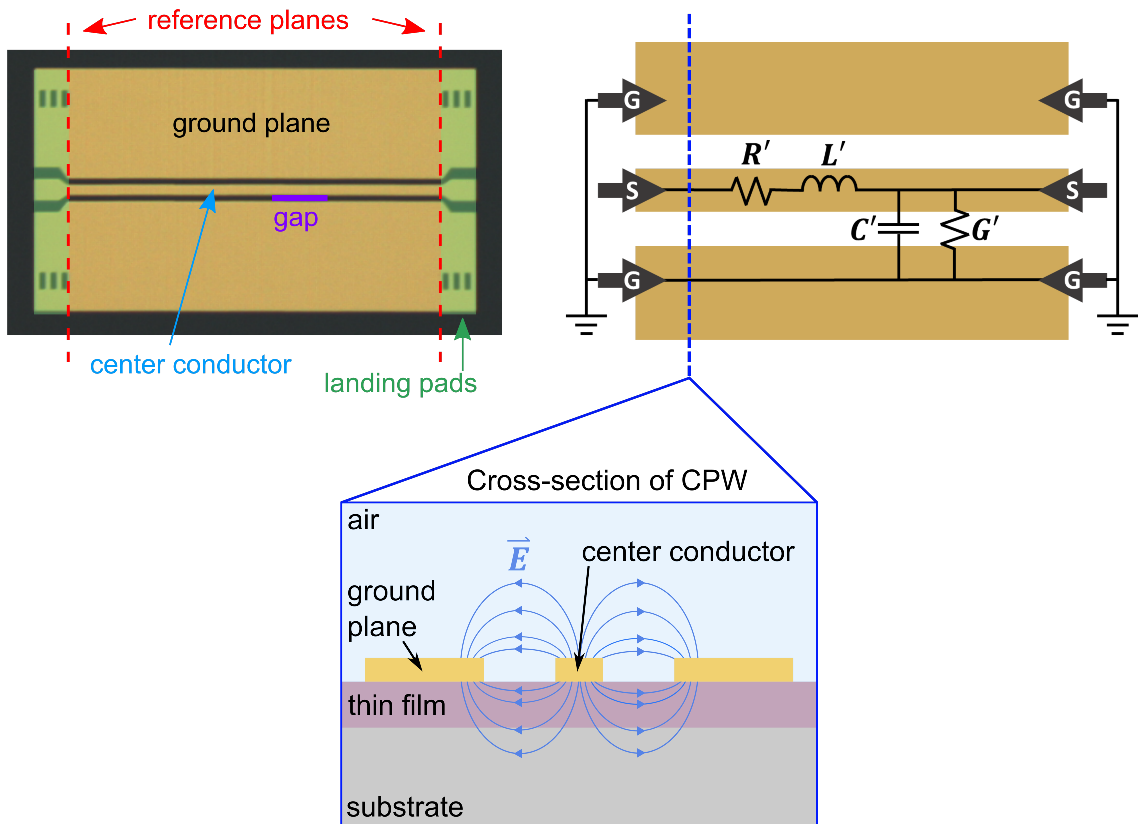

Figure 2.5. (top left) A plan-view image of a CPW with labels for several key parts of the device. (top right) A diagram of a CPW with the distributed circuit model used to describe transmission lines. (bottom) A cross-section diagram of the CPW which highlights how the electric fields in the CPW interact with the adjacent dielectric layers.

CPWs are a type of transmission line - a general term for any structure designed to conduct high-frequency alternating current - so we use the common distributed circuit model for a transmission line of some infinitesimal length, dl:

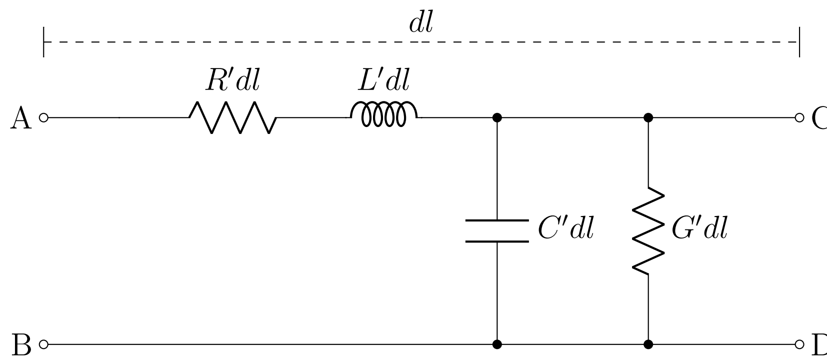

In this model, R', L', C', and G' are respectively, the resistance, inductance, capacitance and conductance *per unit length of transmission line*. These are the "distributed circuit parameters" and they are frequency-dependent quantities. C' and G' are particularly important because these two parameters are linked to the relative permittivity of materials comprising the CPW structure.

The physical origins of the transmission line model are evident in the top right panel of Figure 2.5. As a signal propagates along the center conductor, there is some resistance and inductance per unit length governed by the conductor geometry and the conductivity of the metals. The propagating signal also generates fluctuations in the local charge density on the center conductor relative to the ground planes, which is the origin of the electric fields illustrated in the bottom panel of Figure 2.5. Generally, C' is related to the charge stored between the center conductor and ground planes, while G' accounts for any leakage of charge between these conductors.

CPWs are designed to support the propagation of a quasi-TEM mode, in which the electric and magnetic fields more or less form only in the transverse plane. Assuming the propagation is quasi-TEM and the materials in the CPW structure have a relative permeability, $\mu_r = 1$, R' and L' are determined only by the characteristics of the conductor layers. On the other hand, C' and G' are tied to the relative permittivity of the substrate, film, and superstrate. The capacitance C' increases proportionally with the real part of the relative permittivity (ε'), of these layers like it would in any capacitor. The relationships between the circuit parameters and

material properties in waveguides are described generally by [99, 100]:

$$\begin{aligned} R' &= \frac{\omega}{|i_0|^2}[\int_S \mu''|\mathbf{h}_t|^2 dS + \int_S \varepsilon''|\mathbf{e}_z|^2 dS], \\ L' &= \frac{1}{|i_0|^2}[\int_S \mu'|\mathbf{h}_t|^2 dS + \int_S \varepsilon'|\mathbf{e}_z|^2 dS], \\ C' &= \frac{1}{|v_0|^2}[\int_S \varepsilon'|\mathbf{e}_t|^2 dS + \int_S \mu'|\mathbf{h}_z|^2 dS], \\ G' &= \frac{\omega}{|v_0|^2}[\int_S \varepsilon''|\mathbf{e}_t|^2 dS + \int_S \mu''|\mathbf{h}_z|^2 dS]. \end{aligned} \tag{2.1}$$

where ε' and ε'' are the real and imaginary parts of the permittivity, μ' and μ'' the real and imaginary parts of the permeability, and $\mathbf{e}$ and $\mathbf{h}$ the electric and magnetic fields, respectively. The subscripts t and z represent fields in the transverse (t) and longitudinal (z) directions. Given our assumption of quasi-TEM mode propagation, we neglect the latter term in the above expressions because the electric and magnetic fields should have no longitudinal component.

Taking the distributed capacitance, C', as an example, we first note that our CPW structures include a substrate, film, and air superstrate, each with their own relative permittivity (*i.e.*, ε_{sub}, ε_{film}, and ε_{air}). The electric fields are distributed throughout these layers in varying proportions. Therefore, we consider these regions individually, as follows:

$$C' = \frac{1}{|v_0|^2}[\varepsilon'_{sub} \int_{S_{sub}} |\mathbf{e}_{t,sub}|^2 dS_{sub} + \varepsilon'_{film} \int_{S_{film}} |\mathbf{e}_{t,film}|^2 dS_{film} + \varepsilon'_{air} \int_{S_{air}} |\mathbf{e}_{t,air}|^2 dS_{air}]. \tag{2.2}$$

We see here that the integrals represent the intensity of the electric fields in each region of the CPW structure. We condense each integral into some filling factor, g

that represents the ratio and distribution of the electric fields in each region:

$$C' = \varepsilon'_{sub} \cdot g_{sub} + \varepsilon'_{film} \cdot g_{film} + \varepsilon'_{air} \cdot g_{air}. \tag{2.3}$$

In practice, we use finite element simulations (Section 2.2.7) to generate a "mapping function" which bundles these filling factors into a unified relationship between the measured distributed capacitance, C', and the real part of the relative permittivity of the various layers. Other approaches like the conformal mapping method (CMM) perform a similar role.

We've just described how material properties are related to the circuit parameters used to describe the CPW. The propagation of a signal in the CPW is also related to these same circuit parameters. This relationship is succinctly described by Heaviside's Telegrapher's Equations, which are a formulation of Kirchoff's laws that were developed in the 1880s to describe signal propagation in trans-Atlantic undersea cables [101]. One of the most important results of Heaviside's work is the formulation of a quantity called the propagation constant, γ:

$$\gamma = \sqrt{R' + i\omega L'}\sqrt{G' + i\omega C'}. \tag{2.4}$$

The propagation constant, as it's name implies, is a complex quantity that defines the link between the distributed circuit parameters and the propagation of an electromagnetic wave along the transmission line. Like the distributed circuit parameters, R', L', C', and G', γ also changes with frequency. Equation 2.4 is often

simplified to:

$$\gamma = \alpha + i\beta, \tag{2.5}$$

where α is called the attenuation constant, and β is called the phase constant. Unsurprisingly, α describes the attenuation of the travelling wave per unit length of transmission line in Nepers per meter, and β describes the amount of phase shift accumulated per unit length of transmission line in radians per meter. Figure 2.6 illustrates the physical implications of α and β.

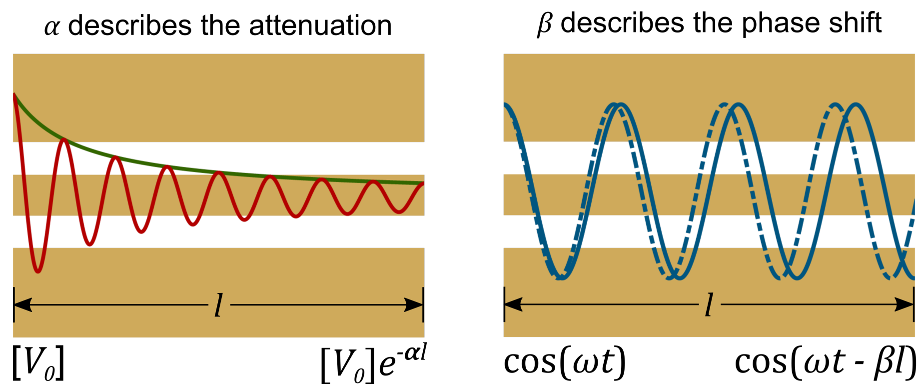

Figure 2.6. (left) α describes how the incident wave is attenuated as it travels along a transmission line of length, l. (right) β describes the phase shift of the propagating wave (dashed line) relative to the incident wave (*i.e.*, if $\beta = 0$, solid line) as it travels along a transmission line of length, l.

If we know the properties of the incident wave and the propagation constant, we can estimate the voltage and current at any point along the transmission line. For example, the voltage of a forward-travelling wave (propagating from port 1 to port 2) in our transmission line is:

$$V(x) = |V_0^+|e^{-\gamma x}, \tag{2.6}$$

or in the time domain:

$$V(x,t) = |V_0^+|e^{-\alpha x}\cos(\omega t - \beta x + \phi), \tag{2.7}$$

where $|V_0^+|$ is the initial voltage amplitude of the wave, x is the position of interest along the transmission line, ω is frequency, and ϕ is the initial phase of the wave. We see the role of α and β in describing the characteristics of the propagating wave quite clearly in Equation 2.7. In practice, we must consider propagation in the forward and reverse directions along our transmission lines, which accounts for effects like reflection:

$$V(x) = |V_0^+|e^{-\gamma x} + |V_0^-|e^{+\gamma x}. \tag{2.8}$$

Now, rather than consider some point x along our transmission line, if we consider a signal that has been transmitted completely across a line of length l, we write Equation 2.8 as:

$$V(l) = |V_0^+|e^{-\gamma l} + |V_0^-|e^{+\gamma l}. \tag{2.9}$$

Equation 2.9 brings us to the transfer (T-) parameter description of a transmission line. T-parameters are closely related to S-parameters (see Appendix B), but are a more convenient formalism for certain applications, which we discuss further in Section 2.2.5. The T-matrix that describes an ideal transmission line of length l is:

$$[\mathbf{T}] = \begin{bmatrix} e^{-\gamma l} & 0 \\ 0 & e^{+\gamma l} \end{bmatrix}, \tag{2.10}$$

where T_{11} describes the forward transmission from port 1 to port 2, and T_{22} the reverse. Fundamentally, our permittivity characterization approach involves using the measured T-parameters (converted from S-parameters) of several CPW transmission lines with different lengths to obtain γ via a special fitting algorithm.

As we saw in Equation 2.4 the distributed circuit parameters R', L', C' and G', are intimately related to γ. In our approach, we work backwards, using our measured γ to determine the distributed circuit parameters and then use the circuit parameters to find the relative permittivity. However, γ on its own is insufficient to isolate the individual distributed circuit parameters R', L', C' and G' from one another. There are a variety of ways to solve this problem. If we know the characteristic impedance of our CPWs, Z_c, we can solve directly for R', L', C' and G' (see Appendix B).

$$Z_c = \frac{\sqrt{R' + i\omega L'}}{\sqrt{G' + i\omega C'}}. \tag{2.11}$$

Unfortunately, while we can accurately measure γ, measurements of Z_c are more convoluted [102, 103]. Ultimately, we will use a different, more reliable approach to extract the circuit parameters C' and G' from γ using finite element simulations, rather than measurements of Z_c. We describe that approach when we discuss our measurement analysis in Section 2.2.6.1. For now, we set aside our theoretical discussion of the CPWs to explore some basic concepts of how we use IDCs

for lower frequency measurements.

2.2.3.2 Planar Interdigital Capacitors (IDCs)

In this section, we describe three key topics related to our use of IDCs for permittivity measurements below 100 MHz. First, we describe the physical structure of the IDC. Second, we present a circuit model which is representative of the IDC. Third, we note the circuit parameters that we will analyze to find the relative permittivity of the materials under test. The analysis itself is described in detail in Section 2.2.6.2.

Figure 2.7 shows a picture and diagram of a typical IDC. On each side of an IDC there is a feedline - a segment of CPW transmission line equivalent to half the length of the "thru" (the shortest CPW), including landing pads. The feedlines simplify calibration, which we discuss in Section 2.2.5. After the feedlines, the IDC opens up into the interdigitated portion of the device. Here, the port 2 signal line continues uninterrupted, forming the "inner conductor" of the IDC and the port 1 signal line (the "outer conductor") forks into two fingers separated from the inner conductor by a gap. The ground planes are skinnier in the interdigitated portion of the IDC to accommodate the wide outer conductor. The gap between the outer conductor and the ground planes should be several times wider than the gap between the inner conductor and outer conductor to minimize parasitic capacitance between the outer conductor and ground planes. The section of the device in which the inner and outer conductors overlap is called the "active length". We measure multiple

IDCs with different active lengths, but the landing pads and feedlines are identical in every IDC.

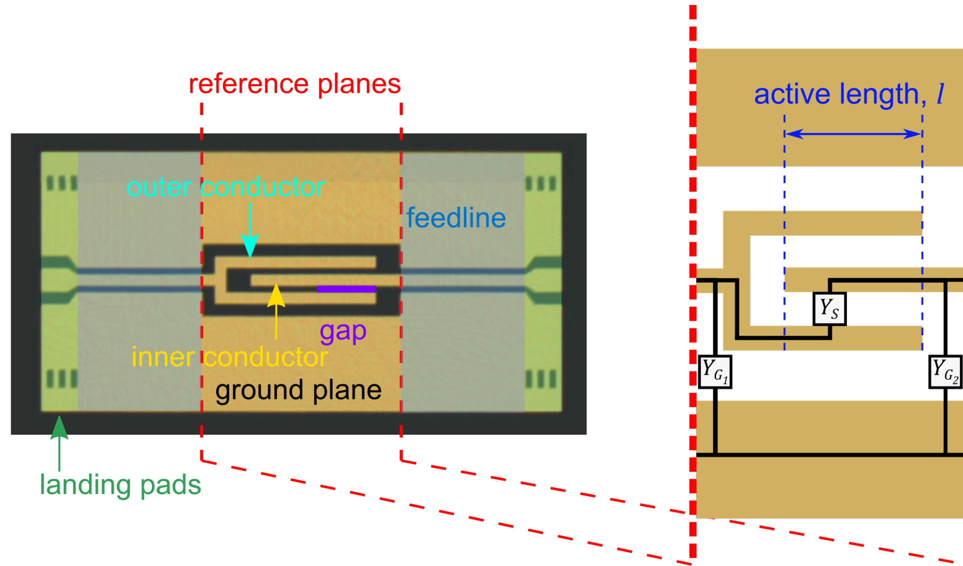

Figure 2.7. (left) A picture of a typical on-wafer IDC. (right) A diagram of the interdigitated portion of the IDC, highlighting the active length region and the π-network circuit model used to describe the IDCs.

Below 100 MHz our IDCs typically act as lumped-element circuits. That is to say that the test signal wavelengths are long relative to the size of our IDCs so voltages are effectively constant in the active length region. At higher frequencies, the onset of distributed effects appears as an anomalous increase in the measured capacitance of the IDC. Finite element simulations provide a simple way to anticipate the usable frequency range of an IDC. In the lumped-element regime, we model the IDCs with the following π-network circuit:

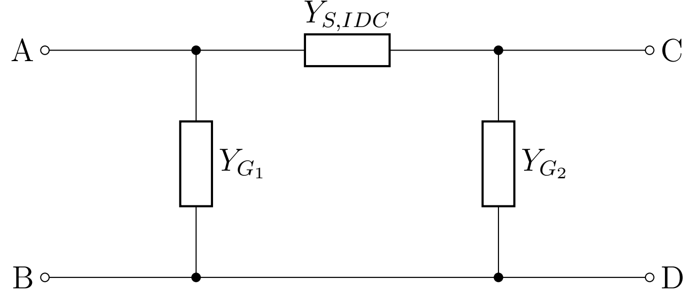

This model is overlaid on the diagram in the right panel of Figure 2.7 to highlight its physical origins. The lumped series admittance between the inner and outer conductors is $Y_{S,IDC}$. Y_{G_1} and Y_{G_2} represent lumped shunt admittances between the signal lines and ground planes on the port 1 and port 2 sides, respectively. If the interdigitated portion of the IDC is well-isolated from the ground planes, Y_{G_1} and Y_{G_2} should be small.

The first goal in our IDC measurements is to determine the lumped series admittance, $Y_{S,IDC}$ which is comprised of the conductance, G_{IDC}, and the capacitance, C_{IDC}:

$$Y_{S,IDC} = G_{IDC} + i\omega C_{IDC}. \tag{2.12}$$

$Y_{S,IDC}$ is proportional to the active length of the IDCs. In our analysis, we will use this relationship to estimate the capacitance and conductance per unit length of the active length region of the IDCs, C'_{IDC} and G'_{IDC}. These quantities are analogous to C' and G' of the CPWs and can likewise be used to calculate the relative permittivity of the substrate and thin film materials as we will describe in Section 2.2.6.2.

2.2.3.3 Calibration-specific devices

Other than CPWs and IDCs, there are a few more devices that we need for certain calibration procedures. The most notable of these devices are the short-circuit reflect, series resistor, series capacitor, and series open calibration standards, which we label S1, Rs, Cs, and Os, respectively. These devices are shown in Figure 2.8.

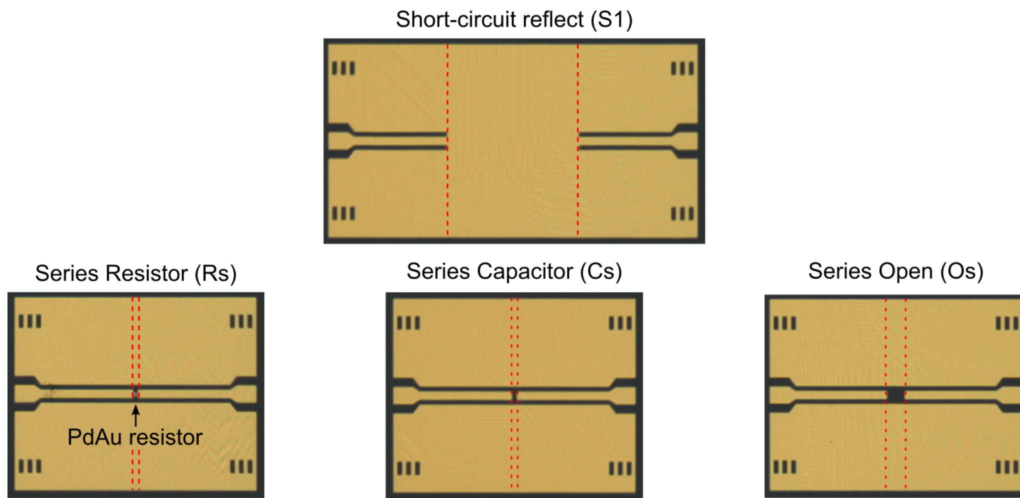

Figure 2.8. Notable calibration-specific devices, including the short-circuit reflect (S1), series resistor (Rs), series capacitor (Cs), and series open (Os). The red dashed lines indicate the default reference planes.

These devices are modifications of the shortest CPW transmission line (labeled L1), which itself acts as a "thru" calibration standard. A thru is a direct connection between the port 1 and port 2 reference planes that is modeled by perfect transmission. As a reminder, the reference planes can be thought of as the physical point at which the calibration is being performed. Everything "behind" the reference planes (between the VNA output port and the reference plane) will be accounted for by the calibration. The default reference planes are located at the center of the thru.

To form the other calibration standards, we bisect the thru at the reference planes into right and left halves, and insert a known circuit between each half.

For the short-circuit reflect standard (S1), we insert a large Au patch that shorts the center conductor of the CPW to the ground plane. In theory, this standard provides perfect reflection of the incident wave (with an inverted phase). The gold patch is at least 200 µm wide in our devices to limit unwanted transmission from port 1 to port 2.

For the series resistor standard (Rs), we split the two halves of the thru and separate them by 10 µm. Between these halves, we replace the Au center conductor with a small embedded PdAu resistor with a DC resistance typically ranging from 40 Ω to 150 Ω. The ground planes are continuous between both halves of the device. This standard acts as a known load between port 1 and port 2, and is used for the aptly named series resistor calibration. The series capacitor (Cs) is identical to the series resistor standard, but is missing the embedded PdAu resistor.

The series open standard (Os) is very similar to the series capacitor, but the two halves of the device are separated by at least 40 µm, to minimize any coupling from one port to the other. Like the short-circuit reflect, this standard theoretically acts as a perfect reflect, but does not affect phase.

2.2.4 On-wafer device layouts and patterns

We arrange the CPWs, IDCs, and other devices into concise patterns for fabrication. In this section we note some important details related to the devices included

on calibration chips and test samples, and how they are configured.

2.2.4.1 Calibration chips

Like their name implies, calibration chips hold our custom-fabricated on-wafer calibration standards. We typically make calibration chips from 2” or 3” wafers. A wafer can produce seven to fifteen 12 mm x 12 mm calibration chips, with each chip containing anywhere from 60 to 100 on-wafer calibration standards. We always use low-loss substrates with a constant relative permittivity near the relative permittivity of the test samples. The large number of devices enables a variety of calibrations and increases the longevity of a calibration chip. We show a typical calibration chip in Figure 2.9, and highlight relevant calibrations that can be performed with different combinations of devices.

The most notable devices on the calibration chip are those used to perform the multiline TRL, series resistor, and LCR meter open-short calibrations, which we explain in Section 2.2.5. Since calibration chips include resistors, at least two fabrication layers are required.

For the multiline Thru-Reflect-Line (TRL) calibration, we include six to nine CPW transmission lines with unique lengths, and a short-circuit reflect (S1). Although a regular TRL calibration can be performed with only two CPWs and the reflect, increasing the number of CPWs and performing multiline TRL reduces uncertainty by providing more independent measurements. The CPW transmission lines are labeled L1, L2, L3, etc. in order of increasing length.

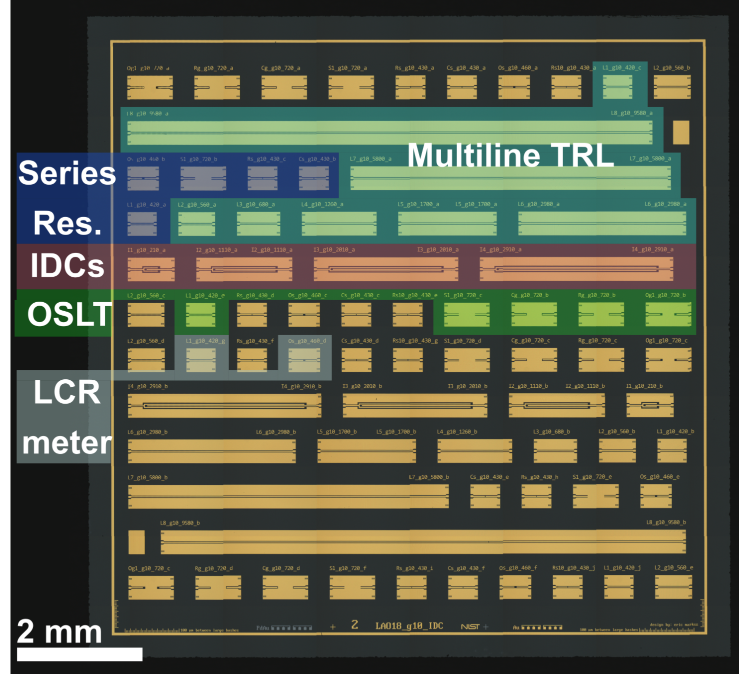

Figure 2.9. A typical calibration chip with highlighted regions showing the different calibrations that can be performed. Non-highlighted regions hold duplicate devices for redundancy.

For the series resistor calibration, we include a series resistor (Rs) and series capacitor (Cs) in addition to the thru (L1) and short-circuit reflect (S1) devices from the multiline TRL set. Finally, for the LCR meter calibration, we add a series open (Os). We also include standards to perform on-wafer Open-Short-Load-Thru (OSLT) calibrations which we use to manually extract switch terms (see Appendix B) if measuring with an older three-sampler VNA. We also include a set of IDCs, which are not used for calibration, but rather to obtain a rudimentary measurement of the calibration chip's substrate permittivity, if desired.

2.2.4.2 Test samples

Test samples are more simple than calibration chips and only require a single conductor layer. Each test sample includes at least four IDCs with unique active lengths for measurements below 100 MHz and multiple CPW transmission lines with unique lengths for measurements from 100 MHz to 110 GHz. The multiple transmission lines are again for multiline TRL, which is how we obtain the propagation constant, γ, of the CPWs on the test sample. An image of a test sample is shown in Figure 2.10.

Most test samples are smaller than calibration chips, so we cannot include as many devices. Generally, we will fit five to seven CPWs on a test sample. As we mentioned earlier, more CPWs improves the accuracy of the multiline TRL result. That said, we must balance this with the cost of space on the test sample and the time to measure each device. Typically, the longest CPW will span the full patternable width of the sample, but the remaining CPW lengths are arbitrary. That said, certain line lengths can improve the accuracy with which multiline TRL calculates γ. Multiline TRL works by comparing measurements of two CPW transmission lines with different lengths, but the algorithm is ill-conditioned when the difference in the accumulated phase between the two measurements is near multiples of 180° (see Eqn. 51 in Ref. [104]). The measured phase changes with line length and frequency. We are often trying to optimize combinations of six or more lines across a wide frequency range. As such, we use a simple Monte Carlo search to find line lengths that minimize the expected uncertainty when provided with a few experimental

parameters like substrate permittivity, frequency range, chip size, etc.

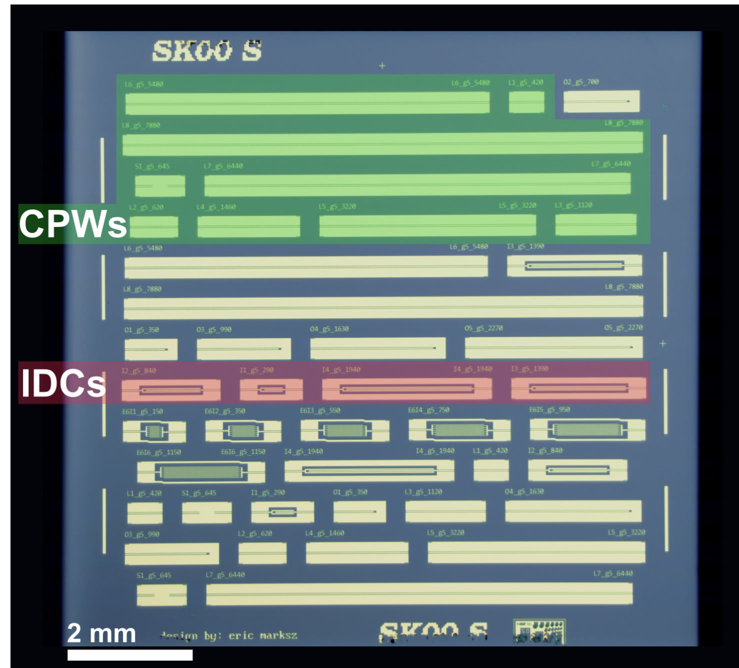

Figure 2.10. A test sample with the IDCs and CPWs highlighted. Additional devices are for redundancy or other experiments.

Device geometries and layouts are often unique to a specific experiment. For example, in order to measure a very thin film, we may use narrow gaps between the center conductor and ground planes of the CPWs to localize more of the electric field in a shallower region. This increases sensitivity to the thin film properties at the cost of increased relative uncertainty in the device dimensions. For materials with anisotropic permittivity, we need to use special bi-directional test patterns to measure both in-plane components of the complex permittivity (example in Appendix A).

2.2.5 Calibration procedures

After preparing the calibration chips and test samples, we begin our measurements, starting with the calibration procedures. We need to perform calibrations because our test signals must pass through several lengths of coaxial cable, connectors, and the GSG probes before arriving at our relatively tiny on-wafer IDCs and CPWs. As a result, the electrical properties of the on-wafer device are "embedded" in the raw measurement data - convolved with the attenuation, phase shift, and reflections from all of the other components. Little useful information about the on-wafer devices can be obtained without first calibrating and correcting the raw data. Figure 2.11 illustrates the difference between raw and corrected S-parameter data.

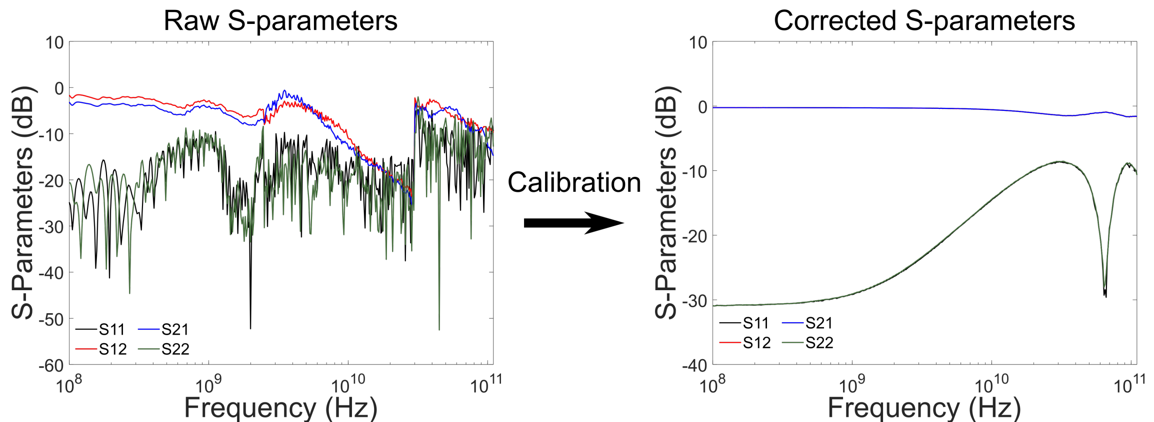

Figure 2.11. Calibrations allow us to "de-embed" the S-parameters of our on-wafer device (here, a 620 µm-long CPW transmission line) by correcting for the unwanted effects of cables, connectors, and probes that are included in the raw measurement data.

Fundamentally, all calibrations involve measuring a series of calibration standards with known or predictable properties. Deviation between the measured behavior and the expected behavior is used to build an "error model" that corrects

for the deviation. By correcting raw measurements with the error model, we remove the unwanted effects and isolate the properties of the device itself. The number and type of calibration standards required depends on the calibration procedure.

We use an eight-term error model for four-sampler VNAs [105]. In general, it is easier to understand and perform the calibrations using the T-parameter formalism (see Appendix B for conversion from S-parameters to T-parameters). T-parameters are convenient for calibration purposes because they allow us to break a large system into its constituent parts and represent each part with a unique T-matrix. For example, we represent the cables, connectors, and probes connected to port 1 as the T-matrix $[\mathbf{X}]$, the same items on port 2 as $[\mathbf{Y}]$, and the on-wafer device connected in between as $[\mathbf{T}]$:

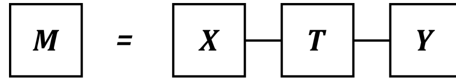

Mathematically, when we "cascade" (*i.e.,* multiply) the T-matrices $[\mathbf{X}]$, $[\mathbf{T}]$, and $[\mathbf{Y}]$, we obtain a T-matrix that represents the whole system, $[\mathbf{M}]$. The T-matrix $[\mathbf{M}]$ happens to correspond to the raw measurement made by the VNA:

$$[\mathbf{M}] = [\mathbf{X}][\mathbf{T}][\bar{\mathbf{Y}}], \tag{2.13}$$

where the overbar on $[\bar{\mathbf{Y}}]$ reflects the fact that $[\mathbf{Y}]$ was originally defined to cascade from right-to-left. The eight-term error model gets its name from the fact that there are eight error coefficients: the elements of the 2 x 2 matrices $[\mathbf{X}]$ and $[\mathbf{Y}]$, which we call the "error boxes" or "error matrices". The goal of our calibrations is to "fill

in" the error boxes so we can de-embed the T-parameters that describe the DUT, $[\mathbf{T}]$, in the following manner:

$$[\mathbf{T}] = [\mathbf{X}]^{-1}[\mathbf{M}][\bar{\mathbf{Y}}]^{-1}. \tag{2.14}$$

Measurements of known calibration standards are used to obtain the error boxes. The geometry of the calibration standards defines some reference plane, which can be thought of as the "end" of the error boxes. That is to say that the error boxes account for the electrical characteristics of everything between the VNA output ports and the reference planes. We noted the location of our typical reference planes on the CPWs and IDCs in Figures 2.5 and 2.7, respectively. Therefore, the corrected T-matrix $[\mathbf{T}]$ represents only the portion of the device between the reference planes.

2.2.5.1 Calibration from 100 MHz to 110 GHz

From 100 MHz to 110 GHz, we use a combination of two calibrations: the series resistor calibration [106] implemented as described in Ref. [107], and the multiline TRL calibration [104], implemented as described in Ref. [108]. These calibrations complement each other. The series resistor calibration is a simple, three-standard calibration with better repeatability relative to multiline TRL below 1 GHz. In addition to defining a set of error boxes, the series resistor calibration can be used to estimate two useful quantities: the mean capacitance per unit length (C_0') and the characteristic impedance of the CPW transmission lines. Multiline TRL, on the other hand, is widely regarded as the most accurate way to determine the propagation

constant of on-wafer CPWs at millimeter-wave frequencies.

All of the standards we need for these calibrations are contained on the calibration chips. Our first step is to measure and correct for the "switch terms" as described in Ref. [105]. Switch terms account for the change in the internal electrical characteristics of the VNA when it switches the signal source between port 1 and port 2. With a four-sampler VNA, we can compute the switch terms directly from measurements of the thru (L1) (see Appendix B).

Next, we measure the remaining transmission lines (L2, L3, ... Ln) and the short-circuit reflect (S1) for the multiline TRL calibration. The minutiae of multiline TRL are numerous, so we refer the reader to Refs. [104, 108, 109] which discuss the theory and implementation of multiline TRL. At its most basic, multiline TRL compares the measured T-matrices $[\mathbf{T_i}]$ and $[\mathbf{T_j}]$ of two transmission lines Li and Lj, which are identical except for their lengths, L_i and L_j. So long as the measurement instrumentation is not reconfigured, the error boxes are identical in both measurements, and we can create some T-matrix $[\mathbf{T_{ij}}]$ representing a line of length $(l_i - l_j)$, which reduces to:

$$[\mathbf{T_{ij}}] = [\mathbf{T_j}][\mathbf{T_i}]^{-1} = \begin{bmatrix} e^{-\gamma(l_j - l_i)} & 0 \\ 0 & e^{+\gamma(l_j - l_i)}. \end{bmatrix} \tag{2.15}$$

Multiline TRL uses the eigenvalues of $[\mathbf{T_{ij}}]$ to compute γ for the CPWs, and most of the elements of the error matrices $[\mathbf{X}]$ and $[\mathbf{Y}]$. In theory, we could accomplish this with only the thru and one longer line (TRL instead of multiline

TRL). However, as we mentioned in Section 2.2.4.2 the additional lines increase the number of independent measurements and limit the frequencies where the problem is ill-conditioned. Both of these aspects serve to reduce the uncertainty in the extracted γ. Finally, the reflect standard (S1) is used to determine the remaining two unknown elements of the error matrices, effectively defining the location of the reference planes.

We use the NIST StatistiCal software package [110] to implement multiline TRL. This software employs orthogonal distance regression and a weighting scheme to weight the most well-conditioned combinations of transmission lines for a given frequency. StatistiCal returns the values for γ and the error boxes when provided with the switch-term corrected S-parameters and lengths of the CPWs. These outputs are accompanied by 95% confidence intervals generated from the covariance matrix, under the assumption that uncertainties are uncorrelated between measurements of two different lines [104].

Multiline TRL calibrates our data relative to the characteristic impedance Z_c of the CPW transmission lines, which is often different than the 50 Ω reference impedance of the VNA (Z_{REF}). There is some "impedance transformer" (a cascade matrix that accounts for impedance mismatch - see Appendix B) bundled into the error boxes [**X**] and [**Y**], but we don't actually know Z_c. The series resistor calibration [106] uses a calibration standard with a known load impedance to estimate Z_c of the CPW transmission lines. For a series resistor calibration, we measure the Rs, Cs, and S1 devices, and perform the calibration as described in Ref. [107], using the DC resistance of the Rs standard as the approximate load impedance. The series

resistor calibration also generates a set of error boxes which can be used in place of those obtained from multiline TRL.

The last step in our calibrations from 100 MHz to 110 GHz is to translate our reference planes from the center of the thru (L1) to the end of the landing pads. We use γ from multiline TRL and Z_c from the series resistor calibration to generate a T-matrix (and impedance transformer, if necessary) that represents a section of transmission line equal in length to the distance between the center of the thru and the landing pads (Equation 2.10). Cascading this T-matrix with the error boxes moves the reference planes to our desired location, the end of the landing pads. This step helps to limit pad capacitance errors when the calibration chip and test samples have different substrate permittivities.

2.2.5.2 Calibration from 1 MHz to 100 MHz

We also use the series resistor calibration to correct our measurements spanning from 1 MHz to 100 MHz. The multiline TRL algorithm is ill-conditioned at these frequencies because the long signal wavelengths produce very little phase difference over the lengths of the CPWs. However, after de-embedding with the error boxes from the series resistor calibration, we can reliably fit the S-parameters of long CPW transmission lines in this frequency range to a transmission line model as described in Ref. [111]. A good fit allows us to directly extract the distributed circuit parameters (R', L', C', and G'), thereby obtaining γ and Z_c from Equations 2.4 and 2.11. This approach is more reliable for bare substrates with constant ca-

pacitance and negligible loss, so C' and G' can be fixed during the first iteration of fitting. We typically use a measurement of the longest line on the calibration chip for this purpose. The distributed circuit parameters can be used to generate γ and then translate reference planes if desired.

2.2.5.3 Calibration from 100 Hz to 1 MHz

We calibrate the LCR meter for our measurements from 100 Hz to 1 MHz with an built-in open-short calibration designed to account for the impedance of the cables, switches, and probes. The LCR meter automatically performs the calibration across all measurement frequencies. After calibration, the LCR meter applies the correction and outputs calibrated data. We refer the reader to Ref. [112] for more detailed information on LCR meter calibrations and measurements.

We configure the LCR meter to measure the series capacitance between the inner and outer conductors of the IDCs. This means that the circuit is connected via the two signal prongs of the GSG probes. Therefore, we use the series open (Os) as the open circuit standard for calibration, and the thru (L1) as the short circuit. These standards set the reference planes at the center of the thru, which corresponds to the end of the IDC feedlines as shown in Figure 2.7.

2.2.6 Test sample measurement and analysis

Once the calibrations are complete, we measure the companion substrate and thin film test samples. A concise description of the analysis detailed below and the

propagation of uncertainty in measurement is included in Appendix B. We also demonstrate this approach with real measurements of a dielectric thin film in Chapter 3.

2.2.6.1 Measurement and analysis of CPWs

For each test sample, we measure the S-parameters of all CPW transmission lines and the short-circuit reflect (S1) from 100 MHz to 110 GHz. Using the error boxes obtained from our calibrations, we correct the raw S-parameters measurements of the CPWs, and then use the corrected S-parameters to perform multiline TRL. This provides an accurate measurement of the propagation constant, γ, of the transmission lines on the test sample.

Our first goal in the analysis is to isolate the distributed capacitance and conductance, C' and G', from γ. As we saw in Equation 2.1, these circuit parameters are linked to the real and imaginary parts of the relative permittivity. If we know the distributed resistance and inductance, R' and L', we can obtain C' and G' as follows:

$$\begin{aligned} C' &= \frac{1}{\omega}\Im[\frac{\gamma^2}{R' + i\omega L'}], \\ G' &= \Re[\frac{\gamma^2}{R' + i\omega L'}]. \end{aligned} \tag{2.16}$$

There are two primary approaches to find R' and L'. In some cases, we can use the quantities R'_{sub} and L'_{sub} from measurements on the companion substrate to extract C' and G' for the test samples with thin films as described in Ref. [41].

It is easier to find R'_{sub} and L'_{sub} for the companion substrate since we specifically choose substrates that will have a constant distributed capacitance and negligible conductance (*i.e.*, C'_{sub} = constant, $G'_{sub} \approx 0$). However, this approach is predicated on the assumption that the dimensions and properties of the devices on the companion substrate and thin film test samples are perfectly identical. We have observed that sample-to-sample variation in the device dimensions is rarely negligible and therefore can distort the resulting C' and G' values.

In general, we can obtain a better result by using simulated values of the distributed resistance and inductance, R'_{sim} and L'_{sim}, to extract C' and G' from γ. We use 2D finite element simulations to generate these quantities (Section 2.2.7). The advantage of using simulations is that we generate unique R'_{sim} and L'_{sim} values that represent the unique devices on each test sample, based on that sample's measured dimensions and conductor properties. Thus, we do not need to assume that the devices on the thin film samples are identical to those on the companion substrate. We perform a frequency sweep simulation to obtain the frequency-dependent R'_{sim} and L'_{sim} values and then extract C' and G' as described in Equation 2.16.

Once we have found C' and G', we are close to determining the real and imaginary parts of the relative permittivity. As we discussed in Section 2.2.3.1, there is some "mapping function" based on the electric field configuration and device geometry that describes the relationship between the material properties and the distributed circuit parameters. If we know this function, f, and measure C', we can determine ε':

$$\varepsilon' = f(C'). \tag{2.17}$$

We use the mapping functions with our measured C' and G' values to obtain our final result: the real (ε') and imaginary (ε'') parts of the relative permittivity from 100 MHz to 110 GHz, as well as the loss tangent ($\tan(\delta) = \varepsilon''/\varepsilon'$). Finite element modeling provides a fast and reliable means to obtain the mapping function, especially since we have already constructed models of our devices to find R'_{sim} and L'_{sim}. We describe the process of obtaining the thin film permittivity mapping functions from simulation in Section 2.2.7 and demonstrate the implementation with real measurements in Chapter 3.

2.2.6.2 Measurement and analysis of IDCs

Next, we measure all of the IDCs on the test samples using the LCR meter (100 Hz to 1 MHz) and a VNA (1 MHz to 100 MHz). Although the latter portion of the analysis is identical for both frequency regimes, we must initially consider the measurements from the two instruments separately, since the process to obtain the lumped series admittance of the IDCs, $Y_{S,IDC}$, is different for each instrument.

The lumped series admittance $Y_{S,IDC}$ is easily obtained from the LCR meter which provides the corrected frequency-dependent capacitance C_{IDC} and dissipation factor D, for each measured IDC:

$$Y_{S,IDC} = D \cdot \omega C_{IDC} + i\omega C_{IDC}. \tag{2.18}$$

The process to obtain $Y_{S,IDC}$ from the VNA measurements from 1 MHz to 100 MHz is slightly different. First, we measure the raw S-parameters of the IDCs and

correct them with the error boxes obtained from the calibrations described in Section 2.2.5.2. We then convert the corrected S-parameters to admittance (Y-) parameters (see Appendix B). A π-network circuit like the one we use to model the IDCs (Section 2.2.3.2) is described by the following 2 x 2 admittance (Y-) matrix:

$$[\mathbf{Y}_{IDC}] = \begin{bmatrix} Y_{G_1} + Y_{S,IDC} & -Y_{S,IDC} \\ -Y_{S,IDC} & Y_{G_2} + Y_{S,IDC} \end{bmatrix}, \tag{2.19}$$

where Y_{G_1} and Y_{G_2} are the lumped shunt admittances on the port 1 and port 2 sides, respectively. The off-diagonal elements of the Y-matrix above hold our quantity of interest, $Y_{S,IDC}$. As such, we can take either Y_{12} or Y_{21}, which should be equivalent, to be the lumped series admittance of the IDC, $Y_{S,IDC}$.

At this point, we have obtained the corrected $Y_{S,IDC}$ from 100 Hz to 100 MHz, and analyze the measurements from the LCR meter and VNA together. We recall that $Y_{S,IDC}$ is comprised of a lumped conductance and lumped capacitance between the inner and outer conductors of the measured IDC:

$$Y_{S,IDC} = G_{IDC} + i\omega C_{IDC}. \tag{2.20}$$

Similar to the CPW devices, the circuit parameters C_{IDC} and G_{IDC} are linked to the real and imaginary parts of the relative permittivity, respectively. However, in the CPW case, we analyzed the *distributed* circuit parameters C' and G', which represented the capacitance and conductance *per unit length*. In the IDCs, C_{IDC} and G_{IDC} describe the total lumped capacitance and conductance of each measured

IDC.

In theory, it is possible to use C_{IDC} and G_{IDC} from a single measured IDC to determine the relative permittivity of a thin film. However, reducing C_{IDC} and G_{IDC} to analogous *per unit length* quantities simplifies our analysis and improves accuracy. We isolate the capacitance and conductance per unit length (C'_{IDC} and G'_{IDC}) *of the active length region* of the IDC by measuring multiple IDCs with different active lengths. Measuring multiple unique IDCs provides more independent measurements which reduces uncertainty. Also, the active length region has an invariant cross-section, which allows us to use 2D finite element simulations to map C'_{IDC} and G'_{IDC} to the material properties like we do for the CPWs.

As we mentioned in Section 2.2.3.2, all of the IDCs on a test sample are identical, except for the change in active length. With this in mind, we break $Y_{S,IDC}$ into two parts:

$$Y_{S,IDC} = Y_0 + l \cdot Y_l'. \tag{2.21}$$

where Y_0 is some offset that accounts for admittance in parts of the IDC like the finger ends and region where the port 1 center conductor forks into two fingers. Since these sections do not change from device-to-device, the admittance Y_0 should be constant across all of the IDCs. In Equation 2.21, l is the active length of the measured IDC, and Y_l' is the admittance per unit length of the active length region. We determine Y_l' from the slope of the line obtained by measuring $Y_{S,IDC}$ for all of the IDCs with different active lengths on a test sample, as illustrated in Figure 2.12.

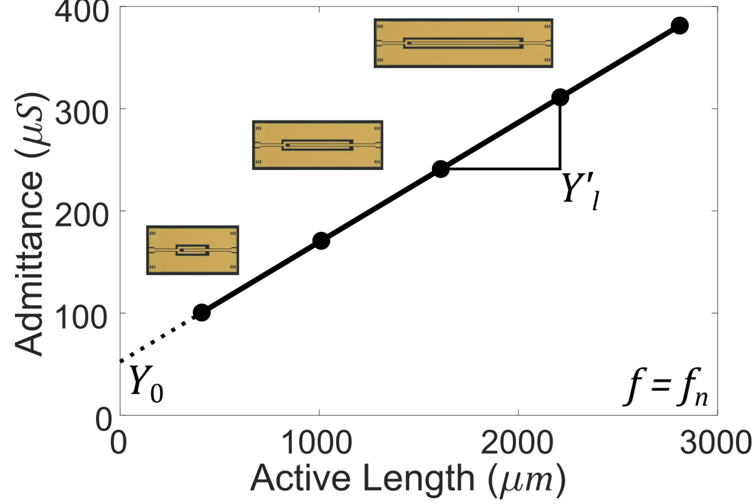

Figure 2.12. We measure multiple IDCs with different active lengths, and use the relationship between the admittance, $Y_{S,IDC}$, and the active length to determine the admittance per unit length of the active length region, Y_l'. We do this at every frequency point, f_n.

Next, we consider the components of Y_l':

$$Y_l' = G_{IDC}' + i\omega C_{IDC}', \tag{2.22}$$

and see that we can obtain the circuit parameters we are interested in from:

$$\begin{aligned} C_{IDC}' &= \frac{1}{\omega}\Im[Y_l'], \\ G_{IDC}' &= \Re[Y_l']. \end{aligned} \tag{2.23}$$

Armed with the capacitance and conductance per unit length, C_{IDC}' and G_{IDC}', we are close to calculating the real and imaginary parts of the relative permittivity. Just like we did for the CPW transmission lines, we use a 2D finite element model of the active length region to develop a mapping function, f_{IDC}, that relates the

circuit parameters of the IDCs to the material properties:

$$\varepsilon' = f_{IDC}(C'_{IDC}), \tag{2.24}$$

and likewise for the imaginary part of the permittivity.

2.2.7 Finite-element modeling (FEM)

We've seen throughout this chapter that finite element simulations form an integral part of our permittivity measurement technique – both to obtain the requisite distributed circuit parameters and map those parameters to material properties.

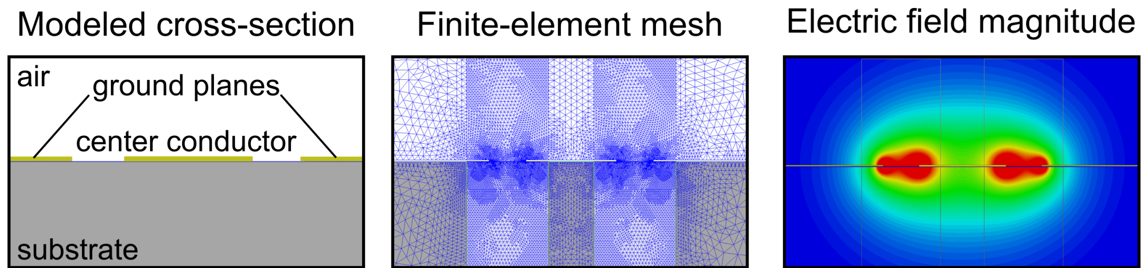

Figure 2.13. (left) We create finite element models of the on-wafer devices for our analysis. (center) The solver refines the mesh until the solution converges. (right) The electric fields are strongest in and around the gaps between the center conductor and ground planes of the CPWs.

We primarily use 2D finite element simulations, which are ideal for our needs. In addition to being faster than 3D simulations, the 2D solvers use discrete approximations of Maxwell's equations to directly report the distributed circuit parameters for a simulated device cross-section. This is ideal, because we can relate the simulated circuit parameters directly to our measured circuit parameters with minimal analysis. Furthermore, the convergence criteria, which ultimately controls how finely

the model is broken up into discrete elements, can based on these circuit parameter values, to minimize convergence error in our results. For example, the software will iteratively refine and solve the model until consecutive passes produce a value for C' that is within 0.5 % of the previous solution.

Our ability to use finite element simulations relies on a few key assumptions. First, to use any finite element model, the simulated structures must accurately represent our real test devices. We ensure this by constructing our models with the measured dimensions for the devices on each test sample. We validate our models by comparing the simulated circuit parameters to the circuit parameters of the CPWs on the companion substrate. Second, 2D simulations are limited to studying TEM mode propagation. Modes with a significant longitudinal component require 3D simulations for proper analysis. The quasi-TEM approximation appears to be valid in our measured frequency range, and this approximation is critical throughout our use and analysis of the CPW transmission lines (for example, when we simplify Equation 2.1). Preliminary modeling of our CPW structures with both 3D finite element and finite difference time domain (FDTD) techniques have suggested that above 100 GHz a mode with a weak longitudinal component may begin to appear in cases where the substrate and superstrate have significantly different permittivity. While this did not appear to be a concern in our measured frequency range (< 1 % the strength of the TEM mode), this is something to consider as we explore advancing our measurements to 145 GHz and beyond.

2.2.7.1 Resistance (R') and inductance (L') simulations

As described above, 2D finite element simulations provide a convenient and accurate way to obtain the distributed resistance and inductance, R'_{sim} and L'_{sim}, which we use to extract C' and G' from measurements of γ at high frequencies. We create a unique model for each test sample (Figure 2.13), incorporating the actual measured dimensions of the devices on that sample and the conductor properties measured via DC resistance measurements. We first model the CPW transmission lines on the companion substrate and use this case to verify that the simulated R'_{sim} and L'_{sim} for the substrate match the R' and L' values that we obtain from the measured γ and estimated Z_c (Equation B.10). As a reminder, we can more confidently estimate the R' and L' values for the companion substrate, because we choose substrate materials that will produce a constant C', and negligible G'. Figure 2.14 shows ideal agreement between the simulated and estimated R', which validates our model.

Modeling the other test samples typically requires only small, but non-negligible, perturbations of the geometric dimensions and conductor properties, so we use the validated model of the companion substrate as our starting point. R' and L' have frequency-dependence due to the skin effect, so our simulations include a frequency sweep spanning our measured frequency range. We consider the simulation to have converged when the values of the circuit parameters change less than 0.5 % per pass across three passes. The simulation mesh (Figure 2.13) is refined by 30 % with each pass until it is sufficiently dense for the solution to converge.

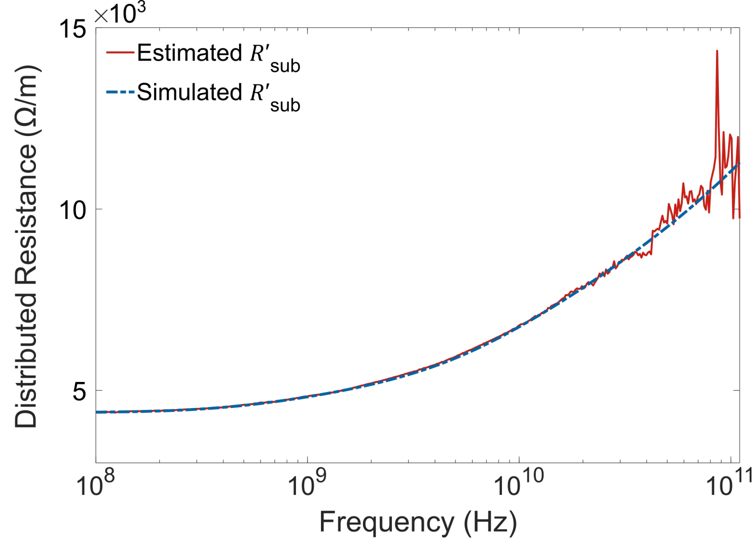

Figure 2.14. The simulated R' agrees quite well with the value estimated from measurement, indicating the validity of our 2D finite element model of the CPW transmission lines.

2.2.7.2 Capacitance (C') and conductance (G') simulations

In addition to using our finite element models to obtain the distributed resistance and inductance, we also use these models to develop the mapping functions relating the distributed capacitance and conductance of the thin film and substrate to the real and imaginary parts of the relative permittivity.

We again start with simulations of the companion substrate to find the relative permittivity of the substrate material. This step is crucial, because we will use the substrate permittivity we calculate here as the substrate permittivity value for the simulations of the thin film test samples. An incorrect substrate permittivity can significantly skew the result for the permittivity of the thin film layer. Fortunately, this process is rather simple. We begin with the the validated simulation that we used to generate R'_{sim} and L'_{sim} for the companion substrate. We then perform a parametric sweep in which we analyze the simulation repeatedly with a range of

substrate permittivity values. We compare the simulated distributed capacitance values (C'_{sim}) with the measured mean distributed capacitance of the companion substrate, C'_0, to determine the permittivity of the substrate, and use this value in our remaining simulations.

Developing the mapping function to determine the permittivity of the thin film layers of the test samples is a similar process. This time, we hold the substrate constant and sweep the relative permittivity values of the thin film layer. We compare the simulated distributed capacitance, C'_{sim}, with the relative permittivity values we swept in the simulation. We typically observe a linear increase in capacitance with increasing thin film permittivity, which indicates that the distribution of the electric fields is relatively constant (Figure 2.15). There can be some deviation in this trend when the permittivity of the simulated thin film is near or less than the substrate permittivity. The tunable dielectric films we study tend to have large permittivity values, so we are almost always mapping in the linear regime. The relationship between the permittivity and capacitance can be modeled many ways, but we usually model it with a line, for simplicity and to facilitate error propagation. In this case, the mapping function becomes:

$$\varepsilon' = a_1(C') + a_2, \tag{2.25}$$

where we determine the mapping coefficients a_1 and a_2 from fitting. We can either map using the total measured capacitance, C'_{tot}, or the portion of the capacitance

attributable to the thin film, C'_{film}, where:

$$C'_{film} = C'_{tot} - C'_{sub}. \tag{2.26}$$

While the results are approximately the same, mapping with C'_{film} can be advantageous in that subtracting the measured substrate capacitance C'_{sub} can remove some systematic noise from the measurements. In this case, the mapping coefficient a_2 will approximately be the substrate permittivity. In practice, the mapping coefficient a_1 is the same for the function relating C' to ε' and for the function relating G' to ε'', which is not necessarily surprising in light of Equation 2.1. The latter mapping function generally has $a_2 = 0$, though, considering the boundary condition that $G' = 0$ corresponds to no dielectric loss ($\varepsilon'' = 0$). This can also be verified by sweeping the loss tangent of the film in simulation. Once we have obtained a valid mapping function, we apply it to our measured circuit parameters to obtain the permittivity. This process is illustrated by Figure 2.15.

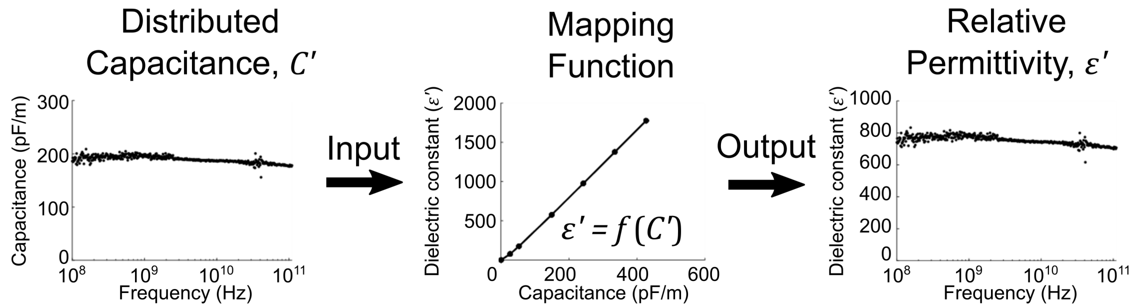

Figure 2.15. We use finite element modeling to obtain a mapping function relating the measured C' and G' to the real and imaginary parts of the relative permittivity, respectively.

Regarding the IDC mapping functions, the process is much the same. We

model the IDC using measured dimensions, and validate the model by comparing the resulting IDC and CPW substrate permittivities. In practice, the slope of the IDC and CPW mapping functions are nearly identical for a given film thickness and conductor geometry.

2.2.8 Electric-field tunability measurements

When testing tunable dielectric materials, one of the most important properties to characterize is the relative tunability. We perform the tunability measurements like we would any other permittivity measurement, but with the addition of a controllable DC bias voltage applied between the center conductor and ground planes of the CPWs. This voltage generates a DC electric field that causes the permittivity of the tunable thin film to change as we described in Chapter 1.

We must modify the measurement setup slightly to enable the application of the DC bias voltage (see Appendix A). Naturally, we must add a voltage source to the measurement setup. To combine the DC voltage with our measurement signal, we insert bias tees between the output ports of the VNA and the coaxial cables leading to the GSG probes. Other than the output leading to the probe, the bias tees have a capacitive arm (connected to the VNA) and an inductive arm (connected to the voltage source). The capacitive arm passes the AC signal to and from the VNA, but protects the VNA from the applied voltage. The inductive arm does the opposite. Due to the bandwidth limitations of the bias tees, we only perform the electric-field-dependent permittivity measurements in the HF frequency regime,

from 100 MHz to 40 GHz. Similarly, we are limited to maximum applied voltages of +/- 200 V.

With this measurement configuration, we perform our calibrations and test measurements as we normally would. However, when we contact the CPWs on the test samples, we also run a subroutine which sweeps through a range of applied DC voltages, and performs an S-parameter measurement at each voltage step. We always sweep up to our maximum desired DC voltage, down to the minimum voltage (i.e. same magnitude as maximum voltage but opposite polarity), and then back up to the maximum voltage before sweeping back to no applied voltage. This allows us to trace out a full hysteresis loop, if the material under test displays hysteretic behavior. Figure 2.16 illustrates how we use these measurements to build a comprehensive picture of the frequency- and field-dependent properties of the tunable dielectric thin films we study.

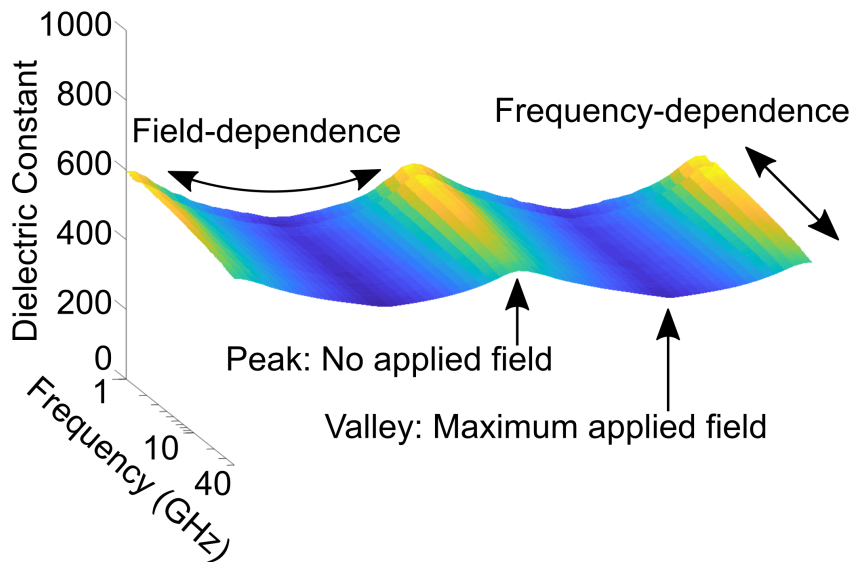

Figure 2.16. A measurement of the permittivity of a tunable dielectric thin film from 1 GHz to 40 GHz, spanning applied fields from $-75\,\mathrm{kV\,cm^{-1}}$ to $75\,\mathrm{kV\,cm^{-1}}$.

2.3 Outlook

In this chapter, we discussed some of the many techniques for measuring the permittivity of materials, and motivated our use of on-wafer IDCs and CPWs to measure the broadband permittivity of thin films. We then described the measurement methodology we use to determine the permittivity of thin films from 100 Hz to 110 GHz. We detailed notable aspects of the measurement instrumentation, on-wafer devices, calibrations, and simulations. A concise description of the analysis procedure, including propagation of uncertainties is included in Appendix B, and the next chapter demonstrates the application of our techniques to measure the relative permittivity of a homogeneous, single-composition dielectric thin film.

Chapter 3

Broadband permittivity characterization of a homogeneous dielectric thin film

3.1 Overview

This chapter serves mainly as a demonstration of the on-wafer broadband permittivty characterization techniques we presented in Chapter 2. Here, we measure the relative permittivity of a homogeneous tunable dielectric thin film from 100 Hz to 110 GHz using IDCs and CPWs patterned on the film surface. We begin with this simple case to familiarize the reader with the practical execution of these measurements before we move on to study more complex and interesting systems, including composition-spread thin films in Chapter 4 and strain-engineered superlattice thin films in Chapter 5.

3.1.1 Material under test: $Ba_{0.5}Sr_{0.5}TiO_3$

For this demonstration, we grew and measured a $Ba_{0.5}Sr_{0.5}TiO_3$ thin film. Like the $BaTiO_3$ we examined in Figure 1.1 when discussing the fundamental concepts of ferroelectricity, $Ba_{0.5}Sr_{0.5}TiO_3$ is a perovskite ferroelectric. In $Ba_{0.5}Sr_{0.5}TiO_3$, half of the Ba^{2+} ions on the corner sites are randomly substituted with slightly smaller Sr^{2+} ions, as we show in Figure 3.1.

We chose to measure this material due to its significant role in microwave tunable dielectrics research. The (Ba,Sr)TiO_3 system has received a lot of attention due to its beneficial balance of tunability and loss tangent, and ability to use the Ba/Sr ratio to control the paraelectric-ferroelectric transition temperature [27, 32]. Chapters 4 and 5, which include studies of various (Ba,Sr)TiO_3-based materials provide more information on this system.

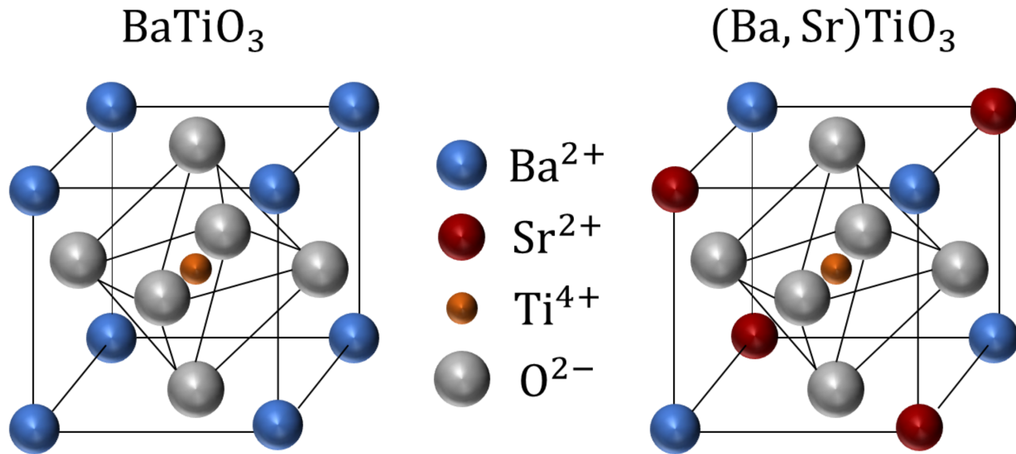

Figure 3.1. (left) The $BaTiO_3$ unit cell. (right) The $Ba_{0.5}Sr_{0.5}TiO_3$ unit cell, showing the random substitution of some Ba^{2+} ions with Sr^{2+} ions.

3.1.2 Growth and basic characterization of the $Ba_{0.5}Sr_{0.5}TiO_3$ film

We grew the $Ba_{0.5}Sr_{0.5}TiO_3$ film using pulsed laser deposition (PLD). This technique, illustrated in Figure 3.2, is a form of physical vapor deposition (PVD) in which a high-powered laser pulse strikes a sintered ceramic target to ablate material from the target surface. The ablated material is ionized by the laser pulse and ejected from the target, expanding outward as a plume of plasma comprised of the elements in the target. The plume material then condenses on the surface of a nearby

heated crystalline substrate to produce a thin film. PLD is a relatively simple way to produce a variety of thin films. Although sample size is limited, PLD can quickly produce high-quality films with stoichiometry closely matching that of the precursor target.

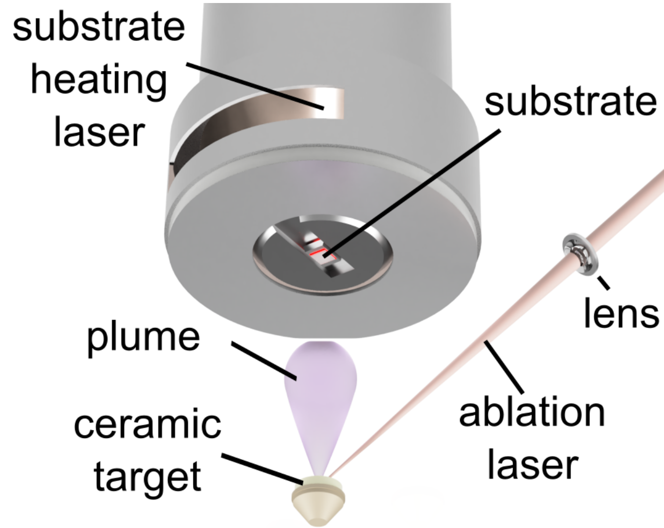

Figure 3.2. A diagram illustrating the PLD growth process.

The $Ba_{0.5}Sr_{0.5}TiO_3$ film we measure in this chapter was grown on a 10 mm x 10 mm square (001)-cut $(LaAlO_3)_{0.3}(Sr_2TaAlO_6)_{0.7}$ (LSAT) substrate ($a = 3.86$ Å), which is fairly well lattice matched with $Ba_{0.5}Sr_{0.5}TiO_3$ ($a \approx 3.96$ Å). The film was approximately 500 nm thick, and grown from a 1" $Ba_{0.5}Sr_{0.5}TiO_3$ target. The ablation laser provided 20 mJ pulses at a repetition rate of 5 Hz. The substrate temperature was 765 °C and the background oxygen partial pressure was 4 Pa.

Following deposition, we verified the crystalline quality of the film with x-ray diffraction (XRD). A $\Theta - 2\Theta$ XRD scan spanning from $2\Theta = 10°$ to $2\Theta = 90°$ is shown in Figure 3.3. The (100), (200), and (300) peaks for both the film and

substrate are prominent features in this scan. The absence of other peaks that are typically observed in randomly-oriented polycrystalline samples indicates that this $Ba_{0.5}Sr_{0.5}TiO_3$ film is highly-oriented and well-aligned with the LSAT substrate. We do note that the weak (002) peak ($\star$) near $2\Theta = 43°$ and the (220) and (202) peaks (†) near $2\Theta = 65°$ may suggest that a very small fraction of tetragonal $Ba_{0.5}Sr_{0.5}TiO_3$ is present in the film. This is not necessarily surprising, as the tetragonal-to-cubic phase transition temperature for $Ba_{0.5}Sr_{0.5}TiO_3$ is not far below room temperature. The composition-dependence of this transition is explored in detail in Chapter 4.

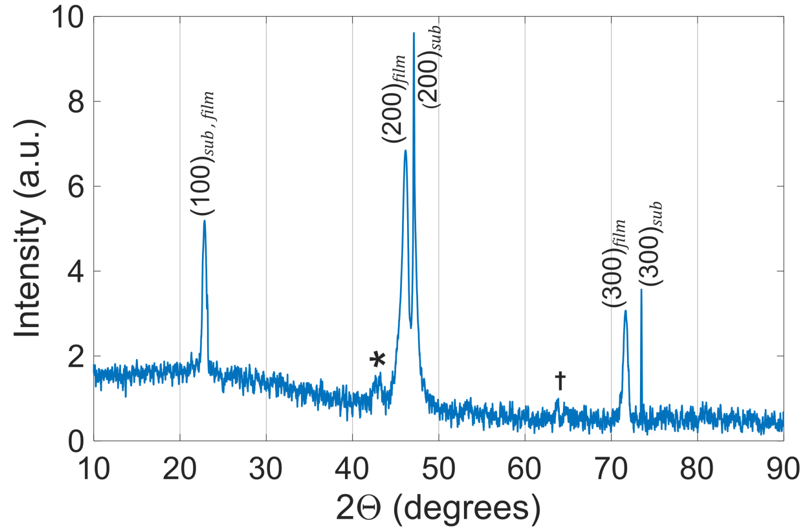

Figure 3.3. The $\Theta - 2\Theta$ XRD scan of the 500 nm thick $Ba_{0.5}Sr_{0.5}TiO_3$ film, taken at room temperature, suggests a preferential orientation of the film matching that of the LSAT substrate.

3.1.3 On-wafer devices and fabrication

We fabricated a pattern of IDCs and CPWs on the surface of the $Ba_{0.5}Sr_{0.5}TiO_3$ thin film to measure the broadband permittivity using the techniques described in Chapter 2. We also co-fabricated an identical pattern on a bare LSAT chip as our

companion substrate. We show the patterned LSAT substrate in Figure 3.4.

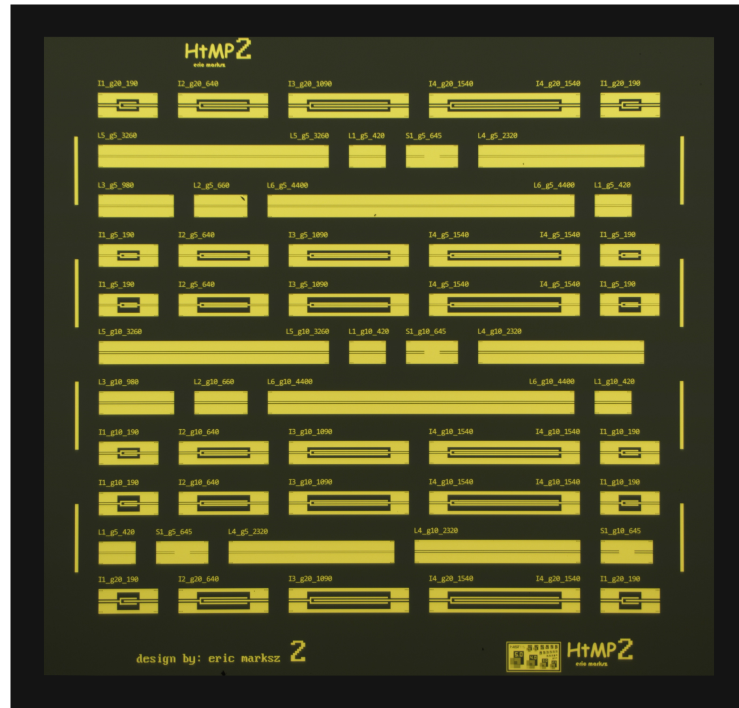

Figure 3.4. A microscope image of the patterned companion substrate.

For the measurements demonstrated in this chapter, we used six CPWs and a short-circuit reflect for measurements above 100 MHz, and four IDCs for measurements below 100 MHz. Other devices in the test pattern were for miscellaneous experiments pertaining to metrology development. The CPW lengths were $l = (0.42,\ 0.66,\ 0.98,\ 2.32,\ 3.26,\ 4.40)$ mm, and the IDC active lengths were $l = (0.19,\ 0.64,\ 1.09,\ 1.54)$ mm. The CPW lengths were selected as described in Chapter 2, though we note that the longest line was shorter than the width of the chip, to improve device yield on the test samples. The center conductor of the CPWs, as well as the inner and outer conductors of the IDCs were all 20 µm wide. The gaps between the center conductor and ground planes of the CPWs, and between the inner and outer conductors of the IDCs were 10 µm wide. The gap between the outer

conductor and ground planes of the IDC was 40 µm, and the ground planes of the CPWs were 150 µm wide.

3.2 Broadband permittivity measurements of the LSAT substrate and $Ba_{0.5}Sr_{0.5}TiO_3$ thin film

After fabricating the test devices on the companion LSAT substrate and $Ba_{0.5}Sr_{0.5}TiO_3$ film, we performed the electrical measurements. Using a VNA, we measured the S-parameters of the IDCs at 201 logarithmically spaced frequency points from 1 MHz to 100 MHz, and measured the S-parameters of the CPWs at 401 logarithmically spaced frequency points from 100 MHz to 110 GHz. The VNA source power was -15 dBm and the IF bandwidth was 100 Hz. For the LCR meter measurements, we measured the capacitance and dissipation factor of the IDCs at 21 logarithmically spaced frequency points from 100 Hz to 1 MHz with a 1 V stimulus amplitude. To perform the calibrations, we used previously-fabricated calibration chips with similar device geometry to the test samples. All measurements presented here were performed at room temperature.

3.2.1 Measurements and analysis of CPWs

We begin by demonstrating how we obtain the capacitance and conductance per unit length of the CPWs (C' and G') from 100 MHz to 110 GHz. After applying the calibrations to correct our measured S-parameters, we used the measurements of all six CPWs and the short-circuit reflect (S1) to obtain the measured propagation

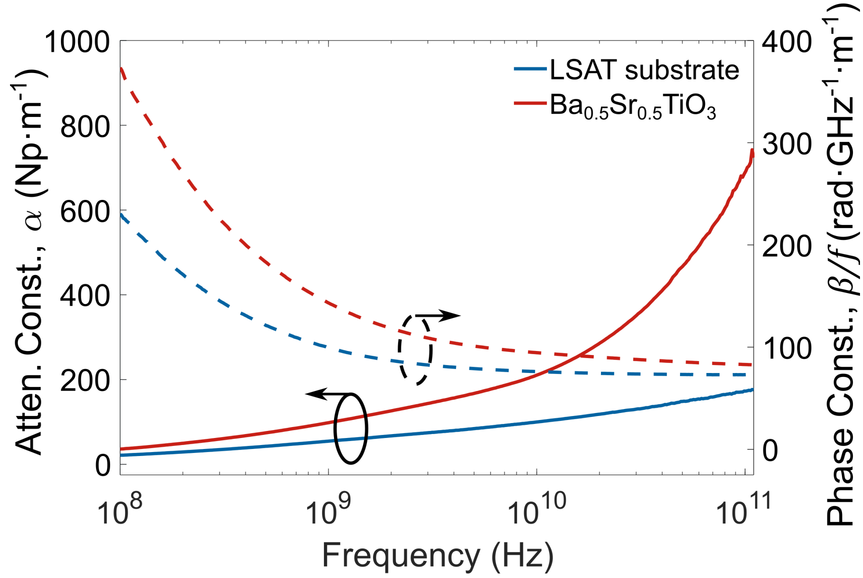

Figure 3.5. The components of the propagation constant for the substrate and film from 100 MHz to 110 GHz.

constant, γ, using multiline TRL. As we discussed in Section 2.2.3.1, γ is our starting point in extracting the distributed circuit parameters that we will use to eventually determine the relative permittivity of the substrate and thin film. In Figure 3.5, we plot the attenuation constant, α and the frequency-normalized phase constant, β/f, recalling that $\gamma = \alpha + i\beta$. While the distributed resistance and inductance (R' and L') both contribute to the frequency-dependence of α and β, we note two salient aspects of the curves in Figure 3.5. In examining the solid lines representing the attenuation constant, α, we see that the curve for the film increases rapidly and diverges from that of the substrate. This is due, at least in significant part, to the increase in dielectric loss of the $Ba_{0.5}Sr_{0.5}TiO_3$ film with increasing frequency, which increases the amount of attenuation. On the other hand, the curves for the phase constant, β, draw closer together as frequency increases. This is partially due to the decrease in the dielectric constant due to dielectric relaxation in the $Ba_{0.5}Sr_{0.5}TiO_3$

film at microwave frequencies.

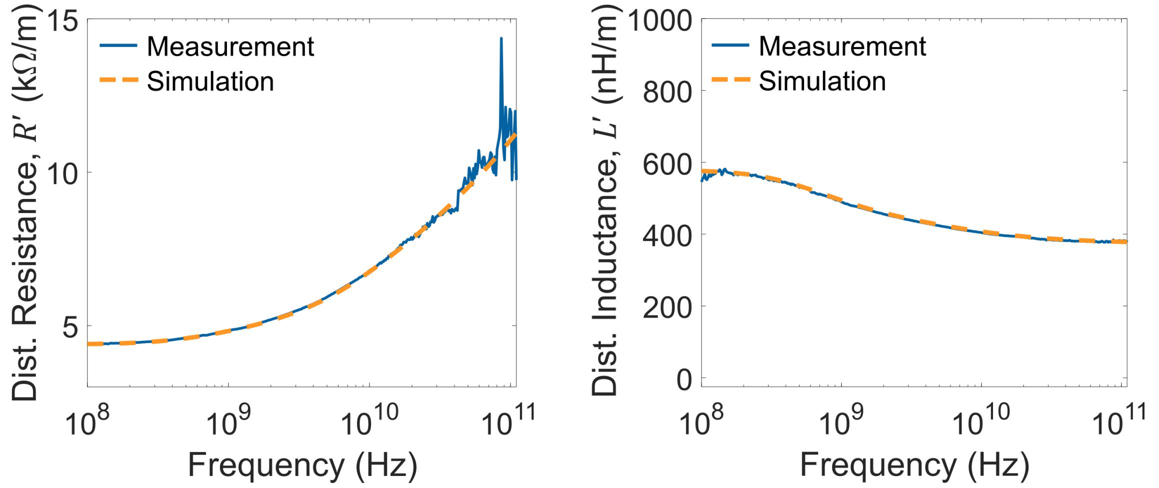

Figure 3.6. The resistance and inductance per unit length of the CPWs on the LSAT substrate.

We can calculate C' and G' from γ using Equation 2.16 if we know the distributed resistance and inductance (R' and L') of the CPWs. As we discussed in Chapter 2, we use finite-element simulations to obtain R' and L'. For validation, we compare the simulated R' and L' values with those estimated from the measurements of the companion LSAT substrate, which we can estimate with reasonable accuracy assuming constant capacitance and negligible conductance. In Figure 3.6 we compare the simulated R' and L' values for the CPWs on the LSAT substrate to the R' and L' values estimated from measurement, which show close agreement.

Once we are confident in the validity of our simulated R' and L' values, we use them to extract the the distributed capacitance and conductance, C' and G', from γ. Figure 3.7 shows C' and G' for the LSAT substrate and the $Ba_{0.5}Sr_{0.5}TiO_3$ sample. The C' and G' values for the $Ba_{0.5}Sr_{0.5}TiO_3$ sample are significantly larger than those of the LSAT substrate. This is unsurprising given the large relative permittivty and

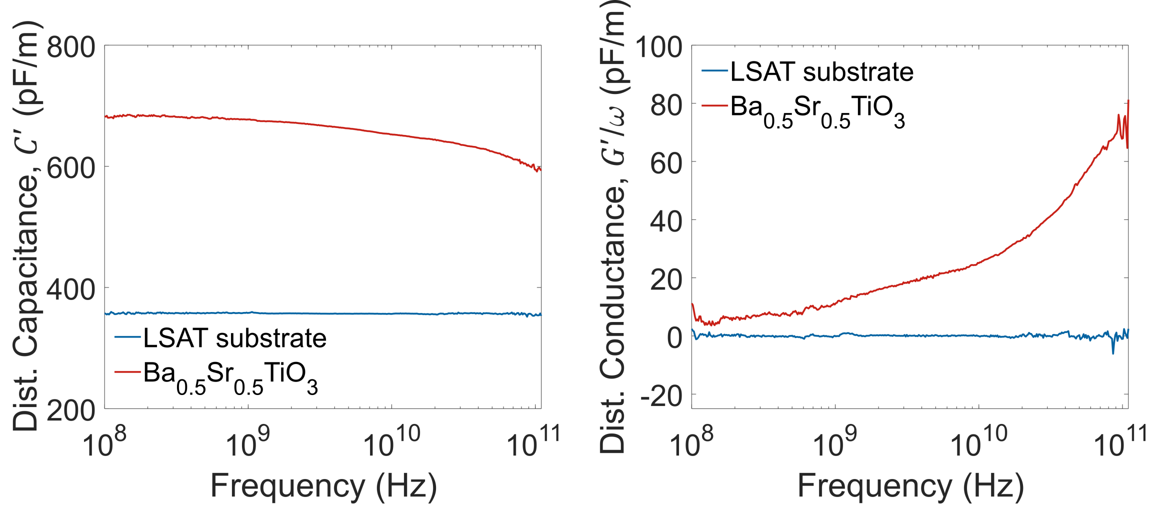

Figure 3.7. The capacitance and conductance per unit length for the LSAT substrate and $Ba_{0.5}Sr_{0.5}TiO_3$ thin film sample.

notable dielectric loss common in $Ba_{0.5}Sr_{0.5}TiO_3$ films. We note that the assumptions we make regarding the CPWs on the LSAT substrate are quite reasonable - C' is constant across the measured frequency range, and G' is negligible. We will use the C' and G' values presented in Figure 3.7 to determine the relative permittivity of the $Ba_{0.5}Sr_{0.5}TiO_3$ film and LSAT substrate using mapping functions obtained from additional finite element simulations. Before performing that mapping, we will demonstrate the process of finding the IDC capacitance and conductance per unit active length (C'_{IDC} and G'_{IDC}) from 100 Hz to 100 MHz in the next section.

3.2.2 Measurements and analysis of IDCs

As we described in Section 2.2.6.2, we measure all four IDCs from 100 Hz to 1 MHz with an LCR meter, and from 1 MHz to 100 MHz with a VNA. The LCR meter records *calibrated* capacitance and dissipation factor data, which we use with Equation 2.18 to find the total series admittance of each IDC. For the

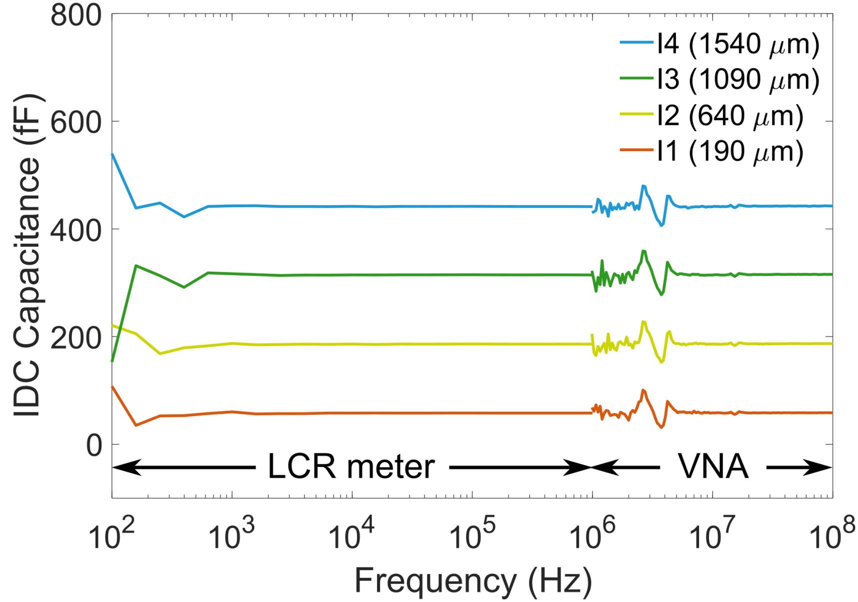

Figure 3.8. The total measured capacitance of the four IDCs on the LSAT substrate (*i.e.,* I1 to I4). The *active length* of each IDC is noted in the legend.

measurements above 1 MHz, we correct the S-parameter measurements with the calibrations described in Section 2.19, convert to Y-parameters, and then extract the total series admittance of each IDC (Equation 2.19). In Figure 3.8, we plot the total measured capacitance (*i.e.,* imaginary part of the admittance divided by angular frequency) of each IDC on the LSAT substrate. We observe the expected trend of increasing capacitance with increasing active length. Additionally, we see nearly perfect agreement between the measurements from the LCR meter and the measurements from the VNA.

The capacitance and conductance *per unit length* of the IDCs, C'_{IDC} and G'_{IDC}, are the quantities we use to determine the relative permittivity of the test materials. We calculate C'_{IDC} and G'_{IDC} from the relationship between the measured admittance and the active length of each IDC. Figure 3.9 shows how the total measured capacitance (C_{IDC}, left) and total measured conductance (G_{IDC}, right) of the IDCs

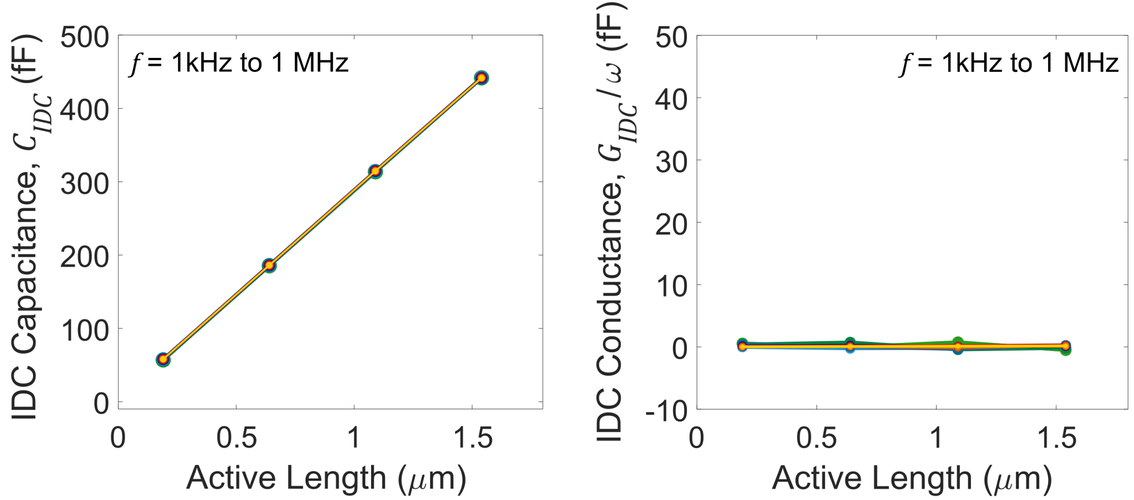

Figure 3.9. (left) The total measured capacitance, C_{IDC}, vs. active length for the IDCs on the LSAT substrate. (right) The total measured conductance, G_{IDC}, vs. active length. Both panels include several lines - each line corresponds to a specific measured frequency point between 1 kHz and 1 MHz.

on the LSAT substrate change with active length. We show these two components of the admittance individually for clarity. In all of our IDC measurements, we observe a linear relationship, which is readily apparent in the left panel of Figure 3.9. Naturally, the slope of this relationship provides our IDC capacitance per unit length, C'_{IDC}. In the right hand panel, which compares G_{IDC} to active length, the relationship is effectively a flat line, since there is virtually no dielectric loss in the LSAT substrate at these frequencies. We still use the slope of this relationship to determine a conductance per unit length, G'_{IDC}, which can be significant when a lossy thin film is present. There are many lines plotted in each panel of Figure 3.9, which all lie more or less on top of each other. Each of these lines represents a specific measurement frequency. The fact that they all line up indicates that the LSAT substrate displays little frequency dependence. By taking the slope at each frequency point, we determine C'_{IDC} and G'_{IDC} from 100 Hz to 100 MHz. In the next section, we will

map C'_{IDC} and G'_{IDC} to the real and imaginary parts of the relative permittivity based on additional finite element simulations.

3.2.3 Extracting relative permittivity from the measured capacitance and conductance

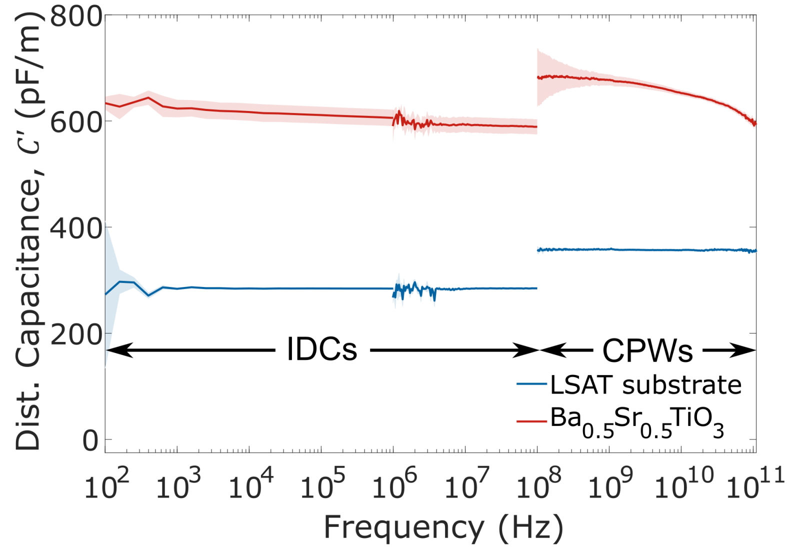

Figure 3.10. The broadband capacitance per unit length of the IDCs (C'_{IDC}) and of the CPWs (C') for the LSAT substrate and the $Ba_{0.5}Sr_{0.5}TiO_3$ film. The shaded regions denote the 95 % CIs

In Figure 3.10, we show the measured capacitance per unit length from 100 Hz to 110 GHz for both the LSAT substrate and the $Ba_{0.5}Sr_{0.5}TiO_3$ film. This figure includes the C'_{IDC} values below 100 MHz, and the C' values from our CPW measurements above 100 MHz. In both device types, the measured capacitance of the thin film sample is much greater than that of the LSAT substrate, which suggests that the film has a large relative permittivity. There is a discrepancy between the measured capacitance per unit length of the IDCs and the CPWs, which is

unsurprising given the disparate cross-sectional geometry of the two devices, and will be accounted for by the permittivity mapping functions. The shaded regions surrounding each curve in Figure 3.10 denote the 95 % confidence intervals (CIs) for the measured capacitance values. These uncertainties are propagated through our analysis as detailed in Appendix B.

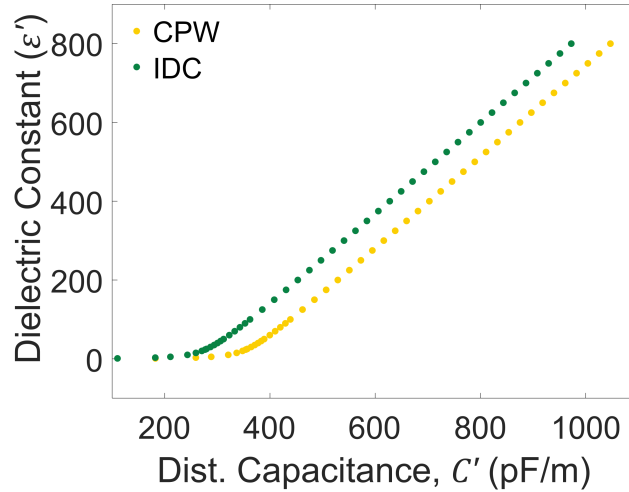

Figure 3.11. The mapping functions obtained from finite element simulations, which relate the measured capacitance per unit length to the relative permittivity of the thin film for the IDCs and CPWs.

We swept the permittivity of the thin film layer in our finite element simulations of the IDC and CPW structures to obtain the mapping functions that convert the measured capacitance and conductance per unit length to relative permittivity. We show the mapping functions for the IDCs and CPWs in Figure 3.11. Although there is an offset between the IDC and CPW mapping functions, they follow a nearly identical trajectory. This is not necessarily surprising, as the electric fields are primarily concentrated in the gaps between the inner conductor and outer conductor of the IDCs, and between the center conductor and ground planes of the CPWs. In both the IDCs and CPWs these gaps are 10 µm wide, and the center conductor of

the CPW and inner conductor of the IDC are 20 µm. Outside of this critical region, the IDCs and CPWs have a different cross-section, resulting in the offset between the two mapping functions.

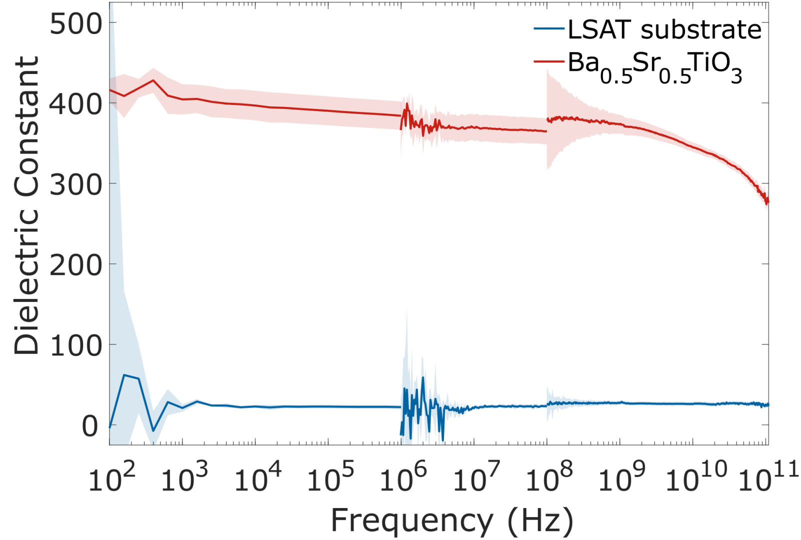

Figure 3.12. The real part of the relative permittivity of the LSAT substrate and $Ba_{0.5}Sr_{0.5}TiO_3$ film, measured from 100 Hz to 110 GHz. Shaded regions indicate the 95 % CIs.

We apply the mapping functions to the broadband capacitance and conductance measurements to obtain the real and imaginary parts of the relative permittivity, respectively. We show the measured dielectric constant of the $Ba_{0.5}Sr_{0.5}TiO_3$ film and the LSAT substrate from 100 Hz to 110 GHz in Figure 3.12, along with the 95 % CI for the measurements. The dielectric constant of the LSAT substrate is relatively constant across the entire measured frequency span, with the values falling within the range from 22 to 24 that is typical for this material. The $Ba_{0.5}Sr_{0.5}TiO_3$ film has a fairly constant dielectric constant of approximately 400 from 100 Hz to 1 GHz, before it begins to decrease due to dielectric relaxation. Broad relaxation at

GHz frequencies is characteristic in $Ba_{0.5}Sr_{0.5}TiO_3$ films and our measured values are within a reasonable range [113]. Reported values of the dielectric constant can vary wildly due to differences in processing and characterization. For example, even our own measurements of a film with a nominally similar composition in Chapter 4 produce a significantly different dielectric constant value. While we used the same permittivity characterization techniques in both experiments, the growth conditions were quite different. Perhaps most importantly, the films were grown from different precursor targets, with the film from this chapter originating from a single $Ba_{0.5}Sr_{0.5}TiO_3$ target, while the film in the subsequent chapter was grown via a two-target process using separate $BaTiO_3$ and $SrTiO_3$ targets. Accurate and consistent characterization is critical in enabling scientists to conclusively determine that a difference in the measured properties of these sensitive materials is in fact due to some change in processing.

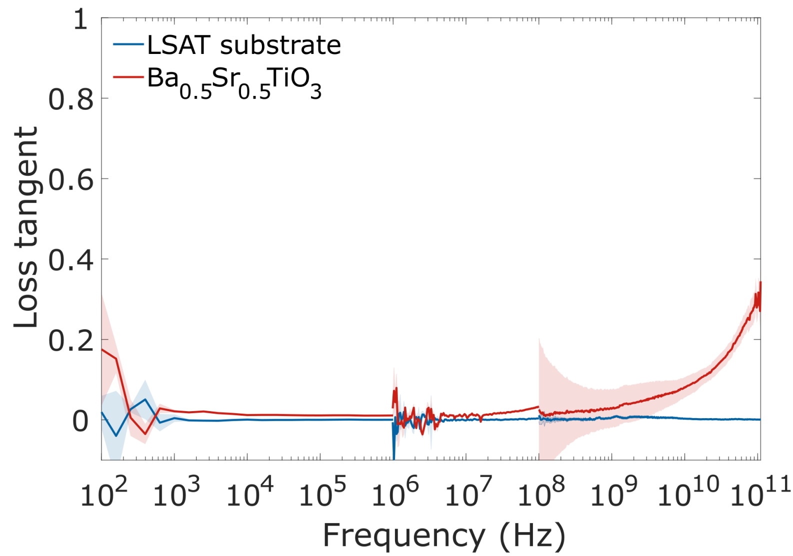

Figure 3.13. The measured loss tangent of the LSAT substrate and $Ba_{0.5}Sr_{0.5}TiO_3$ film, measured from 100 Hz to 110 GHz. Shaded regions indicate 95 % CIs.

We obtain the imaginary part of the relative permittivity by applying the mapping functions to the measured conductance per unit length. In Figure 3.13, we show the measured loss tangent of the LSAT substrate and $Ba_{0.5}Sr_{0.5}TiO_3$ film. The loss tangent is the ratio of the dielectric loss to the dielectric constant, and is the most common quantity used to express loss in dielectric materials. The LSAT substrate displays almost no loss across the entire measured frequency range. The loss is effectively at or below the detection limit ($\tan\delta < 0.005$) of our measurements, and as a result uncertainty in the measured loss tangent exceeds 50 % at many points. The $Ba_{0.5}Sr_{0.5}TiO_3$ film has relatively low loss up to approximately 10 MHz, after which loss begins to increase, and gets especially large at millimeter-wave frequencies. The loss tangent reaches a value of approximately 0.3 at 110 GHz, which is considered very lossy.

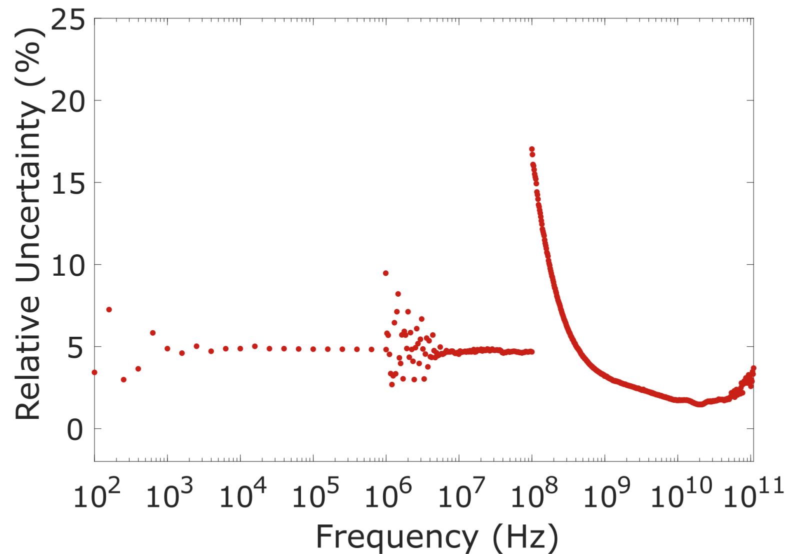

Figure 3.14. The relative uncertainty in the measured dielectric constant of the $Ba_{0.5}Sr_{0.5}TiO_3$ film from 100 Hz to 110 GHz.

As we have mentioned throughout Chapters 1 and 2, one of the most impactful

aspects of this work is our ability to make *accurate* measurements of the dielectric properties of thin films. In Figure 3.14, we highlight the relative uncertainty in the real part of the relative permittivity of the $Ba_{0.5}Sr_{0.5}TiO_3$ film. Uncertainties of this magnitude are fairly typical for our measurements. The uncertainty in the IDC measurements is about 5 % from 100 Hz to 100 MHz, and is primarily due to variance in the measured capacitance from device to device, *i.e.,* deviation from the fit we used to determine C'_{IDC}. For the CPW measurements, the uncertainty is large ($\sim$ 15%) at 100 MHz, where multiline TRL is less effective, but quickly decreases to very low levels of a few percent - highlighting the accuracy with which multiline TRL calculates the propagation constant γ at millimeter-wave frequencies. The uncertainties do begin to increase slightly as the frequency continues to increase, as the short wavelengths of the test signals may increase sensitivity to device-to-device non-uniformity. We must note that although we consider some uncertainties in the physical device structures, we have omitted uncertainty in the thickness of the film here in this error analysis, as we were limited to an less-accurate-than-usual estimate of the film thickness obtained from x-ray reflectometry (XRR), and did not want this to distort our portrayal of typical uncertainties in our measurements. While uncertainty in the film thickness can impact the extracted dielectric constant (but does not significantly affect the loss tangent), this uncertainty term is usually very small. For example, growth techniques like molecular beam epitaxy provide thickness control at the monolayer level, and post-mortem characterization with electron microscopy can provide extremely accurate measurements of the film thickness. We do describe how to include and propagate this source of error in Appendix B. Uncer-

tainty in our measured in-plane dimensions is 1 % to 2 % or less, and uncertainty in our measured conductor thicknesses is less than 1 %. Propagating these sources of error as described in Appendix B provides sub-10 % uncertainties throughout most of the measured frequency range.

3.3 Outlook

In this chapter, we demonstrated the measurement techniques described in Chapter 2 by characterizing the relative permittivity of a $Ba_{0.5}Sr_{0.5}TiO_3$ film and LSAT substrate. The observed values of the dielectric constant and loss tangent agree well with literature values for similar materials, though we again note that tunable dielectric thin films are known for being highly sensitive to environmental conditions during growth and processing, which can lead to large variation in material properties. This highlights one of the most important benefits of our measurement technique. When compared with other on-wafer techniques that can produce uncertainties greater than 40 % at millimeter-wave frequencies, the sub-10 % uncertainties we regularly achieve enable us to more confidently conclude when a difference in measured value is the result of a difference in material properties, or just discrepancy between measurements.

Chapter 4

Broadband characterization of composition-spread tunable dielectric films

4.1 Overview: A need for faster materials discovery and development

Often, selecting the best constituent materials for an electronic device proves challenging for engineers and designers [114]. Sifting through databases of known compounds is time consuming, and if no known material has sufficient properties, the materials discovery cycle must begin. Traditionally, scientists have employed a repetitive trial-and-error approach to test how various combinations of composition, processing, and other variables of interest affect key properties [115]. Modern efforts like the "Materials Genome Initiative" (Figure 4.1) have encouraged the use of high-throughput screening tools, such as combinatorial synthesis, first principles calculations, and machine learning algorithms to accelerate materials discovery [116, 117]. In this chapter, we discuss our combination of transmission line permittivity measurements with combinatorial synthesis to enable the rapid exploration of entire systems of tunable dielectrics for millimeter-wave devices.

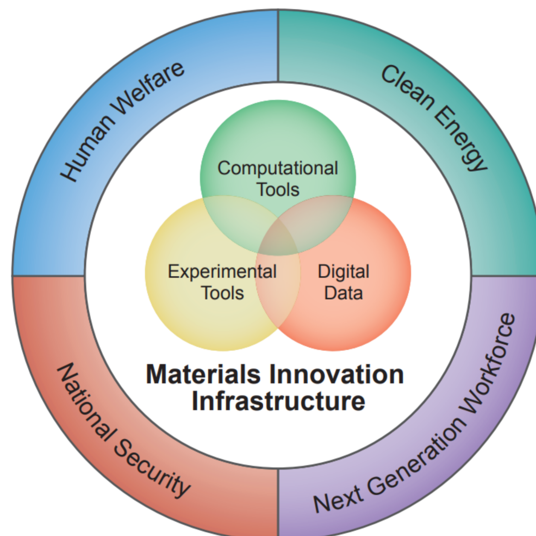

Figure 4.1. The Materials Genome Initiative seeks to leverage computational and experimental tools, as well as digital data, to discover and rapidly develop advanced materials to meet challenges in a variety of disciplines. From [116].

4.1.1 Accelerating materials discovery with combinatorial synthesis

Combinatorial materials synthesis is a high-throughput experimental technique that integrates the synthesis of multiple related compounds into a single growth process. This approach realizes time and cost efficiencies by creating and testing many novel compounds in parallel. Beyond improving efficiency, combinatorial synthesis experiments minimize sample-to-sample variability that can cloud intrinsic data, since all materials in a combinatorial library are exposed to the same conditions [118, 119]. Sample-to-sample inconsistency in growth, processing, and characterization during traditional experiments hinders the development of the computational tools that can further accelerate materials discovery by rapidly screening potential compounds for advantageous properties [120, 37]. The consistent and encompassing data sets produced by combinatorial synthesis experiments are particularly well-positioned to inform and validate such models [121]. Combinatorial synthesis is not

limited to improving computational tools, though, and has proven successful as a standalone method to discover and optimize materials. To date, combinatorial synthesis experiments have identified enhanced materials for gas sensing and catalysis, batteries, rare-earth-free permanent magnets, and more [122, 123, 124, 125, 126].

Combinatorial synthesis experiments do have a few notable limitations. These techniques are primarily suited to the growth of thin films, but thin film properties can often deviate from those of their bulk counterparts. Additionally, the multiple constituent materials used to make a combinatorial library may have incompatible synthesis conditions, or decompose into multiple phases. For example, Ref. [127] describes the combinatorial synthesis of $Sc_xAl_{1-x}N$ thin films via co-sputtering, and observes that the Sc-rich compositions are highly prone to spinodal decomposition. Although this decomposition inhibited the exploration of single-phase high-Sc alloys in that system, it also illustrates one strength of combinatorial synthesis experiments. Growing these $Sc_xAl_{1-x}N$ libraries with varied processing conditions can quickly identify the optimal conditions to maximize Sc incorporation. Finally, we note that growth techniques like PLD allow for dynamic changes to parameters like ablation laser energy and pulse rate, however other factors like substrate temperature and background pressure must be viable for all constituent materials. Preliminary experiments are critical to determine the best balance between the optimal deposition conditions for each of the constituents. In most studies, the combinatorial library is used to identify the optimal material, which is then grown and tested on its own.

Compared to single-composition materials, the characterization of combinato-

rial libraries requires more consideration. High spatial resolution techniques are ideal for targeting discrete compounds in the combinatorial library. Synchrotron XRD is one example of an ideal technique for the structural characterization of combinatorial libraries [128]. The high-brilliance x-rays available in many synchrotron beam lines allow for the realization of µm-scale spot sizes, where the same spot size realized in a traditional lab-based diffractometer would result in an unusable signal-to-noise ratio. Combinatorial libraries can contain hundreds of test compounds and lead to the generation of vast quantities of data. This is a natural opportunity for measurement automation and the application of machine learning algorithms like mean shift theory clustering, which has been demonstrated to streamline the identification of structural evolution trends in combinatorial libraries [129].

4.1.2 Prior studies of composition-spread dielectric thin films

A composition-spread thin film is a type of thin film combinatorial library that consists of a continuous composition gradient between two or more end-member materials. Ferroelectric composition-spread thin films were first explored at low microwave frequencies (up to approximately 5 GHz) in the late 1990s [20, 130, 131]. Ref. [131] demonstrated the microwave dielectric properties of $Ba_{1-x}Sr_xTiO_3$ composition-spread thin films grown by PLD on single-crystal LAO substrates. In that study, dielectric constant and loss tangent data were obtained with scanning evanescent microwave microscopy (SEMM).

As we mentioned in Chapter 2, scanning probe techniques like SEMM are

fast and provide sub-µm resolution, making them ideal for characterizing the dielectric properties of a composition-spread thin film [95]. When the work in Ref. [131] was performed, SEMM measurements were generally limited to a few discrete frequencies below 10 GHz. Further advances shortly after that work used higher-order resonances to enable broadband SEMM measurements to 17 GHz [96]. The authors of that work noted the challenge of extracting quantitative information above 10 GHz, though, where key approximations in the analysis break down. Some studies comparing SEMM measurements with CPW transmission line measurements claimed uncertainties greater than 25 % for the SEMM measurements, even below 10 GHz, [43], though others have achieved better accuracy given certain experimental constraints [132]. While one recent study demonstrated SEMM measurements at 20 GHz, measurements at millimeter-wave frequencies where lumped-element and image charge models may be less reliable have continued to prove challenging, especially for thin film characterization [133]. Recently, the authors of Ref. [134] postulated that their full-wave models of the tip-sample interactions in a SEMM system may enable better quantitative measurements to 100 GHz, but this has not yet been demonstrated experimentally. Although we lose the spatial resolution of SEMM, our desire to characterize the permittivity of our composition-spread thin films at millimeter-wave frequencies provided a natural opportunity to apply our CPW-based techniques.

4.1.3 Measuring the millimeter-wave dielectric properties of composition-spread dielectric thin films

The techniques we discussed in Chapters 2 and 3 are ideal for measuring the complex permittivity of dielectric thin films at microwave and millimeter-wave frequencies. However, they are not an obvious choice for characterizing composition-spread thin films. The need for multiple on-wafer devices spread over a large area ($50\,\mathrm{mm}^2$) presents a challenge. Measurement devices placed at a different points along the composition gradient cannot be used with our preferred multiline techniques. That is to say, all devices used in a set for multiline TRL must probe the same composition.

In the rest of this chapter, we describe how we have modified our techniques to enable the characterization of relative permittivity and tunability in composition-spread thin films. As we mentioned, this approach can't compete with the incredible spatial resolution of SEMM. Still, it provides accurate quantitative measurements at higher frequencies than any other study of composition-spread thin films to date. We demonstrate the technique by measuring the complex permittivity of a composition-spread $Ba_{1-x}Sr_xTiO_3$ thin film from 100 MHz to 110 GHz. Our approach is significantly faster than characterizing one test chip at a time and generates comprehensive and consistent data sets covering a broad and continuous frequency range. This technique provides the materials discovery community with a new method to gain insight on the relationships between composition, structure, and broadband dielectric properties.

4.2 Synthesis of composition-spread thin films

4.2.1 Selection of materials system

There are several reasons we chose $Ba_{1-x}Sr_xTiO_3$ to test our methodology. Many studies over the past two decades have explored this system, on account of its promising tunable dielectric properties. These reports describe the properties of $Ba_{1-x}Sr_xTiO_3$ under a variety of growth and measurement conditions, including the previously mentioned studies of composition-spread $Ba_{1-x}Sr_xTiO_3$ thin films [46, 131, 113]. Since our main goal was to explore how we can characterize the permittivity of composition-spread thin films at millimeter-wave frequencies, this rich body of literature was helpful in providing a general baseline for our expected results. The ferroelectric-paraelectric transition and stark shift in the complex permittivity and tunability between $x = 0$ ($BaTiO_3$, BTO) and $x = 1$ ($SrTiO_3$, STO) also made for an interesting study. While $Ba_{1-x}Sr_xTiO_3$ was an ideal starting point, this technique is theoretically generalizeable to any composition-spread thin film.

4.2.2 Combinatorial pulsed laser deposition

We grew the composition-spread $Ba_{1-x}Sr_xTiO_3$ thin films via PLD in a similar manner to the single-composition $Ba_{0.5}Sr_{0.5}TiO_3$ films described in the previous chapter. We again used an (001)-cut LSAT substrate ($a = 3.86$ Å) since it is well lattice-matched with both BTO ($a = 4.00$ Å, $c = 4.03$ Å) and STO ($a = 3.91$ Å). The precursor materials were 2.5 cm diameter sintered ceramic targets which we ablated with the KrF excimer laser at a pulse rate of 2 Hz and an energy density

of approximately 1.0 J/cm^2. The substrate temperature was maintained at 750 °C and the chamber had a background oxygen partial pressure of 4 Pa.

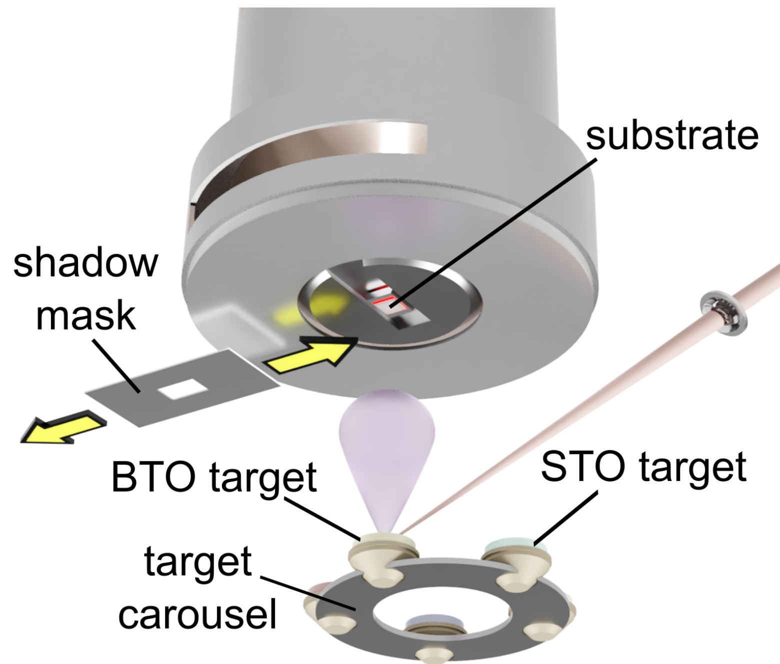

Figure 4.2. The PLD chamber configured for combinatorial synthesis. The target carousel enables selection of the desired precursor target, and the shadow mask controls the spatial distribution of deposited material from the selected target.

Creating the composition gradient in the thin film requires special processing and equipment. We grew the composition-spread thin film from two precursor targets with the end-member compositions, in this case $BaTiO_3$ and $SrTiO_3$. As material was ablated from one of the targets, a programmable shadow mask in the PLD chamber (Figure 4.2) covered a portion of the substrate. The ablated material condenses only on the exposed portion of the substrate, thereby controlling the spatial distribution of the constituent elements. To make the films for this study, we synchronized the mask movement with the ablation of the first target (BTO) to

grow a "thickness wedge" of BTO (Figure 4.3). The target carousel then rotated the second target (STO) into position, and the shadow mask moved in the opposite direction during ablation, creating an opposing thickness wedge of STO and completing one full layer.

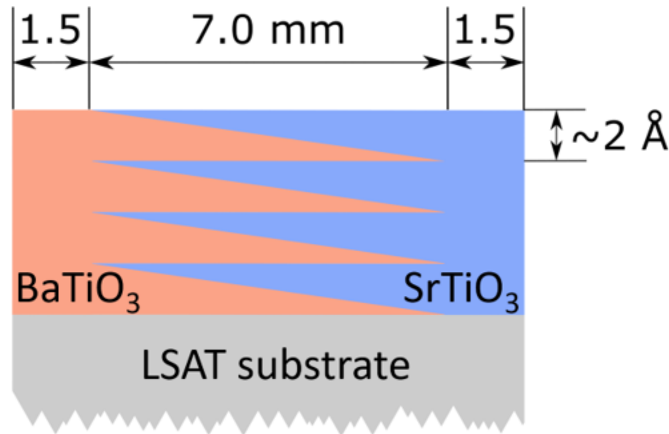

Figure 4.3. The growth process of a composition spread thin film. Thickness wedges of the constituent materials are stacked in an alternating sequence to create the film.

Each full layer is approximately 2 Å thick. Limiting the thickness of each layer to less than the thickness of the unit cell prevents the formation of a superlattice of the two target materials, and instead enables the constituent elements to mix in a solution-like manner during growth. This layering procedure was repeated approximately 620 times, to build up a 125 nm-thick film. The gradient spanned the full range of compositions x in $Ba_{1-x}Sr_xTiO_3$ from $x = 0$ to $x = 1$ across 7 mm. We left approximately 1.5 mm of BTO on one side of the gradient, and 1.5 mm of STO on the other side of the gradient.

4.3 Structural and compositional characterization

4.3.1 X-ray diffraction

After we grew the $Ba_{1-x}Sr_xTiO_3$ composition-spread thin films, we characterized the structure of the films with XRD. The XRD system was specially configured for combinatorial thin film characterization, which covers three aspects. First, the sample was mounted on a motion stage programmed to successively scan multiple points along the composition gradient. Second, an automated routine found the optimal alignment of the x-ray source, sample, and detector for each point scanned. Finally, divergence slits were used to obtain a 1 mm wide spot of Cu-Kα_1 radiation ($\lambda = 1.5406$ Å) to limit the composition range captured in each scan. Both $\Theta - 2\Theta$ and Φ scans were used to verify the structure of the film and its epitaxial growth relative to the LSAT substrate. Long range $\Theta - 2\Theta$ scans (Figure 4.4) spanning from $2\Theta = 10°$ to $2\Theta = 90°$ showed the (100), (200), and (300) peaks for both the film and substrate, suggesting that the $Ba_{1-x}Sr_xTiO_3$ film grew epitaxially on the LSAT substrate. Since this scan was performed after Au electrode deposition, the (111), (200), and (311) peaks for the polycrystalline Au layer are also present.

We also verified the epitaxial cube-on-cube growth of the film via Φ-scans (Figure 4.5). We first located the $(202)_{subs}$ peak, and verified the presence of the adjacent $(202)_{film}$ peak via a short-range $\Theta - 2\Theta$ scan. From there, a 360° Φ scan (*i.e.,* full in-plane rotation of sample) revealed a peak from the {202} family at 90 ° intervals, confirming the four-fold symmetry of our epitaxial $Ba_{1-x}Sr_xTiO_3$ film.

Narrow-range $\Theta - 2\Theta$ scans ($2\Theta = 40$ ° to $2\Theta = 50$ °) capturing the shift in the

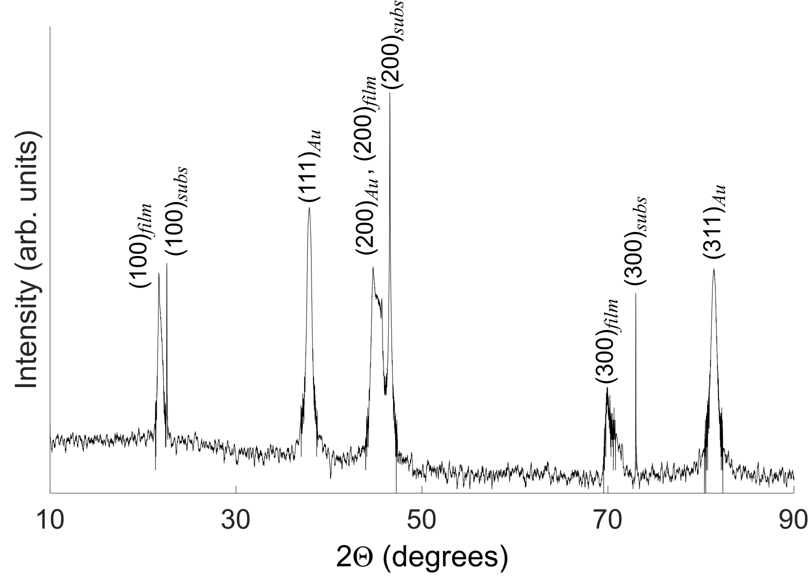

Figure 4.4. $\Theta - 2\Theta$ XRD scan of the composition-spread film from $2\Theta = 10°$ to $2\Theta = 90°$ for a composition of approximately $x \approx 0.5$.

position of the $(002)_{film}$ peak confirmed the existence and profile of the composition gradient in the film (Figure 4.6). The position of the film peaks is proportional to the lattice constant of the film, which is in turn proportional to the composition x in $Ba_{1-x}Sr_xTiO_3$. In Figure 4.6, the $(002)_{film}$ peak moves from a position of $2\Theta = 45.2$ ° for $x = 0$, to a position of $2\Theta = 46.1$ ° for $x = 1$. The $(002)_{subs}$ peak remains at a constant position of $2\Theta = 47.0$ ° across the entire sample, as expected.

These narrow-range scans allow for rudimentary estimates of the composition gradient profile. Since BTO and STO form the isostructural solid solution $Ba_{1-x}Sr_xTiO_3$, we estimate the composition at each scanned point with Vegard's Law [135]:

$$a_{Ba_{1-x}Sr_xTiO_3} = (1 - x)a_{BaTiO_3} + (x)a_{SrTiO_3} \tag{4.1}$$

where $a_{Ba_{1-x}Sr_xTiO_3}$ is the lattice constant of the film with composition x in $Ba_{1-x}Sr_xTiO_3$, a_{BaTiO_3} is the lattice constant of BTO and a_{SrTiO_3} is the lattice con-

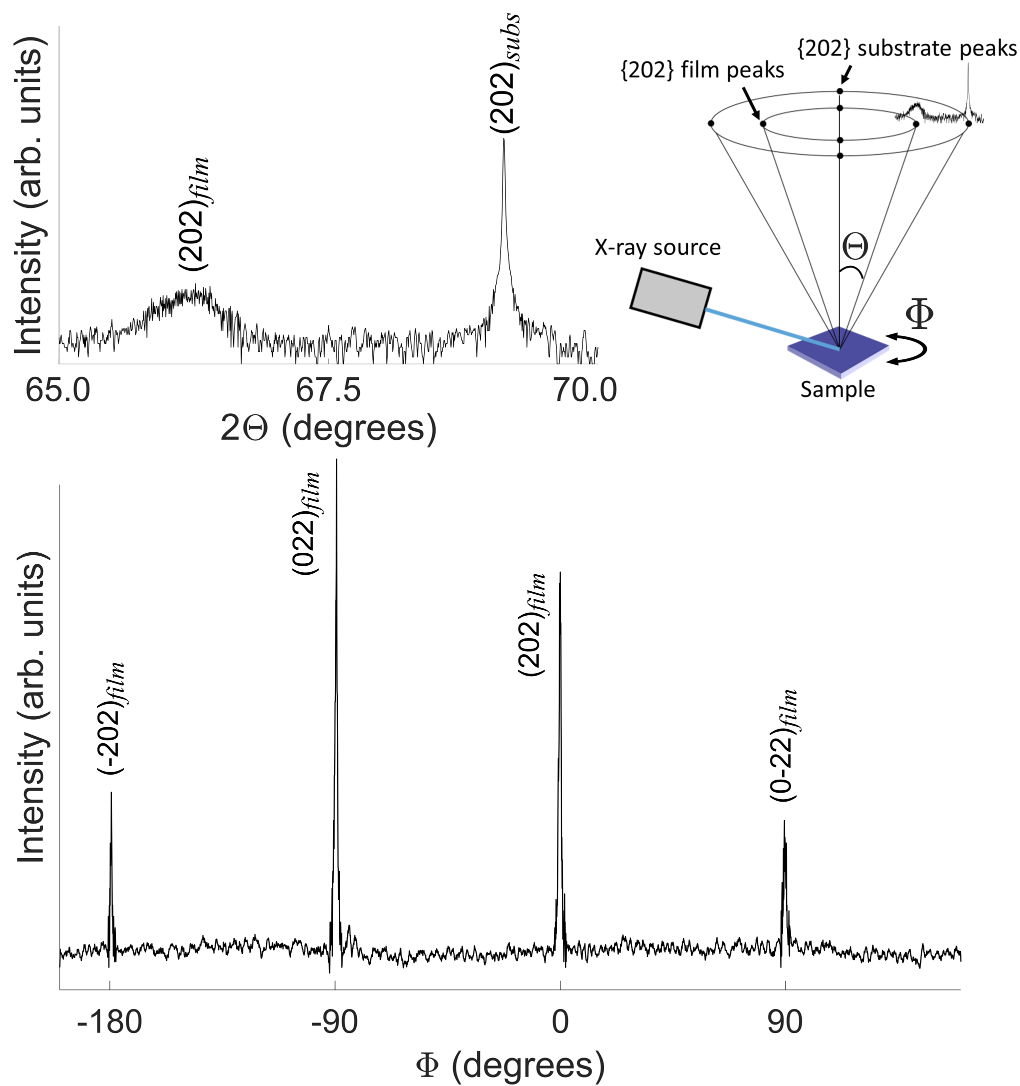

Figure 4.5. (top left) A short range $\Theta - 2\Theta$ scan confirmed that the $(202)_{subs}$ and $(202)_{film}$ peaks are adjacent. (top right) A schematic illustrating the relation between the film and substrate diffraction peaks. (bottom) Full-circle Φ scan of a single composition in the middle of the composition-spread film.

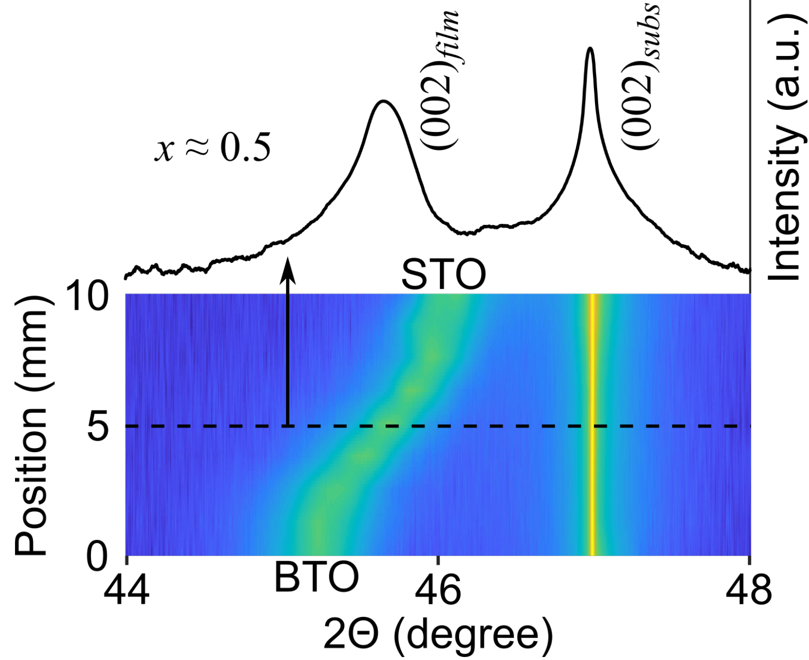

Figure 4.6. The diffraction pattern near the $(002)_{film}$ and $(002)_{subs}$ peaks illustrates the shift in the film lattice parameter across the composition gradient.

stant of STO. Our estimate from Vegard's law showed a linear composition profile (Figure 4.7). However the 1 mm x-ray spot may span an almost 15 at. % compositional range and therefore cannot pinpoint the exact compositions where we measure the dielectric properties. As such, this composition profile estimate simply serves to supplement additional electron-beam based compositional measurements.

4.3.2 Wavelength-dispersive x-ray spectroscopy

Wavelength-dispersive x-ray spectroscopy (WDS) measurements provide a high-resolution, quantitative measurement of the composition profile. We performed these measurements with an electron-probe microanalyzer (EPMA) at an accelerating voltage of 7 kV. The experimentally determined uncertainty on the composition is less than ± 3 at. %. The film and substrate are highly insulating, so they

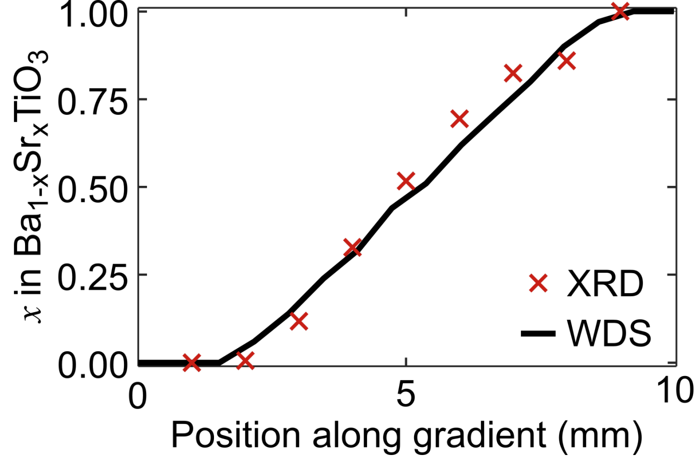

Figure 4.7. XRD and WDS scans were consistent with each other, and showed a linear gradient in the Ba/Sr ratio, as well as the BTO and STO regions on either side of the gradient region.

were carbon coated to prevent surface charging during measurement. As such, these measurements took place after permittivity characterization. The EPMA beam was focused in the gap of the CPWs between the center conductor and ground planes. In this way, the WDS measurements pinpoint the region of the film where the permittivity is measured. We also scanned across sets of devices (*i.e.,* distinct devices, but ones that should all be centered on the same composition) to verify the proper alignment of the test devices relative to the composition gradient, which we discuss further in Section 4.4.1. Our WDS measurements (Figure 4.7) confirmed a highly linear composition gradient spanning the full range of compositions x in $Ba_{1-x}Sr_xTiO_3$ from $x = 0$ to $x = 1$. The gradient profiles observed via XRD and WDS showed good agreement with each other. Both measurements indicated a slight shift in the gradient region. That is to say that the pure $BaTiO_3$ region was larger than the pure $SrTiO_3$ region. Due to redundancies built in to the permittivity test pattern, this did not negatively affect our experiment.

4.3.3 Atomic force microscopy

We measured the surface topography across the composition gradient with atomic force microscopy (AFM). We iteratively optimized the film deposition conditions to minimize surface roughness. Significant surface roughness can have adverse effects on the permittivity test device fabrication and performance. For all scanned points across the entire compositional range in the $Ba_{1-x}Sr_xTiO_3$ thin film from $x = 0$ to $x = 1$, the RMS roughness was less than 1 nm, indicating a very smooth film. For all compositions other than $x = 1$, we observed a particulate film surface. For $x = 1$ (i.e. pure $SrTiO_3$) the film appeared to be flat with some terrace-like features. This may indicate a layer-by-layer growth mechanism, suggesting that the selected deposition conditions were particularly well-suited for the growth of $SrTiO_3$ [136].

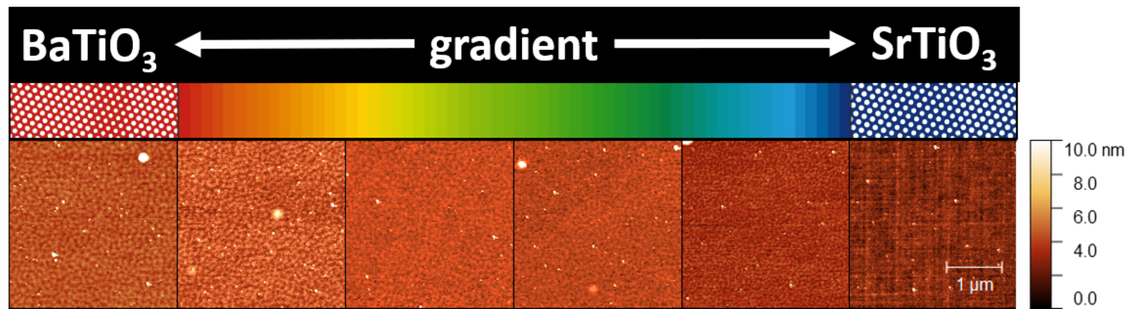

Figure 4.8. AFM scans at different points along the composition gradient.

4.3.4 Scanning electron microscopy

Lastly, we confirmed the thickness of the composition spread thin film via scanning electron microscopy. This took place after all other measurements had been performed, since we cleaved the thin films chips to provide a clean surface

for cross-sectional measurements like the representative image shown in Figure 4.9. The measured film thicknesses were then used to refine the finite element simulations that provide the mapping function relating the measured distributed capacitance of the test devices to the complex permittivity of the thin film.

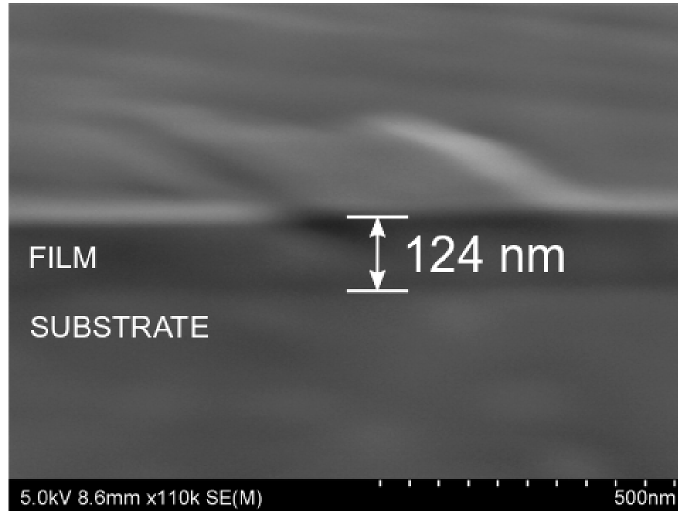

Figure 4.9. Cross-sectional SEM image of a $Ba_{1-x}Sr_xTiO_3$ composition-spread film. Courtesy of Justin Pearson, UMD.

4.4 Transmission line permittivity measurement technique for composition-spread thin films

Chapter 2 described the advantages of transmission line permittivity measurements and the multiline TRL analysis approach. To use these techniques to characterize composition-spread thin films, we need to account for the spatially-varying composition. To properly apply multiline TRL to these films, we consider three criteria. First, all devices in a multiline TRL set must measure the same composition. Second, each measurement should capture only a narrow compositional range, *i.e.,*

the electric fields probing the thin film properties should be localized in a small region. Third, we should include enough sets of devices that we can adequately observe the composition-dependent trends in the dielectric properties.

To address the first point, we employed procedures during film deposition and device fabrication to maintain consistent sample alignment. On the second point, we designed co-planar waveguides with 10 µm-wide gaps between the ground planes and 20 µm-wide center conductor. This localizes the measurements in a 40 µm-wide region, spanning at most a 0.5 at % composition range. Since this range is less than the uncertainty of our compositional measurements themselves, we consider this to adequately target discrete compositions. For the third point, this experiment prompted us to develop new fabrication processes and employ direct-write UV lithography to maximize the amount of on-chip patternable area. As an example of why this is important, we note that our first attempts at implementing this permittivity measurement technique with ten multiline TRL sets (*i.e.,* ten measurable compositions) containing four transmission lines each failed due to a lack of redundancy and missing the end-member compositions. By increasing the patternable area, we increased both the number of measurable compositions, and the redundancy within each multiline TRL set.

4.4.1 Device selection, design, and fabrication

We limited our measurements to the frequency range from 100 MHz to 110 GHz that is most relevant to modern telecommunications. This way we did not

need to squeeze IDC into the limited patternable area. We selected device sets containing five CPWs (L1 to L5) and a short-circuit reflect (S1) to enable multiline TRL while balancing redundancy and space efficiency. To ensure that all devices in a set measure the same composition, we arranged the devices in each set in a single row. While our improvements to the fabrication process minimized the photoresist edge bead, devices still could not be patterned closer than 500 µm to any edge of the chip. This left a 9 mm × 9 mm region for devices. We selected optimal CPW lengths as described in Section 2.2.4.2. We we able to include fourteen rows of devices in the available space, allowing us to measure fourteen distinct points along the composition gradient.

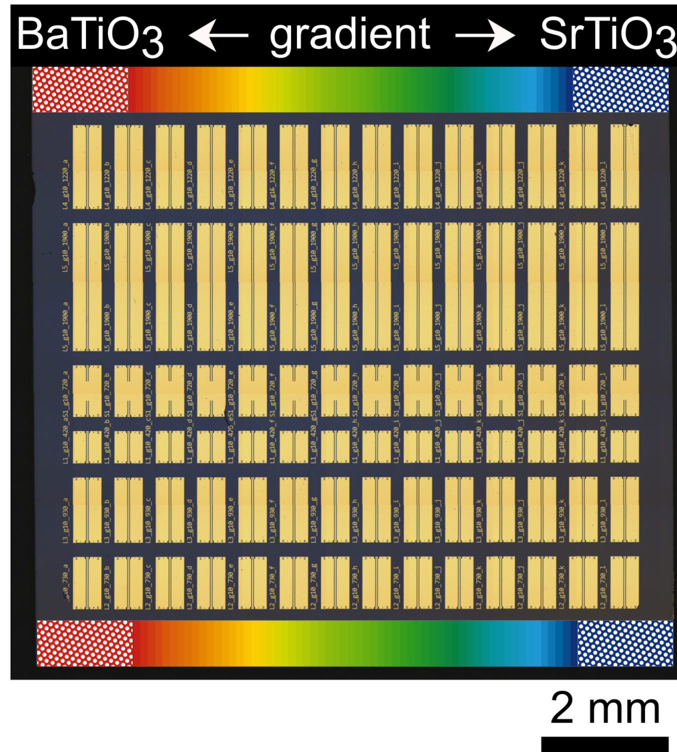

Figure 4.10. Optical microscope image of the patterned composition-spread $Ba_{1-x}Sr_xTiO_3$ chip. Each vertical column of devices corresponds to a complete multiline TRL measurement set which can be used to measure a unique point along the composition gradient.

We patterned the devices using the mask-less photolithography techniques described in Appendix C. The five transmission lines had lengths of l = (0.42, 0.73, 0.93, 1.22, 1.90) mm. The center conductors were 20 μm wide, the ground planes were 200 μm wide, and the gaps between the center conductor and ground planes were 10 μm wide. We used profilometry to measure the conductor thicknesses, and optical microscopy to measure the in-plane device dimensions. We compared WDS compositional measurements at different points within device sets to verify the alignment of the devices to the composition gradient. Variation in the Ba and Sr content between measurements at the center of the row of devices, to measurements at the end of the row of devices was never more than 2 at. %. This variation is within the measurement uncertainty of the EPMA, and indicated good alignment of the test devices to the composition gradient. We also fabricated a companion substrate for the reasons discussed in Chapter 2.

4.4.2 Complex permittivity and electric-field tunability measurement conditions

We performed the calibrations, S-parameter measurements, and complex permittivity analysis of the test devices as described in Chapter 2. To minimize probe adjustment time, identical length devices were measured successively (*i.e.,* we measured all 14 L1 (thru) devices, then measured all 14 S1 (short-circuit reflect) devices, etc.). Only one set of devices on the companion substrate needed to be measured, since the dielectric properties of the substrate are homogeneous.

We also performed electric-field tunability measurements using the techniques described in Section 2.2.8. The DC bias voltage was swept to generate DC electric fields from a minimum field strength of $-75\,\mathrm{kV\,cm^{-1}}$ to a maximum field strength of $75\,\mathrm{kV\,cm^{-1}}$ in the gaps of the CPWs. We selected these limits on the field strength to avoid dielectric breakdown failures in the devices. Due to the time consuming nature of the electric-field tunability sweeps and the large number of devices, these measurements took place over several days. The measurements from each day were corrected with a full calibration that we performed at the beginning of that day. Correcting the measurements with a fresh calibration mitigates the effects of drift or other changes in the measurement instrumentation, thereby allowing us to combine measurements across multiple days into a single analysis.

4.5 Broadband permittivity measurement of the $Ba_{1-x}Sr_xTiO_3$ composition-spread thin films

4.5.1 Composition-dependent permittivity of $Ba_{1-x}Sr_xTiO_3$

The room temperature (298 K) measurements from 100 MHz to 110 GHz revealed drastic changes in the frequency- and composition-dependent relative permittivity of the $Ba_{1-x}Sr_xTiO_3$ thin film, which is shown in Figure 4.11. The real part of the relative permittivity at 110 GHz was approximately 400 for $BaTiO_3$ ($x = 0$), before increasing to a peak value of 650 at compositions of approximately $x = 0.3$ to $x = 0.4$, and finally decreasing to about 100 for $SrTiO_3$ ($x = 1$). This peak in the composition-dependent dielectric constant, clearly observed in the top panel of

Figure 4.11, is consistent with the established behavior of $Ba_{1-x}Sr_xTiO_3$ thin films at room temperature [131, 137, 138].

As we described with Equation 1.6, the peak in dielectric constant generally occurs when the measurement temperature approaches the ferroelectric Curie temperature, T_C. Compositions of $Ba_{1-x}Sr_xTiO_3$ with $x \approx 0.3$ to 0.4 have a T_C near room temperature [131, 139, 140]. The peak in the permittivity coincides with a decrease in the soft mode frequency near T_C [141]. In bulk single crystal ferroelectrics, this composition-dependent (or analogously, temperature-dependent) transition appears as a very sharp peak. However, in our $Ba_{1-x}Sr_xTiO_3$ thin films, we observe a diffuse phase transition (DPT), likely due to local strain and size effects [142, 143].

The bottom panel of Figure 4.11 shows the broad relaxation behavior commonly observed in $Ba_{1-x}Sr_xTiO_3$ thin films. The characteristic relaxation times span from a few-ps for Ba-rich compositions, to sub-ps for Sr-rich compositions. When $x > 0.8$, the frequency dependence is effectively negligible within our measured frequency range. Broad dispersion behavior and other relaxor-like characteristics were previously established in the $Ba_{1-x}Sr_xTiO_3$ system and other DPT ferroelectrics and have been attributed to nano-scale polar regions with some finite distribution of sizes [141]. The composition-dependent relaxation behavior is explored further in Section 4.6 along with our application of the Cole-Cole model.

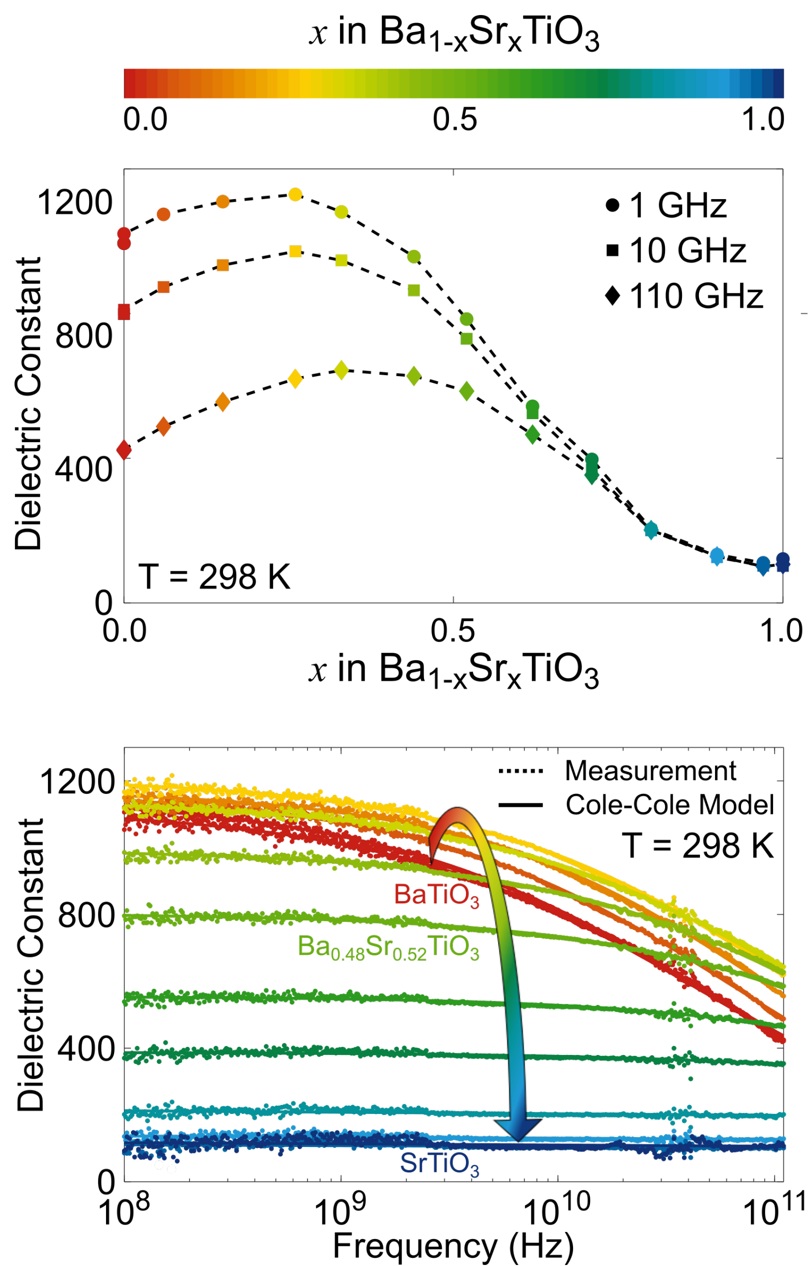

Figure 4.11. (top) The composition-dependent dielectric constant curves at 1 GHz, 10 GHz and 110 GHz. (bottom) The frequency-dependent dielectric constant for all fourteen measured compositions x in $Ba_{1-x}Sr_xTiO_3$ from 100 MHz to 110 GHz.

4.5.2 Composition-dependent loss tangent of $Ba_{1-x}Sr_xTiO_3$

The loss tangent of the composition-spread $Ba_{1-x}Sr_xTiO_3$ thin film also revealed significant composition dependence (Figure 4.12). We observed a monotonic decrease in loss tangent at all measured frequencies as the composition x in $Ba_{1-x}Sr_xTiO_3$ increased from $x = 0$ to $x = 1$. On the Ba-rich side of the composition gradient, the loss tangent was high ($\tan\delta > 0.2$) at millimeter-wave frequencies, but on the Sr-rich side, losses were always very low ($\tan\delta < 0.02$), which agrees well with previously-established behavior in the $Ba_{1-x}Sr_xTiO_3$ system [131]

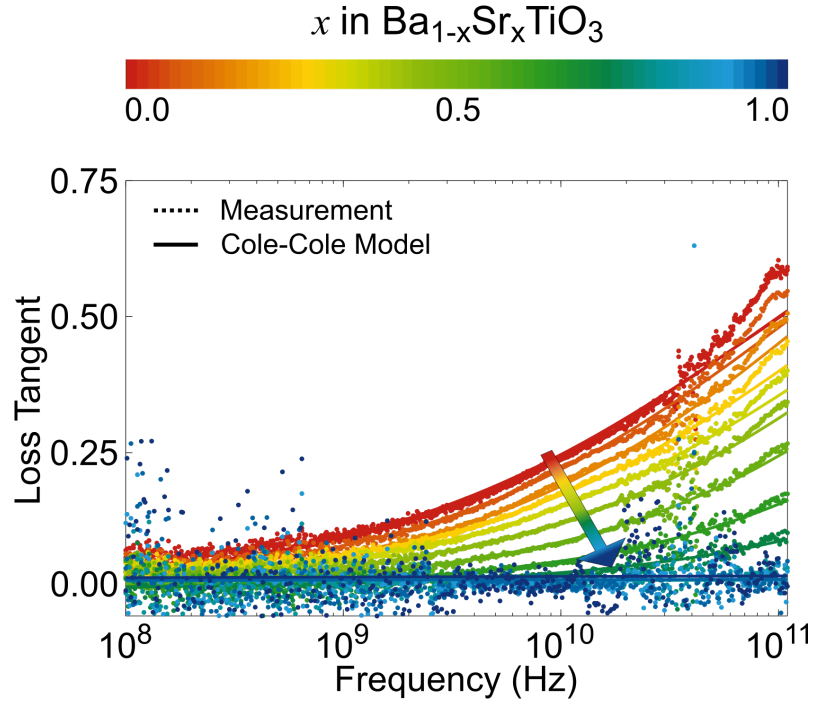

Figure 4.12. The frequency-dependent loss tangent for all fourteen measured compositions x in $Ba_{1-x}Sr_xTiO_3$ from 100 MHz to 110 GHz.

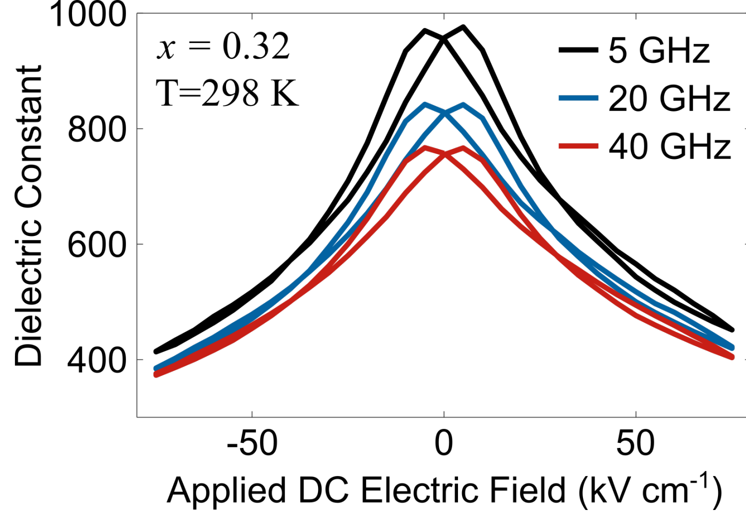

Figure 4.13. The dielectric constant tuning curves for $Ba_{0.68}Sr_{0.32}TiO_3$ at 5 GHz, 20 GHz, and 40 GHz

4.5.3 Electric-field dependence of the permittivity

We must measure the relative tunability of the thin film to understand its value for tunable devices. The 5 GHz, 20 GHz, and 40 GHz dielectric constant tuning curves for a highly-tunable composition x in $Ba_{1-x}Sr_xTiO_3$ near $x \approx 0.3$ are shown in Figure 4.13. There is some hysteresis present in each curve, indicating that the T_C of this composition is above the measurement temperature (298 K) and therefore this composition exhibits ferroelectric behavior. The measured relative permittivity decreases with frequency, which mirrors the same dispersion behavior we observed in Figure 4.11.

While we observe a slight decrease in the relative tunability, n_r (Equation 1.7) with frequency, the value for this composition, and other Ba-rich compositions is fairly consistent around approximately $n_r \approx 50\%$. The broad region of high tunability from $x = 0$ to $x \approx 0.5$ seen in Figure 4.14 likely originates in the DPT nature of these films. The peak in tunability, like the peak in dielectric constant,

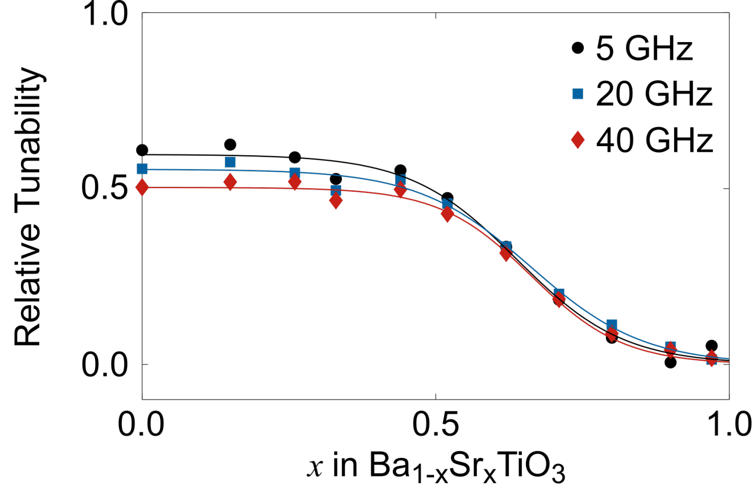

Figure 4.14. The composition-dependent relative tunability, n_r, at measurement frequencies of 5 GHz, 20 GHz, and 40 GHz

generally occurs when the bottom of the free energy potential well we described in Chapter 1 is wide and flat, which coincides with a measurement temperature near T_C. The diffuse phase transition in these thin films provides a correspondingly wide range of high tunability. As more Sr is added, and the material moves deeper into the paraelectric state, the tunability continuously decreases, reaching approximately zero when x in $Ba_{1-x}Sr_xTiO_3$ is approximately $x = 1$.

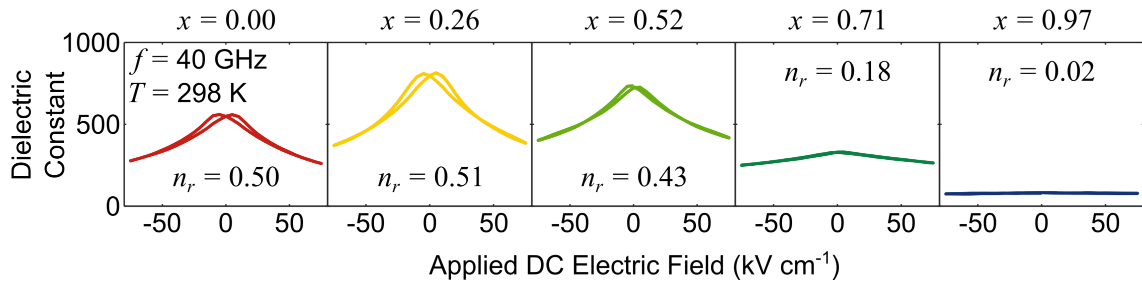

Figure 4.15. The 40 GHz room temperature dielectric constant tuning curves for five notable compositions x in $Ba_{1-x}Sr_xTiO_3$ illustrating the shift in tuning behavior across the ferroelectric-paraelectric transition.

Along with the decrease in relative tunabilty, the tuning behavior itself changes due to the ferroelectric to paraelectric transition. This is evident in Figure 4.15,

which shows the tunability curves for several compositions across the gradient. The Ba-rich ferroelectric compositions display the expected hysteretic tuning curves, but the hysteresis disappears as x in $Ba_{1-x}Sr_xTiO_3$ increases and the film approaches the paraelectric state. We still observe tunability well into the paraelectric state, though it decreases as we move further from T_C, as we saw in Figure 4.14. Eventually, we are so far into the paraelectric state that the sides of the free energy potential well are too steep to allow any appreciable tuning. The fact that our measurement spanned compositions with T_C both above and below our measurement temperature allowed us to observe this interesting range in tuning behavior.

4.6 Modeling the composition-dependent permittivity behavior of $Ba_{1-x}Sr_xTiO_3$

We modeled the frequency-dependent complex permittivity of the composition-spread $Ba_{1-x}Sr_xTiO_3$ thin film with the Cole-Cole model, which is often applied to diffuse phase transition and relaxor ferroelectrics [144, 145, 68, 113]. The Cole-Cole model is a modified Debye model that allows for a distribution of relaxation times [146]. The distribution of relaxation times may arise from the presence of polar nano-regions with a distribution of sizes in the $Ba_{1-x}Sr_xTiO_3$ thin film [67], though the nature of such regions is not fully understood [147].

For each measured composition, we employed a non-linear least squares fitting approach to simultaneously fit the real and imaginary parts of the relative

permittivity to the Cole-Cole model:

$$\varepsilon_r = \varepsilon_\infty + \frac{\varepsilon_s - \varepsilon_\infty}{1 + (i\omega\tau)^\beta} \tag{4.2}$$

where ε_s is the static dielectric constant, ε_∞ is the "infinite frequency" dielectric constant, τ is a characteristic relaxation time, and β is a parameter describing the width of the distribution of characteristic relaxation times. We fixed the value of ε_∞ at 5.8 based on optical measurements of the refractive index [148, 149] and the other parameters were free to vary within reasonable bounds. The Cole-Cole fits (solid lines in Figures 4.11 and 4.12) appear to model the measured data very well. We observe some minor deviation between the model and measurement in the measured loss tangent (Figure 4.12) for Ba-rich compositions above 50 GHz. These additional losses could be radiative in nature [150], or could also indicate the presence of some additional relaxation mechanism. Further measurement capabilities (*e.g.*, reverberation chamber measurements) could help narrow in on the source of this discrepancy.

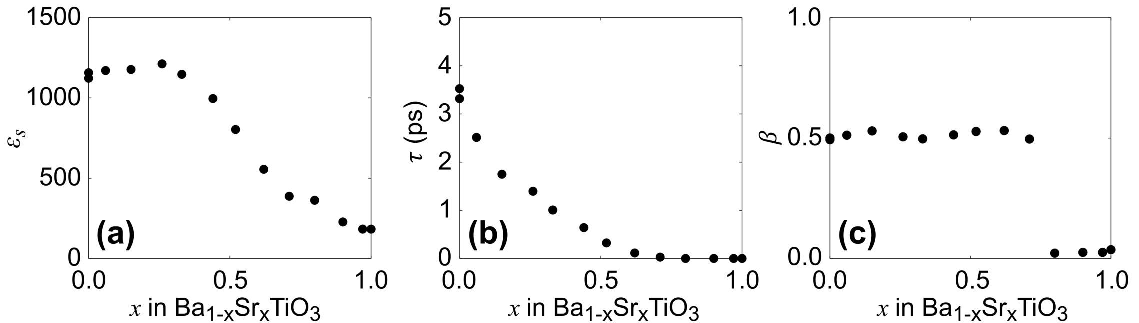

Figure 4.16. The Cole-Cole model parameters for all measured compositions x in $Ba_{1-x}Sr_xTiO_3$

TABLE II. Cole-Cole Model parameters and relative tunability of $Ba_{1-x}Sr_xTiO_3$

x	ε_s	τ (ps)	β	n_r
0.00	1122	3.317	0.50	0.50
0.00	1157	3.524	0.49	—
0.06	1170	2.514	0.51	—
0.15	1177	1.750	0.53	0.51
0.26	1212	1.396	0.51	0.51
0.32	1147	1.007	0.50	0.47
0.44	995	0.643	0.51	0.50
0.52	803	0.324	0.53	0.43
0.62	555	0.115	0.53	0.31
0.71	388	0.030	0.50	0.18
0.80	363	0.001	0.02	0.07
0.90	228	0.001	0.03	0.03
0.97	183	0.001	0.03	0.02
1.00	183	0.001	0.04	—

We provide the fit parameters to the Cole-Cole model for all measured compositions in Figure 4.16 and Table II, along with the measured relative tunability. Unsurprisingly, the parameters are strongly composition dependent. The trend in the static dielectric constant, ε_s, mirrors the composition-dependent trend observed in the measured dielectric constant (top panel of Figure 4.11). The critical relaxation time, τ also displays an interesting trend as it decreases monotonically as Sr is added and x in $Ba_{1-x}Sr_xTiO_3$ decreases. This indicates that the relaxation moves from frequencies in the hundreds of GHz to frequencies above 1 THz as x increases, as expected based on previous theoretical and IR spectroscopic studies [151]. Unfortunately, for very Sr-rich compositions ($x > 0.8$), there is very little dispersion in our measured data and τ reached the lower bound value of 0.001 ps. The parameter representing the width of the distribution of relaxation times, β, was approximately 0.5 for all measured compositions from $x = 0$ to $x = 0.8$, which is in agreement with previous reports [113, 68]. Above $x = 0.8$, β dropped to nearly zero, again a result of the minimal dispersion present in our measured frequency range. The

Cole-Cole model is not ideal for these compositions, and the frequency-dependent permittivity could alternatively be described by a constant value across the measured frequency range. The optimized fit parameters model the measured data quite well, and provide the community a simple way to explore the frequency-dependent dielectric properties of the $Ba_{1-x}Sr_xTiO_3$ system. However, it it likely that measurement frequencies in excess of 1 THz would be needed to fully characterize the relaxations for the Sr-rich compositions [151].

4.7 Outlook

In this chapter, we discussed our development of a novel application of transmission line permittivity measurements to characterize the dielectric properties of composition-spread thin films from 100 MHz to 110 GHz. We demonstrated this technique by characterizing a $Ba_{1-x}Sr_xTiO_3$ composition-spread thin film, spanning the full composition range from $x = 0$ to $x = 1$. The encompassing frequency-, composition-, and voltage- dependent data we generated highlights both the benefits of our measurement technique, and the benefits of applying the principles of combinatorial materials science to understand materials systems and discover new materials.

Beyond providing one of the most comprehensive and consistent studies of the $Ba_{1-x}Sr_xTiO_3$ system to date, the measurements discussed here are a springboard to rapidly exploring other systems like multi-ferroic $Bi_{1-x}Sm_xFeO_3$, and also to further understanding ferroelectric materials as a whole through computational

modeling. We also plan to explore adding temperature-dependence capabilities, and have collaborations underway to develop mesoscale models that may enlighten the relationship between local ordering (*i.e.,* polar nano-regions) and the relaxation behavior.

Chapter 5

Development and characterization of $(SrTiO_3)_{n-1}(BaTiO_3)_1SrO$ Ruddlesden-Popper superlattices

5.1 Overview: Ruddlesden-Popper phases, strain engineering, and targeted chemical pressure

The discovery of enhanced tunable dielectric properties in strained $(SrTiO_3)_nSrO$ Ruddlesden-Popper superlattices (Figure 5.1) [64] highlighted the value of extensive collaboration between first-principles theory, materials growth, integration, and characterization. In that work, gradual developments spanning more than 15 years ultimately led to the demonstration of tunable dielectric films with the best ratio of tunability to loss at the time. In this chapter, we discuss how a similar approach enabled us to further improve these uniquely-structured tunable dielectric materials.

5.1.1 Ruddlesden-Popper tunable dielectric thin films

In 2001, epitaxial $(SrTiO_3)_nSrO$ Ruddlesden-Popper thin films with $n = 1$ to 5 were grown and studied to better understand the electrical behavior of the $SrTiO_3$ system [152]. Until then, single-phase examples of $(SrTiO_3)_nSrO$ with $n > 3$ had never been demonstrated. Prior to that demonstration, several computa-

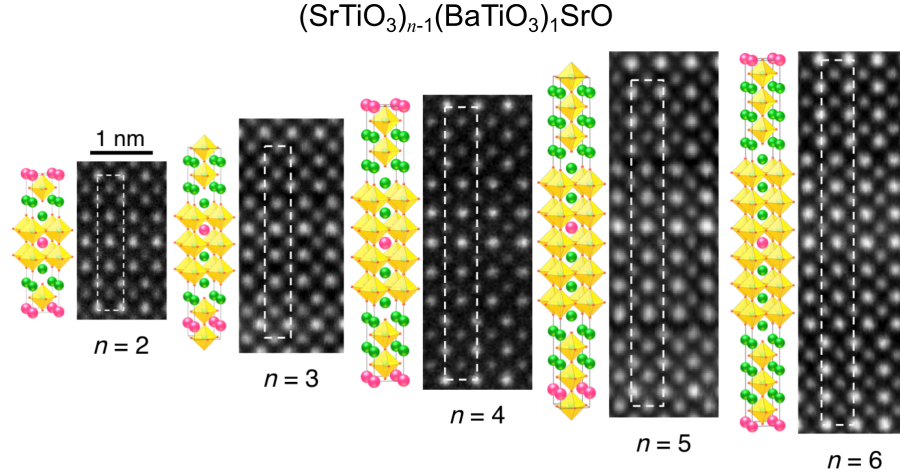

Figure 5.1. The unit cells of the $n = 2$ to 6 $(SrTiO_3)_{n-1}(BaTiO_3)_1SrO$ Ruddlesden-Popper superlattices. These are identical to the $(SrTiO_3)_nSrO$ Ruddlesden-Popper superlattices, with the exception of a BaO layer (red) substituted for a SrO layer.

tional studies had explored the stability of these materials and concluded that the $(SrTiO_3)_nSrO$ Ruddlesden-Popper phases with $n > 3$ are metastable, preferring to decompose into $SrTiO_3$ and $Sr_3Ti_2O_7$ [153, 154].

The successful growth of the $n = 1$ to 5 $(SrTiO_3)_nSrO$ Ruddlesden-Popper thin films demonstrated major advances in materials growth and epitaxial stabilization techniques that had precipitated over the previous decade. Precisely controlled molecular beam epitaxy (MBE) with *in situ* reflection high-energy electron diffraction (RHEED) made it possible to synthesize these metastable phases [155]. This synthesis technique enables the targeted placement of single layers of atoms to produce intricate superlattice structures. Provided cation interdiffusion rates are low, one can “lock in” metastable arrangements. Similar metastable superlattices grown by MBE did not decompose even during annealing under pure oxygen at 1000 °C to minimize the concentration of oxygen vacancies [156].

Transmission line permittivity measurements like those described in Chapter 2

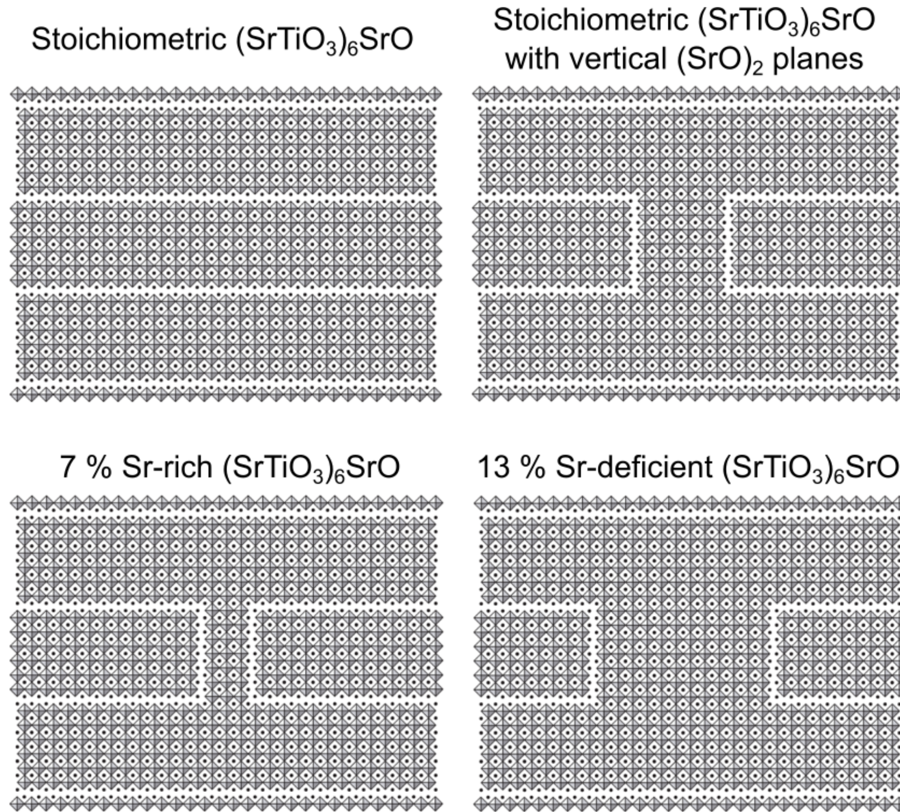

Figure 5.2. Stoichiometric $n = 6$ $(SrTiO_3)_nSrO$ films incorporate horizontal $(SrO)_2$ planes every n layers in the growth direction (top left). These layers may also naturally form in the vertical direction (top right). The density of these vertical $(SrO)_2$ planes fluctuates in response to local non-stoichiometry (bottom left and right). From Ref. [64]

showed very little dielectric loss in $(SrTiO_3)_nSrO$ films with $n = 1$ to 3 [157]. These films had loss tangents below detectable levels (in that study, $\tan\delta < 0.04$) up to 40 GHz, the upper limit of the measurement bandwidth.

The low loss is attributed to an inherently defect-mitigating structure in the $(SrTiO_3)_nSrO$ Ruddlesden-Popper phases, which helps reduce extrinsic dielectric loss. Initially described in 1958 [158], these materials are comprised of a repeating sequence of n blocks of perovskite $SrTiO_3$, sandwiched between double SrO rock-salt layers (Figure 5.1). Another way to think of this structure is as $SrTiO_3$ with crys-

tallographic shear planes containing an extra SrO layer every n layers. The $(SrO)_2$ planes can naturally form in a vertical orientation in addition to the expected periodic, horizontally-oriented $(SrO)_2$ planes. Rather than forming loss-inducing point defects in the $SrTiO_3$, the density of these Sr- and O-rich vertical planes fluctuates in response to local non-stoichiometry (Figure 5.2). This protects the intrinsic quality of the $SrTiO_3$ layers and suppresses extrinsic dielectric losses.

5.1.2 Strain engineering to induce ferroelectricity

While the $(SrTiO_3)_nSrO$ Ruddlesden-Popper films were interesting in their own right, they did not posses notable ferroelectric properties. The Landau-Devonshire theory asserts that stresses and strains can affect ferroelectric transitions and material properties [7]. For example, the application of a load altered the ferroelectric properties of $SrTiO_3$ at cryogenic temperatures [159]. Theorists also proposed that the mechanical boundary condition imposed on a homoepitaxial film clamped to a lattice mismatched substrate could modify the ferroelectric properties of the thin film [160]. In 2004, this technique, known as strain engineering, was demonstrated experimentally to dramatic effect. Not only did strain engineering enhance ferroelectricity in $BaTiO_3$ [161], but more notably it also brought the ferroelectric transition in $SrTiO_3$ from 4 K to room temperature [162]. Unfortunately, there was a simultaneous increase in the dielectric loss to levels too high for device applications. It has since been shown that biaxial tensile strain in similar epitaxial perovskite films can lower the activation barrier for the formation of lossy oxygen

vacancies [163].

It was not clear if strain-engineering would also induce ferroelectricity in the naturally centrosymmetric $(SrTiO_3)_nSrO$ Ruddlesden-Popper phases. Early first principles investigations suggested that Pb_2TiO_4 Ruddlesden-Popper phases would be ferroelectric, but lamented that no known examples of these materials had been observed [164]. Subsequent computational studies suggested that tensile epitaxial strain exceeding 1 % could induce in-plane ferroelectricity in $(SrTiO_3)_nSrO$ Ruddlesden-Popper phases with $n > 2$ [165, 166]. Shortly thereafter, in-plane ferroelectricity in $(SrTiO_3)_nSrO$ films was demonstrated experimentally [64].

The preference for in-plane ferroelectricity in these materials has complex origins. In-plane tensile strain "stretches" the oxygen octahedra of the $SrTiO_3$ allowing for more in-plane movement of the Ti^{4+} cation. More importantly, in these displacive-type ferroelectrics, polarization leads to relative displacements of the Ti^{4+} cations and the O^{2-} anions along the Ti-O-Ti chains. The computational studies in Ref. [166] indicated that these chains must exceed some critical coherence length, n_{crit}, to support robust ferroelectricity. The $(SrO)_2$ planes that occur every n layers in the out-of-plane direction interrupt the continuous Ti-O-Ti chains, suppressing out-of-plane ferroelectricity, leaving in-plane displacement as a favorable polarization mechanism.

The combination of high in-plane tunability and low millimeter-wave dielectric loss in the $n = 6$ $(SrTiO_3)_nSrO$ Ruddlesden-Popper film was very exciting. However, the applicability of these materials to real tunable devices was highly limited, primarily due to the constraints of using epitaxial strain to induce ferroelectricity.

5.1.3 The inherent limitations on strain-engineered materials

As we discussed in the previous section, epitaxial mismatch strain is a means to modify many properties of thin films. Aside from ferroelectric properties, this technique has been demonstrated to enhance multiferroic properties [167], metal-insulator transitions [168], and transport properties in CMOS devices [169].

Unfortunately, relying on epitaxial mismatch strain limits substrate choice and film thickness. Regarding the latter issue, there is well known critical thickness limit, h_c on mismatched epitaxial films, which arises from the elastic energy cost associated with straining each layer of the film from its equilibrium lattice parameter. The larger the lattice mismatch between the substrate and film, the larger this energy cost is. As additional layers are added to the film during growth, the total energy to maintain the strained state of the film increases. Eventually, when the film thickness, t, exceeds h_c, this energy cost outweighs the energy required to form mismatch edge dislocations. At that point ($t > h_c$), edge dislocations form allowing the film to relax to its equilibrium lattice constant. When relaxation occurs, the property enhancement driven by strain engineering disappears. In the case of the $(SrTiO_3)_nSrO$ Ruddlesden-Popper phases, the ferroelectricity vanishes, and therefore they lose their value as a tunable dielectric.

The high-performance $n = 6$ $(SrTiO_3)_nSrO$ films grown on (110) $DyScO_3$ substrates (1.1 % mismatch) described in Ref. [64] could be grown a maximum of 50 nm thick before relaxation and the same films on $GdScO_3$ (1.6 % mismatch) were limited to 25 nm. Those films were too thin to provide significant *device* tunability

in planar microwave devices. Typically, the tunable thin film comprises only a small fraction of a device, and therefore comprises only a portion of the overall device capacitance - as we described in Equation 2.2. The greater the contribution of the tunable thin film layer to the overall capacitance, the greater the overall tunability, or "device tunability" (as opposed to film tunability) will be. Since the device function is dependent on the overall device capacitance, it is important to maximize the device tunability. Figure 5.3 illustrates how device tunability increases with film thickness for a given planar CPW device geometry (here, 20 µm-wide center conductor and 5 µm-wide gaps). While intelligent device design can boost device tunability, incorporating thicker films also has the same effect; both approaches should be used in tandem.

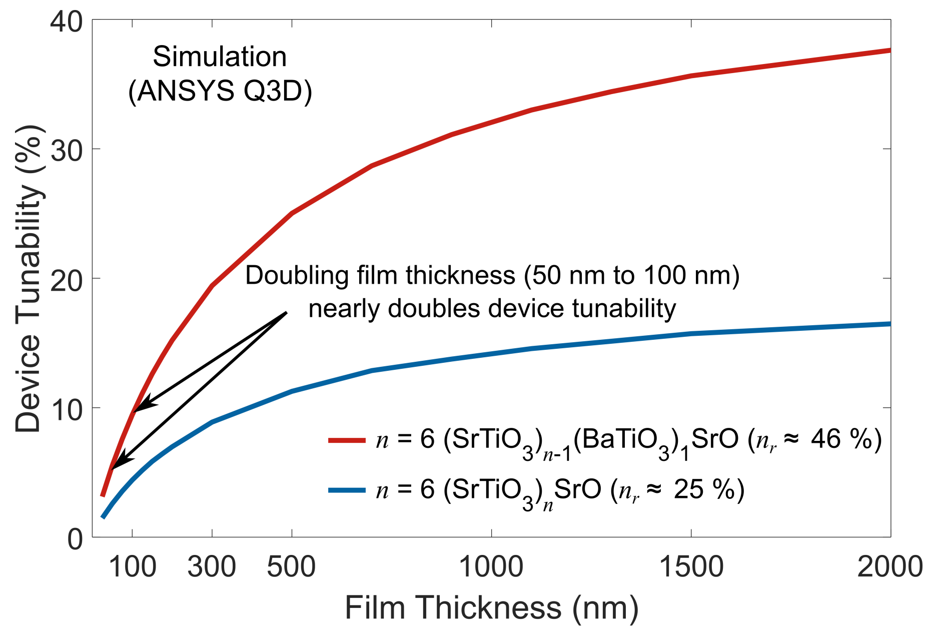

Figure 5.3. The device tunability of a planar microwave device increases with the thickness of the tunable thin film. Shown here are the results for simulated devices incorporating both $n = 6$ $(SrTiO_3)_nSrO$ films and more tunable $n = 6$ $(SrTiO_3)_{n-1}(BaTiO_3)_1SrO$ films.

5.1.4 Enabling thicker tunable films with targeted chemical pressure

Guided by collaborations with first principles theorists, we explored approaches to grow thicker strained films, while maintaining the tunable dielectric performance. Density Functional Theory (DFT) calculations were used to simulate the polar ground states in conventional unit cells of biaxially-strained $(SrTiO_3)_nSrO$ and $(SrTiO_3)_{n-1}(BaTiO_3)_1SrO$ with $n = 6$ (the optimal periodicity for room temperature tunabilty based on the work in Ref. [64]). We then determined a layer-resolved polarization in the material from the relative displacements of the charged species within each layer. The sum of these layer-resolved net polarization values taken over the whole unit cell, P_S, acts as a proxy for the tunability of the material.

Beginning with the high-performing, but thickness-limited $n = 6$ $(SrTiO_3)_nSrO$ on (110) $DyScO_3$ (Figure 5.4a), the first logical path to explore involved simply modeling the same film structure strained to a different substrate with a smaller lattice mismatch. Reducing the mismatch strain from 1.1 % to 0.8 % enables films to be grown more than 100 nm thick, but comes with a significant 25 % reduction in P_S from $24\,\mu C\,cm^{-2}$ to $18\,\mu C\,cm^{-2}$ (Figure 5.4b).

The next scenario we explored was changing the equilibrium lattice constant of the film to reduce the mismatch strain. This is accomplished by alloying with a larger A-site cation. We chose the Ba^{2+} cation, due to its slightly larger radius than Sr^{2+} and known role in tunable microwave dielectrics as $BaTiO_3$. Replacing 20 % of the Sr in the perovskite layers with Ba corresponds to a 0.8 % lattice mismatch with (110) $DyScO_3$, again more than doubling the critical thickness (Figure 5.4c).

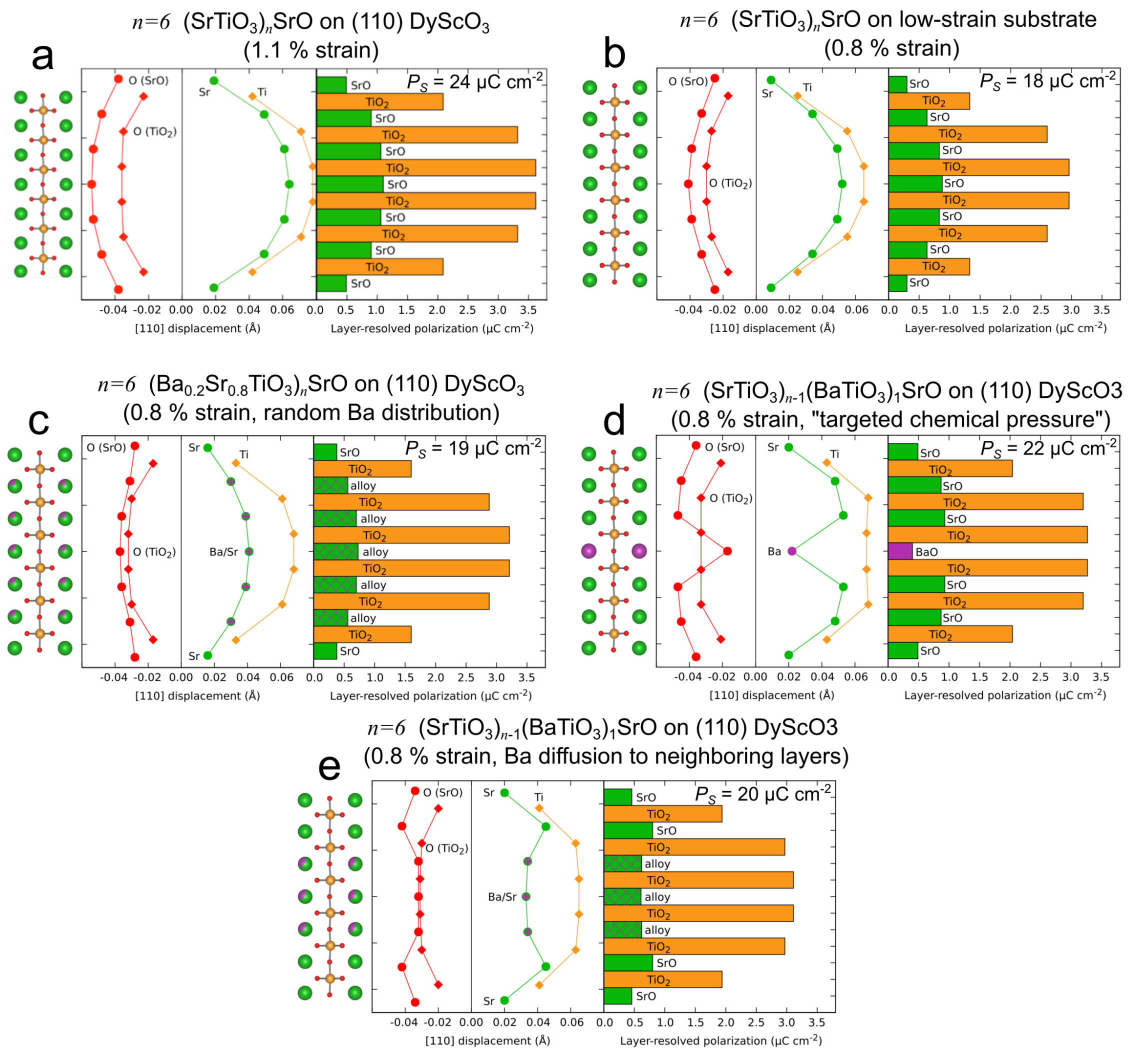

Figure 5.4. First-principles calculations enabled us to determine the polar ground states of the Ruddlesden-Popper superlattices in a variety of strain conditions and atomic configurations. The most relevant calculations, shown here, guided our study to obtain thicker tunable, low-loss dielectric films. Theorist: Gerhard Olsen, Cornell

In this case, P_S was 19 µC cm^{-2}, a small improvement compared to the previous case. The larger, randomly-distributed Ba^{2+} cations may induce an isotropic strain in the surrounding material, possibly distorting the oxygen octahedra and allowing the Ti^{4+} cations to displace more. Indeed, the DFT calculations reveal that any increase of P_S in the random Ba doping case is due to increased polarization in the TiO_2 layers. The isotropic nature of this effect would also lead to distortion of the oxygen octahedra in the out-of-plane direction, which provides no enhancement to the in-plane tunability.

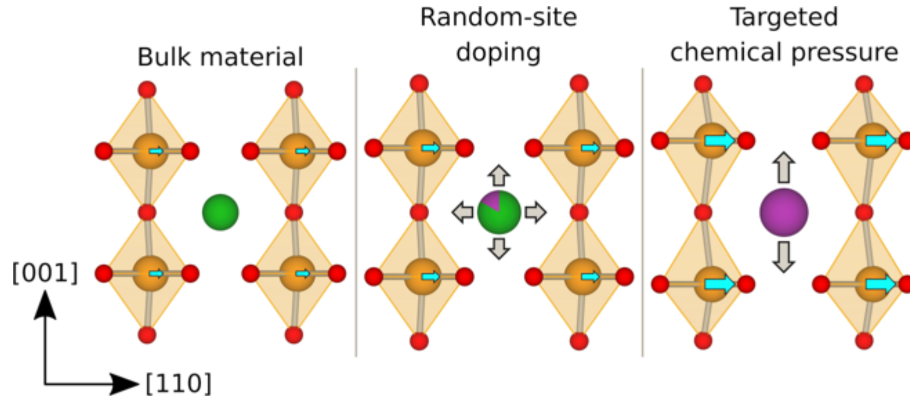

Figure 5.5. The low-strain case (0.8 % mismatch) (left) supports a small ferroelectric instability which allows for only a low degree of polarization. Randomly doping the perovskite layers with a larger A-site cation, can introduce an isotropic strain to the film which increases the in-plane polarization a small amount. However, if the larger cations are targeted into a single layer to create targeted chemical pressure, the increase can be significant.

This led us to an interesting question: is there way to incorporate the larger Ba^{2+} cations to produce a more anisotropic effect that primarily manipulates the in-plane tunability? As we discussed in Section 5.1.1, MBE growth provides enough control to precisely sequence individual layers. With this in mind, we simulated structures in which we replaced one of the SrO layers in the perovskite blocks with a

BaO layer to exert a sort of "targeted chemical pressure" on the surrounding layers (Figure 5.4d). It seems intuitive that this targeted layer with larger Ba cations could act as a sort of integrated buffer layer, boosting the in-plane tensile strain on the adjacent layers. However, we must remember that in these epitaxial films the in-plane lattice constant is fixed to the substrate lattice constant, so this layer primarily creates an expansion in the out-of-plane direction. We would expect this to enable out-of-plane polarization of the Ti^{4+} cations within the adjacent "stretched" oxygen octahedra, but this effect is suppressed by the eventual interruption of the Ti-O-Ti chains by the $(SrO)_2$ layers. In-plane polarization remains the favorable polarization mechanism, and the DFT calculations indicated an enhancement of the in-plane polarization to $P_S = 22\,\mu\mathrm{C\,cm^{-2}}$. While this is not quite as large as the 1.1 % strained $n = 6$ $(SrTiO_3)_nSrO$ films, this $n = 6$ $(SrTiO_3)_{n-1}(BaTiO_3)_1SrO$ film again corresponds to an 0.8 % mismatch, enabling growth beyond 100 nm. The Ti^{4+} cation in the TiO_2 layer immediately next to the BaO layer displaces very slightly less than the Ti^{4+} cation in the TiO_2 layer beyond that (Figure 5.4d). This appears to indicate that the out-of-plane strain from the BaO layer could actually limit the polarizability of the Ti^{4+} cation in the adjacent TiO_2 layer, but enhance polarizability in the layers beyond.

After seeing the exciting simulations of the $n = 6$ $(SrTiO_3)_{n-1}(BaTiO_3)_1SrO$ film with the single targeted BaO layer, we felt that this material merited experimental investigation. Concerned that there could be some interdiffusion of the Sr^{2+} and Ba^{2+} cations, we performed an additional round of calculations to explore the properties if the Ba diffuses to adjacent layers (Figure 5.4e). This calculation re-

vealed that P_S does decrease to $20\,\mu C\,cm^{-2}$ if the Ba is equally distributed across three layers. This is still an enhancement over the un-doped 0.8 % strain case (Figure 5.4b), as well as the randomly Ba-doped case (Figure 5.4c), but highlights that it is important to confine the Ba to as small a region as possible.

5.2 Growth and structural analysis of $(SrTiO_3)_{n-1}(BaTiO_3)_1SrO$ thin films

The DFT calculations revealed that the $(SrTiO_3)_{n-1}(BaTiO_3)_1SrO$ material incorporating the "targeted chemical pressure" BaO layer could enable thicker films with decent tunability. However, it was unclear whether these materials would be stable enough to be grown. As in the case of the $(SrTiO_3)_nSrO$ Ruddlesden-Popper phases, the metastable $n = 6$ $(SrTiO_3)_{n-1}(BaTiO_3)_1SrO$ material lies in a two-phase region of the BaO-TiO_2-SrO phase diagram [170], and there are no reports of bulk Ba-containing Ruddlesden-Popper phases in the literature.

5.2.1 Film synthesis

Initially, we grew 50 nm films of the $(SrTiO_3)_{n-1}(BaTiO_3)_1SrO$ Ruddlesden-Popper phases with $n = 2$ to 6 to test the stability of these materials. The requisite high-precision MBE growth is quite slow, so these thinner films enable faster process development. Once the $n = 2$ to 6 phases had been successfully demonstrated, thicker 100 nm films of the $n = 6$ $(SrTiO_3)_{n-1}(BaTiO_3)_1SrO$ material were then grown for the millimeter-wave devices and tunability characterization.

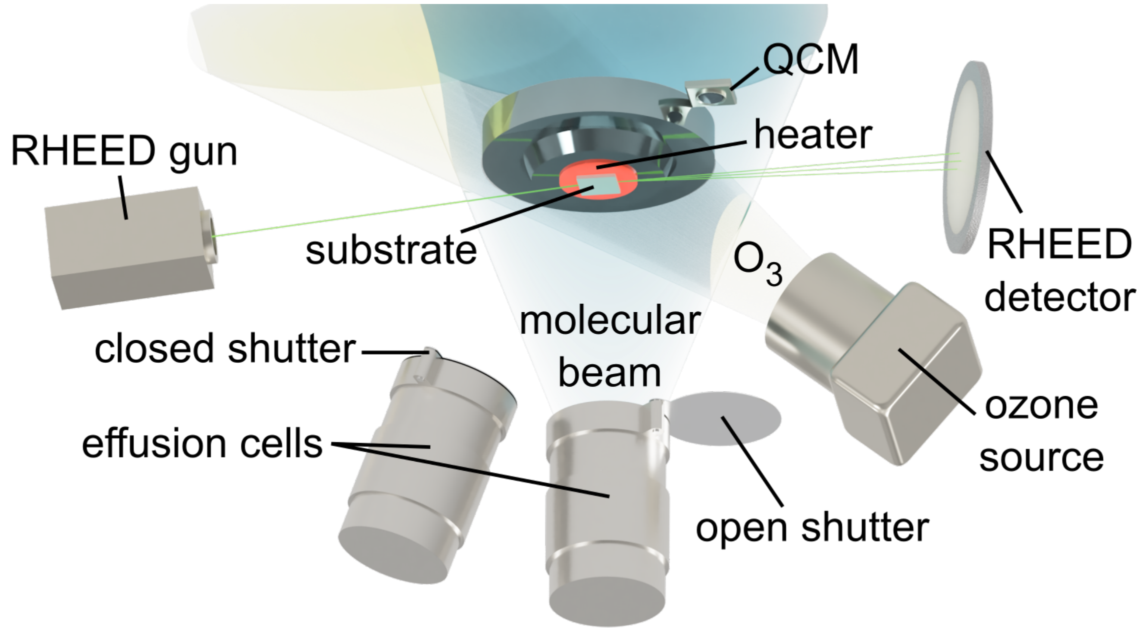

Figure 5.6. A schematic of the molecular beam epitaxy chamber.

The MBE deposition process (Figure 5.6) synthesizes films by evaporation from sources of the individual constituent elements. For these films, Sr and Ba are sourced from Knudsen effusion cells, and Ti is sourced from a Ti-Ball, which is a re-purposed titanium sublimation pump. These oxide films are grown in a background oxygen partial pressure of 1×10^{-6} Torr, with approximately 10 % ozone (O_3). Elemental flux calibrations were first performed with a quartz crystal microbalance (QCM) then refined with RHEED intensity oscillations. These calibrations provide the necessary control to obtain the correct stoichiometry and absolute dose of the SrO, TiO_2 and BaO layers. If the stoichiometry and dose are incorrect by more than approximately 1 % the superlattice will not form properly.

Once the deposition rates have been fully calibrated, the shutters controlling the elemental sources are programmed to open in the correct sequence to grow the desired superlattice. RHEED intensity oscillations are also used to monitor the

layer formation while the shutters are open. The 10 mm × 10 mm (110)-cut $DyScO_3$ ($a_{\text{pseudocubic}} = 3.949$ Å) substrates are affixed with silver paste to a heating block in the chamber which maintains a substrate temperature of 875 °C.

5.2.2 Structural characterization

The structure of the $(SrTiO_3)_{n-1}(BaTiO_3)_1SrO$ films is critical to the tunable dielectric properties. There are two major structural aspects that we must consider. First, the films should be single-phase epitaxial superlattices with the correct layer periodicity and high crystalline quality, which we determine from various XRD scans. Second, the targeted BaO layer should mostly be present in the desired location, and the Ruddlesden-Popper structure should be well-formed, including the various horizontal and vertical $(SrO)_2$ planes. We study these aspects with scanning transmission electron microscopy (STEM) including electron energy-loss spectroscopy (EELS).

5.2.2.1 X-ray diffraction measurements

There are a few features in the $\Theta - 2\Theta$ diffraction pattern of the 100 nm thick $n = 6$ $(SrTiO_3)_{n-1}(BaTiO_3)_1SrO$ thin film (Figure 5.7) that illustrate both the structure and high crystalline quality. The presence of only $\{00\underline{x}\}$ peaks, where x is any positive integer multiple of 2, indicates that the films grew epitaxially on the substrate with the c-axis of the film oriented in the out-of-plane direction, as desired. Rocking curve scans confirmed that the full-width at half-maximum

(FWHM) of the film peaks approached that of the single crystal substrate itself. The $\mathrm{FWHM}_{(00\underline{28}),film}$ = 14 arc sec and the nearby $\mathrm{FWHM}_{(220),subs}$ = 12 arc sec. Such narrow peaks are typical of low defect density single crystalline materials.

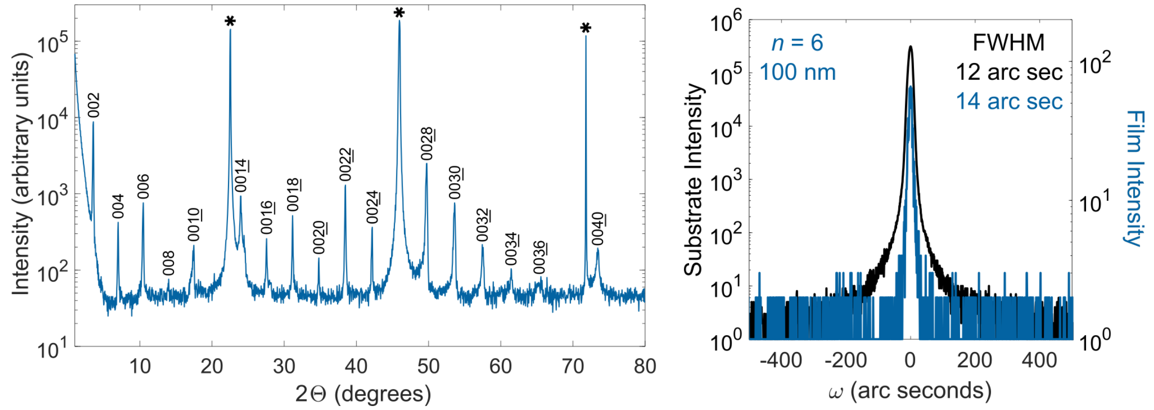

Figure 5.7. (left) The $\Theta - 2\Theta$ diffraction pattern for the 100 nm thick $n = 6$ $(\mathrm{SrTiO_3})_{n-1}(\mathrm{BaTiO_3})_1\mathrm{SrO}$ film on $\mathrm{DyScO_3}$. Substrate peaks are indicated by a $\star$. (right) Rocking curve comparing the width of the $(00\underline{28})_{film}$ and $(220)_{subs}$ peaks. Courtesy of Natalie Dawley, Cornell.

5.2.2.2 Transmission electron microscopy measurements

High-angle annular dark field (HAADF)-STEM is a valuable technique for imaging these materials because it provides visible z-contrast between the constituent elements. The periodic BaO layers in the $n = 6$ $(\mathrm{SrTiO_3})_{n-1}(\mathrm{BaTiO_3})_1\mathrm{SrO}$ are visible as slightly brighter horizontal layers in Figure 5.8. Both horizontal and vertical $(\mathrm{SrO})_2$ faults are visible, creating a "brick and mortar" appearance, which is even more apparent in the adjacent bright field image (which depicts a different region of the film). We also note that there was no indication of the growth of secondary Ba-rich phases in the material.

The distribution of the constituent elements is even more clear upon examina-

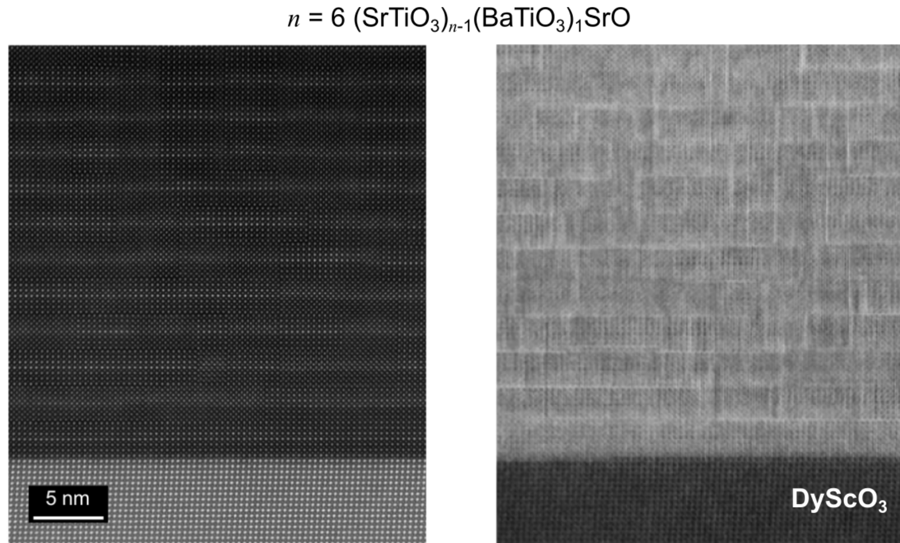

Figure 5.8. HAADF-STEM (left) and bright field STEM (right) images of the $n = 6$ $(SrTiO_3)_{n-1}(BaTiO_3)_1SrO$ thin film on (110) $DyScO_3$. Note: each panel depicts a distinct region of the film. Microscopist: Megan Holtz, Cornell.

tion with EELS (Figure 5.9). The periodic $(SrO)_2$ rock-salt planes are clearly seen in the Ti signal of the $n = 6$ $(SrTiO_3)_{n-1}(BaTiO_3)_1SrO$ thin film, as no Ti is present in these planes. The Ba signal again shows bright horizontal lines for the targeted BaO layers. While the Ba signal is strongest in the targeted layer, there does appear to be some limited diffusion of Ba to the subsequently deposited layer or two. Additionally, where vertical $(SrO)_2$ planes intersected the BaO layer there appeared to be some Ba present at the corners between horizontal and vertical $(SrO)_2$ planes which could indicate that these planes may enable faster diffusion of Ba.

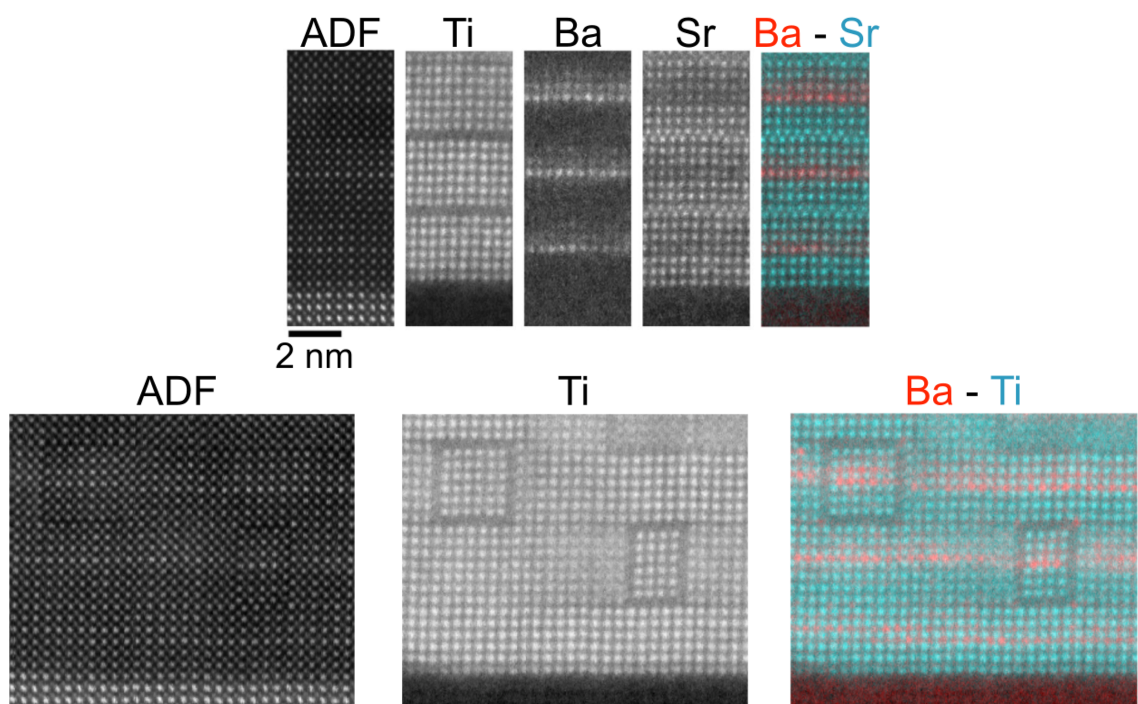

Figure 5.9. (top) Annular dark field (ADF) STEM images and EELS signals of the $n = 6$ $(SrTiO_3)_{n-1}(BaTiO_3)_1SrO$ film that illustrate the formation of the Ruddlesden-Popper structure and inclusion of the targeted BaO layer. (bottom) Larger-area STEM images that depict the horizontal and vertical $(SrO)_2$ planes that are present in the film. Microscopist: Megan Holtz, Cornell.

5.3 Dielectric property measurements of the $(SrTiO_3)_{n-1}(BaTiO_3)_1SrO$ films

5.3.1 Ferroelectric transition temperature measurements

Having verified that the $(SrTiO_3)_{n-1}(BaTiO_3)_1SrO$ superlattice thin films grew as desired, it was time for us to explore the dielectric properties. The DFT calculations and the prior experiments on the $(SrTiO_3)_nSrO$ superlattice films indicated that the $n = 6$ superlattice would provide the highest T_C out of the $n = 2$ to 6 compounds tested. This increase in T_C is attributed to the emergence of the polar soft mode when $n > 2$ and its continued strengthening as n increases [166]. As illustrated in Figure 5.10 the T_C occurs at 172 K for the $n = 6$ $(SrTiO_3)_{n-1}(BaTiO_3)_1SrO$ film on (110) $DyScO_3$ substrate, compared to 180 K for the $n = 6$ $(SrTiO_3)_nSrO$ film on the same substrate.

These observations are unsurprising when we consider the ferroelectric free energy landscape of the in-plane polar distortion of the $n = 2, 4, 6$ members of the $(SrTiO_3)_{n-1}(BaTiO_3)_1SrO$ series and $(SrTiO_3)_nSrO$ series commensurately strained to (110) $DyScO_3$ (Figure 5.10). These 0 K first-principles simulations show that the potential wells for the $(SrTiO_3)_{n-1}(BaTiO_3)_1SrO$ series are shallower than for the $(SrTiO_3)_nSrO$ series with the same n value. This behavior is consistent with the expected reduction in mismatch strain from approximately 1.1 % for $(SrTiO_3)_nSrO$ to lower values for $(SrTiO_3)_{n-1}(BaTiO_3)_1SrO$ (0.1 % to 0.8 % depending on n). The relationship between mismatch strain and the free energy landscape may not

be straightforward, though. Additional first-principles calculations of $(SrTiO_3)_nSrO$ films subject to these lower strains (0.1 % to 0.8 % mismatch) revealed even weaker ferroelectric behavior.

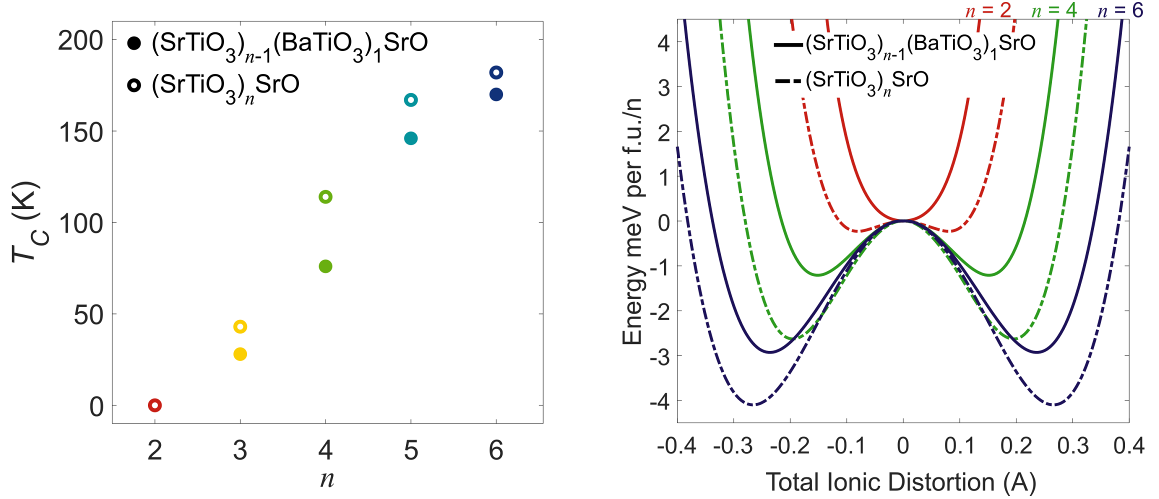

Figure 5.10. (left) The T_C as a function of n, obtained from the peak dielectric constant value (@ 10 kHz) observed during temperature sweeps. (right) The free energy landscape of the in-plane polar distortion for $n = 2, 4, 6$ compounds of the $(SrTiO_3)_{n-1}(BaTiO_3)_1SrO$ and $(SrTiO_3)_nSrO$ strained commensurately to (110) $DyScO_3$ substrates obtained from first-principles calculations.

In light of the time intensive nature of growing thick films and performing the dielectric spectroscopy, we focused only on the $n = 6$ compounds with the closest T_C to room temperature from this point, as these compounds should provide the optimal room temperature tunability of the dielectric properties.

5.3.2 Complex permittivity of 100 nm thick $n = 6$ $(SrTiO_3)_{n-1}(BaTiO_3)_1SrO$ films

We measured the complex permittivty of the 100 nm $n = 6$ $(SrTiO_3)_{n-1}(BaTiO_3)_1SrO$ films from 600 Hz to 110 GHz with the IDC and CPW

transmission line techniques described in Chapter 2. The permittivty measurement devices (Figure 5.11) were patterned directly on the surface of the thin film with the photolithograpy techniques described in Appendix B. The four IDCs for measurements from 600 Hz to 100 MHz had active lengths of $l = (0.21,\ 1.11,\ 2.01,\ 2.91)$ mm, and the seven CPWs for measurements from 100 MHz to 110 GHz had active lengths of $l = (0.42,\ 0.66,\ 0.88,\ 1.34,\ 2.24,\ 4.02,\ 7.50)$ mm. The center conductors were 20 µm wide and the gaps between the center conductors and ground planes were 5 µm wide. We fabricated a companion substrate with identical devices on a bare (110) $DyScO_3$ substrate, and on-wafer calibrations were performed using geometrically similar devices on either (001) LAO or (001) LSAT substrates.

Figure 5.11. The dielectric property measurement test devices patterned on the surface of the 100 nm $n = 6$ $(SrTiO_3)_{n-1}(BaTiO_3)_1SrO$ film.

The dielectric constant of the 100 nm $n = 6$ $(SrTiO_3)_{n-1}(BaTiO_3)_1SrO$ film shows minimal dispersion in the entire measured range from 600 Hz to 110 GHz

and an average value of approximately 350 in the microwave and millimeter-wave regimes (Figure 5.12). There is a small, but noticeable increase in the imaginary part of the permittivity above 10 GHz, as the material becomes lossier. We note that this minimal dispersion and fairly low loss is actually quite similar to the behavior of the $Ba_{1-x}Sr_xTiO_3$ films with comparable Ba content discussed in Chapter 4. While the loss tangents may be comparable, the measured relative tunability of $Ba_{1-x}Sr_xTiO_3$ with that composition is significantly less, as we discuss later.

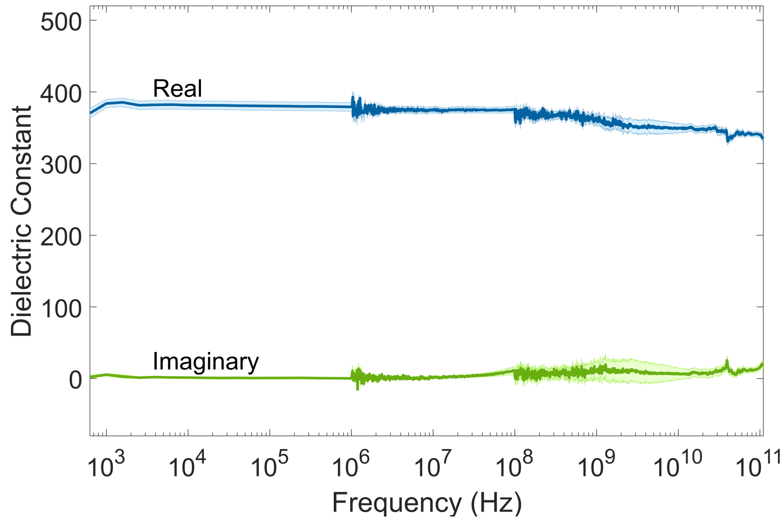

Figure 5.12. The real and imaginary parts of the complex permittivity from 600 Hz to 110 GHz, including 95 % confidence intervals (shaded regions).

In Figure 5.13, we highlight the 100 GHz bandwidth from 10 GHz to 110 GHz that is most relevant for next-generation millimeter-wave devices. Again, the minimal dispersion in the dielectric constant is apparent, along with the moderate increase in loss tangent up to approximately 0.05 at 110 GHz. This loss behavior is comparable to that of the $n = 6$ $(SrTiO_3)_nSrO$ thin films. The similar loss behavior and observation of the vertical and horizontal $(SrO)_2$ faults in the STEM images, supports the notion that the defect-mitigating nature of the Ruddlesden-Popper

structure is intact in these 100 nm $n = 6$ $(SrTiO_3)_{n-1}(BaTiO_3)_1SrO$ films.

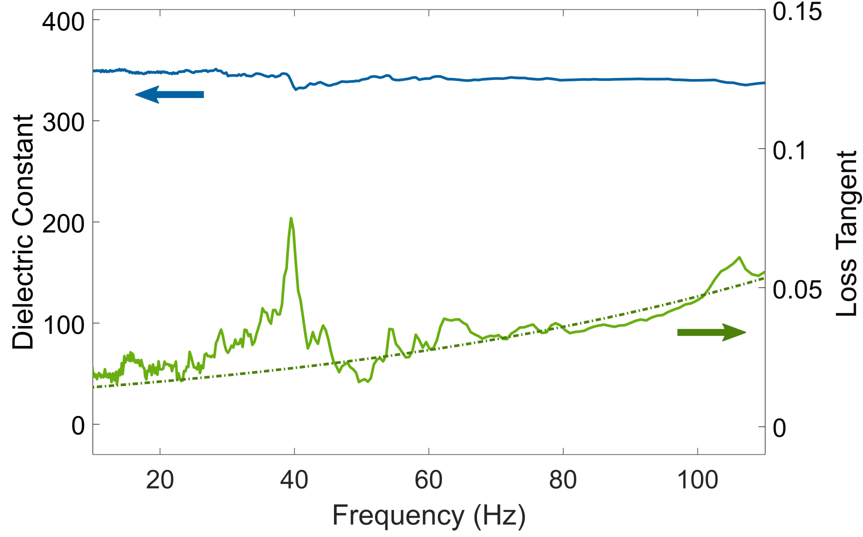

Figure 5.13. The dielectric constant and loss tangent of the 100 nm $n = 6$ $(SrTiO_3)_{n-1}(BaTiO_3)_1SrO$ film in the millimeter-wave telecommunications-relevant frequency bandwidth spanning from 10 GHz to 110 GHz.

5.3.3 Electric field dependence of the dielectric properties

We measured the tunability of the dielectric properties over frequencies from 100 MHz to 40 GHz, and electric field magnitudes from $-400\,\mathrm{kV\,cm^{-1}}$ to $+400\,\mathrm{kV\,cm^{-1}}$. The relative tunability, n_r (Eqn. 1.7), reached more than 45 % under the maximum applied electric field - an exceptionally high value given the low dielectric loss of this material. As illustrated in Figure 5.14, the frequency-independent nature of the dielectric constant in the measured range extends to the electric field-dependent dielectric constant as well, with minimal difference between the 5 GHz, 20 GHz, and 40 GHz tuning curves. The 40 GHz tuning curves for the 50 nm thick $n = 6$ $(SrTiO_3)_nSrO$ film (Ref. [64]) and for the 125 nm thick $Ba_{0.20}Sr_{0.80}TiO_3$ film (Chapter 4) are included in Figure 5.14 for comparison. It is immediately apparent

that the measured relative tunability of the $n = 6$ $(SrTiO_3)_{n-1}(BaTiO_3)_1SrO$ film is largest, with one caveat: the $\pm 400\,\mathrm{kV\,cm^{-1}}$ field used in this case is larger than the maximum field applied in the other two experiments. Within the same electric field range, though, the $Ba_{0.2}Sr_{0.8}TiO_3$ film is least tunable. The $n = 6$ $(SrTiO_3)_nSrO$ film is slightly more tunable, as we expected based on the first-principles calculations discussed in Section 5.1.4.

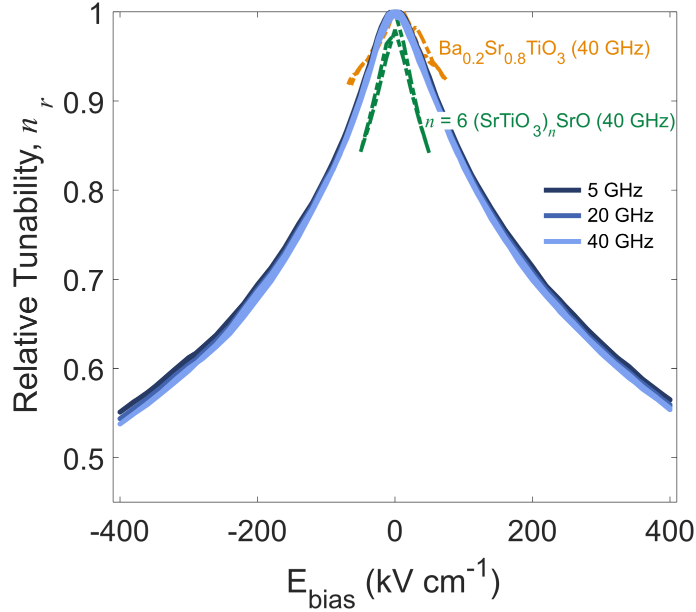

Figure 5.14. The dielectric constant tuning curves for the $n = 6$ $(SrTiO_3)_{n-1}(BaTiO_3)_1SrO$ film at 5 GHz, 20 GHz, and 40 GHz. Also shown is the 40 GHz tuning curve for the $n = 6$ $(SrTiO_3)_nSrO$ film described in Ref. [64] and the 40 GHz tuning curve for the $Ba_{0.2}Sr_{0.8}TiO_3$ film described in Chapter 4.

The reason for limiting the field strength in the original measurements of the $(SrTiO_3)_nSrO$ compounds to $\pm 50\,\mathrm{kV\,cm^{-1}}$ was not reported. However, the tuning curves have not saturated at that maximum field strength, so it is reasonable to expect that the measured relative tunability could be increased by applying a stronger field. In the case of the $Ba_{1-x}Sr_xTiO_3$ composition-spread thin films (Chapter 4), the field was limited to $\pm 75\,\mathrm{kV\,cm^{-1}}$ to avoid dielectric breakdown failures.

It would be interesting to test the dielectric breakdown strength of the thicker $(SrTiO_3)_{n-1}(BaTiO_3)_1SrO$ films, however the $\pm400\,kV\,cm^{-1}$ fields we applied are at the maximum for our available equipment. As the tuning curves for the 100 nm $n = 6$ $(SrTiO_3)_{n-1}(BaTiO_3)_1SrO$ films are also not fully saturated at the maximum field strength, it seems reasonable to expect even greater relative tunability in these films under a stronger applied field.

We then explored how the applied field changes the frequency-dependence of the dielectric constant and loss tangent in the 100 nm $n = 6$ $(SrTiO_3)_{n-1}(BaTiO_3)_1SrO$ film. The magnitude of the dielectric constant decreases significantly as the field strength increases, but the frequency dependence of the dielectric constant (Figure 5.15) is relatively unchanged regardless of the applied voltage. Slight oscillations appear from 100 MHz to 500 MHz as the applied electric field increases in strength. These oscillations are associated with resonant acoustic behavior that occurs in the gaps of the CPW transmission lines due to electrostriction driven by the AC test signal [171, 172]. This behavior only occurs once the film enters a non-centrosymmetric state in response to the applied DC field, and has been observed in similar materials and devices [59].

Perhaps the most interesting aspect of the electric field measurements is that the loss tangent of the 100 nm $n = 6$ $(SrTiO_3)_{n-1}(BaTiO_3)_1SrO$ film increases as the strength of the external electric field increases. This behavior indicates the dominance of intrinsic loss mechanisms like field-induced quasi-Debye losses over extrinsic loss mechanisms like point defect acoustic wave generation. Some extrinsic losses are proportional to the permittivity of the material, and therefore decrease in the pres-

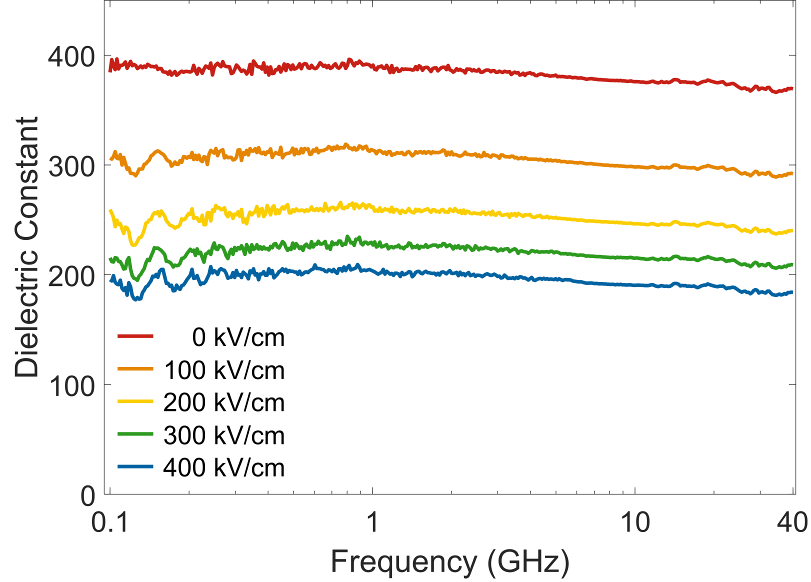

Figure 5.15. The frequency-dependent dielectric constant of the 100 nm $n = 6$ $(SrTiO_3)_{n-1}(BaTiO_3)_1SrO$ film from 100 MHz to 40 GHz under a range of applied electric fields ranging from $0\,kV\,cm^{-1}$ to $400\,kV\,cm^{-1}$.

ence of an applied field [27]. The behavior we observe in Figure 5.16 is uncommon in tunable dielectric thin films which typically contain significant point defect concentrations that increase extrinsic losses and polar nano-regions. While it has yet to be rigorously studied, this behavior suggests that these $(SrTiO_3)_{n-1}(BaTiO_3)_1SrO$ films have lower point defect concentrations and polar nano-regions are not present. This is not necessarily surprising, given the defect-mitigating properties of our $(SrTiO_3)_{n-1}(BaTiO_3)_1SrO$ film with the Ruddlesden-Popper structure. We also note that the electric field dependence of the loss tangent appears to decrease slightly as our measurement frequency increases. There may be a cross-over point above which extrinsic losses dominate, and the loss tangent would decrease with increasing applied electric field strength [46]. Unfortunately, this does not occur within our measurable bandwidth.

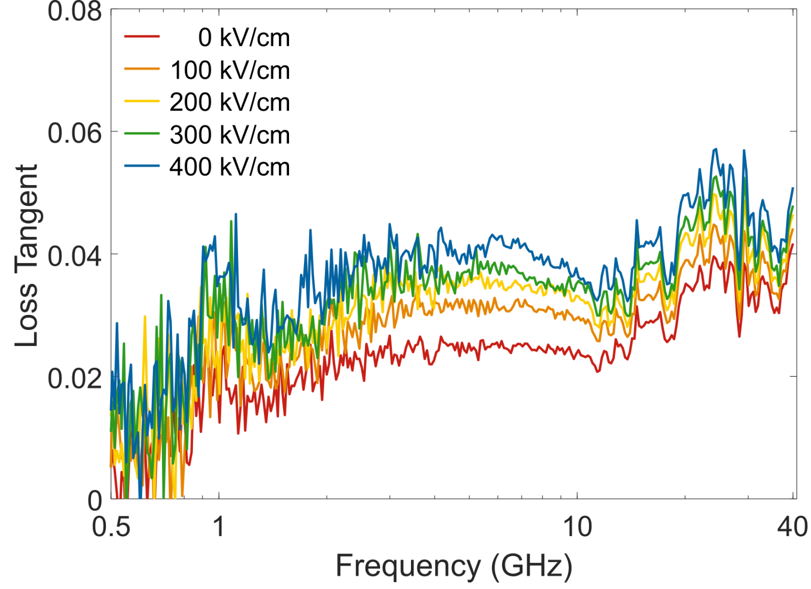

Figure 5.16. The frequency-dependent loss tangent of the 100 nm $n = 6$ $(\mathrm{SrTiO_3})_{n-1}(\mathrm{BaTiO_3})_1\mathrm{SrO}$ film from 500 MHz to 40 GHz under a range of applied electric fields ranging from $0\,\mathrm{kV\,cm^{-1}}$ to $400\,\mathrm{kV\,cm^{-1}}$.

5.3.4 $(\mathrm{SrTiO_3})_{n-1}(\mathrm{BaTiO_3})_1\mathrm{SrO}$ as a high-performance millimeter-wave tunable dielectric

The high relative tunability and low dielectric loss of the 100 nm $n = 6$ $(\mathrm{SrTiO_3})_{n-1}(\mathrm{BaTiO_3})_1\mathrm{SrO}$ film at millimeter-wave frequencies make it ideal for tunable RF devices. One figure of merit (FOM) used to compare the performance of tunable dielectric materials combines these two salient features:

$$\mathrm{FOM} = \frac{n_r}{\tan\delta}. \tag{5.1}$$

The 100 nm $n = 6$ $(\mathrm{SrTiO_3})_{n-1}(\mathrm{BaTiO_3})_1\mathrm{SrO}$ film displays excellent performance in the millimeter-wave spectrum above 30 GHz - even surpassing the FOM of the highly-regarded 50 nm $n = 6$ $(\mathrm{SrTiO_3})_n\mathrm{SrO}$ film (Figure 5.17). Since the loss

tangents are comparable, this increase is largely an effect of the additional tunability obtained by increasing the strength of the applied electric field (this FOM does not consider applied field strength). Figure 5.17 includes curves for the 50 nm $n = 6$ $(SrTiO_3)_nSrO$ film ($E_{max} = 50\,kV\,cm^{-1}$) [64], an established result for a 300 nm thick $Ba_{0.5}Sr_{0.5}TiO_3$ film on (0001) sapphire [113], ($E_{max} = 300\,kV\,cm^{-1}$) and a 400 nm thick $Ba_{0.8}Sr_{0.2}TiO_3$ film in the ferroelectric manifold-domain-wall-variant state on (110) $SmScO_3$ ($E_{max} = 500\,kV\,cm^{-1}$), which used resonant domain-wall motion to achieve high performance at low microwave frequencies [47]. We note that the $400\,kV\,cm^{-1}$ electric field strength applied in our experiment is comparable to the fields applied in most other reports.

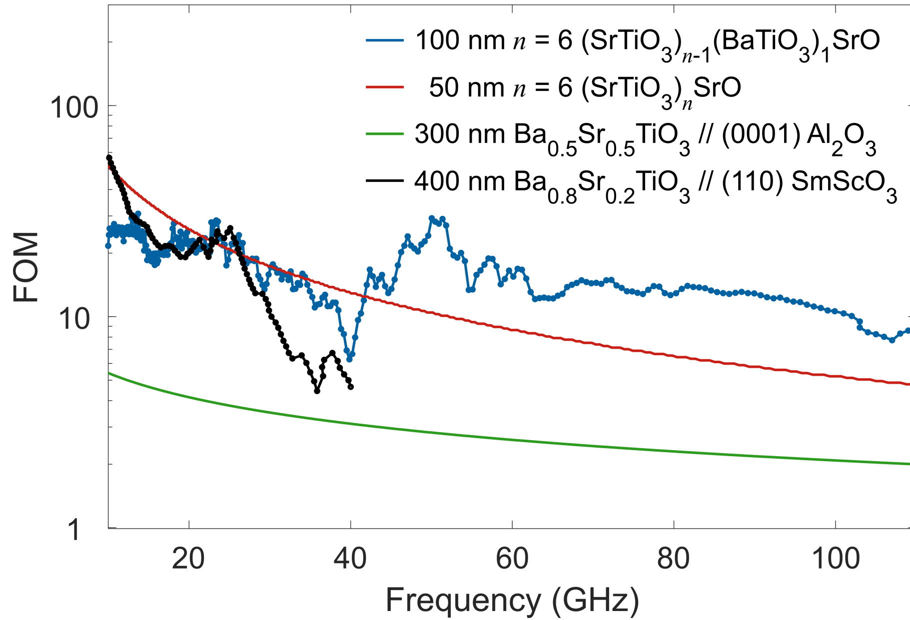

Figure 5.17. The figure of merit (FOM, eqn. 5.1) for the 100 nm $n = 6$ $(SrTiO_3)_{n-1}(BaTiO_3)_1SrO$ film, along with curves for other notable reports of high-performance tunable dielectric thin films for comparison.

5.4 Discussion and outlook

In this work, we sought to obtain thicker strain-engineered tunable dielectric films in order to increase the device tunability of adaptive RF electronics. We began with the high-performance $n = 6$ $(SrTiO_3)_nSrO$ Ruddlesden-Popper films demonstrated in Ref. [64] because of their low loss at millimeter-wave frequencies and high relative tunability. By replacing a single SrO layer in the perovskite $SrTiO_3$ blocks with a BaO layer, we reduced the epitaxial mismatch strain from 1.1 % to 0.8 %, enabling films to be grown beyond 100 nm thick without relaxation. By focusing the larger Ba^{2+} cations in a single layer, we induced "targeted chemical pressure", which provided increased tunability compared to randomly including Ba throughout the material. According to first-principles calculations, this "targeted chemical pressure" induces a more anisotropic deformation of the lattice which allows for additional in-plane displacement of the Ti^{2+} cations in neighboring layers.

Although the theoretical tunability of our 100 nm $n = 6$ $(SrTiO_3)_{n-1}(BaTiO_3)_1SrO$ film is not as large as the 50 nm $n = 6$ $(SrTiO_3)_nSrO$ film, we obtained significant additional film tunability by applying a stronger electric field. The increase in measured film tunability, combined with the increase in film thickness provided almost 10 % device tunability in our CPWs. As the dielectric losses are comparable in both materials, we obtained a notable 200 % improvement in the relevant figure of merit, again illustrating the promise of this class of materials.

Beyond producing a material with excellent tunable dielectric properties, this

work illustrated that the application of strain to improve thin-film properties doesn't have to be limited to the substrate-film lattice mismatch. The experimental realization of these films with "targeted chemical pressure" presents a new degree of freedom for materials-by-design. On a fundamental level, we wonder about the limits of this approach and how else it might be applied to enhance materials. There are certainly many "knobs" that can be turned - from cation species/size, to the number and placement of targeted layers, and more. Particularly, the additional flexibility in substrate lattice constant that this approach may provide is one of the most exciting possibilities. Replacing the small, expensive $DyScO_3$ substrates with a cheaper substrate that is more established for production-scale devices is the single most important step toward the commercial application of these materials. We do recognize that the the slow and expensive MBE growth of these materials is a barrier to commercialization. Advances in faster synthesis techniques like chemical vapor deposition may eventually provide a more efficient route to grow these and similar high-performance films [173].

Chapter 6

Conclusions and future directions

6.1 Summary of results

When we began this work, we wanted to use the best permittivity measurement techniques to discover and characterize the best tunable dielectric materials for millimeter-wave devices. While defining the "best" measurement and material in many ways depends on the final application, the experiments we have discussed in this dissertation represent significant progress in both metrology and the characterization of new tunable dielectrics with enhanced properties. Here we highlight some of the more important points from each chapter.

In **Chapter 1**, we introduced some of the fundamental concepts of tunable dielectric materials and devices, which have the potential to accelerate the development of millimeter-wave telecommunications. Tunable devices like frequency-agile filters and phased-array antennas provide an elegant solution to many of the challenges facing the use of millimeter-wave carrier frequencies like atmospheric attenuation. Tunable devices made of ferroelectric films are among the smallest, fastest, and most reliable. Unfortunately, despite decades of research, there are still many obstacles facing the large-scale commercialization of tunable dielectric devices. To realize the full potential of this technology, we need materials with less dielectric

loss and more tunability, that can be grown quickly and consistently in a form factor suitable for integration. Progress in some of these areas has been hindered, at least in part, by limitations on characterization of the dielectric properties of thin films at millimeter-wave frequencies. Novel tunable dielectrics have been characterized with a wide variety of techniques, often with minimal description of methods and uncertainties. This has clouded our ability to compare materials and properties between different reports as easily as we would like. One of our main goals in this work was to identify and apply characterization techniques that we felt would provide reliable quantitative measurements to facilitate comparison between experiments.

In **Chapter 2**, we delved further into permittivity characterization methods for tunable dielectric materials and motivated our choice to use on-wafer capacitor and transmission line techniques. We detailed how we use these devices to measure the relative permittivity of thin films from 100 Hz to 110 GHz. This extremely wide frequency band covers carrier frequencies for next-generation telecommunications, and allows us to observe dielectric behavior across many timescales. While basic on-wafer capacitor and transmission line measurements are well-established in the literature, we highlighted throughout Chapter 2 some unique aspects of our implementation. For example, we described our use of custom-fabricated on-wafer calibration chips, which contain devices that enable a variety of calibration techniques. This allows us to select the best calibration for a given instrument and frequency range. We also noted our inclusion and use of a companion substrate chip which allows us to refine and validate our finite element simulations, in addition to acting as a predictable reference to better resolve the substrate permittivity and

conductor properties of the devices. We demonstrated our measurement techniques in **Chapter 3** by measuring the relative permittivity from 100 Hz to 110 GHz of a 500 nm thick $Ba_{0.5}Sr_{0.5}TiO_3$ film grown on LSAT substrate by PLD. We presented the process to extract the dielectric constant and loss tangent of the thin film, along with propagated uncertainties, the calculation of which we detail in Appendix B. Among thin film permittivity measurement techniques, our approach yields rather low uncertainties (sub-10%) at millimeter-wave frequencies where many techniques struggle with accuracy. While the main purpose of Chapter 3 was to further familiarize the reader with our measurement process, the measurements themselves are valuable to the tunable dielectrics community. There exist only one or two measurements of $Ba_{0.5}Sr_{0.5}TiO_3$ films up to 110 GHz in the literature, and these contain only a moderate amount of information on how the permittivity was measured, and no mention of uncertainty. While simple $(Ba,Sr)TiO_3$ films may not offer low enough loss for some millimeter-wave device applications, these measurements add to our understanding of how this material, which has had an outsize role in tunable dielectrics research, behaves at high frequencies.

In **Chapter 4**, we described our new high-throughput measurement scheme for composition-spread thin films. Incorporating many principles of the "Materials Genome Initiative", our approach makes it possible to apply combinatorial materials science techniques to accelerate the discovery of better tunable dielectrics. As demonstrated in this work, our measurement technique enabled relative permittivity measurements of 14 unique material compositions on a single 10 mm square test sample from 100 MHz to 110 GHz. The single-sample aspect is particularly

beneficial because it ensures that all measured compositions were processed the same way. Our demonstration mapped the full $Ba_{1-x}Sr_xTiO_3$ system from $x = 0$ to $x = 1$, and also described the synthesis and fundamental materials characterization of the composition-spread thin films. The $Ba_{1-x}Sr_xTiO_3$ system was again interesting because of its notable role in tunable dielectrics research, but also because the ferroelectric-paraelectric phase transition changes with composition and passes through room temperature. Our comprehensive mapping of the $Ba_{1-x}Sr_xTiO_3$ system covered the composition-, frequency-, and electric-field-dependence of the dielectric properties in a way not reported previously, allowing us observe the dramatic shifts from ferroelectric behavior to paraelectric behavior.

Finally, in **Chapter 5**, we presented our development and characterization of strain-engineered superlattice thin films with unprecedented tunable dielectric properties. This work was a progression of earlier investigations of strain-engineered $(SrTiO_3)_nSrO$ Ruddlesden-Popper thin films. Those films took an inherently low-loss material and used epitaxial mismatch strain to induce ferroelectricity, and by extension, tunability. While the tunable dielectric properties were exceptional in these films, the significant lattice mismatch between the substrate and film meant that they couldn't be grown very thick before relaxing, which limited their viability in commercial tunable devices. Guided by first-principles calculations, we found we could grow thicker films and maintain *most* of the tunability by introducing "targeted chemical pressure" in the lattice and reducing the epitaxial mismatch strain. Inspired by the δ-doping approach for semiconductors, we modified the lattice by selectively replacing a single SrO layer at the center of the unit cell with

a slightly larger BaO layer, which enhanced polarizability in nearby layers. This material, $(SrTiO_3)_{n-1}(BaTiO_3)_1SrO$, can be grown more than twice as thick, still maintains the low-loss characteristic of the Ruddlesden-Popper structure, and can achieve almost 50 % relative tunability. This work depended on a close collaboration involving first-principles theory, tightly-controlled epitaxial growth, and our reliable characterization approach and device integration to achieve unprecedented tunable dielectric properties at millimeter-wave frequencies up to 110 GHz.

6.2 Future Directions

Our work has led us to encounter many opportunities to extend our research in new directions. Most of these interesting research opportunities fall into two categories: (1) metrology development and (2) exploration of new materials.

6.2.1 Metrology development

As we have mentioned throughout this work, we feel that accurate and clearly reported measurements of the tunable dielectric properties of thin films are the most important way to promote the development of better materials. To that end, we plan to continue refining our own on-wafer characterization techniques, and facilitating their use in the wider tunable dielectrics community. We also recognize opportunities for us to add brand new capabilities, which we describe below.

One critical gap in our characterization toolbox is our lack of a well-developed on-wafer technique to characterize the out-of-plane permittivity of thin

films at millimeter-wave frequencies. Many monolithic microwave integrated circuits (MMICs) incorporate components like our IDCs and CPWs that generate in-plane electric fields, but micro-strip transmission lines or certain filters that generate out-of-plane fields are also very common. Materials like the strain-engineered films we described in Chapter 5 can have highly anisotropic dielectric properties, so it is important to characterize both the in-plane and out-of-plane permittivity. A couple reports we mentioned in Chapters 1 and 2 addressed many of the challenges facing the use of parallel-plate type devices at high frequencies, but had limited accuracy [39, 59, 40]. After performing full-wave simulations of concentric parallel-plate devices like the ones described in those reports and considering the primary sources of error in previous implementations, there seems to be a path to improve the accuracy of these techniques at millimeter-wave frequencies. Part of our approach will involve developing custom-fabricated calibration standards, rather than using commercially-available generic calibration kits. We expect that these calibrations, along with our current fabrication techniques, modern measurement instrumentation, and finite-element modeling to better understand parasitic effects will dramatically improve our ability to confidently use these techniques to measure the out-of-plane permittivity at millimeter-wave frequencies.

There are some obvious, but valuable, ways we can expand our measurement capabilities. For example, newer commercial network analyzers can measure up to 145 GHz and beyond, providing a clear opportunity to increase our measurement bandwidth. Of course, performing accurate measurements at higher frequencies is not as simple as just plugging in a different network analyzer. Some of our recent 3D

full-wave simulation work has suggested a gradual departure from quasi-TEM behavior in our CPWs above 100 GHz, and radiation may become a concern at higher frequencies. Additional modeling work, and perhaps even reverberation chamber measurements are needed to answer some of these questions and guide device design. In the long term, we hope to close the "terahertz" gap - the difficult to measure frequency region that sits between the electrical (millimeter-wave) and optical (IR) domains. The ongoing development of optically-derived RF sources up to 1 THz at NIST may present opportunities to make progress toward that goal.

Finally, we touch on a unique idea aimed at providing a simple measurement solution to scientists with limited microwave measurement or fabrication capabilities. Some preliminary work with a **S**tandard **T**est **I**DC/**C**PW **K**it for **Cal**ibration and Measurement (StickyCal) illustrated potential viability for measuring the permittivity of bulk materials. This kit is a single flexible PCB that includes IDCs, CPWs, and calibration standards to enable permittivity measurements up to microwave frequencies. Rather than perform tedious fabrication, the PCB is affixed to the material under test with an adhesive layer, and the devices are probed in the same way we probe our on-wafer devices. One previous iteration showed promise, but revealed opportunities to improve measurement sensitivity, accuracy, and bandwidth (up to 20 GHz). By making all of the PCB kits identical to one another, we can use the same analysis and permittivity mapping functions for every kit. This is one of the most exciting aspects - including a compact analysis routine along with the physical kits dramatically simplifies the materials characterization process for the end user, and could provide a way to ensure that characterization techniques

are consistent across experiments. This could mark an interesting improvement in the ability to compare measurement results between various reports.

6.2.2 Exploration of new materials

All of our work developing measurement capabilities for naught if we don't use them to explore materials. We often have a long list of materials to test - not all of of which are tunable dielectrics. Some of these materials push performance boundaries, as the Ruddlesden-Popper superlattices did in Chapter 5, while others illustrate some interesting aspect of materials science like the $Ba_{1-x}Sr_xTiO_3$ composition-spreads we described in Chapter 4. For thin film materials, it is undeniable that the imposition of strain via lattice mismatch or other sources has provided some of the most exciting developments in recent history, and our work has further expanded the possibilities for these techniques.

There are still many unanswered questions regarding the fundamental nature of "targeted chemical pressure" and its future applications, as we began to discuss at the end of Chapter 5. We applied the concept in the simplest way to a system we knew very well, which was a natural starting point. However, we have yet to rigorously test just how much flexibility this new degree of freedom grants in the film-substrate lattice mismatch for strain-engineered thin films. Extensive computational studies are crucial to weed through the large number of possible variables introduced by this approach (*e.g.,* cation size, layer number and placement, etc.). Furthermore, we chose to focus on the film thickness as the first important bar-

rier to overcome, but the reliance on $DyScO_3$ substrates is still an obstacle to the commercial integration of our high-performance $(SrTiO_3)_{n-1}(BaTiO_3)_1SrO$ films, due to their extreme cost and limited size. Our growth collaborators have made preliminary attempts to grow similar materials on other substrates (*e.g.,* sapphire, MgO, or $LaAlO_3$), though scandate substrates likely provide the most flexibility for imposing varying amounts of tensile strain. Another interesting aspect to explore would be to compare the properties of the $n = 6$ $(SrTiO_3)_nSrO$ films on $DyScO_3$ with $(SrTiO_3)_{n-1}(BaTiO_3)_1SrO$ grown on $TbScO_3$ [174]. With both of these cases providing an approximately 1.1 % mismatch, this would demonstrate whether the inclusion of the targeted BaO layer enhances properties beyond providing an increase in the critical thickness of the film, which could guide potential application of these techniques. Future studies will reveal the full extent to which we can use these strain-based techniques to advance the frontiers of materials science.

Though perhaps less exciting than some of the prospects for strain-engineered materials, the exploration of composition and processing variables provides incremental improvement and is especially important for fine tuning materials for commercial application. This is one of the key reasons we developed our measurement technique for combinatorial synthesis experiments. Although we have only discussed oxides in this work, the recent demonstration of ferroelectricity in the $Al_{1-x}Sc_xN$ system [175] offers an exciting opportunity to apply our composition-spread measurement technique. While the properties of this system are still largely unexplored, commercial integration of III-V compounds is well-established. On account of their well-known high acoustic velocity and electromechanical coupling, these materials

may be ideal candidates for the development of enhanced high-frequency *tunable* acoustic-wave filters [176].

Appendix A

Additional relevant information

A.1 Publications related to this work

The work presented in this dissertation and related experiments have lead to several articles, both published and planned. Here are some of the highlights:

- Journal Articles

  - N.M. Dawley & **E.J. Marksz**, A.M. Hagerstrom, G.H. Olsen, M.E. Holtz, *et al.*, "Targeted chemical pressure yields tuneable millimetre-wave dielectric." *Nature Materials.* **19**, 176-181 (2020). https://doi.org/10.1038/s41563-019-0564-4

  - **E.J. Marksz**, A.M. Hagerstrom, X.H. Zhang, N. Al-Hasan, *et al.*, "Broadband, high-frequency permittivity characterization for epitaxial $Ba_{1-x}Sr_xTiO_3$ composition-spread thin films." Under review at *Physical Review Applied.*

  - **E.J. Marksz**, A.M. Hagerstrom, N.D. Orloff, *et al.*, "On-wafer permittivity measurements of thin films from DC to 110 GHz." In preparation for submission to *IEEE Transactions on Microwave Theory and Techniques.*

  - A.M. Hagerstrom, **E.J. Marksz**, X.H. Zhang, *et al.*, "Measurements of Nonlinear Polarization Dynamics in the Tens of Gigahertz." *Physical Review Applied.* **13**, 044026 (2020). https://doi.org/10.1103/PhysRevApplied.13.044026

- Conference Papers

  - N.B. Popovic, **E.J. Marksz**, A.M. Hagerstrom, *et al.*, "Three Planar Devices for Extracting Capacitance per

Unit Length." *2019 IEEE COMCAS*. Tel-Aviv, Israel. https://doi.org/10.1109/COMCAS44984.2019.8958422

- A.M. Hagerstrom, **E.J. Marksz**, C.J. Long, *et al.*, "Frequency- and Electric Field-Dependent Physical Model of Ferroelectric Materials in the Tens of GHz." *2018 IEEE MTT-S IMWS-AMP*. Ann Arbor, MI. https://doi.org/10.1109/IMWS-AMP.2018.8457148

- A.M. Hagerstrom, **E.J. Marksz**, C.J. Long, *et al.*, "Characterization of transmission lines with nonlinear dielectric materials." *2017 90th ARFTG Microwave Measurement Symposium*. Boulder, CO. https://doi.org/10.1109/ARFTG.2017.8255875

- Selected Presentations

  - **E.J. Marksz**, A.M. Hagerstrom, N.D. Orloff, *et al.*, "Broadband characterization of novel dielectric thin films to 110 GHz for 5G radio and mm-Wave electronics." *19th U.S.-Japan Seminar on Dielectric and Piezoelectric Ceramics*. Tsukuba, JP. November 2019.

  - **E.J. Marksz**, A.M. Hagerstrom, N.M. Dawley, *et al.*, "Enabling tunable, low-loss millimeter-wave electronics through the stabilization of strain-engineered oxide superlattices." *Electronic Materials and Applications 2019*. Orlando, FL. January 2019.

  - **E.J. Marksz**, A.M. Hagerstrom, J.A. Drisko, *et al.*, "Unified models of combinatorial ferroelectric films for RF materials discovery." *2019 MRS Fall Meeting*. Boston, MA. November 2018.

A.2 Wafer-probing station configuration

We perform all of our dielectric properties measurements on a wafer-probing station. Although we have several probe stations that provide a variety of capabilities, Figure A.1 depicts one of our probe stations, in a fairly standard configuration.

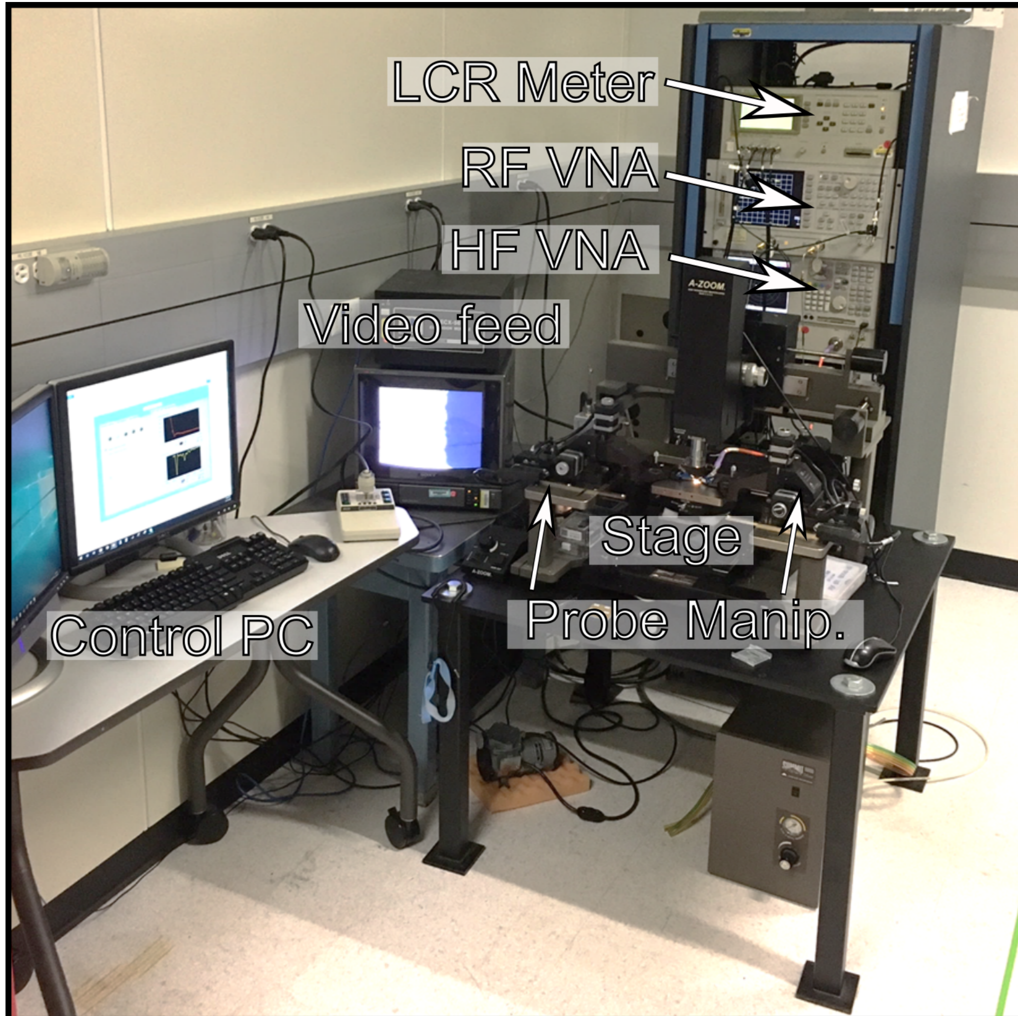

Figure A.1. One of the wafer-probing station configurations we use for the dielectric property measurements.

A.3 Electric-field dependent permittivity measurement configuration

As we described in Section 2.2.8, we make slight modifications to the measurement instrumentation to enable the electric-field dependent permittivity measurements. We use bias tees to combine a DC bias voltage from a voltage source with the AC test signals. We show a diagram of this measurement configuration in Figure A.2, and we show how the bias tees are connected to the VNA in Figure

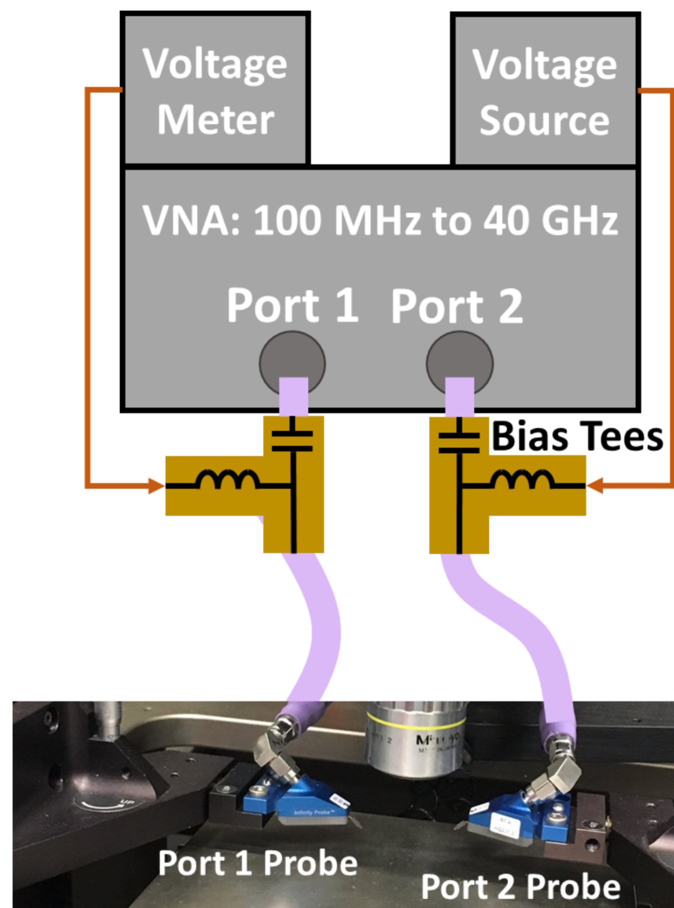

Figure A.2. A diagram of the measurement instrumentation as configured for the electric-field dependent permittivity measurements.

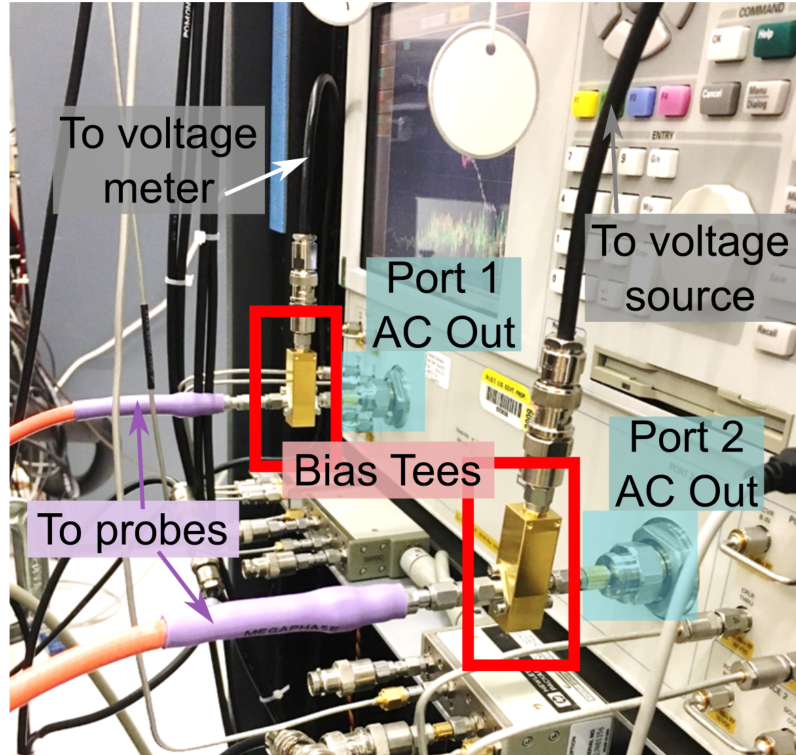

Figure A.3. An image showing how the bias tees are connected to the VNA.

A.4 Bi-directional test patterns for measurements of anisotropic materials

Occasionally, we will measure films or substrates with anisotropic properties, so the permittivity may be different for the two principal in-plane directions. If we want to know the permittivity in both directions, we must use devices that probe both directions. For example, since the CPWs support a quasi-TEM mode, they probe the permittivity in the transverse direction, *i.e.,* “across” the CPW. The simplest way to measure the anisotropic permittivity is to configure the test devices so that one set of devices measures one direction, and another set of devices is patterned perpendicular to the first set, to measure the other direction. An example of such a test pattern is shown in Figure A.4.

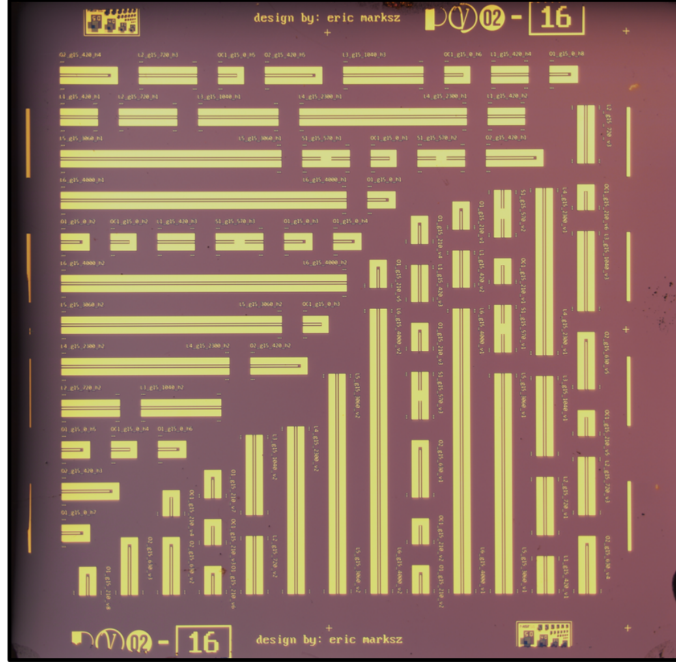

Figure A.4. An image showing a bidirectional test pattern used to measure anisotropic materials.

A.5 Additional experimental data

Here, we include a couple of additional figures with some interesting experimental data pertaining to the $(SrTiO_3)_{n-1}(BaTiO_3)_1SrO$ Ruddlesden-Popper superlattices discussed in Chapter 5. In Figure A.5, we show the $\Theta - 2\Theta$ XRD patterns for 50 nm thick $(SrTiO_3)_{n-1}(BaTiO_3)_1SrO$ films ranging from $n = 2$ to $n = 6$. As was seen in Figure 5.1, the height (c-axis lattice parameter) of the unit cell of the $(SrTiO_3)_{n-1}(BaTiO_3)_1SrO$ materials increases with increasing n. As we would expect, the film peak positions shift to lower angles 2Θ, accordingly. We also show additional HAADF-STEM images of these films in Figure A.6. The changing periodicity of the $(SrO)_2$ planes is clear, and upon close inspection, the expected vertical

$(SrO)_2$ planes that likely play a significant role in reducing dielectric losses can be seen.

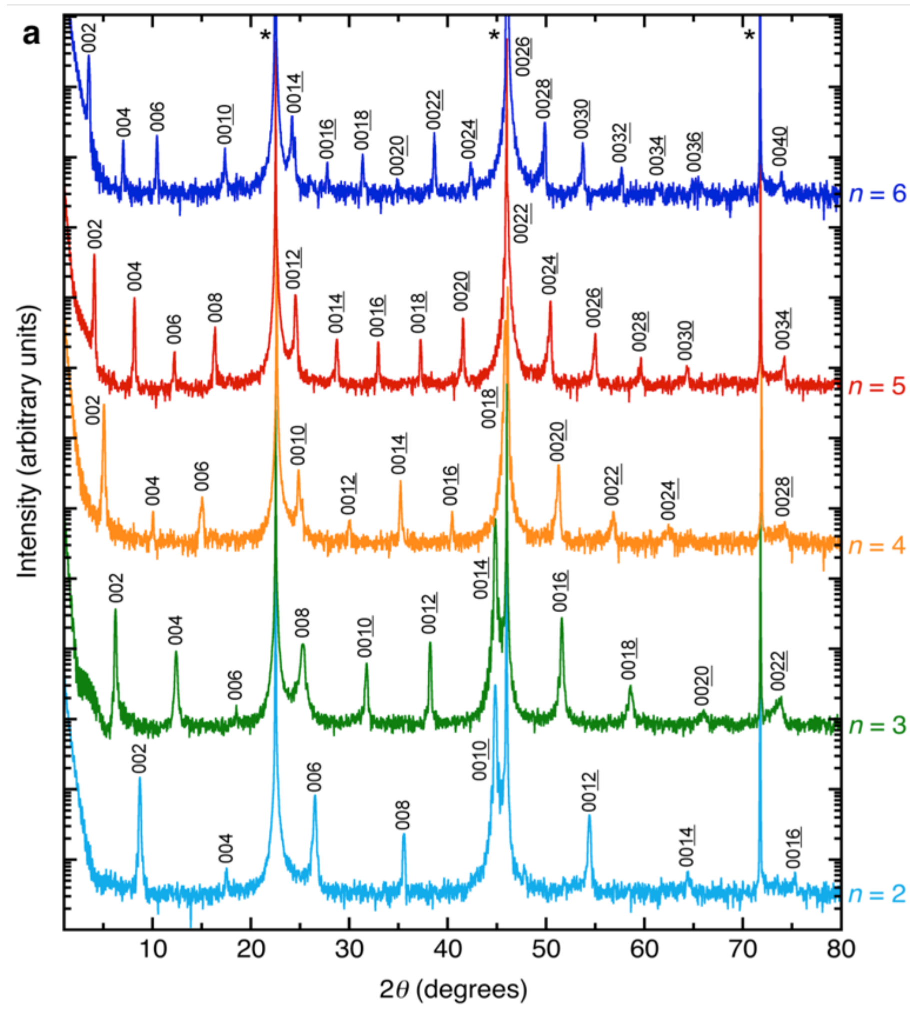

Figure A.5. The $\Theta-2\Theta$ XRD patterns for the 50 nm thick $(SrTiO_3)_{n-1}(BaTiO_3)_1SrO$ films from $n = 2$ to $n = 6$. Courtesy of Natalie Dawley.

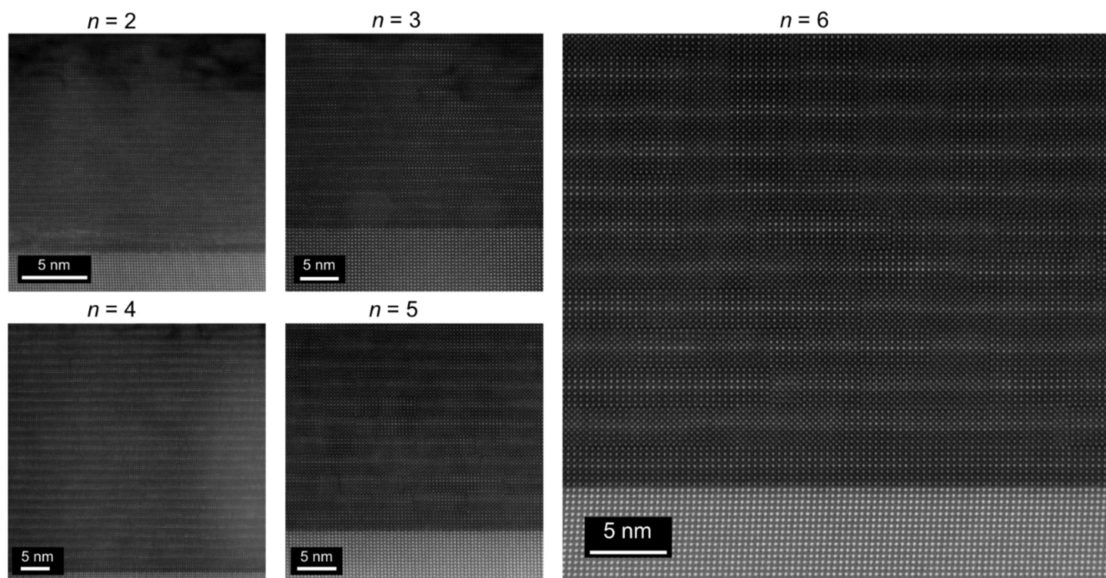

Figure A.6. HAADF-STEM images of the the 50 nm thick $(SrTiO_3)_{n-1}(BaTiO_3)_1SrO$ films from $n = 2$ to $n = 6$. Microscopist: Megan Holtz.

Appendix B

Notable concepts and additional descriptive information pertaining to our permittivity measurements and analysis

B.1 Definition of S-parameters and conversion from a and b waves

Scattering (S-) parameters are mathematical constructs which describe how ac signals propagate through multi-port networks. Fundamentally, S-parameters convey how much of the incident wave is reflected, and how much is transmitted. An n-port network is described by n^2 S-parameters, which are complex values organized in an $n \times n$ S-matrix. The S-matrix is a sort of "black box" representation of the network - without any knowledge of the internal design of the network, we can determine how an incident signal will be affected, if we know the S-matrix. The S-parameters are defined in terms of the incident and reflected/transmitted waves at each port. For a two-port network, the S-matrix can be written:

$$[\mathbf{S}] = \begin{bmatrix} S_{11} & S_{12} \\ S_{21} & S_{22} \end{bmatrix}, \tag{B.1}$$

where S_{11} and S_{22} describe reflection at ports 1 and 2, respectively, and S_{12} and S_{21} describe transmission from port 1 to port 2 and vice-versa. Figure B.1 illustrates the physical significance of these terms.

The S-parameters are ratios of the measured waves a_i and b_i:

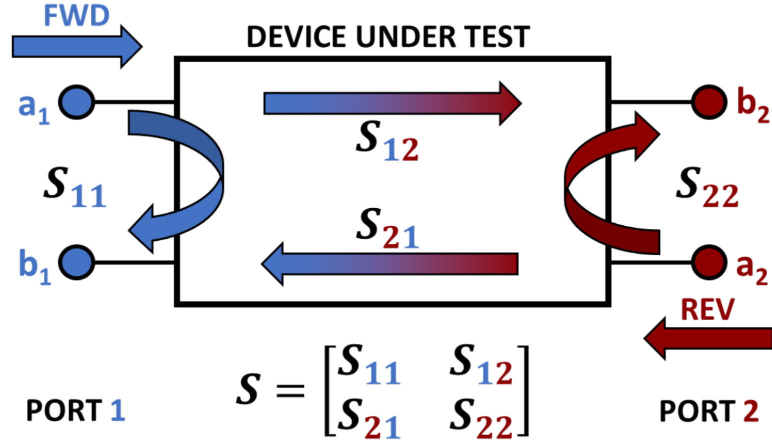

Figure B.1. A graphic illustrating the S-parameters for a two-port network.

$$[\mathbf{S}] = \begin{bmatrix} \frac{b_1}{a_1} & \frac{b_2}{a_1} \\ \frac{b_1}{a_2} & \frac{b_2}{a_2} \end{bmatrix}, \tag{B.2}$$

where a_i represents the incident wave at port i and b_i represents the reflected or transmitted wave at port i. a_i and b_i are defined as:

$$\begin{aligned} a_i &= \frac{1}{2}\frac{(V_i + Z_0 I_i)}{\sqrt{|\Re[Z_0]|}}, \\ b_i &= \frac{1}{2}\frac{(V_i - Z_0^* I_i)}{\sqrt{|\Re[Z_0]|}}. \end{aligned} \tag{B.3}$$

Here, V_i and I_i are the complex voltage and current measured at port i, Z_0 is the reference impedance (conventionally 50 ohms). For four-sampler VNAs like those used in these experiments, all of the a and b waves are measured, and then used to calculate the S-parameters. Furthermore, we calculate Γ_F and Γ_R, the forward and

reverse switch terms, respectively, by:

$$\begin{aligned}\Gamma_F &= \frac{a_2^F}{b_2^F},\\ \Gamma_R &= \frac{a_1^R}{b_1^R},\end{aligned} \tag{B.4}$$

where the superscripts R and F denote that these are the measured quantities when the switch is set to measure in the forward (F) direction (*i.e.,* sourcing on port 1) and vice versa for the reverse direction. Correcting for the switch terms can be carried out as described in Equations 18 - 21 of Ref. [105].

B.2 Conversion between S-parameters and T-parameters

Often, it is more convenient for us to convert S-parameters to T-parameters. The conversion from S-parameters to T-parameters is as follows:

$$[\mathbf{T}] = \frac{1}{S_{21}} \begin{bmatrix} -det(\mathbf{S}) & S_{11} \\ -S_{22} & 1 \end{bmatrix}, \tag{B.5}$$

and the conversion from T-parameters to S-parameters is:

$$[\mathbf{S}] = \frac{1}{T_{22}} \begin{bmatrix} T_{12} & det(\mathbf{T}) \\ 1 & -T_{22} \end{bmatrix}. \tag{B.6}$$

B.3 Conversion between S-parameters and Y-parameters

Likewise, we prefer to convert our measured S-parameters to Y-parameters for certain parts of the IDC analysis. We convert S-parameters to Y-parameters in the

following way:

$$[\mathbf{Y}] = \frac{1}{Z_R \cdot D} \begin{bmatrix} (1 - S_{11})(1 + S_22) + S_{12}S_{21} & -2S_{12} \\ -2S_{12} & (1 + S_{11})(1 - S_22) + S_{12}S_{21} \end{bmatrix}, \quad \text{(B.7)}$$

where Z_R is the reference impedance and $D = (1 + S_{11})(1 + S_{22}) - S_{12}S_{21}$.

B.4 Impedance transformers

In the measurement network, whenever there is a transition from one section with some impedance Z_m to a different section with a different impedance, Z_n, we say that there is an impedance mismatch. Just as light is reflected at the boundary between materials with mismatched indices of refraction, there is some reflection of our microwaves that results from impedance mismatches in our system. We describe these mismatches using special T-matrices called "impedance transformers". The impedance transformer $[Q|_n^m]$ describes the transition from the impedance Z_m on the left-hand side of the interface to the impedance Z_n on the right-hand side. $[Q|_n^m]$ can be determined in the following way:

$$[Q|_n^m] = \frac{1}{\sqrt{4Z_m Z_n}} \begin{bmatrix} (Z_n + Z_m) & (Z_n - Z_m) \\ (Z_n - Z_m) & (Z_n + Z_m) \end{bmatrix}. \quad \text{(B.8)}$$

These impedance transformer matrices are useful, because they provide a way to account for the effects of the mismatch when cascading T-matrices representing sections of a network that have different impedances. We refer the interested reader

to Ref. [99] for more information on their use.

B.5 Calculating R', L', C' and G' from γ and Z_c

As we noted in Chapter 2, the measured propagation constant, γ, is not enough on its own to isolate the individual distributed circuit parameters R', L', C' and G' from one another. One way to solve this problem is to measure the characteristic impedance of the CPW, Z_c:

$$Z_c = \frac{\sqrt{R' + i\omega L'}}{\sqrt{G' + i\omega C'}}. \tag{B.9}$$

Given this expression for Z_c, the distributed circuit parameters are:

$$\begin{aligned} R' &= \Re[\gamma Z_c], \\ L' &= \frac{1}{\omega}\Im[\gamma Z_c], \\ C' &= \frac{1}{\omega}\Im[\frac{\gamma}{Z_c}], \\ G' &= \Re[\frac{\gamma}{Z_c}]. \end{aligned} \tag{B.10}$$

Unfortunately, measurements of Z_c can be more challenging [102]. This is partly because our ability to accurately measure transmission exceeds our ability to accurately measure the minimal amounts of reflection in the CPW transmission lines. Some approaches enable the estimation of Z_c from error boxes [103], like those obtained from a series resistor calibration, though even these estimates begin to suffer at very high frequencies. For example, we see in Figure B.2 that relative to

simulated values of the distributed resistance (R'), values extracted using γ and Z_c display increased non-physical variation above approximately 40 GHz.

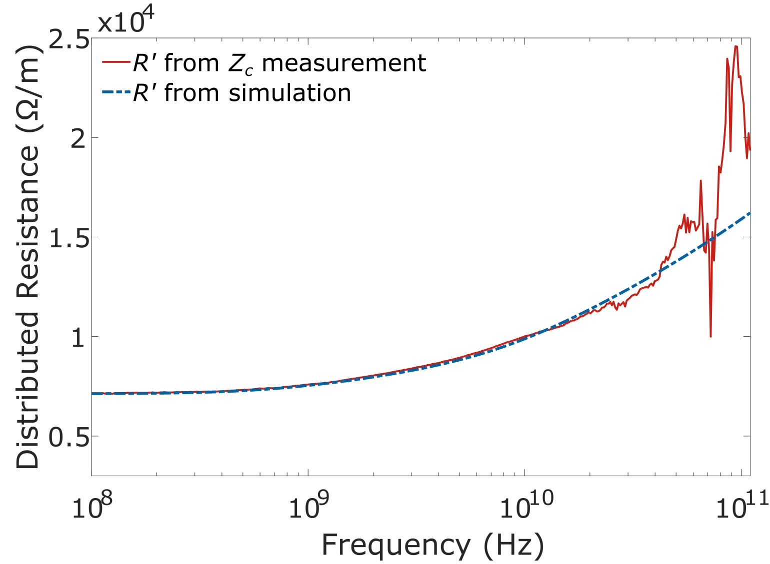

Figure B.2. Compared with a simulated value for the distributed resistance, R', the value extracted from γ and Z_c displays significant variation at high frequencies.

B.6 Analysis and Error Propagation for CPW and IDC measurements

While Chapter 2 provided significant detail regarding the analysis of our permittivity measurements, the individual steps were dispersed throughout a discussion of the theory and reasoning behind our approach. In this section, we provide a more concise rendition of our analysis to highlight it's simplicity and elegance for the interested reader. We also include the steps necessary to incorporate and propagate uncertainties from a variety of sources. We do this in hopes that more permittivity measurements will be accompanied by confidence intervals in the future, to aid in drawing comparisons between experiments.

We begin with the measurements of the CPWs. We will start from the propagation constant, γ, since each experiment may use different calibrations, or obtain the propagation constant using a different technique. In our case the NIST StatistiCal software provides the frequency-dependent effective permittivity, ε_{eff}, which is analogous to γ. We find gamma from the following expression:

$$\gamma = i\beta_0\sqrt{\varepsilon_{eff}}, \tag{B.11}$$

where β_0 is the free space phase constant ($\beta_0 = 2\pi f/c$). StatistiCal also provides $\Delta\varepsilon_{eff}$, uncertainties representing a 95 % confidence interval around the reported value for ε_{eff}. We convert $\Delta\varepsilon_{eff}$ to $\Delta\gamma$, the uncertainty in γ as follows:

$$\Delta\gamma = \frac{i\beta_0}{2}\frac{1}{\sqrt{\varepsilon_{eff}}}\Delta\varepsilon_{eff}. \tag{B.12}$$

We recall now that the propagation constant, γ, is:

$$\gamma = \sqrt{R' + i\omega L'}\sqrt{G' + i\omega C'}. \tag{B.13}$$

where R', L', C', and G' are the *frequency-dependent* resistance, inductance, capacitance, and conductance per unit length of transmission line. We use known values of γ, R', and L' to determine C', and G'. Although we will use simulated R' and L' values to determine C', and G' for the test samples, we first compute the estimated R'_{sub}, and L'_{sub} values for the companion substrate. We use these to validate our finite element simulations as described in Chapter 2. We also use the associated

uncertainties, $\Delta R'_{sub}$ and $\Delta L'_{sub}$ as our uncertainty in R' and L' for all of the test samples, under the assumption that these are relatively consistent from chip-to-chip, so long as all of the chips were co-fabricated. We obtain the estimated R'_{sub}, and L'_{sub} values by taking γ from multiline TRL, assuming that the substrate conductance is negligible $G'_{sub} = 0$, and that the substrate capacitance, C'_{sub} is some constant value, C'_0. We find the C'_0 by using the transmission line fitting approach discussed in Ref. [111], which works well at frequencies below a few GHz. We take the mean C'_{sub} value from fitting below a few GHz as C'_0, and the deviation around that mean as a basic $\Delta C'_0$. Alternatively, if our calibration chip is also our companion substrate, we can obtain a C'_0 and $\Delta C'_0$ from the series resistor calibration [107]. We obtain R'_{sub}, and L'_{sub} in the following way:

$$\begin{aligned} R'_{sub} &= \Re[\frac{\gamma^2}{i\omega C'_0}], \\ L'_{sub} &= \frac{1}{\omega}\Im[\frac{\gamma^2}{i\omega C'_0}], \end{aligned} \tag{B.14}$$

and propagate uncertainties from $\Delta\gamma$ and $\Delta C'_0$:

$$\begin{aligned} \Delta R'_{sub} &= \sqrt{(\frac{dR'}{d\gamma})^2(\Delta\gamma)^2 + (\frac{dR'}{dC'_0})^2(\Delta C'_0)^2}, \\ \Delta L'_{sub} &= \sqrt{(\frac{dL'}{d\gamma})^2(\Delta\gamma)^2 + (\frac{d'L}{dC'_0})^2(\Delta C'_0)^2}, \end{aligned} \tag{B.15}$$

where:

$$\begin{aligned}\frac{dR'}{d\gamma} &= \Re[\frac{2\gamma}{i\omega C_0'}],\\ \frac{dR'}{dC_0'} &= \Re[\frac{-\gamma^2}{i\omega C_0'^2}],\\ \frac{dL'}{d\gamma} &= \Im[\frac{2\gamma}{i\omega^2 C_0'}],\\ \frac{dL'}{dC_0'} &= \Im[\frac{-\gamma^2}{i\omega^2 C_0'^2}].\end{aligned} \tag{B.16}$$

At this point, we simulate the R' and L' values for all of the test samples, and compare the simulated and measured R'_{sub}, and L'_{sub} to validate the simulations. Assuming the agreement is good, we then take the measured γ for each of the test samples, obtained from multiline TRL, and use the unique simulated R'_{sim}, and L'_{sim} values to obtain C' and G' for each test sample in the following way:

$$\begin{aligned}C' &= \frac{1}{\omega}\Im[\frac{\gamma^2}{R'_{sim} + i\omega L'_{sim}}],\\ G' &= \Re[\frac{\gamma^2}{R'_{sim} + i\omega L'_{sim}}].\end{aligned} \tag{B.17}$$

We then propagate uncertainties from $\Delta\gamma$, $\Delta R'$ and $\Delta L'$, which is a bit more tedious than our uncertainty propagation up to this point. To help simplify, we break γ into its real and imaginary parts, *i.e.,* the attenuation constant, α, and the phase constant β. Correspondingly, we break $\Delta\gamma$ up into $\Delta\alpha = \Re[\Delta\gamma]$ and $\Delta\beta = \Im[\Delta\gamma]$

and evaluate each separately. We then propagate the uncertainties as follows:

$$\Delta C' = \sqrt{(\frac{dC'}{d\alpha})^2(\Delta\alpha)^2 + (\frac{dC'}{d\beta})^2(\Delta\beta)^2 + (\frac{dC'}{dR'})^2(\Delta R')^2 + (\frac{dC'}{dL'})^2(\Delta L')^2},$$
$$\Delta G' = \sqrt{(\frac{dG'}{d\alpha})^2(\Delta\alpha)^2 + (\frac{dG'}{d\beta})^2(\Delta\beta)^2 + (\frac{dG'}{dR'})^2(\Delta R')^2 + (\frac{dG'}{dL'})^2(\Delta L')^2}, \quad \text{(B.18)}$$

where:

$$\begin{aligned}
(\frac{dC'}{d\alpha}) &= \frac{2}{\omega}\frac{R'\beta - L'\alpha\omega}{R'^2 + L'^2\omega^2}, \\
(\frac{dC'}{d\beta}) &= \frac{2}{\omega}\frac{R'\alpha + L'\beta\omega}{R'^2 + L'^2\omega^2}, \\
(\frac{dC'}{dR'}) &= \frac{1}{\omega}(\frac{2\alpha\beta}{R'^2 + L'^2\omega^2} - \frac{4R'^2\alpha\beta - 2L'R'\omega(\alpha^2 - \beta^2)}{(R'^2 + L'^2\omega^2)^2}), \\
(\frac{dC'}{dL'}) &= \frac{1}{\omega}(\frac{\omega(\beta^2 - \alpha^2)}{R'^2 + L'^2\omega^2} + \frac{2L'^2\omega^3(\alpha^2 - \beta^2) - 4L'R'\alpha\beta\omega^2}{(R'^2 + L'^2\omega^2)^2}), \\
(\frac{dG'}{d\alpha}) &= 2\frac{R'\alpha + L'\beta\omega}{R'^2 + L'^2\omega^2}, \\
(\frac{dG'}{d\beta}) &= 2\frac{L'\alpha\omega - R'\beta}{R'^2 + L'^2\omega^2}, \\
(\frac{dG'}{dR'}) &= \frac{\alpha^2 - \beta^2}{R'^2 + L'^2\omega^2} - \frac{(2R'^2\omega^2(\alpha^2 - \beta^2) + 4L'R'\alpha\beta\omega}{(R'^2 + L'^2\omega^2)^2}), \\
(\frac{dG'}{dL'}) &= \frac{2\alpha\beta\omega}{R'^2 + L'^2\omega^2} - \frac{(2L'R'\omega^2(\alpha^2 - \beta^2) + 4L'^2\alpha\beta\omega^3)}{(R'^2 + L'^2\omega^2)^2}.
\end{aligned} \quad \text{(B.19)}$$

Once C' and G' for the test samples have been calculated as described above, we use our finite element simulations to generate the functions needed to map C' and G' to the dielectric constant (ε') and dielectric loss (ε''), respectively. Recall that the relative permittivity (ε_r) is comprised of these two components: $\varepsilon_r = \varepsilon' + i\varepsilon''$.

In theory, there are a variety of functions which could be used to perform the mapping, however in the high-film-permittivity regime the functions are most easily

represented as lines of the form

$$\varepsilon' = aC' + b, \\ \varepsilon'' = aG', \tag{B.20}$$

as we discussed in Chapter 2 and showed in Chapter 3. a and b here are parameters determined by fitting the output data from a simulation in which we parametrically sweep the permittivity of the thin film layer, and then fit the relationship between the film permittivity and the output capacitance from simulation, C'_{sim}. In practice, we have found that a is the same in the mapping functions for both C' and G', though $b = 0$ in the latter case. (which is reasonable given the boundary condition that no dielectric loss should correspond with no conductance in the thin film). If necessary, this can be verified by performing a similar sweep of the thin film loss tangent in the simulation.

Given our mapping function of the form shown in Equation B.20, we can determine the uncertainty in the real (ε') and imaginary (ε'') parts of the relative permittivity as follows:

$$\Delta\varepsilon' = \sqrt{(\frac{d\varepsilon'}{da})^2(\Delta a)^2 + (\frac{d\varepsilon'}{dC'})^2(\Delta C')^2 + (\frac{d\varepsilon'}{db})^2(\Delta b)^2} = \sqrt{C'^2\Delta a^2 + a^2\Delta C' + \Delta b^2}, \\ \Delta\varepsilon'' = \sqrt{(\frac{d\varepsilon''}{da})^2(\Delta a)^2 + (\frac{d\varepsilon''}{dG'})^2(\Delta G')^2} = \sqrt{G'^2\Delta a^2 + a^2\Delta G'}. \tag{B.21}$$

While we obtained $\Delta C'$ and $\Delta G'$ as described in Equation B.18, finding Δa and Δb, the uncertainty in the mapping co-efficients, is less obvious. These coefficients

are an opportunity to incorporate uncertainties related to the geometric dimensions of the device structures in simulation. When fitting the coefficients for the mapping function, we use the approach described by York in Ref. [177], which provides uncertainties in the mapping coefficients (*i.e.,* Δa and Δb) when given uncertainties in the input vectors, in our case, the simulated thin film permittivity $\Delta\varepsilon'_{sim}$ and the simulated capacitance per unit length $\Delta C'_{sim}$. Since we specify the thin film permittivity as a simulation input, $\Delta\varepsilon'_{sim} = 0$. However, uncertainty in the dimensions and properties of the simulated structures creates uncertainty in the simulated capacitance per unit length C'_{sim}. That uncertainty could be expressed as:

$$\Delta C'_{sim} = \Bigg[(\frac{dC'_{sim}}{d\sigma_{Au}})^2(\Delta\sigma_{Au})^2 + (\frac{dC'_{sim}}{dt_{Au}})^2(\Delta t_{Au})^2 + (\frac{dC'_{sim}}{dt_{film}})^2(\Delta t_{film})^2 + (\frac{dC'_{sim}}{dw_{gap}})^2(\Delta w_{gap})^2 + (\frac{dC'_{sim}}{dw_{cc}})^2(\Delta w_{cc})^2 + (\frac{dC'_{sim}}{d\varepsilon'_{subs}})^2(\Delta\varepsilon'_{subs})^2 \Bigg]^{1/2}, \quad \text{(B.22)}$$

where σ_{Au} is the conductivity of the simulated conductor layer, t_{Au} is the thickness of the conductor layer, t_{film} is the film thickness, w_{gap} is the width of the gap between the center conductor and ground planes, w_{cc} is the width of the center conductor, and ε'_{subs} is the permittivity of the substrate in simulation. Since we do not have a discrete expression from which to obtain all of the relevant partial derivatives in Equation B.22, we suggest the use of the sensitivity analysis functions that are built in to a number of finite-element simulation packages. Such an analysis will compute an approximation for these derivatives by perturbing the variable of interest around its nominal value. In practice, it may not always be desirable to include all of these sources of uncertainty, due to the time-intensive nature of performing all of the

required simulations. Often, terms like the uncertainty due to the width of the center conductor can be very small, especially with good fabrication. As we mentioned, using the approach of Ref. [177] to determine the mapping coefficients also provides the uncertainty in those coefficients, Δa and Δb when given the uncertainty in $\Delta C'_{sim}$. At this point, our analysis is complete, with Equation B.20 having provided the real and imaginary parts of the relative permittivity, and Equation B.21 having expressed the uncertainty in those values.

The analysis of the IDCs is much more simple, and uncertainty calculations more rudimentary, compared to the CPWs. Rather than regurgitate analysis steps that are already clearly explained in Chapter 2 and demonstrated in Chapter 3, we offer a brief remark here on how we determine uncertainty in measurements of our IDCs. Recall that we compare the active length and measured series admittance $Y_{S,IDC}$ of each IDC to determine the admittance per unit length of the active length region of the IDCs (see 2.21). When we do so, we use the standard deviation of the measured series admittance of each IDC around the line of best fit as an approximation for our uncertainty in the admittance per unit length of the active region, $\Delta Y'(l)$. We can break $\Delta Y'(l)$ into its real and imaginary components to determine the uncertainty in the capacitance and conductance per unit active length of the IDCs (*i.e.,* $\Delta C'_{IDC}$ and $\Delta G'_{IDC}$). Uncertainty in device dimensions and properties can be propagated from simulation as described above for the CPWs, and included when mapping the results to the relative permittivity.

Appendix C

Detailed description of device fabrication techniques

Precise microfabrication of the IDC and CPW measurement devices is requisite for our broadband characterization technique. This appendix describes our typical microfabrication processes for calibration wafers and test chips. Here, we define wafers as round substrates, typically greater than 50 mm in diameter, and chips as rectangular substrates, typically 10 mm by 10 mm. Substrate thicknesses range from 0.3 mm to 1.5 mm. Fabrication on wafers is slightly easier than fabrication on chips, as processing is more automated for wafers and edge bead non-uniformity is less of a concern. Wafers can be diced into chips after fabrication.

Processing steps are identical for both wafers and chips, with a couple exceptions that are noted throughout this Appendix, and follow the general sequence described in Figure C.1 and illustrated in Figure C.2.

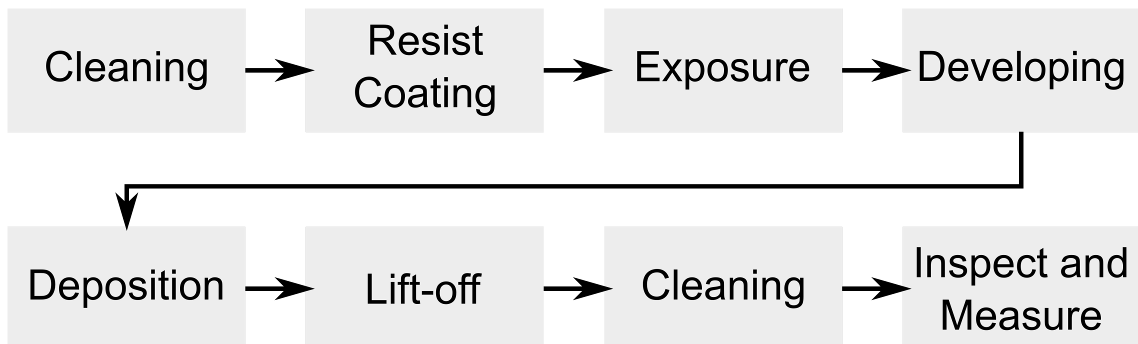

Figure C.1. The general process flow sequence for lift-off fabrication of devices on chips and wafers.

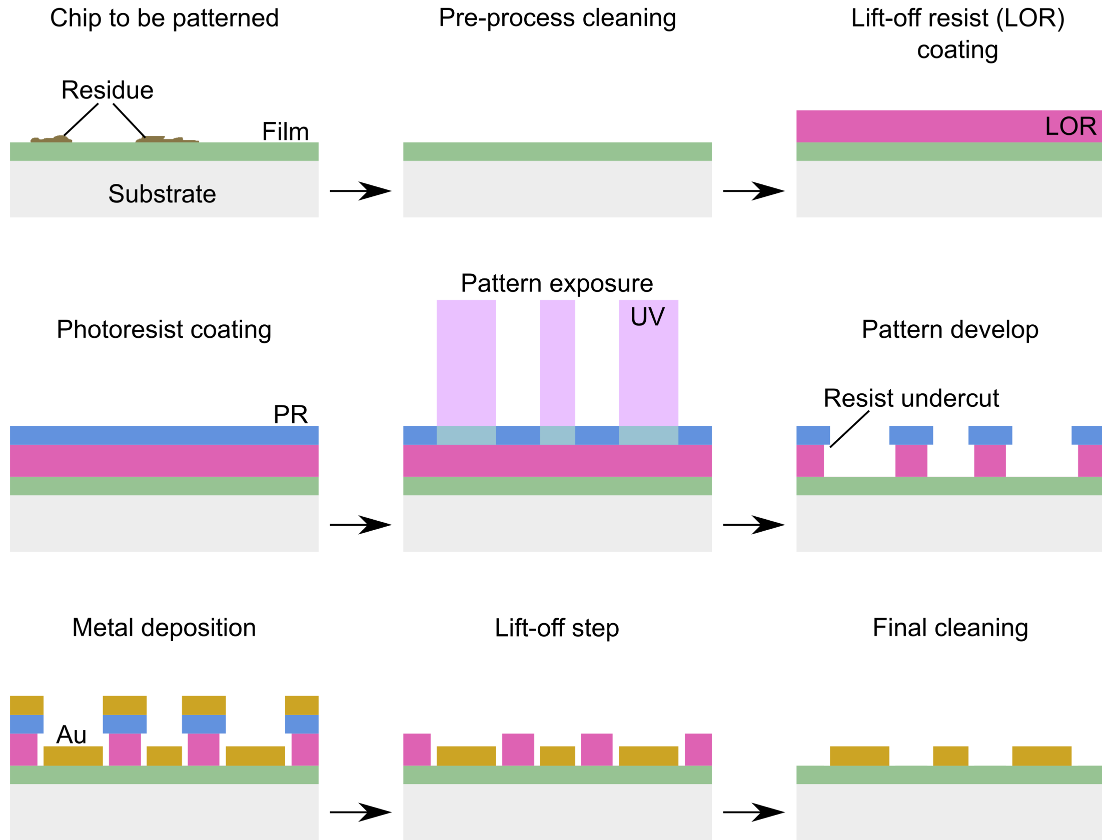

Figure C.2. An illustration of the key steps in our device fabrication process.

C.1 Cleaning

After receiving chips or wafers to study, we bring them into the NIST Boulder Microfabrication Facility, a 1700 m^2 Class 100 cleanroom. Our first step is to inspect the materials with optical microscopy to verify their condition. We then perform an initial cleaning routine to remove any organic residues or particulate matter that may have contaminated the chips (for simplicity, we use chips from now on to mean both chips and wafers, unless noted otherwise) during transit. The cleaning process consists of sonication in acetone for 5 minutes, followed by sonication in isopropanol for 5 minutes. Wafers are then rinsed with water in a spin-rinse-dryer, while chips

are simply dried with nitrogen gas. Typically, this process is sufficient to remove any unwanted matter, but not always. If additional cleaning is needed, we first sonicate for additional time at higher power. If additional residue remains, we then soak and sonicate the chips in 80 °C *n*-methyl-2-pyrrolidone (NMP) solvent. As a very last resort to remove significant organic residues, we will treat the chips with NanoStrip, a buffered piranha etch solution (H_2SO_4 + H_2O_2). This step is rarely required and could damage sensitive films. Finally, all chips or wafers are cleaned with a 60 W O_2 plasma for five minutes immediately before resist coating.

C.2 Resist coating

After cleaning, we coat the chips with the resist layers via spin coating. We first spin on the lift-off resist (LOR) layer which is not photo-sensitive, but rather acts as a spacer that prevents metal from depositing on the sidewalls of the pattern. To properly perform this function, the LOR layer should be at 2 to 5 times thicker than the desired metal layer thickness. The LOR layer thickness primarily depends on two factors: resist viscosity and spin speed. We primarily use two types of LOR resist, LOR 5A (less viscous) and LOR 10A (more viscous). The supplier suggests spin conditions (Figure C.3) to obtain a certain layer thickness. Unfortunately, working with small chips requires a trade-off. Thicker metal layers (>500 nm) may provide more consistent contact over a large number of probe landings, but this necessitates the use of the more viscous LOR 10A resist, and slower spin speeds ($\sim$ 2000 rpm). This unfortunately produces a larger edge bead region that can exceed 1 mm in

width on all edges of the chip. For a 10 mm square chip, this significantly reduces the area available for devices. For thin metal layers, fast spins with LOR 5A provide more patternable area, and anecdotally, more consistent coating. Due to the larger overall area, this is not typically an issue when patterning devices on wafers.

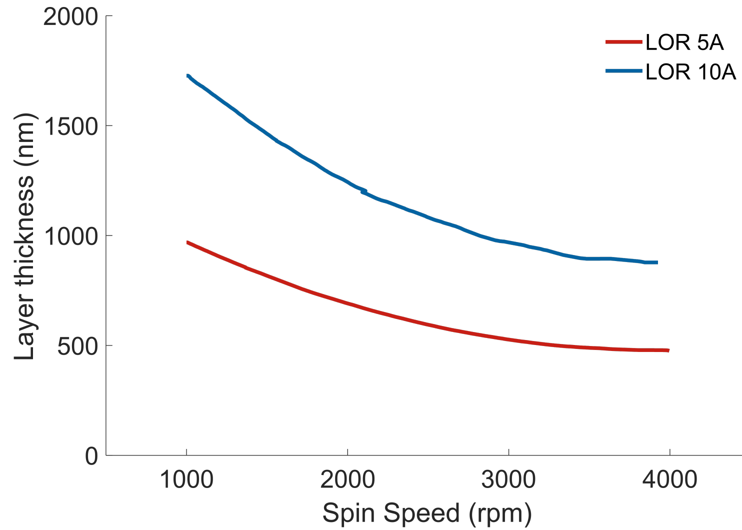

Figure C.3. Spin curves for the LOR 5A and LOR 10A resists.

Once the LOR layer has been deposited, we inspect the resist for defects, clean any excess resist from the back of the chips, and bake them on a hotplate at 170 °C for 5 minutes. The bake conditions control the etch rate of the LOR layer during the develop step. The stated conditions produce an approximate etch rate of $15\,\mathrm{nm\,s^{-1}}$.

After baking, we coat a second resist layer on top of the LOR layer. This layer is a positive photoresist, SPR660L, typically spun on at 3200 rpm for 60 seconds, to produce a layer approximately 1 µm thick. After inspecting for defects, we bake the chip for 60 seconds at 90 °C, to remove excess solvent from the resist.

If there are any defects in either of the resist layers, we must strip the resists with acetone and hot NMP, and begin the process again from the initial cleaning

step.

C.3 Exposure

All wafers and chips that are 10 mm by 10 mm or larger are exposed using a Heidelberg MLA150 mask-less aligner, which is a direct-write lithography tool. Smaller or oddly-shaped chips are exposed using a traditional photomask and mask aligner (Karl Süss MA6). The circuit patterns are generated in a CAD software (Xic, KLayout) and transferred directly to the MLA150 tool. Chips are loaded and exposed one at a time. First, an automatic detection routine locates and finds the edges of the chip. An alignment procedure is then performed if there are alignment crosses patterned on the sample (*i.e.,* if this is not the first layer). Once the alignment has been verified, the laser rasters over the sample to expose the pattern. A focus-dose test should be performed to determine the optimal settings for the laser (405 nm), which can depend on the properties of the substrate and film materials.

The SPR660L resist requires a post-exposure bake at 110 °C for 60 seconds before developing the patterns.

C.4 Developing

The patterns are developed by soaking the chips in a tetramethylammonium hydroxide (TMAH) solution, which dissolves the exposed areas of the SPR660L and the underlying LOR resist. For most develops, we use an auto-develop station, which coats the chip with the TMAH solution, rinses the TMAH solution off with

water after a set amount of develop time, and then dries the chip. Typically, we use a 40 second + 40 second double-puddle develop. That is, the TMAH solution is applied, and allowed to dissolve the resist for 40 seconds before being rinsed away, and then fresh developer is applied for an additional 40 seconds before a final rinse. The application of fresh TMAH solution results in a more consistent develop rate.

It takes roughly 40 seconds for the developer solution to clear through the SPR660L layer, and another 40 seconds to clear the LOR down to the substrate and create an approximately 0.5 µm undercut. Undercut is the distance that the top resist layer overhangs the LOR layer (see Figure C.2). Without sufficient undercut, metal will deposit on the sidewalls of the LOR layer, leaving "lift-off spikes" on the edges of the metal and negatively affecting the devices. In general, wafers develop in a more consistent fashion than chips. This is likely due to the fact that the resist layers on chips may be less uniform, and the baking processes may be less consistent for chips (*e.g.,* placement on hot plate). If additional develop time is required it is added in shorter intervals (5 to 10 seconds). Patterns are fully inspected before metal deposition.

C.5 Deposition

Metal layers are deposited by e-beam evaporation. In this process, a focused electron beam bombards a source metal target, causing evaporation of the metal atoms. Eventually the gaseous metal atoms precipitate on the surface of the chip to grow a thin metal film. E-beam evaporation is a highly directional deposition

technique, making it well-suited to lift-off.

Wafers can be loaded directly into the evaporation tool, but chips must first be affixed with wax to a carrier wafer and then loaded in the tool. The process chamber is first pumped to $< 1 \times 10^{-6}$ Torr, then back-filled with O_2 for a short RF plasma surface cleaning to promote adhesion of the metal layers. After cleaning, the chamber is again pumped down to $< 1 \times 10^{-6}$ Torr before metal deposition. We generally deposit either Ti, Au, or PdAu. Ti is an adhesion layer that we deposit before depositing other metals, Au is our metal of choice as a general conductor layer, and PdAu is a resistor layer for certain calibration standards. For a resistor layer, we deposit 1.2 nm of Ti, followed by 7 to 12 nm of PdAu, depending on the desired resistance. For a conductor layer, we deposit 6 to 10 nm of Ti followed by 250 to 500 nm of Au. The maximum Au thickness depends on the thickness of the LOR layer as discussed above.

C.6 Lift-off

After the metals have been deposited, we perform the lift-off procedure. First, if chips are mounted on a carrier wafer with wax, we remove them from the carrier wafer. Then, the wafer or chips are put in a beaker with 100 mL of acetone to soak and dissolve the SPR660L layer, carrying away the excess metal that was deposited on this resist. The beaker can either be put in a sonicator on very low power, or left to soak for several hours. Sonication under too high power can pulverise the metal into a fine powder. In general, it is best to have the metals release from the

surface as large flakes which are less likely to re-deposit on the chip surface. Once it appears that all of the excess metal has lifted off the chips, they are rinsed and transferred to another beaker with 100 mL of clean acetone and gently sonicated to ensure there are no remaining metal flakes on the chips. At this point, the LOR layer is still intact to protect the chip surface, but can be removed now that the excess metal is gone. The LOR layer is removed by soaking in 100 mL of NMP at 80 °C, and the chips are cleaned one final time, as described in Section C.1.

C.7 Inspection and measurement

At this point all of the devices have been patterned. We do a final inspection with the optical microscope to check for any defects in the devices like scratches or holes. We also measure a selection of device dimensions at 100× magnification to determine the actual dimensions and the uncertainty those dimensions. These dimensions are critical inputs for the simulations which we perform during the analysis of our broadband permittivity measurements. We also scan several of the devices with a contact profilometer to determine the thickness of our metal layers. Once this is complete, the chips are ready to be brought out of the clean room for experiments.

Bibliography

[1] J. Valasek. “Piezo-Electric and Allied Phenomena in Rochelle Salt”. In: *Physical Review* 17.4 (1921), pp. 475–481. DOI: 10.1103/physrev.17.475.

[2] A. von Hippel et al. “High dielectric constant ceramics”. In: *Industrial Engineering Chemistry* 38.11 (1946), pp. 1097–1109. DOI: 10.1021/ie50443a009.

[3] B Wul and JM Goldman. “Ferroelectric switching in $BaTiO_3$ ceramics”. In: *CR Acad Sci URSS* 51 (1946), p. 21.

[4] Gene H. Haertling. “Ferroelectric Ceramics: History and Technology”. In: *Journal of the American Ceramic Society* 82.4 (1999), pp. 797–818. DOI: 10.1111/j.1151-2916.1999.tb01840.x.

[5] A. F. Devonshire. “XCVI. Theory of barium titanate - Part I”. In: *The London, Edinburgh, and Dublin Philosophical Magazine and Journal of Science* 40.309 (1949), pp. 1040–1063. DOI: 10.1080/14786444908561372.

[6] A. F. Devonshire. “CIX. Theory of barium titanate, Part II”. In: *The London, Edinburgh, and Dublin Philosophical Magazine and Journal of Science* 42.333 (1951), pp. 1065–1079. DOI: 10.1080/14786445108561354.

[7] A. F. Devonshire. “Theory of ferroelectrics”. In: *Advances in Physics* 3.10 (1954), pp. 85–130. DOI: 10.1080/00018735400101173.

[8] J. C. Slater. “Theory of the Transition in KH2PO4”. In: *Journal of Chemical Physics* 9.1 (1941), p. 16. DOI: 10.1063/1.1750821.

[9] Malcolm E Lines and Alastair M Glass. *Principles and applications of ferroelectrics and related materials*. Oxford university press, 2001. ISBN: 019850778X.

[10] H. Jaffe and D. A. Berlincourt. “Piezoelectric transducer materials”. In: *Proceedings of the IEEE* 53.10 (1965), pp. 1372–1386. DOI: 10.1109/proc.1965.4253.

[11] G. W. McMahon. “Performance of Open Ferroelectric Ceramic Cylinders in Underwater Transducers”. In: *The Journal of the Acoustical Society of America* 36.3 (1964), pp. 528–533. DOI: 10.1121/1.1918994.

[12] A. M. Glass. “Investigation of the Electrical Properties of $Sr_{1`x}Ba_xNb_2O_6$ with Special Reference to Pyroelectric Detection”. In: *Journal of Applied Physics* 40.12 (1969), pp. 4699–4713. DOI: 10.1063/1.1657277.

[13] JM Herbert. *Ferroelectric transducers and sensors*. Vol. 3. CRC Press, 1982. ISBN: 0677059108.

[14] Kenji Uchino. *Ferroelectric Devices 2nd Edition*. CRC Press, Inc., 2009, p. 367. ISBN: 1439803757, 9781439803752.

[15] M. DiDomenico, D. A. Johnson, and R. H. Pantell. “Ferroelectric Harmonic Generator and the Large Signal Microwave Characteristics of a Ferroelectric Ceramic”. In: *Journal of Applied Physics* 33.5 (1962), pp. 1697–1706. DOI: 10.1063/1.1728812.

[16] M. J. Lancaster, J. Powell, and A. Porch. “Thin-film ferroelectric microwave devices”. In: *Superconductor Science and Technology* 11.11 (1998), pp. 1323–1334. DOI: 10.1088/0953-2048/11/11/021.

[17] Yoshihiro Arimoto and Hiroshi Ishiwara. “Current Status of Ferroelectric Random-Access Memory”. In: *MRS Bulletin* 29.11 (2011), pp. 823–828. DOI: 10.1557/mrs2004.235.

[18] Orlando Auciello, James F Scott, and Ramamoorthy Ramesh. “The physics of ferroelectric memories”. In: *Physics today* 51.7 (1998), pp. 22–27.

[19] J. T. Evans and R. Womack. “An experimental 512-bit nonvolatile memory with ferroelectric storage cell”. In: *IEEE Journal of Solid-State Circuits* 23.5 (1988), pp. 1171–1175. DOI: 10.1109/4.5940.

[20] H. Chang et al. “Combinatorial synthesis and high throughput evaluation of ferroelectric/dielectric thin-film libraries for microwave applications”. In: *Applied Physics Letters* 72.17 (1998), pp. 2185–2187. DOI: 10.1063/1.121316.

[21] P. C. Joshi and M. W. Cole. “Mg-doped $Ba_{0.6}Sr_{0.4}TiO_3$ thin films for tunable microwave applications”. In: *Applied Physics Letters* 77.2 (2000), pp. 289–291. DOI: 10.1063/1.126953.

[22] A. Kozyrev et al. “Nonlinear response and power handling capability of ferroelectric $Ba_xSr_{1`x}TiO_3$ film capacitors and tunable microwave devices”. In: *Journal of Applied Physics* 88.9 (2000), pp. 5334–5342. DOI: 10.1063/1.1314327.

[23] A. Tombak et al. “Voltage-controlled RF filters employing thin-film barium-strontium-titanate tunable capacitors”. In: *IEEE Transactions on Microwave Theory and Techniques* 51.2 (2003), pp. 462–467. DOI: 10.1109/tmtt.2002.807822.

[24] Ali Tombak. “A Ferroelectric-Capacitor-Based Tunable Matching Network for Quad-Band Cellular Power Amplifiers”. In: *IEEE Transactions on Microwave Theory and Techniques* 55.2 (2007), pp. 370–375. DOI: 10.1109/tmtt.2006.889349.

[25] O. G. Vendik, S. P. Zubko, and M. A. NikolSki. “Microwave loss-factor of $Ba_xSr_{1-x}TiO_3$ as a function of temperature, biasing field, barium concentration, and frequency”. In: 92.12 (2002), p. 7448. DOI: 10.1063/1.1524314.

[26] X.X. Xi et al. “Oxide Thin Films for Tunable Microwave Devices”. In: *Journal of Electroceramics* 4.2 (2000), pp. 393–405. DOI: 10.1023/a:1009903802688.

[27] A. K. Tagantsev et al. “Ferroelectric Materials for Microwave Tunable Applications”. In: *Journal of Electroceramics* 11.1/2 (2003), pp. 5–66. DOI: 10.1023/b:jecr.0000015661.81386.e6.

[28] N. Setter et al. “Ferroelectric thin films: Review of materials, properties, and applications”. In: *Journal of Applied Physics* 100.5 (2006), p. 051606. DOI: 10.1063/1.2336999.

[29] P. Bao et al. “Barium strontium titanate thin film varactors for room-temperature microwave device applications”. In: *Journal of Physics D: Applied Physics* 41.6 (2008), p. 063001. DOI: 10.1088/0022-3727/41/6/063001.

[30] Spartak Gevorgian. *Ferroelectrics in microwave devices, circuits and systems: physics, modeling, fabrication and measurements.* Springer Science Business Media, 2009. ISBN: 1848825072.

[31] L. B. Kong et al. “Electrically tunable dielectric materials and strategies to improve their performances”. In: *Progress in Materials Science* 55.8 (2010), pp. 840–893. DOI: 10.1016/j.pmatsci.2010.04.004.

[32] Guru Subramanyam et al. “Challenges and opportunities for multi-functional oxide thin films for voltage tunable radio frequency/microwave components”. In: *Journal of Applied Physics* 114.19 (2013), p. 191301. DOI: 10.1063/1.4827019.

[33] Mailadil T Sebastian, Rick Ubic, and Heli Jantunen. *Microwave materials and applications.* John Wiley Sons, 2017. ISBN: 1119208564.

[34] Cheng-Xiang Wang et al. “Cellular architecture and key technologies for 5G wireless communication networks”. In: *IEEE communications magazine* 52.2 (2014), pp. 122–130.

[35] Bob Witte. *FCC 5G Spectrum Allocation Demands 3 Breakthrough Innovations.* Keysight Technologies, Inc. 2016.

[36] David B. Cruickshank Michael D. Hill. “Ceramic materials for 5G wireless communication systems”. In: *American Ceramic Society Bulletin* 98.6 (2019).

[37] Jason R. Hattrick-Simpers, John M. Gregoire, and A. Gilad Kusne. “Perspective: Composition–structure–property mapping in high-throughput experiments: Turning data into knowledge”. In: *APL Materials* 4.5 (2016), p. 053211. DOI: 10.1063/1.4950995.

[38] Ramamoorthy Ramesh and Darrell G. Schlom. “Creating emergent phenomena in oxide superlattices”. In: *Nature Reviews Materials* 4.4 (2019), pp. 257–268. DOI: 10.1038/s41578-019-0095-2.

[39] Ma Zhengxiang et al. “RF measurement technique for characterizing thin dielectric films”. In: *IEEE Transactions on Electron Devices* 45.8 (1998), pp. 1811–1816. DOI: 10.1109/16.704383.

[40] Par Rundqvist et al. “Non-Destructive Microwave Characterization of Ferroelectric Films on Conductive Substrates”. In: *Integrated Ferroelectrics* 60.1 (2004), pp. 1–19. DOI: 10.1080/10584580490440828.

[41] M. Ouaddari et al. “Microwave characterization of ferroelectric thin-film materials”. In: *IEEE Transactions on Microwave Theory and Techniques* 53.4 (2005), pp. 1390–1397. DOI: 10.1109/TMTT.2005.845759.

[42] James Baker-Jarvis, Michael D. Janezic, and Donald C. DeGroot. "High-frequency dielectric measurements". In: *IEEE Instrumentation Measurement Magazine* 13.2 (2010).

[43] D. J. Barker et al. "Uncertainties in the permittivity of thin films extracted from measurements with near field microwave microscopy calibrated by an image charge model". In: *Measurement Science and Technology* 25.10 (2014), p. 105601.

[44] S. S. Gevorgian and E. L. Kollberg. "Do we really need ferroelectrics in paraelectric phase only in electrically controlled microwave devices?" In: *IEEE Transactions on Microwave Theory and Techniques* 49.11 (2001), pp. 2117–2124. DOI: 10.1109/22.963146.

[45] G. H. Jonker and J. H. Van Santen. "Properties of Barium Titanate in Connection with Its Crystal Structure". In: *Science* 109.2843 (1949), pp. 632–635.

[46] Cedric J. G. Meyers et al. "(Ba,Sr)TiO_3 tunable capacitors with RF commutation quality factors exceeding 6000". In: *Applied Physics Letters* 109.11 (2016), p. 112902. DOI: 10.1063/1.4961626.

[47] Zongquan Gu et al. "Resonant domain-wall-enhanced tunable microwave ferroelectrics". In: *Nature* 560.7720 (2018), pp. 622–627. DOI: 10.1038/s41586-018-0434-2.

[48] V. L. Gurevich and A. K. Tagantsev. "Intrinsic dielectric loss in crystals". In: *Advances in Physics* 40.6 (1991), pp. 719–767. DOI: 10.1080/00018739100101552.

[49] AK Tagantsev. "Low-frequency dielectric relaxation in centrosymmetric crystals". In: *Zh. Eksp. Teor. Fiz* 53 (1981), pp. 1087–1098.

[50] K. R. Subbaswamy and D. L. Mills. "Theory of microwave absorption in wide-band-gap insulators: The role of thermal phonon lifetimes". In: *Physical Review B* 33.6 (1986), pp. 4213–4220. DOI: 10.1103/PhysRevB.33.4213.

[51] AK Tagantsev. "Dielectric losses in displacive ferroelectrics". In: *Journal of Experimental and Theoretical Physics* 86 (1984), p. 2215.

[52] A.K. Tagantsev. "Effect of a weak electric field on the dielectric losses in centrosymmetric ferroelectrics of the displacement type". In: *Soviet Physics* 50.5 (1979), pp. 948–955.

[53] Alexander Tagantsev. "DC-electric-field-induced microwave loss in ferroelectrics and intrinsic limitation for the quality factor of a tunable component". In: *Applied Physics Letters* 76.9 (2000), pp. 1182–1184. DOI: 10.1063/1.125976.

[54] K. F. Astafiev, A. K. Tagantsev, and N. Setter. "Quasi-Debye microwave loss as an intrinsic limitation of microwave performance of tunable components based on $SrTiO_3$ and $Ba_xSr_{1`x}TiO_3$ ferroelectrics". In: *Journal of Applied Physics* 97.1 (2005), p. 014106. DOI: 10.1063/1.1829149.

[55] Alexander K. Tagantsev and Konstantin F. Astafiev. "Quasi-Debye microwave loss in perovskite ferroelectrics". In: *Integrated Ferroelectrics* 39.1-4 (2001), pp. 251–260. DOI: 10.1080/10584580108011948.

[56] RA Cowley and GJ Coombs. "Paraelectric, piezoelectric and pyroelectric crystals: II Phase transitions". In: *Journal of Physics C: Solid State Physics* 6.1 (1973), p. 143.

[57] Orest G. Vendik and Leon T. Ter-Martirosyan. "Influence of charged defects on the dielectric response of incipient ferroelectrics". In: *Journal of Applied Physics* 87.3 (2000), pp. 1435–1439. DOI: 10.1063/1.372031.

[58] Ernst Schlomann. "Dielectric Losses in Ionic Crystals with Disordered Charge Distributions". In: *Physical Review* 135.2A (1964), A413–A419. DOI: 10.1103/physrev.135.a413.

[59] A. Vorobiev et al. "Microwave loss mechanisms in $Ba_{0.25}Sr_{0.75}TiO_3$ thin film varactors". In: *Journal of Applied Physics* 96.8 (2004), pp. 4642–4649. DOI: 10.1063/1.1789631.

[60] C. Elissalde and J. Ravez. "Ferroelectric ceramics: defects and dielectric relaxations". In: *Journal of Materials Chemistry* 11.8 (2001), pp. 1957–1967. DOI: 10.1039/b010117f.

[61] Roger A. De Souza. "The formation of equilibrium space-charge zones at grain boundaries in the perovskite oxide $SrTiO_3$". In: *Physical Chemistry Chemical Physics* 11.43 (2009), p. 9939. DOI: 10.1039/b904100a.

[62] Da Yu Wang and Kazumasa Umeya. "Spontaneous Polarization Screening Effect and Trap-State Density at Grain Boundaries of Semiconducting Barium Titanate Ceramics". In: *Journal of the American Ceramic Society* 74.2 (1991), pp. 280–286. DOI: 10.1111/j.1151-2916.1991.tb06875.x.

[63] Hong-Cheng Li et al. "Thickness dependence of dielectric loss in $SrTiO_3$ thin films". In: *Applied Physics Letters* 73.4 (1998), pp. 464–466. DOI: 10.1063/1.121901.

[64] Che-Hui Lee et al. "Exploiting dimensionality and defect mitigation to create tunable microwave dielectrics". In: *Nature* 502.7472 (2013), p. 532.

[65] G. Arlt. "The role of domain walls on the dielectric, elastic and piezoelectric properties of ferroelectric ceramics". In: *Ferroelectrics* 76.1 (1987), pp. 451–458. DOI: 10.1080/00150198708016967.

[66] L. Eric Cross. "Relaxor ferroelectrics". In: *Ferroelectrics* 76.1 (1987), pp. 241–267. DOI: 10.1080/00150198708016945.

[67] Takashi Teranishi, Takuya Hoshina, and Takaaki Tsurumi. "Wide range dielectric spectroscopy on perovskite dielectrics". In: *Materials Science and Engineering: B* 161.1 (2009), pp. 55–60. DOI: https://doi.org/10.1016/j.mseb.2008.11.039.

[68] James C. Booth, Ichiro Takeuchi, and Kao-Shuo Chang. "Microwave-frequency loss and dispersion in ferroelectric $Ba_{0.3}Sr_{0.7}TiO_3$ thin films". In: *Applied Physics Letters* 87.8 (2005), p. 082908. DOI: 10.1063/1.2033139.

[69] Xiao-Yu Zhang et al. "Ferroelectric $Ba_xSr_{1-x}TiO_3$ thin-film varactors with parallel plate and interdigital electrodes for microwave applications". In: *Journal of Applied Physics* 104.12 (2008), p. 124110. DOI: 10.1063/1.3053424.

[70] M. Al Ahmad et al. "Wide-Tunable Low-Field Interdigitated Barium Strontium Titanate Capacitors". In: *IEEE Microwave and Wireless Components Letters* 17.11 (2007), pp. 769–771. DOI: 10.1109/lmwc.2007.908044.

[71] *Cisco Visual Networking Index: Global Mobile Data Traffic Forecast Update 2017 to 2022*. Cisco white paper, 2019. URL: https://www.cisco.com/c/en/us/solutions/collateral/service-provider/visual-networking-index-vni/white-paper-c11-738429.pdf.

[72] Maria Rita Palattella et al. "Internet of Things in the 5G Era: Enablers, Architecture, and Business Models". In: *IEEE Journal on Selected Areas in Communications* 34.3 (2016), pp. 510–527. DOI: 10.1109/jsac.2016.2525418.

[73] T. S. Rappaport et al. "Millimeter Wave Mobile Communications for 5G Cellular: It Will Work!" In: *IEEE Access* 1 (2013), pp. 335–349. DOI: 10.1109/access.2013.2260813.

[74] R. Aigner et al. *RF-Filters in mobile phone applications*. 12th International Conference on Solid State Sensors, Actuators, and Microsystems. 2003.

[75] Rich Ruby. "A Snapshot in Time: The Future in Filters for Cell Phones". In: *IEEE Microwave Magazine* 16.7 (2015), pp. 46–59. DOI: 10.1109/mmm.2015.2429513.

[76] Spartak Gevorgian. "Agile microwave devices". In: *IEEE Microwave Magazine* 10.5 (2009), pp. 93–98. DOI: 10.1109/mmm.2009.932830.

[77] E. E. Altshuler and R. A. Marr. "A comparison of experimental and theoretical values of atmospheric absorption at the longer millimeter wavelengths". In: *IEEE Transactions on Antennas and Propagation* 36.10 (1988), pp. 1471–1480. DOI: 10.1109/8.8635.

[78] Hong Wonbin et al. "Study and prototyping of practically large-scale mmWave antenna systems for 5G cellular devices". In: *IEEE Communications Magazine* 52.9 (2014), pp. 63–69. DOI: 10.1109/mcom.2014.6894454.

[79] A. Mahmud et al. "A 1-GHz active phase shifter with a ferroelectric varactor". In: *IEEE Microwave and Wireless Components Letters* 16.5 (2006), pp. 261–263. DOI: 10.1109/lmwc.2006.873529.

[80] C. K. Ong and P. Wang. *Microwave tunable devices based on patterned ferroelectric thin film*. 17th IEEE-ISAF. Santa Fe, NM: IEEE, 2008. DOI: 10.1109/isaf.2008.4693754.

[81] T. S. Kalkur et al. "Tunable RF Filters Fabricated Using MOCVD Deposited Graded Composition BST Films". In: *Integrated Ferroelectrics* 126.1 (2011), pp. 28–33. DOI: 10.1080/10584587.2011.574978.

[82] Hai Jiang et al. "Miniaturized and Reconfigurable CPW Square-Ring Slot Antenna Loaded With Ferroelectric BST Thin Film Varactors". In: *IEEE Transactions on Antennas and Propagation* 60.7 (2012), pp. 3111–3119. DOI: 10.1109/tap.2012.2196918.

[83] Rosa De Paolis et al. "High-Tunability and High Q-Factor Integrated Ferroelectric Circuits up to Millimeter Waves". In: *IEEE Transactions on Microwave Theory and Techniques* 63.8 (2015), pp. 2570–2578. DOI: 10.1109/tmtt.2015.2441073.

[84] C. Hogan. "The low-frequency problem in the design of microwave gyrators and associated elements". In: *IRE Transactions on Antennas and Propagation* 4.3 (1956), pp. 495–501. DOI: 10.1109/tap.1956.1144430.

[85] Holger Maune et al. "Nonlinear ceramics for tunable microwave devices". In: *Microsystem Technologies* 17.2 (2011), pp. 213–224. DOI: 10.1007/s00542-011-1235-9.

[86] M. D. Janezic and J. Baker-Jarvis. "Full-wave analysis of a split-cylinder resonator for nondestructive permittivity measurements". In: *IEEE Transactions on Microwave Theory and Techniques* 47.10 (1999), pp. 2014–2020. DOI: 10.1109/22.795077.

[87] Chen Gao et al. "High spatial resolution quantitative microwave impedance microscopy by a scanning tip microwave near-field microscope". In: *Applied Physics Letters* 71.13 (1997), p. 1872. DOI: 10.1063/1.120444.

[88] Stanislaw S. Stuchly, Maria A. Rzepecka, and Magdy F. Iskander. "Permittivity Measurements at Microwave Frequencies Using Lumped Elements". In: *IEEE Transactions on Instrumentation and Measurement* 23.1 (1974), pp. 56–62. DOI: 10.1109/tim.1974.4314218.

[89] M. D. Janezic et al. "Permittivity characterization of low-k thin films from transmission-line measurements". In: *IEEE Transactions on Microwave Theory and Techniques* 51.1 (2003), pp. 132–136. DOI: 10.1109/TMTT.2002.806925.

[90] Andrew K. Jonscher. "Dielectric relaxation in solids". In: *Journal of Physics D: Applied Physics* 32.14 (1999), R57–R70. DOI: 10.1088/0022-3727/32/14/201.

[91] X. D. Xiang and C. Gao. "Quantitative complex electrical impedance microscopy by scanning evanescent microwave microscope". In: *Materials Characterization* 48.2-3 (2002), pp. 117–125. DOI: 10.1016/s1044-5803(02)00277-2.

[92] D. E. Steinhauer et al. "Surface resistance imaging with a scanning near-field microwave microscope". In: *Applied Physics Letters* 71.12 (1997), pp. 1736–1738. DOI: 10.1063/1.120020.

[93] P. De Wolf, E. Brazel, and A. Erickson. "Electrical characterization of semiconductor materials and devices using scanning probe microscopy". In: *Materials Science in Semiconductor Processing* 4.1-3 (2001), pp. 71–76. DOI: 10.1016/s1369-8001(00)00174-8.

[94] Alexander Tselev et al. "Near-field microwave scanning probe imaging of conductivity inhomogeneities in CVD graphene". In: *Nanotechnology* 23.38 (2012), p. 385706.

[95] Gao Chen et al. "Quantitative scanning evanescent microwave microscopy and its applications in characterization of functional materials libraries". In: *Measurement Science and Technology* 16.1 (2005), p. 248.

[96] Alexander Tselev et al. "Broadband dielectric microwave microscopy on micron length scales". In: *Review of Scientific Instruments* 78.4 (2007), p. 044701. DOI: 10.1063/1.2719613.

[97] C. P. Wen. "Coplanar Waveguide: A Surface Strip Transmission Line Suitable for Nonreciprocal Gyromagnetic Device Applications". In: *IEEE Transactions on Microwave Theory and Techniques* 17.12 (1969), pp. 1087–1090. DOI: 10.1109/tmtt.1969.1127105.

[98] Hewlett-Packard. *HP4284A Precision LCR Meter Operation Manual*. https://wiki.epfl.ch/carplat/documents/hp4284a_lcr_manual.pdf. 1998. URL: https://wiki.epfl.ch/carplat/documents/hp4284a_lcr_manual.pdf.

[99] Roger B. Marks and Dylan F. Williams. "A General Waveguide Circuit Theory". In: *Journal of Research of the National Institute of Standards and Technology* 97.5 (1992), pp. 533–562. DOI: 10.6028/jres.097.024.

[100] John R Brews. "Transmission line models for lossy waveguide interconnections in VLSI". In: *IEEE Transactions on Electron Devices* 33.9 (1986), pp. 1356–1365.

[101] Oliver Heaviside. *Electrical Papers*. Vol. II. London: The Electrician, 1892.

[102] Roger B Marks and Dylan F Williams. "Characteristic impedance determination using propagation constant measurement". In: *IEEE Microwave and Guided Wave Letters* 1.6 (1991), pp. 141–143.

[103] Dylan F Williams, Uwe Arz, and Hartmut Grabinski. "Characteristic-impedance measurement error on lossy substrates". In: *IEEE Microwave and Wireless Components Letters* 11.7 (2001), pp. 299–301.

[104] R. B. Marks. "A multiline method of network analyzer calibration". In: *IEEE Transactions on Microwave Theory and Techniques* 39.7 (1991), pp. 1205–1215. DOI: 10.1109/22.85388.

[105] Roger B. Marks. “Formulations of the Basic Vector Network Analyzer Error Model including Switch-Terms”. In: *50th ARFTG Conference Digest*. IEEE, 1997, pp. 115–126. DOI: 10.1109/arftg.1997.327265.

[106] Dylan F. Williams and David K. Walker. “Series-Resistor Calibration”. In: *50th ARFTG Conference Digest*, pp. 131–137. DOI: 10.1109/arftg.1997.327267.

[107] Nathan D. Orloff et al. “A Compact Variable-Temperature Broadband Series-Resistor Calibration”. In: *IEEE Transactions on Microwave Theory and Techniques* 59.1 (2011), pp. 188–195. DOI: 10.1109/tmtt.2010.2091200.

[108] D. F. Williams, C. M. Wang, and U. Arz. “An optimal multiline TRL calibration algorithm”. In: *IEEE MTT-S International Microwave Symposium Digest*. Vol. 3. 2003, pp. 1819–1822. DOI: 10.1109/MWSYM.2003.1210494.

[109] D. C. DeGroot, J. A. Jargon, and R. B. Marks. “Multiline TRL revealed”. In: *60th ARFTG Conference Digest, Fall 2002*. Pp. 131–155. DOI: 10.1109/ARFTGF.2002.1218696.

[110] NIST. *On-wafer Calibration Software, https://www.nist.gov/services-resources/software/wafer-calibration-software*. Web Page. 2019. URL: https://www.nist.gov/services-resources/software/wafer-calibration-software.

[111] James C. Booth et al. “Quantitative Permittivity Measurements of Nanoliter Liquid Volumes in Microfluidic Channels to 40 GHz”. In: *IEEE Transactions on Instrumentation and Measurement* 59.12 (2010), pp. 3279–3288. DOI: 10.1109/tim.2010.2047141.

[112] BK-Precision. In: (), LCR Meter Guide, https://bkpmedia.s3.amazonaws.com/downloads/guides/en–us/lcr_meter_guide.pdf.

[113] Gregory Houzet et al. “Dispersion and loss of ferroelectric $Ba_{0.5}Sr_{0.5}TiO_3$ thin films up to 110 GHz”. In: *Applied Physics Letters* 93.5 (2008), p. 053507. DOI: 10.1063/1.2969469.

[114] E. Zschech et al. “Advanced MOSFET Gate Dielectrics for High-Performance Microprocessors: Materials Selection and Analytical Challenges”. In: *Advances in Solid State Physics*. Ed. by B. Kramer. Berlin, Heidelberg: Springer Berlin Heidelberg, 2006, pp. 375–389. ISBN: 978-3-540-32430-0. DOI: 10.1007/11423256_30.

[115] Eric J. Amis, Xiao-Dong Xiang, and Ji-Cheng Zhao. “Combinatorial Materials Science: What’s New Since Edison?” In: *MRS Bulletin* 27.4 (2011), pp. 295–300. DOI: 10.1557/mrs2002.96.

[116] National Science and Technology Council. *Materials genome initiative for global competitiveness*. Executive Office of the President, National Science and Technology Council, 2011.

[117] M. L. Green et al. “Fulfilling the promise of the materials genome initiative with high-throughput experimental methodologies”. In: *Applied Physics Reviews* 4.1 (2017), p. 011105. DOI: 10.1063/1.4977487.

[118] Robert York. “Tunable dielectrics for RF circuits”. In: *Multifunctional adaptive microwave circuits and systems* 1 (2009), pp. 159–207.

[119] X. D. Xiang et al. “A Combinatorial Approach to Materials Discovery”. In: *Science* 268.5218 (1995), pp. 1738–1740. DOI: 10.1126/science.268.5218.1738.

[120] Bobby G. Sumpter et al. “A bridge for accelerating materials by design”. In: *NPJ Computational Materials* 1 (2015), p. 15008. DOI: 10.1038/npjcompumats.2015.8.

[121] Tim Mueller, Aaron Gilad Kusne, and Rampi Ramprasad. “Machine learning in materials science: Recent progress and emerging applications”. In: *Reviews in Computational Chemistry* 29 (2016), pp. 186–273.

[122] Jingsong Wang et al. “Identification of a Blue Photoluminescent Composite Material from a Combinatorial Library”. In: *Science* 279.5357 (1998), pp. 1712–1714. DOI: 10.1126/science.279.5357.1712.

[123] Yuji Matsumoto et al. “Combinatorial investigation of spintronic materials”. In: *MRS bulletin* 28.10 (2003), pp. 734–739.

[124] S. Fujino et al. “Combinatorial discovery of a lead-free morphotropic phase boundary in a thin-film piezoelectric perovskite”. In: *Applied Physics Letters* 92.20 (2008), p. 202904. DOI: 10.1063/1.2931706.

[125] MA Al-Maghrabi et al. “Combinatorial studies of $Si_{1-x}O_x$ as a potential negative electrode material for Li-Ion battery applications”. In: *Journal of The Electrochemical Society* 160.9 (2013), A1587–A1593.

[126] M. A. Aronova et al. “Combinatorial libraries of semiconductor gas sensors as inorganic electronic noses”. In: *Applied Physics Letters* 83.6 (2003), pp. 1255–1257. DOI: 10.1063/1.1600822.

[127] Kevin R. Talley et al. “Implications of heterostructural alloying for enhanced piezoelectric performance of (Al,Sc)N”. In: *Physical Review Materials* 2.6 (2018). DOI: 10.1103/physrevmaterials.2.063802.

[128] J. M. Gregoire et al. “High-throughput synchrotron X-ray diffraction for combinatorial phase mapping”. In: *Journal of Synchrotron Radiation* 21 (2014). DOI: 10.1107/S1600577514016488.

[129] Aaron Gilad Kusne et al. “On-the-fly machine-learning for high-throughput experiments: search for rare-earth-free permanent magnets”. In: *Scientific Reports* 4 (2014), p. 6367. DOI: 10.1038/srep06367.

[130] H. Chang and Ichiro Takeuchi. “A low-loss composition region identified from a thin-film composition spread of $(Ba_{1-x-y}Sr_xCa_y)TiO_3$”. In: *Applied Physics Letters* 74.8 (1999), pp. 1165–1167. DOI: 10.1063/1.123475.

[131] K. S. Chang et al. "Multimode quantitative scanning microwave microscopy of in situ grown epitaxial $Ba_{1-x}Sr_xTiO_3$ composition spreads". In: *Applied Physics Letters* 79.26 (2001), pp. 4411–4413.

[132] Alexander N. Reznik and Vladimir V. Talanov. "Quantitative model for near-field scanning microwave microscopy: Application to metrology of thin film dielectrics". In: *Review of Scientific Instruments* 79.11 (2008), p. 113708. DOI: 10.1063/1.3020705.

[133] D. J. Barker et al. "Comparison of scanning evanescent microwave microscopy with co-planar waveguide methods of characterization of $Ba_{0.5}Sr_{0.5}TiO_3$ thin films". In: *18th IEEE ISAF*, pp. 1–6. DOI: 10.1109/ISAF.2009.5307571.

[134] Bi-Yi Wu et al. "Full-wave modeling of broadband near field scanning microwave microscopy". In: *Scientific Reports* 7.1 (2017). DOI: 10.1038/s41598-017-13937-5.

[135] L. Vegard. "Die Konstitution der Mischkristalle und die Raumfullung der Atome". In: *Zeitschrift fur Physik* 5.1 (1921), pp. 17–26. DOI: 10.1007/bf01349680.

[136] Michael J. Aziz. "Film growth mechanisms in pulsed laser deposition". In: *Applied Physics A* 93.3 (2008), pp. 579–587. DOI: 10.1007/s00339-008-4696-7.

[137] S. U. Adikary and H. L. W. Chan. "Ferroelectric and dielectric properties of sol–gel derived $Ba_xSr_{1`x}TiO_3$ thin films". In: *Thin Solid Films* 424.1 (2003), pp. 70–74. DOI: 10.1016/s0040-6090(02)00918-5.

[138] Y. Gim et al. "Microstructure and dielectric properties of $Ba_{1`x}Sr_xTiO_3$ films grown on $LaAlO_3$ substrates". In: *Applied Physics Letters* 77.8 (2000), pp. 1200–1202. DOI: 10.1063/1.1289272.

[139] B. H. Hoerman et al. "Dielectric properties of epitaxial $BaTiO_3$ thin films". In: *Applied Physics Letters* 73.16 (1998), p. 2248. DOI: 10.1063/1.121691.

[140] Robert C. Pullar et al. "Manufacture and measurement of combinatorial libraries of dielectric ceramics: Part II. Dielectric measurements of $Ba_{1`x}Sr_xTiO_3$ libraries". In: *Journal of the European Ceramic Society* 27.16 (2007), pp. 4437–4443. DOI: https://doi.org/10.1016/j.jeurceramsoc.2007.04.008.

[141] Takashi Teranishi et al. "Polarization behavior in diffuse phase transition of $Ba_xSr_{1`x}TiO_3$ ceramics". In: *Journal of Applied Physics* 105.5 (2009), p. 054111. DOI: 10.1063/1.3089250.

[142] Soma Chattopadhyay et al. "Size-induced diffuse phase transition in the nanocrystalline ferroelectric $PbTiO_3$". In: *Physical Review B: Condensed Matter* 52.18 (1995), pp. 13177–13183. DOI: 10.1103/physrevb.52.13177.

[143] T. M. Shaw et al. "The effect of stress on the dielectric properties of barium strontium titanate thin films". In: *Applied Physics Letters* 75.14 (1999), pp. 2129–2131. DOI: 10.1063/1.124939.

[144] RR Cole and KS Cole. “Dispersion and Absorption in Dielectrics I. Alternating Current Characteristics”. In: *J Chem Phys* 9 (1941), p. 341.

[145] Kenneth S Cole and Robert H Cole. “Dispersion and absorption in dielectrics II. Direct current characteristics”. In: *The Journal of Chemical Physics* 10.2 (1942), pp. 98–105.

[146] Peter Josef William Debye. *Polar molecules*. 1929.

[147] Hiroyuki Takenaka et al. “Slush-like polar structures in single-crystal relaxors”. In: *Nature* 546.7658 (2017), pp. 391–395. DOI: 10.1038/nature22068.

[148] S. H. Wemple, M. Didomenico, and I. Camlibel. “Dielectric and optical properties of melt-grown $BaTiO_3$”. In: *Journal of Physics and Chemistry of Solids* 29.10 (1968), pp. 1797–1803. DOI: 10.1016/0022-3697(68)90164-9.

[149] B. Panda et al. “Optical properties of RF sputtered strontium substituted barium titanate thin films”. In: *Thin Solid Films* 332.1-2 (1998), pp. 46–49. DOI: 10.1016/s0040-6090(98)01012-8.

[150] M. Riaziat, R. Majidi-Ahy, and I. J. Feng. “Propagation modes and dispersion characteristics of coplanar waveguides”. In: *IEEE Transactions on Microwave Theory and Techniques* 38.3 (1990), pp. 245–251. DOI: 10.1109/22.45333.

[151] Jeevaka Weerasinghe et al. “Emergence of central mode in the paraelectric phase of ferroelectric perovskites”. In: *MRS Communications* 3.1 (2013), pp. 41–45. DOI: 10.1557/mrc.2013.5.

[152] J. H. Haeni et al. “Epitaxial growth of the first five members of the $Sr_{n+1}Ti_nO_{3n+1}$ Ruddlesden–Popper homologous series”. In: *Applied Physics Letters* 78.21 (2001), pp. 3292–3294. DOI: 10.1063/1.1371788.

[153] Michael A. McCoy, Robin W. Grimes, and William E. Lee. “Phase stability and interfacial structures in the SrO–$SrTiO_3$ system”. In: *Philosophical Magazine A* 75.3 (1997), pp. 833–846. DOI: 10.1080/01418619708207205.

[154] Claudine Noguera. “Theoretical investigation of the Ruddlesden-Popper compounds $Sr_{n+1}Ti_nO_{3n+1}$ (n=1-3)”. In: *Philosophical Magazine Letters* 80.3 (2000), pp. 173–180. DOI: 10.1080/095008300176308.

[155] D. G. Schlom et al. “Oxide nano-engineering using MBE”. In: *Materials Science and Engineering B* 87.3 (2001), pp. 282–291. DOI: 10.1016/s0921-5107(01)00726-7.

[156] Darrell Schlom. “The Controlled Synthesis of Metastable Oxides Utilizing Epitaxy and Epitaxial Stabilization”. In: *Ferroelectric Thin Films*. Ed. by W. Tian et al. Vol. 655. Warrendale: Materials Research Society, 2003, pp. CC7.8.1–CC7.8.6.

[157] N. D. Orloff et al. “Broadband dielectric spectroscopy of Ruddlesden–Popper $Sr_{n+1}Ti_nO_{3n+1}$ (n=1,2,3) thin films”. In: *Applied Physics Letters* 94.4 (2009), p. 042908. DOI: 10.1063/1.3046792.

[158] S. N. Ruddlesden and P. Popper. “The compound $Sr_3Ti_2O_7$and its structure”. In: *Acta Crystallographica* 11.1 (1958), pp. 54–55. DOI: 10.1107/s0365110x58000128.

[159] Hiromoto Uwe and Tunetaro Sakudo. “Stress-induced ferroelectricity and soft phonon modes in $SrTiO_3$”. In: *Physical Review B* 13.1 (1976), pp. 271–286. DOI: 10.1103/physrevb.13.271.

[160] N. A. Pertsev, A. G. Zembilgotov, and A. K. Tagantsev. “Effect of Mechanical Boundary Conditions on Phase Diagrams of Epitaxial Ferroelectric Thin Films”. In: *Physical Review Letters* 80.9 (1998), pp. 1988–1991. DOI: 10.1103/physrevlett.80.1988.

[161] K. J. Choi et al. “Enhancement of Ferroelectricity in Strained $BaTiO_3$ Thin Films”. In: *Science* 306.5698 (2004), pp. 1005–1009. DOI: 10.1126/science.1103218.

[162] J. H. Haeni et al. “Room-temperature ferroelectricity in strained $SrTiO_3$”. In: *Nature* 430.7001 (2004), pp. 758–761. DOI: 10.1038/nature02773.

[163] Jonathan R. Petrie et al. “Strain Control of Oxygen Vacancies in Epitaxial Strontium Cobaltite Films”. In: *Advanced Functional Materials* 26.10 (2016), pp. 1564–1570. DOI: 10.1002/adfm.201504868.

[164] Craig J. Fennie and Karin M. Rabe. “First-principles investigation of ferroelectricity in epitaxially strained Pb_2TiO_4”. In: *Physical Review B* 71.10 (2005). DOI: 10.1103/physrevb.71.100102.

[165] Jeehye Lee and Tomás A. Arias. “Structural phase transitions in Ruddlesden-Popper phases of strontium titanate: Ab initio and modulated Ginzburg-Landau approaches”. In: *Physical Review B* 82.18 (2010). DOI: 10.1103/physrevb.82.180104.

[166] Turan Birol, Nicole A. Benedek, and Craig J. Fennie. “Interface Control of Emergent Ferroic Order in Ruddlesden-Popper $Sr_{n+1}Ti_nO_{3n+1}$”. In: *Physical Review Letters* 107.25 (2011). DOI: 10.1103/physrevlett.107.257602.

[167] N. Waterfield Price et al. “Strain Engineering a Multiferroic Monodomain in Thin-Film $BiFeO_3$”. In: *Physical Review Applied* 11.2 (2019). DOI: 10.1103/physrevapplied.11.024035.

[168] F. S. Razavi et al. “Epitaxial strain induced metal insulator transition in $La_{0.9}Sr_{0.1}MnO_3$ and $La_{0.88}Sr_{0.1}MnO_3$ thin films”. In: *Applied Physics Letters* 76.2 (2000), pp. 155–157. DOI: 10.1063/1.125687.

[169] T. Ghani et al. “A 90nm high volume manufacturing logic technology featuring novel 45nm gate length strained silicon CMOS transistors”. In: 2003 IEEE International Electron Devices Meeting. DOI: 10.1109/iedm.2003.1269442.

[170] W. Kwestroo and H. A. M. Paping. “The Systems BaO-SrO-TiO2, BaO-CaO-TiO_2, and SrO-CaO-TiO_2”. In: *Journal of the American Ceramic Society* 42.6 (1959), pp. 292–299. DOI: 10.1111/j.1151-2916.1959.tb12957.x.

[171] O. G. Vendik and L. T. Ter-Martirosyan. "Electrostrictive mechanism of microwave losses in a planar strontium titanate film capacitor". In: *Technical Physics* 44.8 (1999), pp. 954–959. DOI: 10.1134/1.1259412.

[172] O. G. Vendik and A. N. Rogachev. "Electrostriction mechanism of microwave losses in a ferroelectric film and experimental confirmation". In: *Technical Physics Letters* 25.9 (1999), pp. 702–704. DOI: 10.1134/1.1262605.

[173] M. Jungbauer et al. "Atomic layer epitaxy of Ruddlesden-Popper $SrO(SrTiO_3)_n$ films by means of metalorganic aerosol deposition". In: *Applied Physics Letters* 105.25 (2014), p. 251603. DOI: 10.1063/1.4905055.

[174] Reinhard Uecker et al. "Large-lattice-parameter perovskite single-crystal substrates". In: *Journal of Crystal Growth* 457 (2017), pp. 137–142. DOI: 10.1016/j.jcrysgro.2016.03.014.

[175] Simon Fichtner et al. "AlScN: A III-V semiconductor based ferroelectric". In: *Journal of Applied Physics* 125.11 (2019), p. 114103. DOI: 10.1063/1.5084945.

[176] Wenbo Wang et al. "High performance AlScN thin film based surface acoustic wave devices with large electromechanical coupling coefficient". In: 105.13 (2014), p. 133502. DOI: 10.1063/1.4896853.

[177] Derek York et al. "Unified equations for the slope, intercept, and standard errors of the best straight line". In: *American Journal of Physics* 72.3 (2004), pp. 367–375. DOI: 10.1119/1.1632486.